Title

Design of additively manufactured multi-functional metamaterials

Author

Yao, Desheng

Publication Date

2023

Peer reviewed|Thesis/dissertation

UNIVERSITY OF CALIFORNIA

Los Angeles

Design of additively manufactured multi-functional metamaterials

A dissertation submitted in partial satisfaction of the

requirements for the degree Doctor of Philosophy

in Civil Engineering

by

Desheng Yao

2023

ABSTRACT OF THE DISSERTATION

Design of additively manufactured multi-functional metamaterials

by

Desheng Yao

Doctor of Philosophy in Civil Engineering

University of California, Los Angeles, 2023

Professor Jian Zhang, Co-Chair

Professor Xiaoyu Zheng, Co-Chair

Architected metamaterials are a class of engineered materials with artificially designed structure at micro- or nano-scale that exhibit unusual properties by the interplay between the constitutive materials and the engineered architectures. Recent advancement in additive manufacturing has enabled the integration of functionalities with structural metamaterials via mixing multi-functional particles with 3D-printable materials. However, accurate design of functional performance of as-fabricated metamaterial has not been demonstrated for the following reasons. Attributed to weak interfacial behaviors, physical mixture of functional particles with 3D-printable matrix demonstrates low functional performances, which is several orders of magnitude of homogeneous functional materials. Prior studies has employed surface functionalization to enhance the effective

performance of functional composites, while the effect of this process remains elusive. Additionally, despite that the structure properties of metamaterials have been thoroughly studied, it is still unclear how the concept of structural metamaterials can be translated to multi-functional coupling behaviors (i.e., electro-mechanical coupling, thermo-electric coupling, etc.).

This work aimed to develop a theoretical design framework which will enable accurate creation of functional performance via guiding the formulation of constitutive material and architectural design of multi-functional metamaterial. In specific, a theoretical model, effective interphase model, is established to characterize the interaction between functional particles and matrix materials, which enables the realization of desired functional properties of composite colloids for additive manufacturing via tuning the formulating parameters like particle loading, surface functionalization level, etc. Next, design of effective performance of functional metamaterial via manipulating its spatial arrangement is investigated and demonstrated. This design strategy is applied in tailoring the anisotropy of piezoelectric material constrained by the intrinsic crystal structure, decoupling the electro-mechanical responses in each orthogonal directions as load orientation and magnitude sensor, and creating all physically feasible actuation modes as actuators with simple electrode arrangements. Additionally, a machine learning based design framework is developed to inverse design the desired compressive response of metamaterials. This machine learning framework breaks the limitation on designing a few mechanical properties of existing methods and enables the re-creation of full temporal and spatial mechanical response of metamaterials. In general, this work provides a comprehensive design methodology of functional behaviors which characterizes the effect of both the constitutive material properties and architectures of multi-functional metamaterials.

The dissertation of Desheng Yao is approved.

Ertugrul Taciroglu

Ximin He

Jian Zhang, Committee Co-Chair

Xiaoyu Zheng, Committee Co-Chair

University of California, Los Angeles

2023

Table of Contents

List of Figures

List of Tables

List of Acronyms

PZT Lead zirconate titanate

PVDF Polyvinylidene fluoride

AM Additive manufacturing

FEA Finite element analysis

ML Machine learning

FDM Fused deposition modeling

SLS Selective laser sintering

CNT Carbon nanotube

SLA Stereolithography

UV Ultraviolet

EIM Effective interphase model

RVE Representative volume element

PBC Periodic boundary condition

PμSL Projection micro-stereolithography

FTIR-ATR Fourier-transform Infrared Spectroscopy Attenuated Total Reflectance

NRMSE Normalized root-mean-square error

SGD Stochastic gradient descent

CF Carbon Fiber

ABS Acrylonitrile butadiene styrene

TPU Thermo-Plastic Polyurethane

GBR Gradient Boosting regressor

RFR Random Forest regressor

MLPC Multilayer Perceptron Classifier

Acknowledgements

I would like to express my sincere gratitude to Prof. Xiaoyu (Rayne) Zheng's dedicated instruction and understanding during the process of pursuing my Ph.D. degree, especially during the time I suffered from family misfortune. I am grateful for the opportunity Dr. Zheng provided me to cultivate the ability and experience in scientific research.

I am deeply grateful to all the members of my committee who provided constructive advices on my research and assisted me in completing my Ph.D. degree at UCLA.

I wish to extend my heartfelt appreciation to my family members and friends for their unwavering support throughout my journey. They have always been my pillar of strength, motivating me to strive forward.

I would like to acknowledge my group mates at the Advanced Manufacturing and Metamaterials Laboratory (AMML) for their invaluable advice and support.

I would like to express my gratitude to my collaborators, with whom I had the opportunity to work on various projects.

I would like to acknowledge ICTAS Junior Faculty Award, NSF CMMI 1727492, US Air Force Office of Scientific Research (FA9550-18-1-0299, N00014-20-1-2504, and FA9550-21-1-0241), US Office of Naval Research Young Investigator Award (N00014-18-1-2553), US Office of Naval Research (N00014-19-1-2723 and N00014-20-1-2504:P00001), US Defense Advanced Research Projects Agency (D20AP00001-02), National Science Foundation (2048200 and 2119643) and

Startup support from Virginia Tech, University of California, Los Angeles and University of California, Berkeley for funding support.

Chapter 3 is reproduced from "**D. Yao**, H. Cui, R. Hensleigh, P. Smith, S. Alford, D. Bernero, S. Bush, K. Mann, H. F. Wu, M. Chin-Nieh, G. Youmans, X. Zheng, Achieving the upper bound of piezoelectric response in tunable, wearable 3D printed nanocomposites, Advanced Functional Materials, 1903866, 2019". DOI: https://doi.org/10.1002/adfm.201903866

Chapter 4.2 is reproduced from "H. Cui, R. Hensleigh, **D. Yao**, D. Maurya, P. Kumar, M. Kang, S. Priya, X. Zheng, Three-dimensional printing of piezoelectric materials with designed anisotropy and directional response", Nature Materials, volume 18, pages234–241 2019". DOI: https://doi.org/10.1038/s41563-018-0268-1

Chapter 4.3 is a manuscript in preparation for publication.

Chapter 4.4 is reproduced from "H. Cui, **D. Yao**, H. Lu, A Calderon, Z. Xu, S. Davaria, Z. Wang, P. Mercier, P. Tarazaga, X. Zheng, Design and printing of proprioceptive three-dimensional architected robotic metamaterials, Science, 2021, Vol 376, Issue 6599, page1287-1293". DOI: 10.1126/science.abn0090

Chapter 5 is reproduced from "C. Ha, **D. Yao**(contribute equally), Z. Xu, C. Liu, H. Liu, D. Elkins, M. Kile, V. Deshpande, Z. Kong, M. Bauchy, and X. Zheng, Rapid inverse design of metamaterials based on prescribed mechanical behavior through machine learning, Nature Communications, 14, 5765 (2023)". DOI: https://doi.org/10.1038/s41467-023-40854-1

Vita

Education

Doctor of Philosophy, Civil Engineering Expected: Dec. 2023
UCLA, Los Angeles, CA
Doctor of Philosophy, Mechanical Engineering Transferred to UCLA, Sep. 2019
Virginia Tech, Blacksburg, VA
Master of Science, Mechanical Engineering Jun. 2017
Lehigh University, Bethlehem, PA
Bachelor of Engineering, Mechanical Engineering Jun. 2015
Beihang University, Beijing, China

Publications

- H. Cui, R. Hensleigh, **D. Yao**, D. Maurya, P. Kumar, M. Kang, S. Priya, X. Zheng, "Three-dimensional printing of piezoelectric materials with designed anisotropy and directional response", ***Nature Materials, volume 18, pages234–241 2019***.
- **D. Yao**, H. Cui, R. Hensleigh, P. Smith, S. Alford, D. Bernero, S. Bush, K. Mann, H. F. Wu, M. Chin-Nieh, G. Youmans, X. Zheng, "Achieving the upper bound of piezoelectric response in tunable, wearable 3D printed nanocomposites", ***Advanced Functional Materials, 1903866, 2019*** (Featured on Front Cover).
- H. Cui, **D. Yao**, et. al., "Design and printing of proprioceptive three-dimensional architected robotic metamaterials", ***Science, 2021, Vol 376, Issue 6599, page1287-1293***
- C. Ha, **D. Yao**(contributed equally), et. al., "Rapid inverse design of metamaterials based on prescribed mechanical behavior through machine learning", ***Nature Communications, 14, 5765 (2023).***
- R Hensleigh, H Cui, Z Xu, J Massman**, D Yao,** J Berrigan, X Zheng, "Charge-programmed three-dimensional printing for multi-material electronic devices", ***Nature Electronics, volume 3 page 216-224, 2020***.
- N JRK Gerard, M Oudich, Z Xu, **D Yao**, H Cui, C J Naify, A Ikei, C A Rohde, X Zheng, Y Jing, "Three-Dimensional Trampolinelike Behavior in an Ultralight Elastic Metamaterial", ***Physical Review Applied, volume 16 Issue 2***.

Presentations

- **D. Yao**, H. Cui, R. Hensleigh, X. Zheng, "Achieving the Upper Bound of Piezoelectric Response in Tunable, Wearable 3D Printed Nanocomposites", ***International Solid Freeform Fabrication Symposium-Additive Manufacturing Conference, Austin, Texas, Aug. 2019***
- **D. Yao**, H. Cui, R. Hensleigh, X. Zheng "Achieving the Upper Bound of Piezoelectric Response in Tunable, Wearable 3D Printed Nanocomposites", ***Materials Science & Technology, Portland, Oregon, Oct. 2019 (1st Place Prize in the Annual Material Advantage Graduate Student Poster Contest)***

- H. Cui, **D. Yao**, R. Hensleigh, X. Zheng "Rational design and printing of precision piezoelectric actuators", ***American Society of Precision Engineering, Austin, Texas, Jan. 2020***
- **D. Yao,** C. Ha, X. Zheng "Rapid creation of metamaterial with prescribed mechanical behaviors" ***TMS Annual Meeting, Anaheim, California, Mar. 2022***

Chapter 1 Introduction

In this chapter, a general introduction to functional materials and architected metamaterials is presented. The motivation and objective of the studies is displayed in the conclusion of this chapter. The primary goal of this chapter is to provide readers with a comprehensive understanding of the context and rationale behind the research work presented in this dissertation.

1.1 Functional materials

Functional materials are materials that process particular native behaviors and functionalities of their own. These materials are often found in ceramics, metals, polymers, and organic molecules. Different from structural materials, these functional materials demonstrate property changes (i.e., shape morphing, electric charge accumulation, etc.) in response to a determined stimuli (i.e., thermal, mechanical, electric loading). Attributed to their unique behaviors, functional materials have been wildly used in smart devices. Herein, several representative types of functional materials and their corresponding applications is presented below.

1.1.1 Piezoelectric material:

Piezoelectricity denotes the linear electro-mechanical coupling behaviors of crystalline material, which demonstrate electric charge accumulation on the surface when subject to mechanical loads, or vice versa, experience mechanical strain with external electric field applied. In additional to the linear behavior of electro-mechanical coupling, piezoelectric materials also display superior frequency responses. Attributed to these advantages, piezoelectric materials are commonly employed as stress/strain sensors and actuators.

There are two categories of piezoelectric materials: piezoelectric ceramic like lead zirconate titanate (PZT), and piezoelectric polymer like Polyvinylidene fluoride (PVDF).

1.1.2 Shape memory material:

Shape memory materials are a class of materials that is capable of reverting from one configuration to a different one when being heated or otherwise triggered. Shape memory materials can usually sustain large deformation strain, so they are mostly used as actuators in the field of aerospace, automotive, and medical devices. There are two categories of shape memory materials: shape memory alloys and shape memory polymers.

1.1.3 Magnetostrictive material:

Magnetostrictive materials are substance that undergo mechanical deformation (either change in shape or dimension) in response to an applied magnetic field. Unlike piezoelectricity, magnetostriction is a nonlinear functional response, and magnetostrictive materials are usually used in diverse range of application scenarios, such as vibration absorbers, underwater sonar, and ultrasonic sensors.

Attributed to their unique behaviors that correlate different physical quantities, researchers have performed extensive studies on the additive manufacturing (AM) of functional materials. Realizing 3D printing of functional materials enables the freeform fabrication of multi-functional devices suitable for customization and personalization, which also reduces waste and environmental impact of the manufacturing process. Additionally, these research work further provides the opportunity of direct fabrication the next generation of smart system integrated with multiple functionalities.

In the current fabrication approaches, functional materials, processed as infill phase (i.e., nano-particles), are mixed with 3D-printable matrix forming the composite feedstock for AM. However, the interaction between functional phase and matrix phase remains elusive, which present significant challenge of accurate design and characterization of functional behaviors of as-fabricated materials.

In this work, author developed a theoretical model to precisely describe the effective material performances, taking into account of all parameters of functional feedstock. The developed model enables the selection of optimal design formulation satisfying the requirement of functional and structural performances of the materials.

1.2 Architected metamaterial

Architected metamaterials are a class of engineered materials with artificially designed structure at micro- or nano-scale that exhibit unusual properties by the interplay between the constitutive materials and the engineered architectures. Additive manufacturing (AM) enables the structural properties to be tailored in ways that are impossible in bulk materials, via the microarchitecture design of three-dimensional (3D) metamaterials. In specific, these materials can exhibit exotic properties such as negative Poisson's ratio[1-3], negative compressibility[4,5], ultralightness and ultrastiffness, shape recoverability[6-8], and multiple stable states[9-11].

The architected metamaterials can be classified into two main categories: structural metamaterials and functional metamaterials. Structural metamaterials are exploited for their load-bearing capabilities and mechanical behaviors, and used primarily to define the shape or configuration of the object. In contrast, attributed to the unusual behavior of constitutive material, functional

metamaterials are employed to achieve specific functionalities, and realize the process and transmission of the physical signals.

Mechanical properties and their designs strategies of structural metamaterials have been extensively studied. The exotic mechanical properties give rises to application of structural metamaterials in different fields across a wide range of scales. For instance, in automotive field, architected honeycomb structures are employed for the purpose of impact reduction and energy absorption[12]. Meanwhile, previous researchers have proposed various design methodology to achieve desired mechanical properties.

- Theoretical approaches employ analytically derived equations to correlate the design parameters with the target structural behaviors[13]. This type of design methods is established on the basis of the deformation mechanics, and demonstrates satisfactory accuracy in certain quantities like elastic modulus of metamaterials.

- Topology optimization is a numerical design approach that exploits finite element analysis (FEA) to approximate the target properties with iterative performance simulation and adjustment on the initial design[14,15]. Constitutive equations of material are invoked in these methods and they show negligible deviation in a wide range of designed quantities.

- Machine learning (ML) based design methods utilize complex mathematical model to establish the relationship between design parameters with target properties on computer[16-18]. With high-quality training data, ML based method can provide high design accuracy.

Integration of functionalities with structural metamaterials endows the material with the capability to perform certain functions. However, it remains unknown that how to transfer the concept of

structural metamaterial to multi-physics coupling behaviors. In this work, author developed a systematic design framework that effectively correlate the functional response with architectural design of metamaterials, enabling accurate realization of arbitrary functionalities of interest.

1.3 Research goal and research framework

My research work aims to develop a comprehensive design framework which enables the precise creation of desired functional response via tuning the constitutive material formulation and arranging the micro-architecture of multi-functional metamaterials.

To achieve the proposed research objective, I have developed my research framework, as presented in Figure 1-1, with a focus on two major aspects: base material formulation and micro-architecture design.

First, I established a theoretical model capable of fully characterizing the effective properties of the composite feedstock, and further predicting optimal composition parameters 3D-printable functional materials.

Next, I developed a systematic design strategy of micro-architecture for the realization of arbitrary anisotropy and decoupled functional responses of piezoelectric materials.

Lastly, I employed ML based design framework for the creation of full temporal and spatial response of structural metamaterials.

This comprehensive design framework enables us to systematically design the effective behaviors and complete temporal responses of functional metamaterial with tailored property orientations.

The outcome of this work set up the foundation of designing and creating the next generation of smart devices, integrated with multiple functionalities, for various application scenarios.

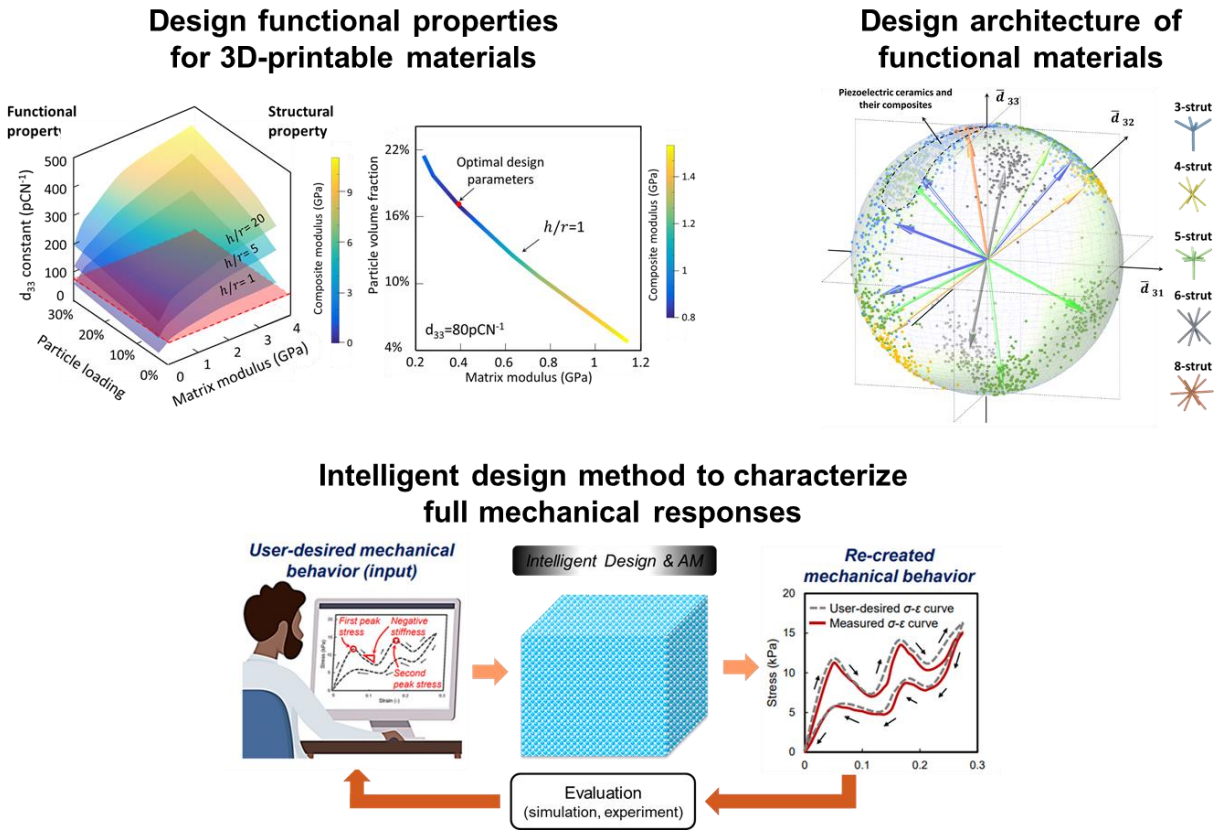

Figure 1-1. Research framework

1.4 Research questions

The dissertation's primary research questions are presented below, and their corresponding responses are provided in the subsequent chapters.

Research Question 1 How to design the formulation of functional composite feedstock to achieve desired properties?

Research Question 2 What is the rational of tailoring effective response of functional metamaterial with architecture design?

Research Question 3 What is the purpose of designing full material response in temporal domain? Why ML based method is required?

1.5 Dissertation outline

Additive manufacturing of functional material with or without architected micro-architecture has been demonstrated in prior research. While, precisely designing and tailoring the effective properties is still not addressed, which presents significant challenges on the further application of functional metamaterials. This dissertation is structured in a way that each chapter, ranging from chapter 3 to 5, addresses each individual challenge. In specific, the author identifies the critical issues related to each challenge and demonstrates the corresponding solutions.

Chapter 2 describes a comprehensive review of current status of additive manufactured functional materials. The existing AM techniques for the fabrication of functional composite feedstock is provided. The effect of surface process of active infill phase on the effective functional behaviors of as-fabricated composite parts is discussed. Additionally, a literature review of the architected functional metamaterial design is performed, with the emphasis on the limitation in the application of these design methods in specific tasks. Next, the scientific challenges and research objectives proposed to address corresponding challenges is presented in this chapter. To sum up, this chapter provides a detailed analysis on the two main contributing factors, namely the base material properties and the architectural design, of effective properties of additively manufactured functional metamaterials.

Chapter 3 demonstrated the development of theoretical model to instruct the design formulation of 3D-printable composite feedstock with desired functional and structural properties. In addition to the loading of active infill phase and material properties of both infill and matrix phases, the interfacial interaction between these two phases plays an important role in the resulting functional performances. The author developed a theoretical model to fully characterize the effective behaviors, taking into account the effect of all design parameters of the functional composite feedstock. The theoretical prediction is validated by numerical simulation and experimental testing results, demonstrating the potential of accurate design of functional performances. The developed theoretical model is capable of guiding optimal selection of feedstock composition, enabling the realization of high functional responses across a wide range of mechanical compliance range, which is suitable for different application scenarios.

Chapter 4 describes the systematic design strategy of piezoelectric metamaterial to realize arbitrary functional responses. The author developed a comprehensive design framework to translate the concept of structural metamaterial to the multi-physics coupling behaviors, which enables the realization of arbitrary anisotropy of piezoelectric properties, decoupled directional strain responses, and all feasible actuation mode of piezoelectric metamaterials. The intrinsic mechanics of structural metamaterial and the coupling with functional responses is investigated. The developed design framework eliminates the requirement of complicated spatial and orientation arrangement of piezo-active components and sophisticated set up of electrodes. The author demonstrated the experimental validation of each design cases for the validation of the general application of the developed design strategy.

Chapter 5 presents the development of ML based design framework which enables the creation of full compressive response of the metamaterial with high accuracy. Leveraging the forward surrogate model and inverse generative model, the developed ML framework is capable of predicting the metamaterial design while bypassing the one-to-many issues commonly happened in the inverse design tasks. Additionally, via utilizing the experiment based training data, the ML takes account of the effect of fabrication errors on the tested response of as-fabricated metamaterials. Exploration of tailored mechanical responses is demonstrated via tuning the input features of ML framework, which proves the capabilities of creation the behaviors unseen in conventional materials. The developed ML framework represents progress toward a rapid inverse design and manufacturing methodology that allows for prescribing the full spatial and temporal behaviors of a product.

Chapter 6 summarizes the main outcomes and contribution made in the study, along with the future research directions to address the remaining constraints and challenges in the design of multi-functional metamaterials.

Chapter 2 Overview of functional responses of additively manufactured materials

This chapter describes a comprehensive review of current status of additive manufactured functional materials. It starts with displaying the existing AM techniques for the fabrication of functional composite feedstock. The effect of surface process of active infill phase on the effective functional behaviors of as-fabricated composite parts is discussed. Then, a literature review of the architected functional metamaterial design is performed, with the emphasis on the limitation in the application of these design methods in specific tasks. Next, the scientific challenges and research objectives proposed to address corresponding challenges is presented in this chapter. In general, this chapter provides a detailed analysis on the two main contributing factors, namely the base material properties and the architectural design, of effective properties of additively manufactured functional metamaterials.

2.1 Additive manufacturing of functional materials

Additive manufacturing (AM), also known as 3D printing, is a revolutionary manufacturing process which enables rapid creation of objects with complex geometries and desired dimensions. AM of structural materials with all types of fabrication techniques has been extensively investigated in the previous research. On the basis of these well-studied outcomes, researchers have studied the approach to integrate the functionalities into 3D printed objects. The commonly used solution is to mix the pre-processed functional infill phases (particles or fibers) with a matrix phase available for 3D printing. In this dissertation, the author picked piezoelectricity as a representative case of functionalities for its broad application in sensing and actuation.

Kim et al developed a fused deposition modeling (FDM) based piezoelectric composite printing technique with in-situ activation of piezoelectricity during fabrication process[19]. In this demonstrated technique, the piezo-active powders ($BaTiO_3$) were mixed with dissolved polymer matrix (PVDF), forming the composite feedstock for 3D printing. The piezoelectric property d_{33} of as-fabricated composite samples reaches 0.1 pC/N at the powder loading of 15 wt%, which is over two orders of magnitude lower than that of corresponding bulk piezoelectric ceramics (d_{33} > 300pC/N).

Qi et al demonstrated a selective laser sintering (SLS) based piezoelectric composite printing process with carbon nanotube (CNT) added in the composite[20]. The piezo-active particles ($BaTiO_3$) were coated with CNT first via sonication and stirring, and the processed particles were then mixed with matrix powder forming the material for fabrication. The piezoelectric property d_{33} of as-fabricated composite samples reaches 2.1 pC/N at the powder loading of 60 wt%, which is also much lower than that of bulk $BaTiO_3$ceramics (d_{33} > 300pC/N).

Mitkus et al presented a stereolithography (SLA) based piezoelectric composite printing process with conductive nanofillers added in the colloids[21]. The piezo-active particles ($BaTiO_3$) were dispersed in ultraviolet (UV) sensitive photopolymer, and the mixed colloids were solidified with UV light. The piezoelectric property d_{33} of as-fabricated composite samples reaches 1 pC/N at the powder loading of 30 vol%, which is also much lower than that of bulk $BaTiO_3$ceramics (d_{33} > 300pC/N).

2.2 Surface functionalization of piezoelectric particles

Attributed to functionality-processability tradeoff, the obtained piezoelectric coefficients d_{33} of as-fabricated composite, printed by various AM techniques, demonstrate the fact that simple physical mixture of functional particles and matrix phase gives rise to effective properties over two orders of magnitude lower than that of pure ceramics. Increasing particle concentration leads to agglomeration[22], high viscosity[23], and significant light absorption[24], making it difficult to manufacture fully complex micro-architectures or free form-factors. Additionally, the incompatibilities between high stiffness nanoparticle and low stiffness polymer, resulting in poor interfacial adhesion[25], reduce stress transfer efficiency from the polymer matrix to the piezoelectric inclusions, and suppress the functional performance.

Kim et al explored surface functionalization of a low concentration of $BaTiO_3$ nanoparticles (below 2vol%, i.e., 10wt%) to covalently bind them to the polymer matrix[26]. They have demonstrated significant enhancement of the piezoelectric coefficient as compared to non-functionalized dispersion, from ~5 pC/N to ~40 pC/N.

This surface functionalization can enhance particle-polymer compatibility, and enables the production of complex, three-dimensional piezoelectric micro-architectures with high concentrations of piezoelectric nanoparticles while maintaining processability. However, the mechanism of the electro-mechanical property enhancement via the interface between the active nano-inclusion and the structural monomer matrix remains elusive.

2.3 Architectural design of piezoelectric metamaterial

Structural properties of architected metamaterial have been thoroughly studied, and prior research have demonstrated various exotic material behaviors unseen in the constitutive counterpart. Following the similar approach, translating the concept of architectural design to multi-physics coupling behaviors should provide novel responses different from homogeneous functional materials.

Yang et al presented a series of piezoelectric metamaterial designs, which enables the realization of nonzero term for all components in the piezoelectric coefficient tensor[27]. For bulk PZT, only 5 out of 18 piezoelectric coefficients are nonzero values ($d_{31}=d_{32}\neq 0$, $d_{33}\neq 0$, $d_{15}=d_{24}\neq 0$). The researchers assembled multiple piezo-active elements, where each element displays a unique material orientation (poling direction), with various pairs of driving electrodes to achieve target macroscopic deformation.

While, the challenge in fabrication process, brought by sophisticated material orientation and complex driving voltage arrangement, constraints the general application of this piezoelectric metamaterial. Additionally, as the designed metamaterials is the assembly of multiple bulk pieces of piezoelectric elements, they are not capable a uniform deformation on the boundary, which further limits their application in actuation tasks.

2.4 Scientific challenges and research objectives

2.4.1 Designing the functional properties of 3D printable material feedstock

The physical mixture of active phase with 3D printable matrix phase yields low effective functional response of as-fabricated samples. Increasing the concentration of active phase is capable of enhancing the functional behaviors to a certain extent. However, attributed to the functionality-processibility tradeoff, the increased loading of functional particles yields serious issues in fabrication process, such as particle agglomeration, high viscosity, and severe light absorption.

Surface functionalization process has been employed to improve interfacial adhesion between different phases and subsequently functional responses. But the mechanism of improvement in electro-mechanical coupling responses still remain elusive.

Therefore, the resulting function responses obtained from existing AM techniques rely on experimental trials. And there is no theoretical design methodology to guide composite formulation to achieve desired functional response before fabrication process.

2.4.2 Designing the micro-architecture of functional metamaterials

Different from mechanical properties, functional behaviors is generally anisotropy material responses. Therefore, the design methodology of mechanical quantities cannot be directly translated to functional properties. Existing theoretical design formulas only consider the relationship between effective mechanical properties with the design parameters of the structural metamaterials. Additionally, the correlation between macroscopic and local strain/stress field, the

multi-physics coupling of constitutive materials, and the summation method of all effective contribution of individual units should be accounted in the design of functional metamaterials.

2.4.4 Research objective

Constitutive material properties and architectural design are two contributing factors that determine the effective responses of the functional metamaterials. This dissertation focuses on designing functional responses of additively manufactured metamaterials. In specific, the author developed a theoretical model to instruct the optimal composition formulation of material feedstock for achieving the desired functional and structural properties. Furthermore, the author established a general design methodology of micro-architecture, which enables the creation of arbitrary material anisotropy and decoupled strain responses of functional metamaterials. This dissertation emphasizes the design of effective functional responses as the instruction of the AM process of functional materials.

The dissertation's main research objectives are as follows:

1. To understand the effect of all contribution factors of functional responses, including functional phase concentration, material properties of both infill and matrix phases, interfacial interactions, etc.;

2. To establish a comprehensive theoretical model to reveal the relationship between multi-physics coupling behavior and micro-architecture of metamaterials;

3. To investigate the design method to create the entire temporal responses of structural metamaterial.

Chapter 3 Design functional properties of 3D-printable materials

This chapter described the theoretical model that fully characterizes the effective functional behaviors of a composite material and its application in guiding the formulation of 3D printable feedstock with target functional responses. The chapter starts with the establishment of the theoretical model, adopted from a classic micro-mechanics model. The parameters quantifying the interfacial interactions are obtained with experimental measurements. Next, the theoretical prediction is validated with experimental measurement and numerical simulation. The validated theoretical model is then used to formulate a design map of multi-functional response of functionalized piezoelectric composites. With this design map, two test cases with different requirements of functional and structural properties are demonstrated.

3.1 Development of theoretical model – effective interphase model (EIM)

Herein, to capture the physical foundation of the observed electromechanical properties at a variety of loading conditions and surface functionalization level, we establish the theoretical model and quantify the effective electromechanical properties that arise from the tunable structural parameters of the active and matrix phases. To predict the functional performance of the nanocomposite, we express the electromechanical properties of the piezoelectric materials as[28]:

$$E_{\mathrm{iJMn}} = \begin{cases} C_{\mathrm{iJMn}} & \text{for J, M} = 1,2,3 \\ e_{\mathrm{nij}} & \text{for J} = 1,2,3, \text{M} = 4 \\ e_{\mathrm{imn}} & \text{for J} = 4, \text{M} = 1,2,3 \\ -\kappa_{\mathrm{in}} & \text{for J} = \text{M} = 4 \end{cases} \quad (3.1)$$

Where C_{ijmn}, e_{imn} and κ_{in} $(\mathrm{i}, \mathrm{j}, \mathrm{m}, \mathrm{n} = 1,2,3)$ are the elastic moduli, the piezoelectric constant and the dielectric constant of the material, respectively. The effective property of the composite is

evaluated through the calculation of the electromechanical property matrix E_{iJMn}. The piezoelectric charge constant d_{33}, that quantifies the polarization per unit stress, is calculated as:

$$d_{33} = \sum_{i=1}^{3} e_{3ii} C_{ii33}^{-1} \qquad (3.2)$$

where C_{ii33}^{-1} represents the corresponding term in the compliance matrix, the inverse of the elastic stiffness matrix C_{ijmn}.

While existing analytical models, including the law-of-mixture model[29] and laminate models[30], etc., have been used to calculate the effective properties of laminates, they are not suitable for characterizing the scenarios where the morphology and the distribution of the active inclusion affect the effective performance of the composite[31]. Mori-Tanaka model[32-36], a classic micromechanical model, has been used to evaluate the effective property of nanocomposite. However, after surface functionalization, the covalent bonds between the surface linker and the monomer matrix generate an interphase region (Figure 3-1a), which inhibits the relative sliding between the piezo-active inclusion and the polymer matrix[37]. This enhanced interfacial behavior was not captured in the above-mentioned Mori-Tanaka model which assumes matrix and the inclusion are assumed perfectly bonded[38].

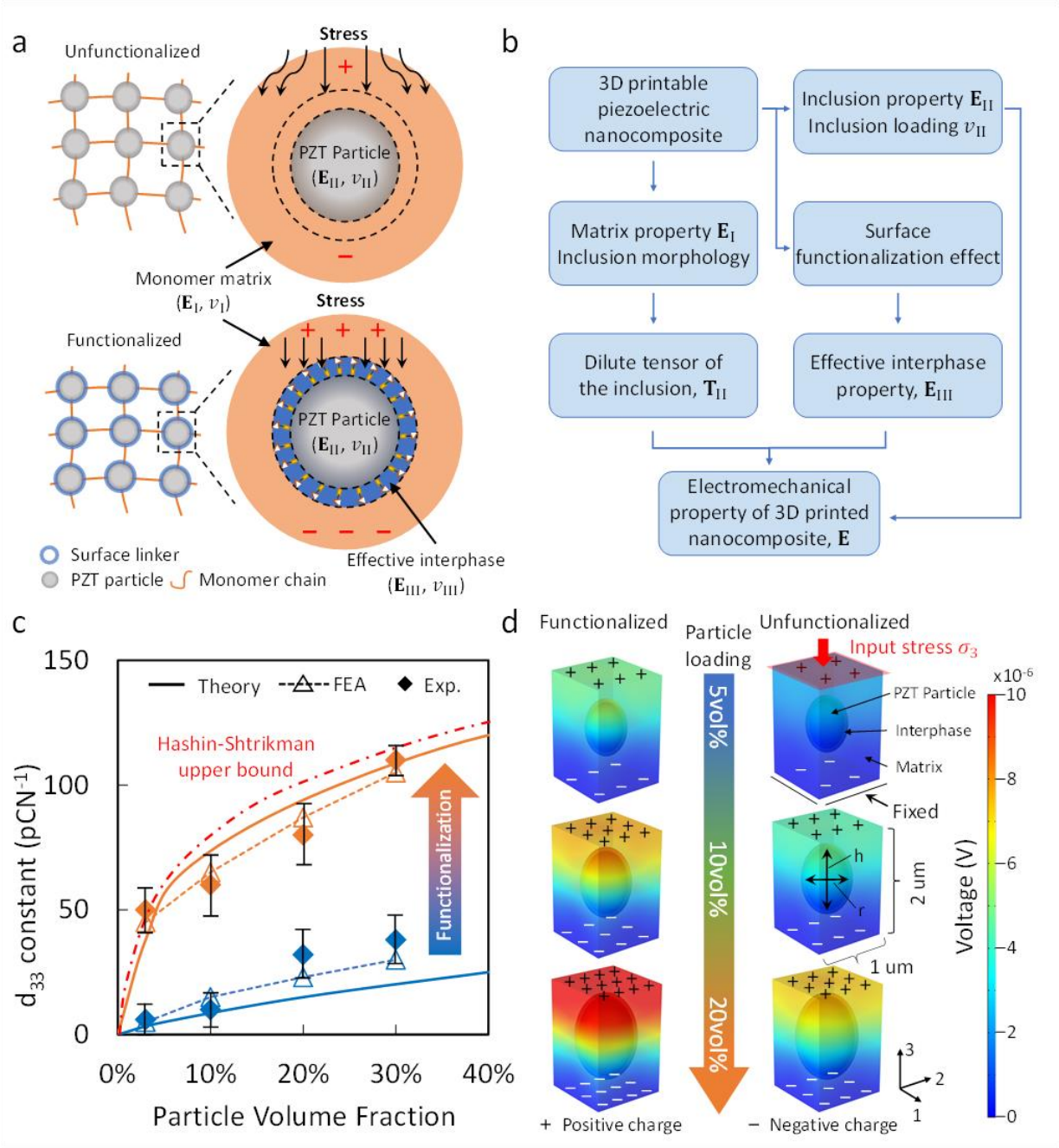

Figure 3-1. Effective interphase model for characterization of functional responses of piezoelectric composites. (a) Schematics of our effective interphase model for calculating piezoelectric response of functionalized PZT colloids. The dashed lined region represents the effective interphase with electromechanical properties ($\mathbf{E}_{III}$, ν_{III}) formed by the covalent linkage from surface functionalization that connects the active and monomer phase. For non-functionalized case the property of such effective interphase approaches zero and can be incorporated into the model. (b) Flow chart summarizing the effective interphase model for calculating the electromechanical performance of the 3D printable piezoelectric nanocomposite.

(c) Theoretical numerical and experimental results of piezoelectric charge constant d_{33} of functionalized and nonfunctionalized nanocomposite against a range of particle volume loadings. (d) FEA results of functionalized (Left) and nonfunctionalized (Right) RVE with different volume fractions.

Here, to describe the effective electromechanical property of the functionalized piezoelectric nanocomposite, we introduced a generalized effective interphase model to capture the interfacial effect between inclusion and matrix phases. The theoretical prediction of the functional behavior of the nanocomposite takes account of the constituent material electromechanical property (matrix property $\mathbf{E}_{\mathrm{I}}$ and inclusion property $\mathbf{E}_{\mathrm{II}}$), nano-inclusion morphology (dilute concentration tensor $\mathbf{T}_{\mathrm{II}}$), and the interfacial interaction between phases (surface functionalization effect) as shown in Figure 3-1a and 3-1b. And the effective property of composite including the interfacial region is given as:

$$\mathbf{E} = \mathbf{E}_{\mathrm{I}} + \left((v_{\mathrm{II}} + v_{\mathrm{III}})(\mathbf{E}_{\mathrm{III}} - \mathbf{E}_{\mathrm{I}})\mathbf{T}_{\mathrm{III}} + v_{\mathrm{II}}(\mathbf{E}_{\mathrm{II}} - \mathbf{E}_{\mathrm{III}})\mathbf{T}_{\mathrm{II}}\right)(v_{\mathrm{I}}\mathbf{I} + (v_{\mathrm{II}} + v_{\mathrm{III}})\mathbf{T}_{\mathrm{III}})^{-1} \quad (3.3)$$

where $\mathbf{E}$ is the effective electromechanical stiffness matrix of the as-printed composite which is denoted as E_{iJMn} from Eq. (3.1); $\mathbf{E}_{\mathrm{i}}$ (i=I, II, III) is the electromechanical property matrix of the matrix phase (I), the active material phase (II) and the interphase region(III), respectively; $\mathbf{I}$ is the identity matrix; v_{i} (i=I, II, III) is the volume fraction of the corresponding phase; $\mathbf{T}_{\mathrm{II}}$ and $\mathbf{T}_{\mathrm{III}}$ is the dilute concentration tensor for the nanoparticle and the interphase, which is dependent on the morphology and volume fraction of the particle.

While Poisson's ratio v^{III}, piezoelectric constant e and dielectric constant κ of the interface CH_2-CH_2 groups can be considered consistent with those of the polymer matrix[39], their Young's modulus C^{III} are enhanced by the functionalization level at the nanoparticle interface as the surface coverage of the linkers increases. This allows one to tune the effective stiffness $\mathbf{E}_{III}$ of the interphase region by tuning the degree of functionalization.

3.2 Theoretical derivation of the electro-mechanical properties of the piezoelectric composite

Governing equation of the piezoelectricity, effective stiffness matrix E

To characterize the performance of piezoelectric polymer composite, we start from the governing equations of piezoelectricity given as[28]:

$$\sigma_{ij} = C_{ijmn}\varepsilon_{mn} - e_{nij}E_n \quad (3.4)$$

$$D_i = e_{imn}\varepsilon_{mn} + \kappa_{in}E_n \quad (3.5)$$

where σ_{ij}, D_i, ε_{mn} and E_n (i, j, m, n=1, 2, 3) are stress, electric displacement, strain and electric field, respectively. C_{ijmn}, e_{imn} and κ_{in} are the elastic moduli, piezoelectric constant, and dielectric constant of the piezoelectric material, respectively. Rearranging equation yields the compact form of:

$$\Sigma_{iJ} = E_{iJMn}Z_{Mn} \quad (3.6)$$

where i, n=1, 2, 3 and J, M=1, 2, 3, 4. The stress-electric displacement Σ_{iJ}, the strain-electric field Z_{Mn} and the effective electromechanical stiffness E_{iJMn} are in the form of:

$$\Sigma_{\mathrm{iJ}} = \begin{cases} \sigma_{\mathrm{ij}} & \text{for J} = 1,2,3 \\ D_{\mathrm{i}} & \text{for J} = 4 \end{cases} \quad (3.7)$$

$$Z_{\mathrm{Mn}} = \begin{cases} \varepsilon_{\mathrm{Mn}} & \text{for M} = 1,2,3 \\ -E_{\mathrm{n}} & \text{for M} = 4 \end{cases} \quad (3.8)$$

$$E_{\mathrm{iJMn}} = \begin{cases} E_{\mathrm{iJMn}} & \text{for J, M} = 1,2,3 \\ e_{\mathrm{nij}} & \text{for J} = 1,2,3, \text{M} = 4 \\ e_{\mathrm{imn}} & \text{for J} = 4, \text{M} = 1,2,3 \\ -\kappa_{\mathrm{in}} & \text{for J} = \text{M} = 4 \end{cases} \quad (3.9)$$

The piezoelectric behavior of the piezoelectric polymer composite is characterized by the stiffness matrix E_{iJMn}.

Mori-Tanaka model

The overall property of the heterogeneous piezoelectric material is evaluated by taking the volume-averaged piezoelectric field and displacement matrix as[32]:

$$\bar{\boldsymbol{\Sigma}} = \sum_{r=1}^{N} v_r \bar{\boldsymbol{\Sigma}}_r \quad (3.10)$$

$$\bar{\mathbf{Z}} = \sum_{r=1}^{N} v_r \bar{\mathbf{Z}}_r \quad (3.11)$$

where r denotes the phase (r=1 represents the matrix phase), v_{r} is the volume fraction of the r-th phase in the composite, and the overbar represent the volume averaged quantity. The constitutive equation Eq. 3.6 could be expressed as:

$$\bar{\boldsymbol{\Sigma}} = \mathbf{E}\bar{\mathbf{Z}} \quad (3.12)$$

And the volume-average strain-electric field in phase *r* is:

$$\overline{\boldsymbol{\Sigma}}_{\mathrm{r}} = \mathbf{A}_{\mathrm{r}}\overline{\boldsymbol{\Sigma}} \quad (3.13)$$

where $\mathbf{A}_{\mathrm{r}}$ is the concentration tensor of the *r*-th phase, and

$$\sum_{\mathrm{r}=1}^{\mathrm{N}} v_{\mathrm{r}}\mathbf{A}_{\mathrm{r}} = \mathbf{I} \quad (3.14)$$

where $\mathbf{I}$ is the identity matrix. Combining Eq. 3.10 to Eq. 3.14 yields the effective electromechanical matrix $\mathbf{E}$ in terms of effective stiffness of each phase as[40]:

$$\mathbf{E} = \mathbf{E}_{\mathrm{I}} + \sum_{\mathrm{r}=1}^{\mathrm{N}} v_{\mathrm{r}}(\mathbf{E}_{\mathrm{r}} - \mathbf{E}_{1})\mathbf{A}_{\mathrm{r}} \quad (3.15)$$

The Mori-Tanaka model[38,41], a classical micromechanical model assuming perfect bonding between the matrix and the composite, has been widely used to predict the effective property of piezoelectric nanocomposite. The concentration tensor $\mathbf{A}_{\mathrm{r}}$ given by the Mori-Tanaka model is[38,41]:

$$\mathbf{A}_{\mathrm{r}} = \mathbf{T}_{\mathrm{r}}^{\mathrm{dil}}(c_1\mathbf{I} + \sum_{\mathrm{r}=1}^{\mathrm{N}} v_{\mathrm{r}}\mathbf{T}_{\mathrm{r}}^{\mathrm{dil}})^{-1} \quad (3.16)$$

$$\mathbf{T}_{\mathrm{r}}^{\mathrm{dil}} = (\mathbf{I} + \mathbf{S}_{\mathrm{r}}\mathbf{E}_{\mathrm{I}}^{-1}(\mathbf{E}_{\mathrm{r}} - \mathbf{E}_{\mathrm{I}}))^{-1} \quad (3.17)$$

Where $\mathbf{T}_{\mathrm{r}}^{\mathrm{dil}}$ is the dilute tensor; $\mathbf{S}_{\mathrm{r}}$ is the piezoelectric Eshelby tensor determined by the inclusion morphology. Rearranging Eq. 3.15 to Eq.3.17 yields the effective property of the composite as:

$$\mathbf{E} = \left(v_1\mathbf{E}_{\mathrm{I}} + v_2\mathbf{E}_{\mathrm{II}}\mathbf{T}_{\mathrm{II}}^{\mathrm{dil}}\right)\left(v_1\mathbf{I} + v_{\mathrm{II}}\mathbf{T}_{\mathrm{II}}^{\mathrm{dil}}\right)^{-1} \quad (3.18)$$

where **E** is the effective electromechanical stiffness of the composite, which was denoted as E_{iJMn} previously, $\mathbf{E}_i$ (i=I, II) is the electromechanical property matrix of the corresponding phase (I and II represents matrix, nanoparticle respectively), and v_i (i=I, II) is the volume fraction of the corresponding phase

Effective interphase model

Due to the incompatibility of hydrophilic nanoparticle and hydrophobic polymer[25], the poor interfacial-interaction adhesion of the piezo-active inclusions reduces the stress transfer efficiency from the polymer matrix to the piezoelectric active material, suppressing the functional performance of the as-fabricated composite[42]. Through the functionalization process, strong covalent bonds between monomer matrix and surface agent grafted on the PZT particle are formed, which enhances the interfacial behavior and improves the stress transfer efficiency[37]. However, this elevated interfacial interaction performance is not characterized by the Mori-Tanaka model. Hence, a modified Mori-Tanaka model, the effective interphase model[43], was invoked to theoretically predict the electromechanical property of the piezoelectric polymer composite incorporating the interfacial effect between inclusion and matrix phases as shown in Figure 3b. The effective interphase model was developed to evaluate the mechanical property of the composite previously. Here, to characterize the functional performance of the piezoelectric nanocomposite, we generalized this effective interphase model by utilizing the effective electromechanical stiffness E_{ijMn} of piezoelectric material in the theoretical expression. Then the effective piezoelectric property of the composite is given as:

$$\mathbf{E} = \mathbf{E}_{\mathrm{I}} + ((v_{\mathrm{II}} + v_{\mathrm{III}})(\mathbf{E}_{\mathrm{III}} - \mathbf{E}_{\mathrm{I}})\mathbf{T}_{\mathrm{III}}^{\mathrm{dil}} + v_{\mathrm{II}}(\mathbf{E}_{\mathrm{II}} - \mathbf{E}_{\mathrm{III}})\mathbf{T}_{\mathrm{II}}^{\mathrm{dil}})\left(v_{\mathrm{I}}\mathbf{I} + (v_{\mathrm{II}} + v_{\mathrm{III}})\mathbf{T}_{\mathrm{III}}^{\mathrm{dil}}\right)^{-1} \quad (3.19)$$

The variables and the subscripts are the same as those in the Mori-Tanaka model. In the effective interphase model, a third phase (interphase) is considered and represented by III. $\mathbf{E}_{\mathrm{III}}$ and v_{III} represent the effective property and the volume fraction of the interphase, respectively. The dilute matrix of the particle $\mathbf{T}_{\mathrm{II}}^{\mathrm{dil}}$ is different from it in the Mori-Tanaka model as:

$$\mathbf{T}_{\mathrm{II}}^{\mathrm{dil}} = \mathbf{I} - \mathbf{S}[\mathbf{S} + (\mathbf{E}_{\mathrm{II}} - \mathbf{E}_{\mathrm{I}})^{-1}\mathbf{E}_{\mathrm{I}}]^{-1} \qquad (3.20)$$

$\mathbf{T}_{\mathrm{III}}^{\mathrm{dil}}$ is the dilute matrix of the interphase as:

$$\mathbf{T}_{\mathrm{III}}^{\mathrm{dil}} = \mathbf{I} - \mathbf{S}\{\frac{v_{\mathrm{II}}}{v_{\mathrm{II}} + v_{\mathrm{III}}}[\mathbf{S} + (\mathbf{E}_{\mathrm{II}} - \mathbf{E}_{\mathrm{I}})^{-1}\mathbf{E}_{\mathrm{I}}]^{-1} + \frac{v_{\mathrm{III}}}{v_{\mathrm{II}} + v_{\mathrm{III}}}[\mathbf{S} + (\mathbf{E}_{\mathrm{III}} - \mathbf{E}_{\mathrm{I}})^{-1}\mathbf{E}_{\mathrm{I}}]^{-1}\} (3.21)$$

3.3 Effective interphase properties measurement

Here, to experimentally identify and evaluate the interphase mechanical properties for our model, nanomechanical characterizations[44] were conducted on functionalized PZT-polymer films. The normal displacement and the lateral force profiles were extracted from a laterally-scratching indenter (90^{o} conical indenter with radius 738nm) while holding the constant vertical force that probes into the scratched films (Figure 3-2a and 3-2b). The interphase region is characterized by the area where scratch depth increases or decreases gradually[45] (see Figure 3-2). We can then extract the volume fraction v_{III} and the effective modulus $\mathrm{C}^{\mathrm{III}}$ of the interphase region from the scratch depth profile and the lateral force curve, respectively (detailed derivations see Method). Here the superscripts I, II and III in the modulus C^{i} (i=I, II, III) represent the polymer matrix, piezoelectric inclusion and interphase region, respectively.

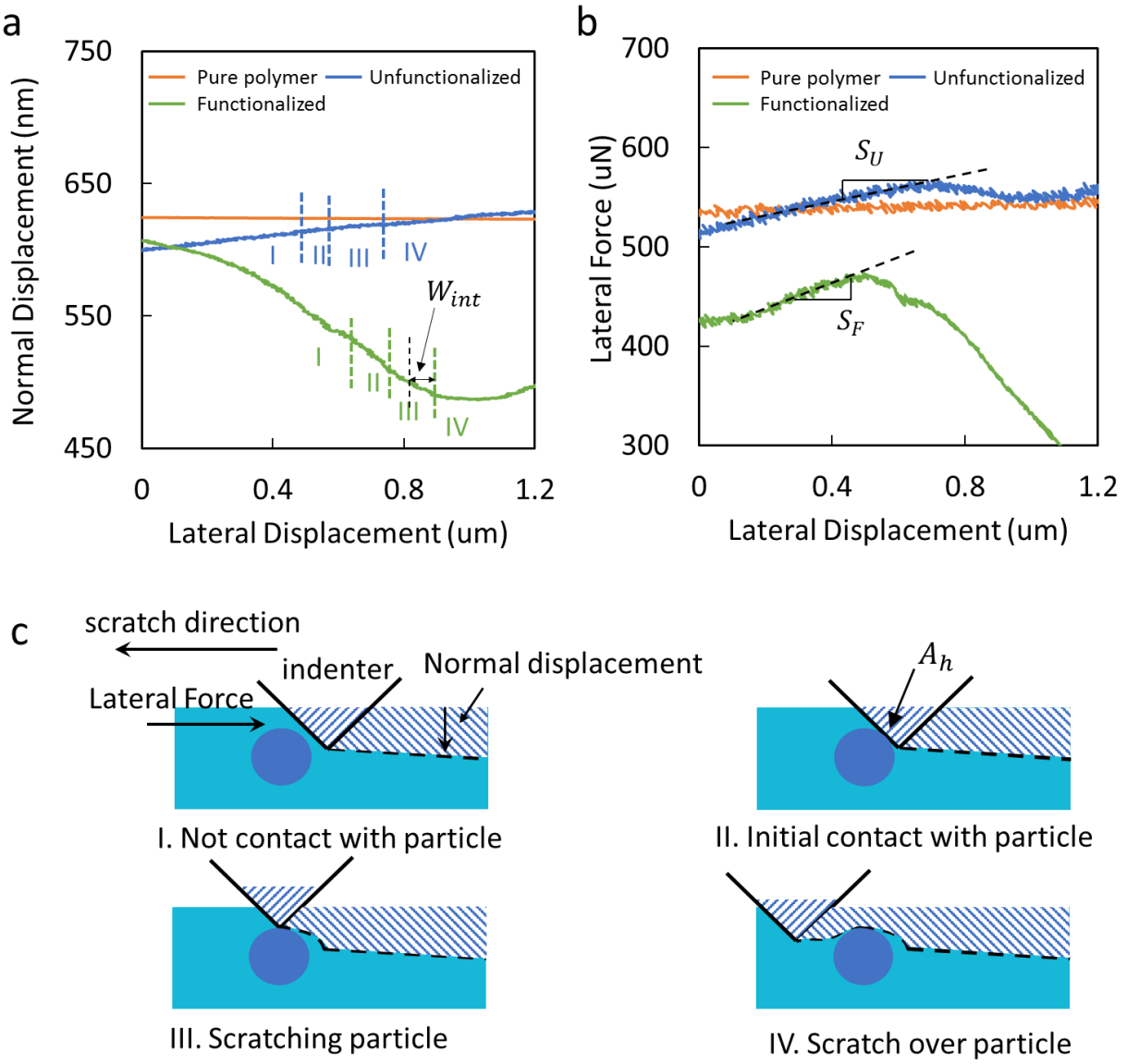

Figure 3-2. Scratch test to obtain interphase stiffness and width used in the theoretical and numerical calculation. (a) Scratch depth profile obtained in the scratch test. (b) Lateral force curve obtained in the scratch test. (c) Four phases within the scratch process and corresponding scratch depth profile.

Nanoindentation is a variety of indentation hardness tests applied to nanoscale measurement[44].

During the nanoindentation process, the indenter probes into the measured sample in the

perpendicular direction to the sample surface under a constant force applied by the transducer. A force-displacement curve is obtained by continuously measuring the vertical probe displacement. The stiffness of the measured sample equals the initial slope of the unloading portion in the force-displacement curve. The modulus of the indented material C_2 is obtained as[46]:

$$E_r = \frac{S}{2\beta}\sqrt{\frac{\pi}{A}} \qquad (3.4)$$

$$E_r = \left(\frac{1-{v_1}^2}{C_1} + \frac{1-{v_2}^2}{C_2}\right)^{-1} \qquad (3.5)$$

where S is the slope of the force-displacement curve extracted from the nanoindentation test, β=1 for the conical indenter used in the indentation test, and A is the contact area. E_r is the reduced modulus for the indented test, C_i and v_i (i=1,2) are the modulus and Poisson's ratio of the corresponding phase, where 1 represents the indenter and 2 represents the indented material.

Different from traditional nanoindentation tests where the indenter only vertically probes into the measured sample, the horizontal translation of the indenter is introduced in the scratch test[47]. The indenter continuously moves in the horizontal plane while holding constant vertical load probing into the measured sample, extracting scratch depth profile and a lateral force curve as shown in Figure 3-2a and 3-2b, correspondingly. As shown in Figure 3-2c, the scratch process could be separated into four periods corresponding to continuous regions in the scratch depth profile: I), the indenter has no contact with the particle; II), the leading edge of the indenter is in contact with the particle; III), the indenter is scratching over the particle region; IV), the indenter has passed the particle. The interphase region is characterized by the area that the scratch depth increases or decreases gradually as shown in Figure 3-2a[45], and the thickness of the interphase region is

extracted from the width of the corresponding region. Here, the thickness of the interphase region is measured around 50nm for functionalized film.

Then, we extracted the interphase region's simplified stiffness from the slope of the lateral force curve. As shown in Figure 3-2b, the simplified stiffness of the functionalized (S_F) and nonfunctionalized nanocomposite (S_U) is extracted from the corresponding curve. The reduced modulus of the interphase region is obtained as:

$$E_r = \frac{S_i}{2\beta}\sqrt{\frac{\pi}{A_h}} \qquad (3.6)$$

where i=U, F represent the nonfunctionalized and functionalized composite, respectively; A_h is the cross-section area of the indenter in the horizontal direction. Following Eq. 3.6, we obtained the effective modulus of the interphase region, which was used in the theoretical and numerical calculation along with the thickness of the interphase. For instance, the effective modulus of the interphase region of PZT-PEGDA composite is 1.38GPa and 178MPa for the functionalized and unfunctionalized case, respectively.

3.4 Validation of effective interphase model

To validate our theoretical prediction on the surface functionalization effect, we conducted numerical analysis in the COMSOL Multiphysics FEA software[48]. The material properties of the piezo-active inclusion, the interphase region, and the monomer matrix are consistent with those used in the theoretical model. We establish a cubic representative volume element (RVE)[49] model to simulate the effective piezoelectric response of the functionalized nanoparticle matrix over a wide range of the particle loading and inclusion aspect ratios. The periodic boundary conditions

(PBC)[49] are enforced to ensure the RVE effectively characterizes the deformation of the macroscopic piezoelectric nanocomposite. In addition, to prevent the rigid body motions and to provide a zero-potential surface for voltage output, the bottom surface of the RVE is fixed in 3-direction and grounded. The piezoelectric voltage output of the RVE is induced by the input stress applied at the top surface (Figure 3-1d), where the color represents the magnitude of the induced voltage. An elevated voltage output trend can be readily visualized with increasing volume fractions in functionalized and unfunctionalized cases, all induced by the same external stress. The piezoelectric charge constant d_{33} of the RVE is evaluated by the ratio between the effective electric displacement D_3^{eff} (average of the electric displacement on the top surface) and the input mechanical stress σ_3^{input} as:

$$d_{33} = \frac{D^{\text{eff}}}{\sigma_{33}} \qquad (3.7)$$

Moreover, we measured the piezoelectric coefficients of the 3D printed piezoelectric materials with preconfigured parameters (with and without functionalization, particle volume loading v_{II} and matrix modulus C^{I}). The fabrication of piezoelectric nanocomposite material starts with the functionalization of the piezoelectric particles. We use trialkoxysilane-methacrylate functionalized PZT, with reaction conditions optimized to provide maximum grafting[50]. After functionalization of the nanoparticles, the functionalization agent is covalently grafted to the piezoelectric nanoparticle surface, Figure 3-3a. The agent provides a sterically hindered surface in the liquid state[51], and after curing by UV-light strong covalent chemical bonds (CH_2-CH_2 group), connect the modified piezoelectric particles with the photo-polymer matrix. This matrix-inclusion linkage enables effective stress transfer between different phases and facilitates composites dispersion uniformity despite high inclusion content. These modified PZT particles are then high-energy ball

milled into an ultraviolet-sensitive monomer with ultra-high concentrations[50] (up to 50vol%, i.e., ~87wt%). This UV-sensitive dispersion is printed with a custom-made large area projection micro-stereolithography (PμSL) system[50] where a tape-casting recoating process[52] is designed to ensure accurate control of the colloidal paste thickness prior to UV pattern exposure (Figure 3-3b). A variety of as-printed piezo-active materials with complex 3D micro-architectures and flexibilities are shown in Figure 3-3c to 3-3f. To active the piezoelectric polarizations, a 5V/um uniform electric field was applied to pole these piezoelectric nanocomposites for one hour under room temperature[53] (Figure 3-4).

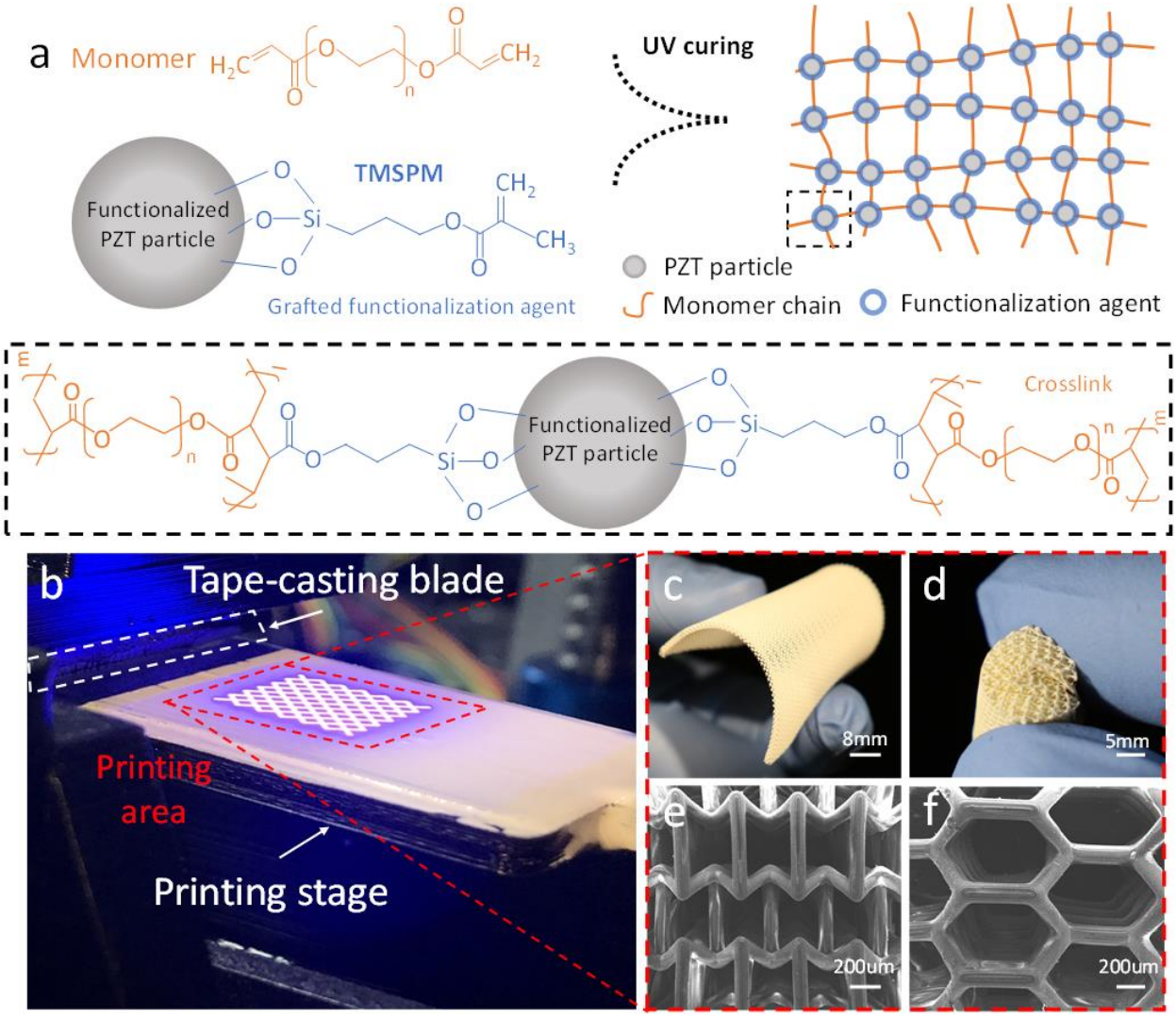

Figure 3-3. Fabrication process of functionalized piezoelectric composites. (a) Chemical structure of the UV-sensitive monomer matrix and the functionalized PZT particles. (b) Custom PuSL fabrication system for piezoelectric nanocomposite. (c)-(f) Additive manufactured piezoelectric complex structures with fine surface finish.

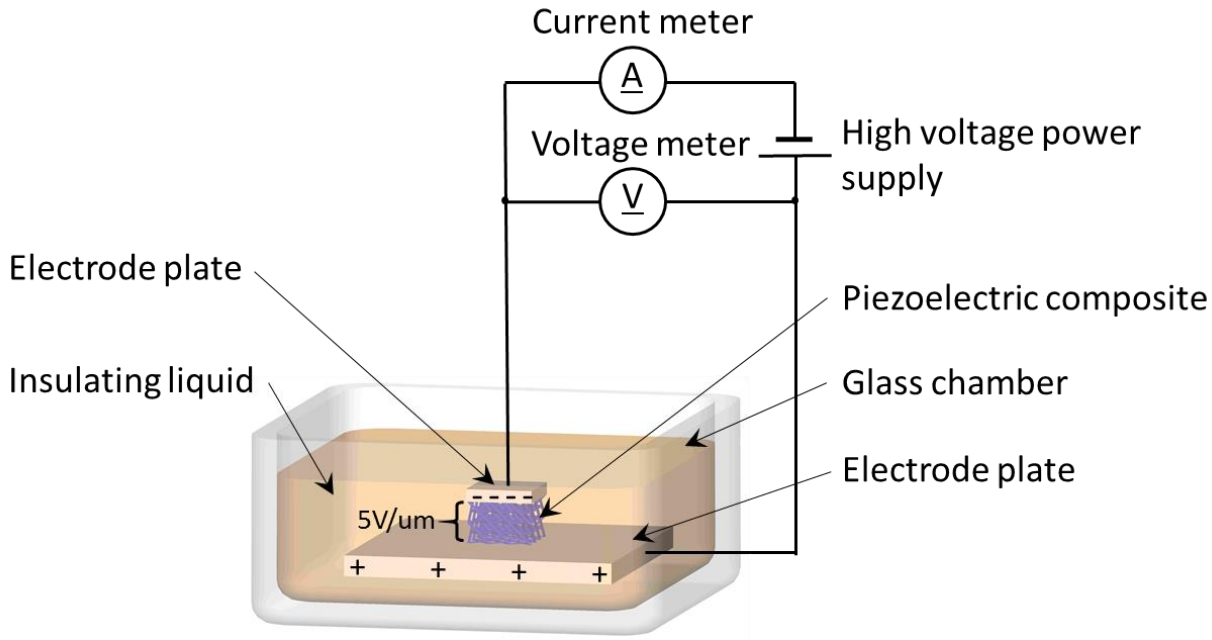

Figure 3-4. Schematic of poling setup.

To evaluate the surface functionalization and ensure maximum grafting, we measured the response via the Fourier-transform Infrared Spectroscopy Attenuated Total Reflectance (FTIR-ATR) of thoroughly cleaned PZT particles with various surface agent loadings or functionalization reaction times as shown in Figure 3-5a and 3-5b. The spectrum focuses on the carbonyl and alkene of the methacrylate surface groups nominally at 1710 cm^{-1} and 1630 cm^{-1} respectively. The increasing intensity with higher loading and reaction time indicates increasing grafting of the functionalization agent to the PZT particles until a maximum is reached where no further gain in intensity is achieved. The free methacrylate groups on the fully modified particle surface provide steric interference and favorable interactions with the acrylic pre-polymer dispersion allowing

high-quality, agglomeration-free state. The piezoelectric voltage output of the as-printed nanocomposite is measured via cyclical loadings from a standard shaker and data acquisition system connected with a 40M Ω resistor (see Figure 3-6a and 3-6b). Figure 3-5c shows significantly elevated voltage output via surface functionalization of 30vol% (~74wt%) loaded piezo-active feedstock, which exceeds the performance of commercial piezoelectric polymer material, polyvinylidene fluoride (PVDF), and previous 3D printed piezoelectric nanocomposites[26] by over three times. Here, the overall dimension of all samples (functionalized PZT composite, unfunctionalized, commercial PVDF) and the force magnitude of the cyclical loading applied to these samples are the same. The piezoelectric charge constant d_{33}, defined as the induced electric charge density per unit applied stress, was evaluated to quantify the piezoelectric behavior of the as-fabricated nanocomposite after calibrating the measurement system with standard piezoelectric films (Figure 3-6d).

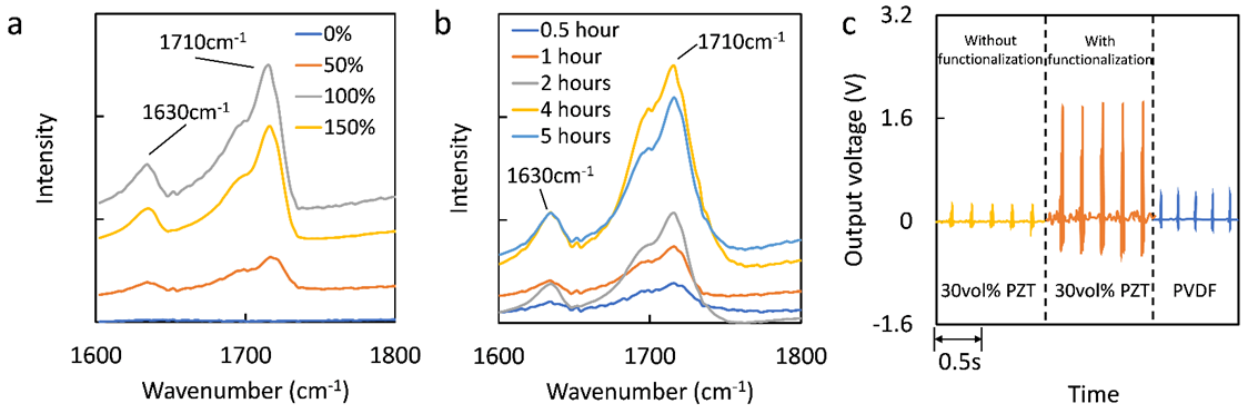

Figure 3-5. Characterization of piezoelectric particles with different surface process conditions. Fourier-transform Infrared Spectroscopy (FTIR) of PZT particles with (a) different loading of surface functionalization agent or (b) reaction time. (c) Comparison of voltage output of functionalized, 30vol% PZT nanocomposites with non-functionalized PZT composite and PVDF polymer (Sigma-Aldrich, MO, USA) induced by the same stress of 48kPa.

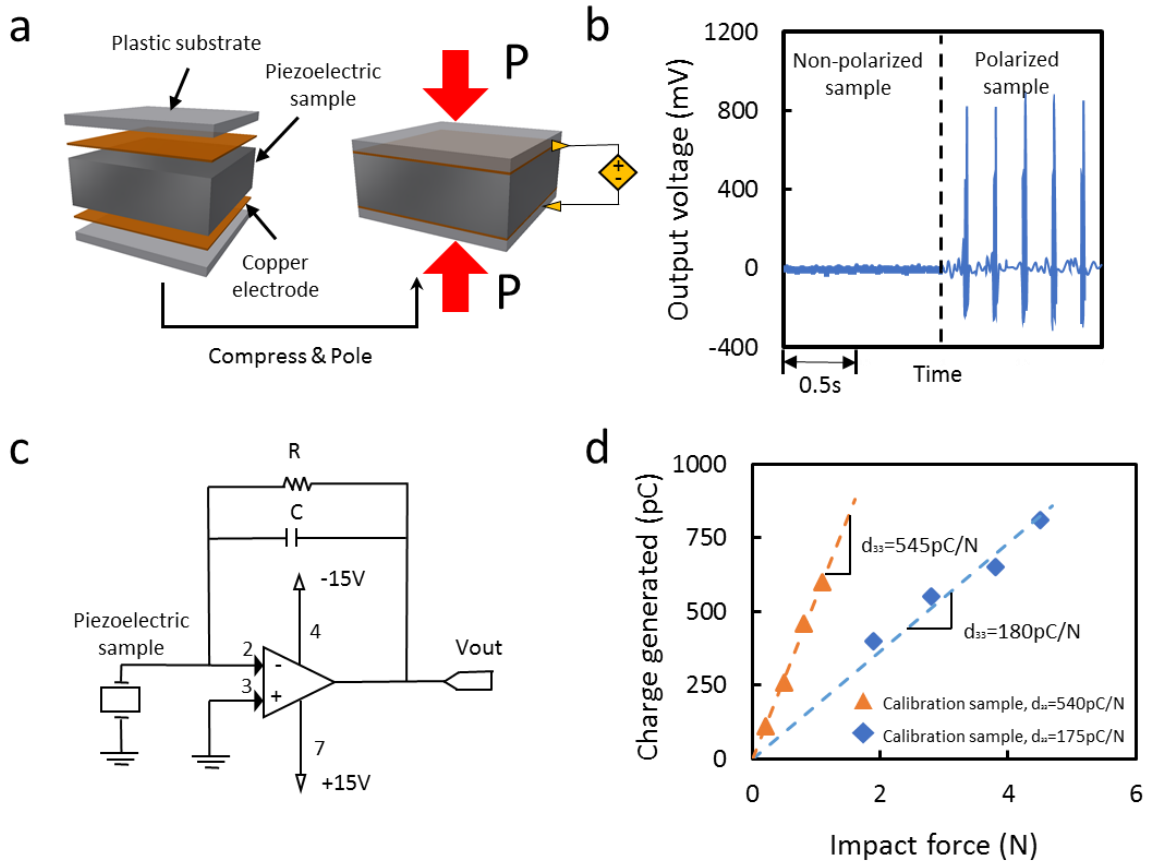

Figure 3-6. Measurement of piezoelectric coefficient of as-fabricated samples. (a) Schematic of the tested sample assembly. (b) The piezoelectric voltage output of the as-fabricated sample before and after polarization. (c) The circuit used to quantify the piezoelectric charge constant, d_{33}. (d) The calibration curve of the measuring system with standard samples. The error of the measurement is within 5%.

The as-fabricated piezoelectric nanocomposites were polarized and then assembled to remove the triboelectric effect (see Figure 3-6a). The stress induced voltage output was quantified through a measuring circuit as shown in Figure 3-6c, and the piezoelectric charge constant was calculated with this voltage. We observed over 10 times enhancement of piezoelectric charge constant (d_{33}) through surface functionalization at 3vol% (~17wt%) PZT particle loading (Figure 3-1c), consistent with theoretical predictions and numerical simulations. Piezoelectric charge constant

was increased over 100% at higher PZT volume fraction (for example from 38pC/N to 110pC/N at 30vol% i.e., ~74wt% concentration). This consistency between theoretical prediction, numerical analysis and experimental measurement, as shown in Figure 3b, indicates that generalized effective interphase model could precisely evaluate the functional performance of nanocomposite.

Here, we invoked the Hashin-Shtrikman as the theoretical upper bound of the piezoelectric property of nanocomposite as[54]:

$$\mathbf{P}_{\text{upper}} = \mathbf{P}_{\text{II}} + (1 - v_{\text{II}})\{(\mathbf{P}_{\text{I}} - \mathbf{P}_{\text{II}})^{-1} + v_{\text{II}}\mathbf{S}\mathbf{P}_{I}^{-1}\}^{-1} \quad (3.8)$$

where $\mathbf{P}_{\text{i}}$ (i=I, II) is the effective compliance matrix of the monomer matrix (i=I) and the piezo-active inclusion (i=II), respectively; v_{II} is the particle volume fraction of the nanocomposite; **S** is the piezoelectric Eshelby matrix. As indicated in Figure 3-1b, the electromechanical property of the composite significantly is enhanced via particle surface functionalization, approaching the theoretical upper bound.

3.5 Multi-functional design map of functionalized piezoelectric nanocomposite

The effective interphase framework presented here allows us to access the effects of constituent parameters from the 3D printable raw material feedstock on the electromechanical properties of the bulk nanocomposites. Our methodology enables users to reverse design 3D printable feedstock parameters that can achieve target electro-mechanical and structural properties after printing. To optimize the piezoelectric performance, we investigated the piezoelectric property of the composites with a range of polymer matrix moduli, morphologies of the perovskite inclusion and the interfacial strength between the active and inactive phases via controlling functionalization. Increasing the molecular weight (M_n) of the uncured monomer feedstock decreases polymer

crosslink density during the UV curing process, and lowers the mechanical modulus, Figure 4a. This allows us to modulate the electromechanical property $\mathbf{E}_I$ of the matrix phase, by tuning the molecular weight/mechanical modulus of the polymer C^I. Additionally, we employed our model to tune the functional performance of the piezoelectric nanocomposite via varying the morphology of the piezo-active nanomaterials. An enhanced piezoelectric charge constant d_{33} is achieved via increasing the aspect ratio (h/r) of the active phase while maintaining particle concentration, Figure 3-7b. Increasing the grafting density elevated the resulting effective electromechanical properties of the interphase ($\mathbf{E}_{III}$) based on our effective interphase model, resulting in elevated piezoelectric constants (d_{33}) at a given nano-inclusion loading (Figure 3-7c).

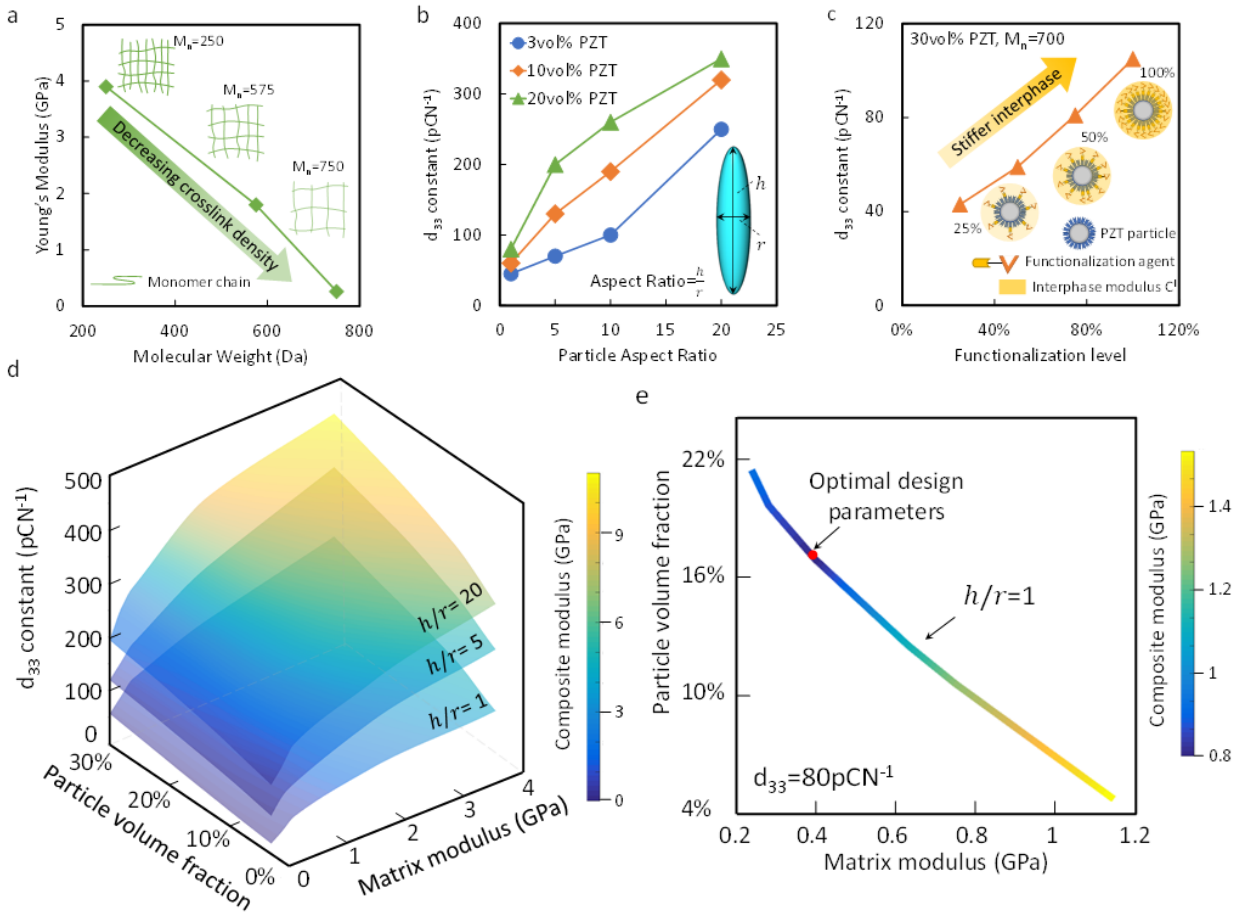

Figure 3-7. Formulation of multi-functional design map of functionalized piezoelectric composites. (a) The measured Young's modulus of the UV cured monomer matrix with different molecular weight. (b) The effect of functionalized inclusion aspect ratio at a constant volume fraction predicted by the theoretical model. d_{33} increases with the aspect ratio of PZT particle. (c) The theoretically predicted piezoelectric charge constant of the 30vol% PZT composite with a range of functionalization level (matrix molecular weight, M_n=700). (d) Design map (d_{33}, E) of the 3D printable multi-functional piezoelectric nanocomposites as a function of nanoparticle loading within the dispersion and monomer stiffness. Each surface represents functionalized nanocomposite with a constant aspect ratio of the nanoparticle. (e) The optimal combination of the design parameters with given piezoelectric charge constant.

By tuning the aspect ratio of functionalized nanoparticle inclusion and the polymer matrix stiffness of the piezoelectric nanocomposite, a wide range of composite stiffness along with high functional response can be simultaneously attained. As shown in Figure 3-7d, we present the design map for obtaining multi-functional property pairs (piezoelectric charge constants and structural compliance) via configuring the monomer modulus and parameters of the functionalized PZT nanoparticle inclusions. The piezoelectric charge constant d_{33} of the printable nanocomposite is plotted against a range of volume loading of the PZT particles and the UV curable monomer stiffness. A series of surfaces are generated where each point on the surface corresponds to a set of design parameters (i.e., particle volume fraction v_{II}, monomer matrix stiffness C^I, and the aspect ratio of the piezo-active inclusion h/r). The height of the surfaces represent the magnitude of d_{33}, and the color indicates the effective mechanical modulus of the nanocomposite. For instance, with a target piezoelectric charge constant (i.e., d_{33}=80pCN^{-1}), the mechanical stiffness of the resulting composite is modulated via tuning the stiffness of the monomer and the PZT particle loading (Figure 3-7d) volume fractions. Within the design curve, where the color for each point represents the Young's modulus of the resulting composite (from softer to stiffer), a combination of volume fraction of the PZT inclusion and the monomer stiffness can be configured to reach the target d_{33} constant.

The requirement of high-stiffness for high-response makes achieving highly flexible piezoelectric sensors particularly challenging. Wearables and biomedical implants may particularly require low-stiffness piezoelectric sensors due to the strains and soft tissues involved, but simultaneously require high-response due to their low sensor input forces. Our modeling directs nanocomposite development towards this area of highly-flexible and high-response nanocomposites. We compared the designed performance of the piezoelectric nanocomposite with that of existing 3D printed piezoelectrics[19,26,55-59]. As shown in Figure 3-8, the designed nanocomposite exceeds the functional property of other 3D printable piezoelectrics, while occupying a wide range of compliance range (i.e., from 5.5×10^{-11} Pa^{-1} to 3×10^{-8} Pa^{-1}). Our design strategies imply that target structural flexibility while retaining high sensitivity and detection ranges can be simultaneously achieved via rational selections of constituent material parameters, as will be demonstrated below.

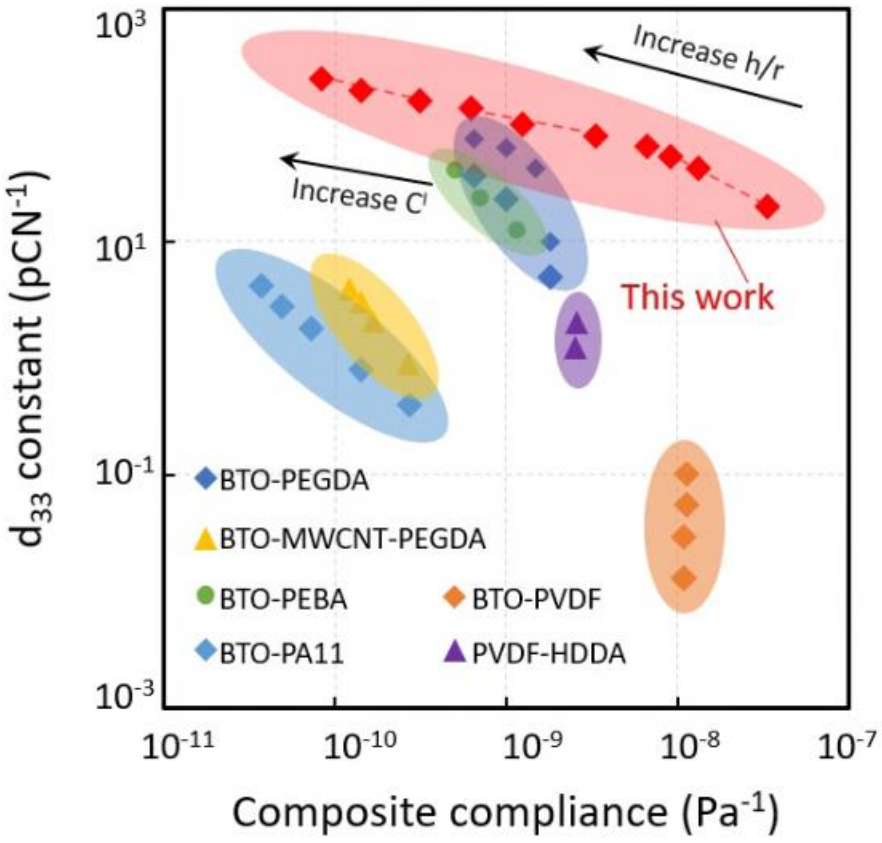

Figure 3-8. Comparison of piezoelectric charge constant d_{33} and mechanical compliance between piezoelectric nanocomposite presented in this work with other 3D printed composite materials.

3.6 Flexible, conformal self-sensing material for low air pressure detection

The possibility of achieving high sensitivity and flexibility of the bulk piezoelectric composites motivated us to explore its potential applications as conformal highly sensitive air flow sensor, where the pressure induced by air flow (lower than 50 Pa) could be detected. Here, we fabricated a 15cm^2 micro-architected octet-truss lattice structure with the 3vol% (~17wt%) piezo-active colloidal and attached it on a curved surface, as shown in Figure 3-9a to 3-9c. The radius and the node-to-node length of each strut are 150um and 1.8mm, respectively. We used a UV light source with 14.8mWcm^{-2} light power intensity to solidify each layer of the piezoelectric colloidal. Stretchable, paintable silver electrodes (TED PELLA, Leitsilber 200 Silver Paint) are painted on both sides of the lattice and connected to two copper leads. The voltage outputs of the conformal piezoelectric lattice induced by air flow were collected with a data acquisition system (NI USB-6356). The air flow with different flow direction (Θ) was applied via squeezing a 3mL pipet with a constant distance between the sensor and pipet. The air pressure was calibrated using a highly sensitive precision force gauge (DBCR-20N APPLIED MEASUREMENTS LIMITED) prior to the experiment. The highest voltage (~3mV) is observed at inflow angle 90°, while the signals are reduced (~2mV) with other two angles (Θ=45° and 135°), as shown in Figure 3-9d. Additionally, we compared the piezoelectric voltage output of a PVDF film and a non-functionalized lattice with the functionalized piezoelectric lattice. As shown in Figure 3-9e, the functionalized piezoelectric flexible sensor generates ~3mV and ~1mV voltages with 164Pa and 43Pa air pressure, respectively, while the PVDF can only detect high air flow pressure (164Pa) with ~0.8mV output and not

detectable at 43Pa. The nonfunctionalized lattice failed to detect air low. The high sensitivity at ultralow-stiffness highlights their potential as highly sensitive yet flexible and conformal wearables not achievable in current transducer materials.

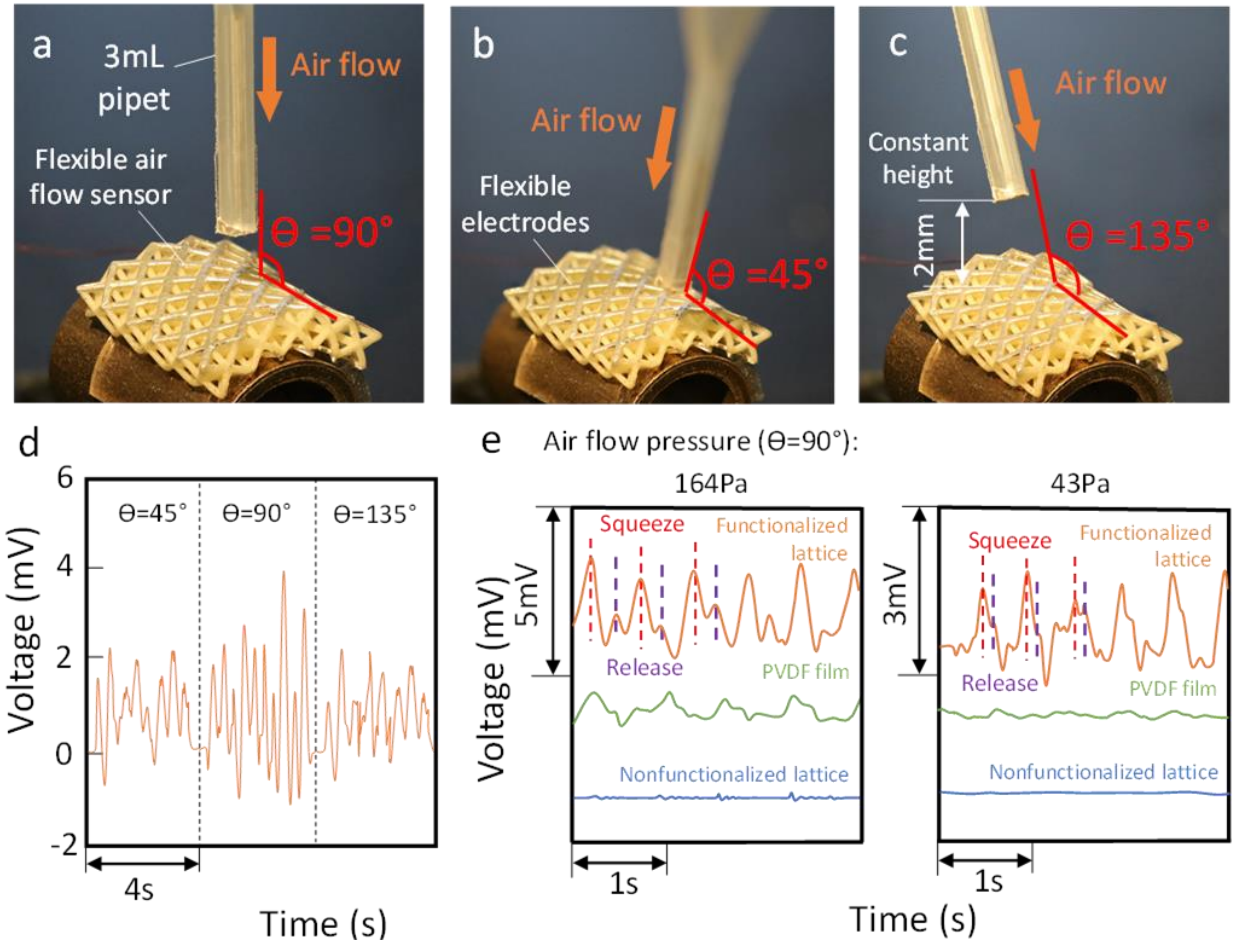

Figure 3-9. Flexible, conformal piezoelectric lattices for air-flow detection. (a-c) Optical image of the conformal flexible air flow sensor with air flow applied in Θ =45°, 90° and 135° directions. The distance between the pipet and the lattice was kept as 2mm. (d) Voltage output of the flexible air flow sensor as a function of time with air flow applied in Θ =45°, 90° and 135° direction. (e) Voltage output of the functionalized lattice, PVDF film and the nonfunctionalized lattice as a function of time. The air flow is generated by squeezing or releasing the pipet continuously. Θ was kept as 90°.

3.7 Wireless, self-sensing boxing glove

In addition to the low-pressure detection, we demonstrated the case where mechanical stiffness, energy absorbing, and high magnitude pressure sensing mapping capabilities were introduced into a sporting wearable device. Here, we 3D printed flexible piezoelectric lattice with stretch dominated micro-architectures with a designed thickness (5mm) and then inserted into a boxing glove (Figure 3-10a) to provide spatially resolved and time-resolved mapping of reaction punching forces exerted to knuckles of the hand during boxing activities. The overall dimension of the lattice is 50mm×80mm×5mm, while each impact probing area is 10mm×10mm. The radius and the node-to-node length of the strut are 300um and 3mm, respectively. After polarization, the entire 3D printed piezoelectric lattice is active and can be probed from anywhere within the material, providing the new opportunity for sensing where user configures and defines arbitrary locations for sensing and data output where electrodes are applied. The lattice overall dimension, modulus and d_{33} are calibrated using force sensor to ensure that the highest punching force that an athlete could produce are within the linear elastic detection range of the lattice material within the boxing glove (Figure 3-11a). Here, 8 pairs of electrodes corresponding to the knuckles of a hand are attached onto the 3D printed lattice. We integrate our self-sensing, energy absorbing composite with a microcontroller (WEMOS D1 Mini) and multiplexer (BOB-09056, SparkFun Electronics), which allow the data from the 8 pairs of electrodes to be sent, received and hosted over a Wi-Fi connection. As shown in Figure 3-10a (cross section), we then attach the lattices conformally to the hand and embedded it into a sport boxing glove (Title Classic Boxing Gloves). The stress-induced voltages from the lattice are then wirelessly transmitted to a data receiving device (cell phone) with a custom-made user interface to read the force data. With the calibrated d_{33} constants and force measurements of the lattices, force magnitude distributions are displayed onto the

custom user interface. Figure 3-10b shows the as-fabricated conformal lattice. Figure 3-10c plots the measured punch force magnitude of a series of applied, calibrated forces (from 50N to 400N) on the as-fabricated conformal lattice. The significant gap (green area) between the punch force and transmitted force reveals the structural impact absorbing capabilities of the smart piezoelectric lattices. This application highlights the multi-functional utility of the designed piezoelectric materials. Figure 3-10d and 3-10e show the optical images of the glove when it hits a wall by a direct strike and right hook, respectively. Spatial distribution of force magnitudes obtained from the prescribed electrodes attached on the lattice is then displayed onto the receiving device, as shown in Figure 3-10f and 3-10g. The red shaded area denotes the probing points while the dashed lines denote other locations where the electrodes can be attached to read data output. Additionally, the impact force distribution restored at grid pattern can be interpolated to cover the entire area. Testing of over 6000 times punching was conducted to confirm the repeatability and durability of these lattice materials (Figure 3-11b).

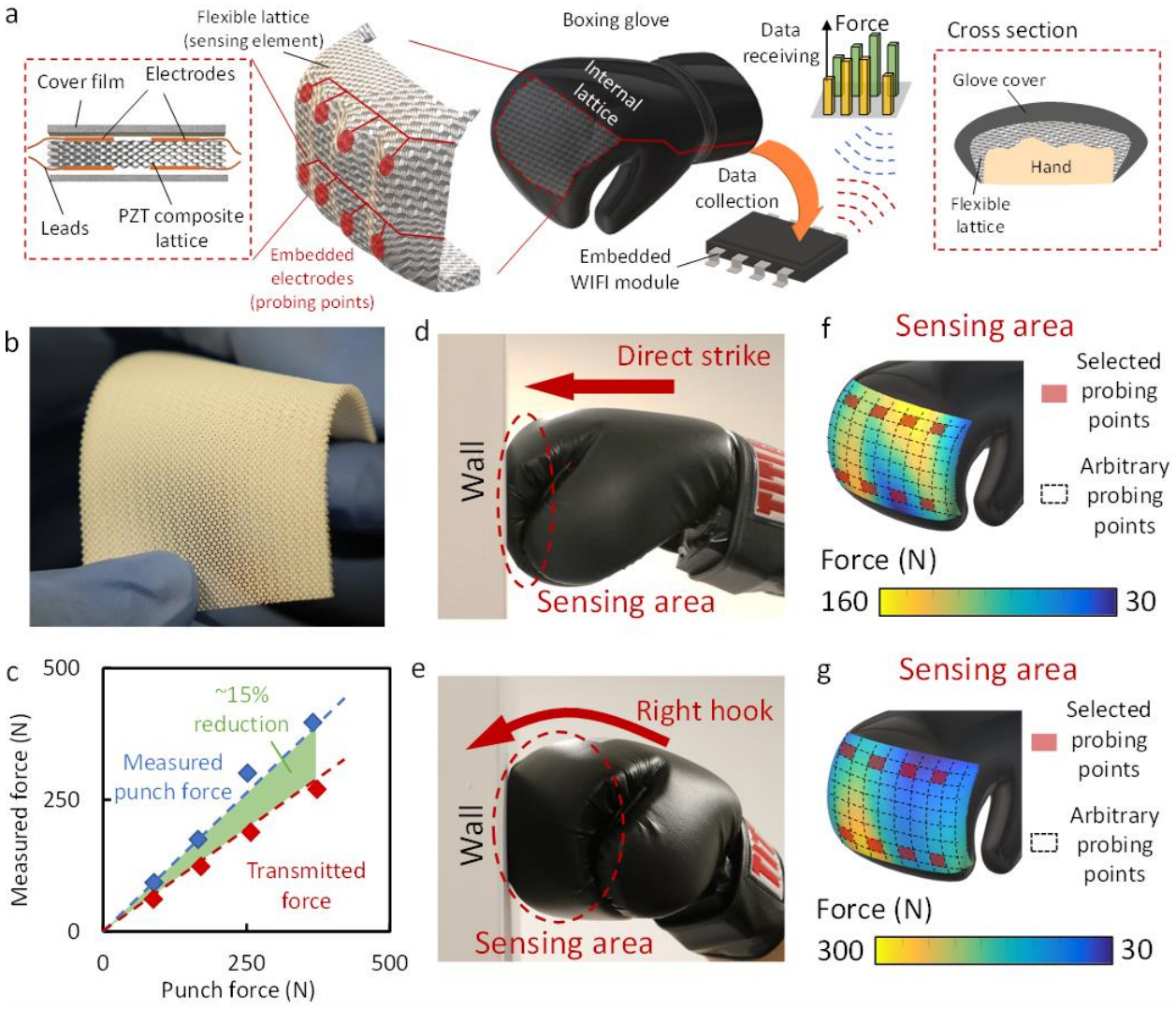

Figure 3-10. Wireless, self-sensing boxing glove. (a) Schematics of the wireless self-sensing boxing glove. A 3D printed flexible piezoelectric lattice with stretch dominated micro-architectures is inserted into a boxing glove to provide spatially resolved and time resolved mapping of reaction punching forces exerted to knuckles of the hand during boxing activities. (b) Optical image of the flexible, self-sensing lattice. (c) Measured punch force and transmitted force versus the applied punch force. The green shaded area between the measured punch force and transmitted force reveals energy absorption of the flexible lattice. (d)-(e) Optical image of the glove when it hits a wall by direct strike and right hook, respectively. (f)-(g) Spatial distribution of force magnitudes obtained from the prescribed electrodes attached on the lattice. The red shaded area denotes the probing points while the dashed lines denote other locations where the electrodes can be attached to read data output.

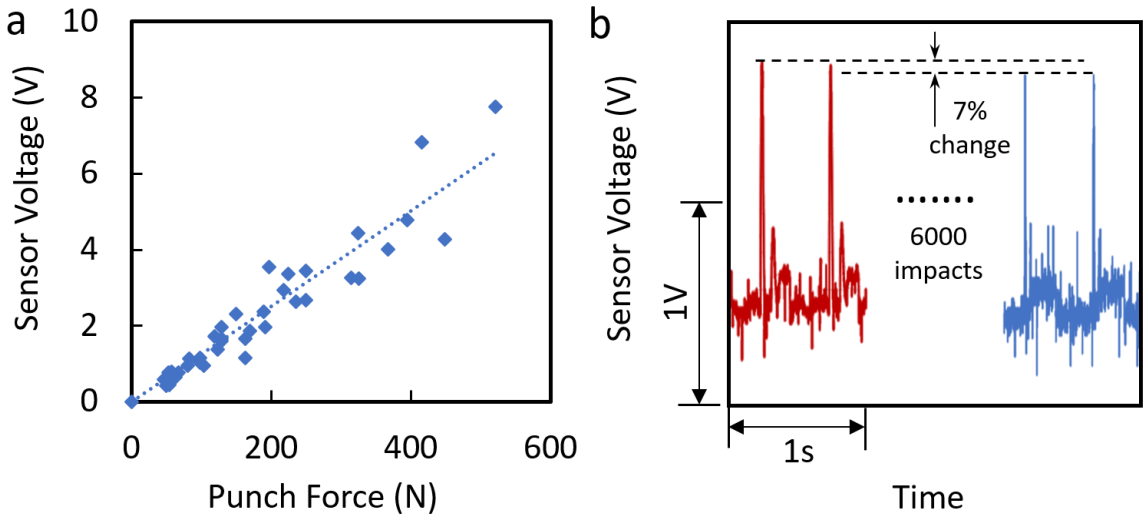

Figure 3-11. Detected voltage signal transmitted from wireless boxing gloves. (a) Voltage output of the sensor as a function of punch force ranging from 0N to 550N. (b) Sensor voltage output as a function of time with over 6000 times 100N impact.

3.8 Conclusion

In this chapter, we demonstrated a class of piezoelectric materials with high piezoelectric responsiveness and compliance via exploiting the effects of the nanoparticle-matrix functionalization on the electromechanical performance of the piezoelectric nanocomposite. We proposed a generalized effective interphase model to quantify the electromechanical properties of the 3D printable nanocomposite. We show through theoretical, numerical calculations and experimental measurements that, increasing the surface functionalization level enables an effective interphase region which enhances the electromechanical performance of the piezoelectric nanocomposite. Maximizing the surface functionalization level approaches the upper bound of piezoelectric coefficient at a given particle loading and enables uniform 3D printable dispersion despite high piezoelectric particle loading over 30vol% (~74wt%), as compared to the 3vol%

(~17wt%). Our design and additive manufacturing routes allow for achieving target flexibilities while keeping high piezoelectric responses via rational designs of inclusion morphologies and monomer stiffness of the constituent materials. Our approach enables printing transducers and smart wearables with arbitrary, complex micro-scale architectures, and are compatible with commercially available light-based processes. It introduces a new paradigm for smart materials, where wearables, cushions, and structures are themselves responsive and capable of providing three-dimensional stress sensing data without the needs for integrating sensor patches. The designed 3D printable piezoelectric nanocomposites that go beyond the existing compliance and functional property tradeoff highlight their potentials as the next generation of flexible self-sensing materials and wearables.

Chapter 4 Design micro-architecture of piezoelectric metamaterials

This chapter displays the comprehensive design methodology of piezoelectric metamaterial, which enables the creation of arbitrary functional responses. This chapter starts with the analysis of the rational of designing the functional responses with architectural design of metamaterial. Next, the developed design method is applied to break the constraint of intrinsic crystalline structures and to achieve arbitrary orientation of piezoelectric coefficient vector. Subsequently, the decoupled strain response of piezoelectric metamaterial is investigated for full information detection of applied load. Additionally, all physically feasible actuation modes of piezoelectric metamaterial is studied and demonstrated.

4.1 Rational of designing functional responses via tailoring the micro-architecture of metamaterials

When subject to an external loading, the macroscopic strain field is in consistent with the local strain field of an infinitesimal volume for homogeneous material, indicating there is no strain transformation from macroscopic to local scale (Figure 4-1a). Attribute to the consistency in strain fields at different dimension scale, the functional behaviors of a material are solely dependent on the intrinsic crystalline structure. Once the material is fabricated, it is almost impractical to tailor its functional responses.

The beauty of structural metamaterials is the strain transformation mechanism enabled by the artificially designed micro-architecture. As presented in Figure 4-1b, the strain field on each individual ligaments is correlated with macroscopic strains field by a transformation matrix as:

$$\boldsymbol{\varepsilon}^{\mathrm{k}} = \mathbf{N}^{\mathrm{k}}\boldsymbol{\varepsilon}_{\mathrm{M}}\ (\mathrm{k} = \mathrm{i}, \mathrm{j} \ldots) \qquad (4.1)$$

Where $\boldsymbol{\varepsilon}^{\mathrm{k}}$ and $\boldsymbol{\varepsilon}_{\mathrm{M}}$ denote the local strain field on k-th ligament and macroscopic strain field, respectively; $\mathbf{N}^{\mathrm{k}}$ is the transformation matrix of strain field, which is dependent on the spatial orientation of k-th ligament. Therefore, we are able to manipulate the local strain field of metamaterials via tuning the spatial arrangement of constitutive ligaments.

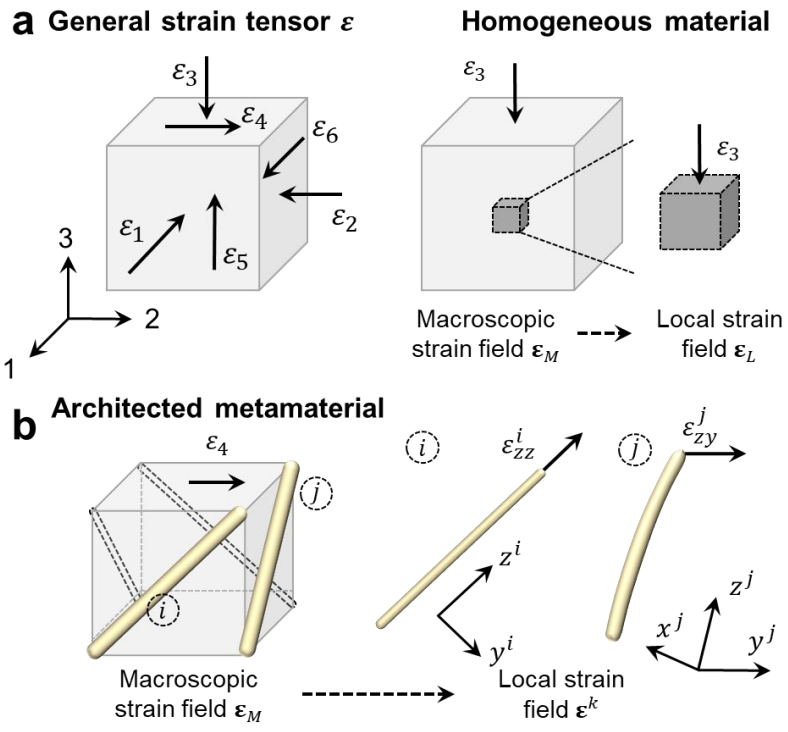

Figure 4-1. Strain transformation enabled by architected metamaterial.

Coupled with piezoelectricity of the base material, we can tailor the effective contribution of each piezo-active ligament as:

$$\mathbf{D}^{\mathrm{k}} = \mathbf{d}\mathbf{C}^{\mathrm{k}}\boldsymbol{\varepsilon}^{\mathrm{k}} = \mathbf{d}\mathbf{C}^{\mathrm{k}}\mathbf{N}^{\mathrm{k}}\boldsymbol{\varepsilon}_{\mathrm{M}} \qquad (4.2)$$

Where **d** and $\mathbf{C}^k$ denote the piezoelectric coefficient and mechanical stiffness tensor, respectively; $\mathbf{D}^k$ is the effective displacement contribution of k-th ligaments. Hence, the effective functional responses of piezoelectric metamaterial are tailored via tuning the spatial orientation and corresponding electric displacement contribution of each constitutive ligaments.

4.2 Designing piezoelectric coefficient vector anisotropy

4.2.1 Theoretical design strategy of piezoelectric coefficient vector anisotropy

We have developed a strategy to realize the full design space of piezoelectric coefficients through the spatial arrangement of piezoelectric ligaments. Our scheme involves analyzing configurations of projection patterns from a 3D node unit classified by connectivity. The evolutions of projection patterns give rise to diverse electric displacement maps (Figure 4-2a to 4-2h), from which the piezoelectric coefficient tensor space d_{3M} (M=1~3) can be designed, going beyond the limitations of the monolithic piezoelectric ceramics, polymers and their composite feedstock whose piezoelectric coefficients are located in the {- - +} quadrants[60-63] and {+ + -} quadrants[64,65].

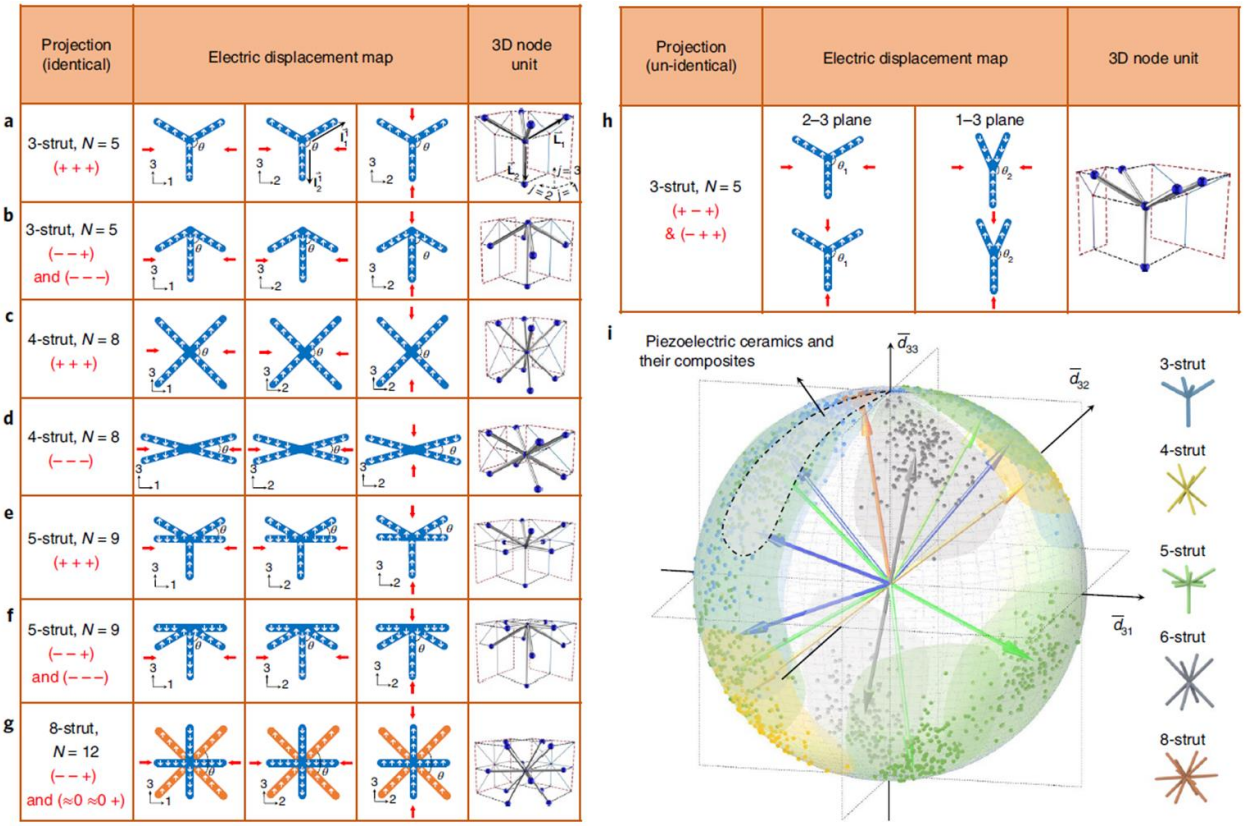

Figure 4-2. Design of piezoelectric metamaterials for tailorable piezoelectric charge constants. Designing 3D node units by configuring the projection patterns. (a)–(g), Node unit designs from 3-, 4-, 5- and 8-strut identical projection patterns, respectively. A node unit with higher nodal connectivity can be constructed by superposition of projection patterns comprising a smaller number of projected struts. (h), Node unit with dissimilar projection patterns showing decoupled d_{31}, d_{32}. The white arrows in the projection patterns pointing towards the positive or negative 3-direction indicate the positive or negative electric displacement contribution to poling direction 3. Red arrows in a–h indicate the compression loading along the 1-, 2- or 3-direction. (i), A dimensionless piezoelectric anisotropy design space accommodating different 3D node unit designs with distinct d_{3M} distributions; each d_{3M} is normalized by the length of the vector $\{d_{31}, d_{32}, d_{33}\}$ and thus d_{31}, d_{32} and d_{33} form a right-handed 3D coordinate system. The dimensionless piezoelectric coefficients of their parent monolithic piezoelectric ceramics and their composites are labelled within the dashed region, $\{- - +\}$ quadrant.

The analytical model is established to characterize the relationship between the piezoelectric charge constant tensor and the projection pattern parameters. The effective piezoelectric charge

constant, d_{nKL}, is defined to correlate the induced effective electric displacement, D_n, of a 3D unit cell with applied stress, σ_{KL}, as:

$$D_n = d_{nKL}\sigma_{KL} \quad (4.3)$$

. D_n, d_{nKL} and σ_{KL} represent the effective electric displacement field, the effective piezoelectric charge constant tensor, and externally applied stress field defined in the global 1-2-3 system (Figure 4-2a, n, K, L=1~3). We compute the d_{nKL} of a node unit under applied stress through collecting and volume-averaging the electric displacement contributions $D_n^{(i)}$ and stress in equilibrium with σ_{KL} from all strut members, $\bar{L}_i$,

$$\begin{cases} D_n = \dfrac{1}{V}\sum_{i=1}^{N}\int_{V_i} D_n^{(i)}\,dV_i \\ \sigma_{KL} = \dfrac{1}{V}\sum_{i=1}^{N}\int_{V_i} \delta_{kK}\delta_{lL}\sigma_{kl}^{(i)}\,dV_i \end{cases} \quad (4.4)$$

, where V_i is the volume of the i-th strut; V is the effective volume of the node unit cell; $\sigma_{KL}^{(i)}$ is the stress-state of the i-th strut in the global 1-2-3 system, respectively, k, l=1~3; δ_{kK} and δ_{lL} represent the Kronecker delta to identify the stress components that are in equilibrium with the externally applied load. We introduce a local beam coordinate system x-y-z for struts, and relate the stress in the global 1-2-3 system ($\sigma_{KL}^{(i)}$) and local x-y-z system ($\sigma_{pq}^{(i)}$) by a linear transformation operator containing strut orientation information:

$$\sigma_{kl}^{(i)} = N_{kp}^{(i)}\sigma_{pq}^{(i)}(N_{lq}^{(i)})^T \quad (4.5)$$

, where p, q=x, y, z, $N^{(i)}$ represents the coordinate system transformation matrix containing components with respect to the projection pattern angle (θ_j, j=1~3)[66] and has a form of:

$$N^{(i)} = \begin{bmatrix} \cos\theta_2 & 0 & \sin\theta_2 \\ 0 & 1 & 0 \\ \sin\theta_2 & 0 & -\cos\theta_2 \end{bmatrix} \begin{bmatrix} 1 & 0 & 0 \\ 0 & \cos\theta_1 & \sin\theta_1 \\ 0 & \sin\theta_1 & -\cos\theta_1 \end{bmatrix} \begin{bmatrix} \cos\theta_3 & \sin\theta_3 & 0 \\ \sin\theta_3 & -\cos\theta_3 & 0 \\ 0 & 0 & 1 \end{bmatrix} \quad (4.6)$$

Substituting Eq. (4.5) into Eq. (4.3) and (4.4) yields the expression of the effective charge constants d_{nKL}:

$$d_{\mathrm{nKL}} = \frac{D_{\mathrm{n}}}{\sigma_{\mathrm{KL}}} = \frac{\sum_{i=1}^{N} A_i |L_i| d_{nkl} N_{kp}^{(i)} \sigma_{pq}^{(i)} (N_{lq}^{(i)})^T}{\sum_{i=1}^{N} A_i |L_i| \delta_{kK} \delta_{lL} N_{kp}^{(i)} \sigma_{pq}^{(i)} (N_{lq}^{(i)})^T} = \frac{\sum_{i=1}^{N} d_{nkl} N_{kp}^{(i)} \sigma_{pq}^{(i)} (N_{lq}^{(i)})^T}{\sum_{i=1}^{N} \delta_{kK} \delta_{lL} N_{kp}^{(i)} \sigma_{pq}^{(i)} (N_{lq}^{(i)})^T} \quad (4.7)$$

where A_i and $|L_i|$ is the area of cross section and length of the i-th strut. These two variables are assumed to be the same for all struts in the node unit.

This allows the design of d_{nKL}, or equivalently in Voigt notation, d_{nM}, according to the projection pattern configurations (by convention, KL→M: 11→1; 22→2; 33→3; 12→4; 13→5; 23→6). We demonstrate the application of the method by designing d_{nM} according to the relative orientation θ between the projected struts. Here, to convert the tensor notation (KL→M), the coordinate system transformation matrix $N^{(i)}$ (3×3 dimensions) is expanded and rearranged to form the stress transformation matrix $T^{(i)}$ (6×6 dimensions).

With the developed design methodology, the dimensionless piezoelectric tensor space, $\bar{d}_{3\mathrm{M}}$, is defined by normalizing $d_{3\mathrm{M}}$ by the length of the vector, $\{d_{31}, d_{32}, d_{33}\}$. To capture the broadest possible design space, we start with the minimum number of intersecting micro-struts at a node that can be tessellated into 3D periodic lattices. All intersecting struts are represented as vectors

originating from the node, i.e., $\bar{L}_i$ (i=1~N, N is the node unit connectivity). In building our projection patterns, we define $\bar{l}_i$ as the 2D projection of $\bar{L}_i$ onto three orthogonal planes through the global 1-2-3 coordinate system of the 3D piezoelectric cube (Figure 4-2a**,** $\vec{L}_i = \frac{1}{2}\sum_j^3 \vec{l}_i^j$, j =1, 2, or 3). As an example, we use piezoelectric ceramic and its composites having $\bar{d}_{3M}$ distributed in the {- - +} quadrants[60-63] as the base material to construct the electric displacement maps. The white arrows pointing upwards or downwards against the 3-direction indicate the positive or negative electric displacement response of the strut along the 3-direction (i.e., poling direction).

Configuring the projection patterns in these planes results in diverse electric displacement maps, allowing access to different quadrants of the d_{3M} property space. A basic 3D node unit containing 3, 4, and 5 intersecting struts on the projection patterns are illustrated in Figure 4-2a to 4-2f. We start with 3D node units with identical 3-strut projection patterns on 1-3 and 2-3 planes, i.e. d_{31}= d_{32} (Figure 4-2a and 4-2b). Configuring the projection pattern via rotating the relative orientations of two of the projected struts ($\theta = \angle\vec{l}_1^1\vec{l}_2^1$) redistributes the electric displacement contributions as indicated by the white arrows reversing directions in the projection pattern (Figure 4-2a and 4-2b). This results in the $\bar{d}_{3M}$ tensor shifting from {+ + +} quadrant, to highly anisotropic distribution near the positive $\bar{d}_{3M}$ axis {0 0 +}, to {- - +} quadrant with negative d_{31} and d_{32} as well as positive d_{33} (Figure 4-2i). Further decrease of the relative orientation reverse all values of the d_{3M} to occupy the {- - -} quadrant. Similarly, for a 4-strut or 5-strut projection pattern with two axis-symmetry, decreasing the relative orientation ($\theta = \angle\vec{l}_1^1\vec{l}_2^1$) of projected struts results in the change of d_{3M} distribution from {+ + +} quadrant to {- - -} quadrant (Figure 4-2i) or {- - +} due to the competition of the opposite electric displacement contributions within the struts (Figure 4-2c to 4-2f).

Our designs can be broadened by increasing the 3D node unit connectivity through superposition (Figure 4-2g). Micro-architectures with high nodal connectivity are deformed predominantly by compression or tension[13,67]. The d_{33} increases with additional nodal connectivity as compared to lower connectivity cases in which strain energy from strut bending does not contribute to the electric displacement in the 3-direction.

Moreover, our designs are not restricted to identical projection patterns where d_{31} and d_{32} are coupled. 3D node unit designs with dissimilar projection patterns allow independent tuning of d_{31} and d_{32} ("out of 45º plane" distribution of d_{3M}, Figure 4-2i, $d_{31} \neq d_{32}$). We configure the dissimilar electric displacement maps via independently varying the relative orientations θ_1 and θ_2 on 1-3 and 2-3 planes (Figure 4-2h). The compression along 1-direction and 2-direction on the 3D node unit therefore generate different electric displacement maps and result in the decoupling of d_{31} and d_{32} (Figure 4-2h).

Configuring the projection patterns generate various designs of architectures which occupy different quadrants of the $\bar{d}_{3M}$ distribution space as shown in Figure 4-2i, where $M = 1{\sim}3$. These families of 3D node units constitute a broad 3D piezoelectric constant selection where d_{3M} occupy desired quadrants of the property space, in contrast to the piezoelectric coefficients obtained by piezoelectric square foam models[68]. This rich design space creates an enormous palette of novel applications as demonstrated in later sections.

4.2.2 Experimental validation of designed anisotropy of piezoelectric metamaterials

To evaluate the piezoelectric responses of the designed piezoelectric metamaterials, we printed cubic lattices comprised of periodic unit cells stacked along three principle directions and poled

them under uniform electric fields. A shaker with an integrated force sensor exerts cyclical loadings on the samples. We measured the generated voltages (in 3-direction) induced by the applied stress with a resistor connected to a data acquisition system. We found excellent agreement of the measured $\{d_{31}, d_{32}, d_{33}\}$ signatures with the designed response to force from different directions. Here, *N*=5 designs (3-strut projection pattern, Figure 4-2a and 4-2b) are used to demonstrate the different voltage output patterns due to the distinct distributions of d_{3M}. As identical cyclic loadings (~0.5N, sawtooth loading profile) are applied along three orthogonal directions, significant differences in the voltage output patterns are observed for three distinct designs (Figure 4-3a to 4-3c). The *N*=5 piezoelectric metamaterial of $\theta = 75^{\circ}$ (Figure 4-3a) outputs a positive voltage when loaded in 3-direction, while the sample generates a negative voltage as loaded in 1- or 2- direction. In contrast, Figure 4-3b shows the voltage outputs of our N=5, $\theta = 90^{o}$ lattice in 3-direction being positive while voltage output in 1- or 2- direction being supressed, exhibiting highly anisotropic response. By further increasing θ to 120º, the voltage outputs in all 1, 2, 3 directions are positive when loaded in any directions, as shown in Figure 4-3c, due to its all positive d_{3M} distribution.

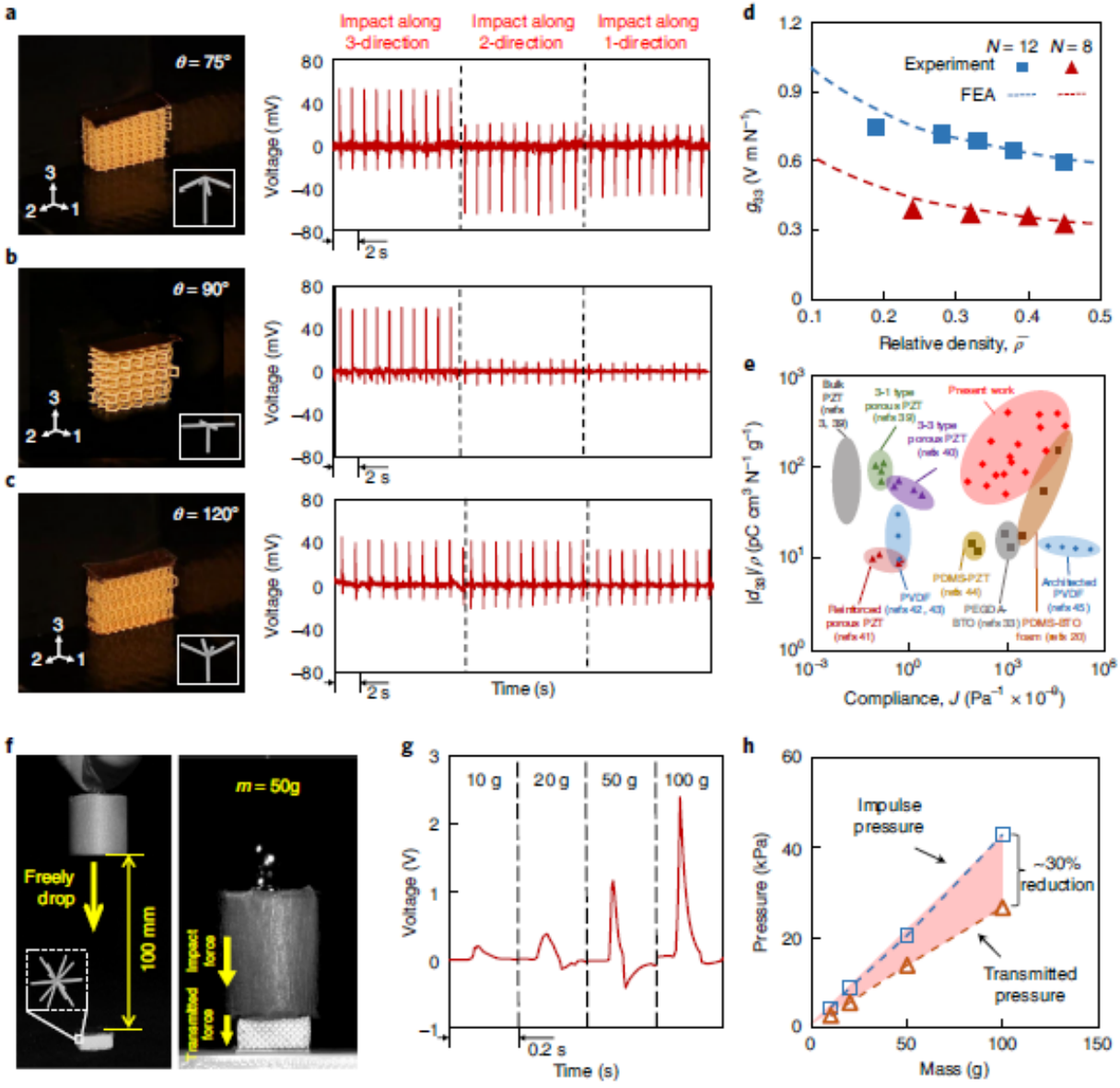

Figure 4-3. Measurement of 3D piezoelectric responses. (a)–(c), Optical images of representative piezoelectric metamaterials comprised of N = 5 node units and their corresponding real-time voltage outputs under impact coming from the 1-, 2- and 3-directions, respectively. (d), Experimental and finite element analysis (FEA) results of the effective piezoelectric voltage constant g_{33} eff versus the relative density of N = 8 and N = 12 lattice materials. (e), Comparison of specific piezoelectric charge coefficients and elastic compliance between the piezoelectric metamaterials presented in this study and typical piezoelectric materials. (f), Drop-weight impact test on the as-fabricated piezoelectric lattice (N = 12). (g), The real-time voltage output of the lattice corresponding to various drop weights. The transient impact stress activates the electric displacement of the metamaterial in the 3-direction, shown as the trace of the voltage output against the impact time. (h), Impulse pressure and transmitted pressure versus the mass of the drop weights. The significant gap (shaded area) between the detected impulse pressure and transmitted pressure

reveals simultaneous impact energy absorption and self-monitoring capability of the 3D piezoelectric metamaterial.

To assess the mechanical-electrical conversion efficiency, the effective piezoelectric voltage constant g_{33} defined as the induced electrical field per unit applied stress, was quantified by measuring the d_{33} and permittivities of the as-fabricated metamaterials. The resistor used in the apparatus is replaced by a circuit to quantify the charge generated in response to applied stress. The d_{33} and g_{33} are then quantified by the ratio of the applied load and the generated charge. The g_{33} results of the metamaterial comprised of highly-connected structure (N=12 and N=8) are shown in Figure 4-3d. Remarkably, g_{33} increases with decreasing relative density, indicating a potential application as a simultaneously light-weight and highly-responsive sensor. The measured d_{33} over their mass density (i.e., $|d_{33}|/\rho$) and compliance are plotted against all piezoelectric materials (Figure 4-3e). We found that these low density and flexible piezoelectric metamaterials achieve over 2 times higher specific piezoelectric constant than piezoelectric polymer (PVDF) and a variety of flexible piezoelectric composites (Figure 4-3e**,** Figure 4-4). Additionally, enhancement of the hydrostatic figures of merits can be obtained via unit cell designs with all identical signs of the $g_{3M}\{+ + +\}$ and $d_{3M}\{+ + + \}$ coefficients (Figure 4-5). This enhanced piezoelectric constant along with the highly connected 3D micro-architecture makes the 3D piezoelectric metamaterial an excellent candidate for simultaneous impact absorption and self-monitoring. A series of standard weights ranging from 10g to 100g were sequentially dropped onto the as-fabricated 3D piezoelectric lattice (N =12) attached on a rigid substrate (Figure 4-3f) to impact the piezoelectric metamaterial. The transient impact stress activates the electric displacement of the metamaterial in the 3-direction, shown as the trace of the voltage output against the impact time (Figure 4-3g).

The impulse pressure on the piezoelectric metamaterial calculated via the measured d_{33}, and the measured pressure transmitted to the rigid substrate against time are traced in Figure 4-3h. The significant gap (shaded area) between the impulse pressure and transmitted pressure reveals the impact energy absorption and protection capability of our piezoelectric 3D metamaterial as a potential smart infrastructure[69,70].

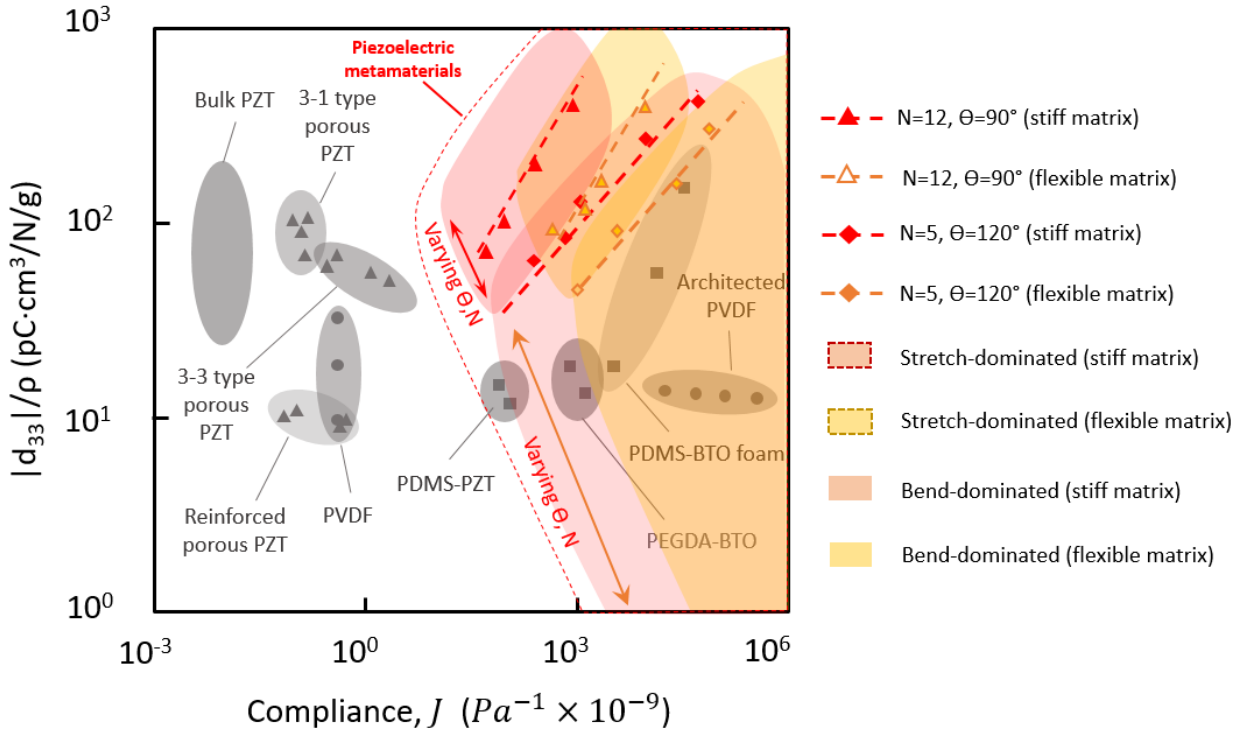

Figure 4-4. Comparison of specific piezoelectric charge coefficients and tunable elastic compliance between the piezoelectric metamaterials presented in this study and typical piezoelectric materials.

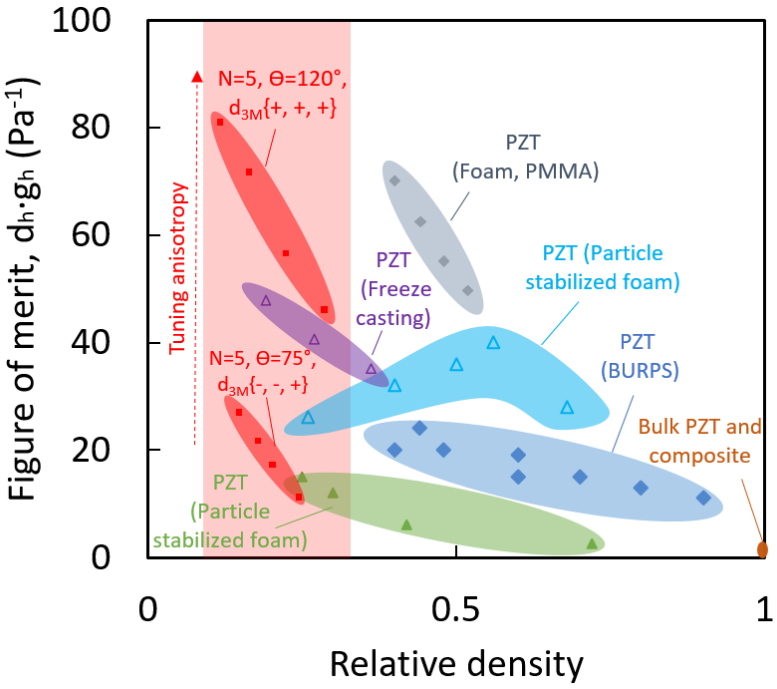

Figure 4-5. FOM of porous and bulk piezoelectric materials.

4.2.3 Theoretical prediction of the dimensionless d constants

We first calculated the analytical results of the N=5 structure with different relative orientations of projected struts denoted in manuscript. To determine the analytical results of $\bar{d}_{3M}$, we followed the analytical model in the manuscript. The effective electric displacement and effective stress are:

$$D_n^{eff} = \frac{1}{V}\sum_{i=1}^{N}\int_{V_i} D_n^{(i)} dV_i \quad (4.8)$$

$$\sigma_{KL}^{eff} = \frac{1}{V}\sum_{i=1}^{N}\int_{V_i} \delta_{Kk}\delta_{Ll}\sigma_{kl}^{(i)} dV_i \quad (4.9)$$

where $\sigma_{kl}^{(i)}$ and $D_n^{(i)}$ ($n\ k\ l = 1,2,3$) are, respectively, the stress matrix and electric displacement vector of each strut in the global coordinate system, V and V_i are, respectively, the volume of the unit cell and of the i-th strut. According to Eq. 4.3, d_{3M}^{eff} in matrix becomes

$$\begin{Bmatrix} d_{31}^{eff} \\ d_{32}^{eff} \\ d_{33}^{eff} \end{Bmatrix} = \begin{Bmatrix} \frac{D_3^{eff}}{\sigma_{11}} \\ \frac{D_3^{eff}}{\sigma_{22}} \\ \frac{D_3^{eff}}{\sigma_{33}} \end{Bmatrix} \quad (4.10)$$

As shown in Figure 4-6, the architecture design with symmetric constraints (e.g., same projection pattern in 1-3 and 2-3 plane) significantly reduces the complexity of Eq. 4.8 and Eq. 4.9 by grouping identical struts (i.e., identical electric displacement contribution, identical strut length, diameter and cross-sectional shape). This allows the evaluation of the contribution of different type of struts to effective electric displacement field. As shown in Figure 4-7a, two groups of identical struts are identified: i). strut parallel to 3-axis ($\vec{L}_5$); ii) struts that are not parallel to the 3-axis ($\vec{L}_1, \vec{L}_2, \vec{L}_3, \vec{L}_4$). It is therefore sufficient to represent the group by one strut in each group.

	Projection (Identical)	Electric displacement map			3D Node unit	Theoretical prediction {d_{31}, d_{32}, d_{33}}	Numerical calculation			FEA results {d_{31}, d_{32}, d_{33}}
							31 mode	32 mode	33 mode	
a	N=5, Θ=15° (- - +)					{-0.69, -0.69, 0.19}				{-0.70, -0.70, 0.16}
b	N=5, Θ=30° (- - +)					{-0.68, -0.68, 0.27}				{-0.67, -0.67, 0.30}
c	N=5, Θ=75° (- - +)					{-0.46, -046, 0.76}				{-0.44, -0.44, 0.79}
d	N=5, Θ=90° (~0 ~0 +)					{-0.28, -0.28, 0.92}				{-0.25, -0.25, 0.94}
e	N=5, Θ=120° (+ + +)					{0.48, 0.48, 0.73}				{0.46 0.46, 0.77}
f	N=5, Θ=150° (+ + +)					{0.64, 0.64, 0.43}				{0.63, 0.63, 0.45}
g	N=5, Θ=165° (- - +)					{0.69, 0.69, 0.24}				{0.68, 0.68, 0.27}

Figure 4-6. The comparison between analytical results, experiment results and numerical results of the N=5 lattices.

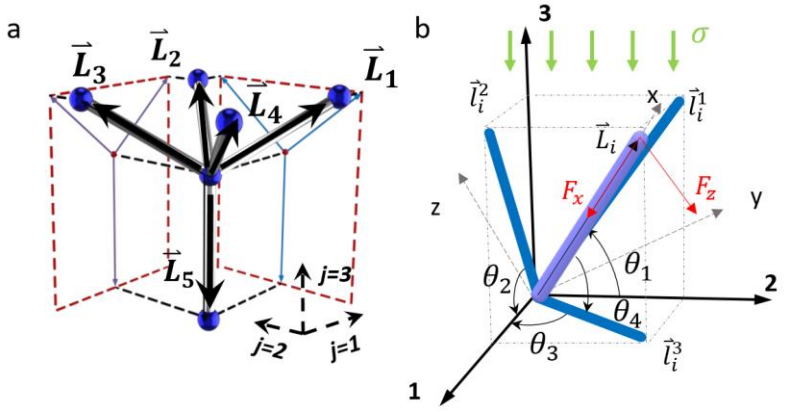

Figure 4-7. Identification of two types of struts. a) Schematic of the N=5 design. b) Schematic of a single strut with two coordinate systems.

Below we derive a closed-form expression of effective piezoelectric charge constant d as a function of spatial orientations of ligaments within a unit cell. We started from force equilibrium of a single strut and established a local coordinate system (x-y-z coordinate system) and the global coordinate system (1-2-3). The parameters of these two-coordinate systems are shown in Figure 4-7b. The x-axis of the local coordinate system is parallel to strut space vector $\vec{L}_i$. The axial stress $\sigma_{pq}^{(i)}$ is firstly calculated in the local coordinate system (x-y-z), then will be transformed to the global coordinate system $\sigma_{kl}^{(i)}$ $(k, l = 1,2,3)$. The correlation between stress matrix in local coordinate system and global coordinate system is achieved through the transformation matrix N^i as:

$$\sigma_{kl}^{(i)} = N^i \sigma_{pq}^{(i)} (N^i)^T \quad (4.11)$$

. Similarly, the electrical displacement contribution of each strut can be expressed as:

$$D_n^{(i)} = d_{nkl} \sigma_{kl}^{(i)} = d_{nkl} N^i \sigma_{pq}^{(i)} (N^i)^T \quad (4.12)$$

Hence, we derived the expression of the transformation matrix N^i correlating the local coordinate system to the global coordinate system to calculate the effective electrical displacement D_n^{eff} and effective stress σ_{KL}^{eff}, and further calculate effective charge constants.

According to Euler's rotation theorem, any coordinate system transformation may be described using three angles. In this situation, the force components that we considered is axial force ($\vec{F}_x$), which is in alignment with strut space vector $\vec{L}_i$, and shear force ($\vec{F}_z$), which is perpendicular to the

strut space vector $\vec{L}_i$. Here, we derive the transformation matrix via rotating the 1-axis of the global coordination system such that it overlaps with the x-axis of the local coordinate system of a single strut $\vec{L}_i$ and then define the rest of the coordinates. By doing this, the transformation matrix for 1st-4th and 5th strut can be written as:

$$\begin{bmatrix} N_{11}^i & N_{12}^i & N_{13}^i \\ N_{21}^i & N_{22}^i & N_{23}^i \\ N_{31}^i & N_{32}^i & N_{33}^i \end{bmatrix} = \begin{bmatrix} \cos\theta_3\cos\theta_4 & -\sin\theta_3 & -\cos\theta_3\sin\theta_4 \\ \sin\theta_3\cos\theta_4 & \cos\theta_3 & -\sin\theta_3\sin\theta_4 \\ \sin\theta_4 & 0 & \cos\theta_4 \end{bmatrix} \quad (4.13)$$

$$\begin{bmatrix} N_{11}^5 & N_{12}^5 & N_{13}^5 \\ N_{21}^5 & N_{22}^5 & N_{23}^5 \\ N_{31}^5 & N_{32}^5 & N_{33}^5 \end{bmatrix} = \begin{bmatrix} 0 & 0 & 1 \\ 0 & 1 & 0 \\ -1 & 0 & 0 \end{bmatrix} \quad (4.14)$$

For d_{33}^{eff}, regrouping Eq. 4.8 and 4.9 by identical struts yields

$$D_3^{eff} = \frac{1}{V}\{d_{31}\ \ d_{32}\ \ d_{33}\}\left(4A_1|L_1|\begin{Bmatrix}\sigma_{11}^1\\ \sigma_{22}^1\\ \sigma_{33}^1\end{Bmatrix} + A_5|L_5|\begin{Bmatrix}\sigma_{11}^5\\ \sigma_{22}^5\\ \sigma_{33}^5\end{Bmatrix}\right) \quad (4.15)$$

$$\sigma_{33} = \frac{1}{V}(4A_2|L_2|\sigma_{33}^1 + A_5|L_5|\sigma_{33}^5) \quad (4.16)$$

Consider a remote compressive stress σ along z direction that is applied to the infinite lattice structure consists of the node unit. From force equilibrium, the total force applied on the node unit F can be given as:

$$F = 4\sigma L^2\sin^2\theta_3\cos^2\theta_4 \quad (4.17)$$

Under this z-direction stress σ, the vertical strut ($\vec{L}_5$) is subject to normal stress, while other strut ($\vec{L}_1, \vec{L}_2, \vec{L}_3, \vec{L}_4$) are subject to a combination of normal and shear stresses. From equilibrium, the local stress matrix of strut group ($\vec{L}_1, \vec{L}_2, \vec{L}_3, \vec{L}_4$) is:

$$\sigma_{pq}^{(i)} = \frac{\sigma L^2}{A_1}\begin{bmatrix} \sin^2\theta_3\cos^2\theta_4 sin\theta_4 & 0 & \sin^2\theta_3\cos^3\theta_4 \\ 0 & 0 & 0 \\ \sin^2\theta_3\cos^3\theta_4 & 0 & 0 \end{bmatrix} \qquad (4.18)$$

Similarly, the local stress matrix of vertical strut ($\vec{L}_5$) is:

$$\sigma_{pq}^{(5)} = \frac{4\sigma L^2}{A_5}\begin{bmatrix} \sin^2\theta_3\cos^2\theta_4 & 0 & 0 \\ 0 & 0 & 0 \\ 0 & 0 & 0 \end{bmatrix} \qquad (4.19)$$

By substituting Eq. 4.18 and 4.19 into Eq. 4.11, the global stress matrix is obtained. Then substitute Eq. 4.15 and 4.16 into Eq. 4.10, we obtain d_{33}^{eff} for the $N = 5$ structure as:

$$d_{33}^{eff} = \frac{-\cos^2\theta_3\cos^2\theta_4\sin\theta_4 d_{31} - \sin^2\theta_3\cos^2\theta_4\sin\theta_4 d_{32} + (\sin\theta_4(1+\cos^2\theta_4)+1)d_{33}}{2+2\sin\theta_4} \qquad (4.20)$$

Similarly, d_{31}^{eff} could be obtained as:

$$d_{31}^{eff} = \frac{-\cos^3\theta_3\cos^2\theta_4\sin\theta_4 d_{31} - \sin^2\theta_3\cos\theta_3\cos^2\theta_4\sin\theta_4 d_{32} + \cos\theta_3\sin\theta_4(1+\cos^2\theta_4)d_{33}}{2\sin\theta_3\cos\theta_4} \qquad (4.21)$$

Due to symmetry, $d_{31}^{eff} = d_{32}^{eff}$.

It should be noted that since the bending stress is symmetric to the neutral surface of the strut (integration of bending stress over cross-section area is zero), it does not contribute to the effective electric displacement and charge constant.

4.2.4 Expanded architectures and their d_{3M} distributions

We also demonstrate our design scheme and calculate the distribution of d_{3M}^{eff} of *N*=12 structure, as shown in Figure 4-8. We denoted the local and global stresses of each strut in vector form. The stretching-dominated deformation mechanism gives rise to negligible bending and shear stresses, it is easier to express the local and global stresses in vector form.

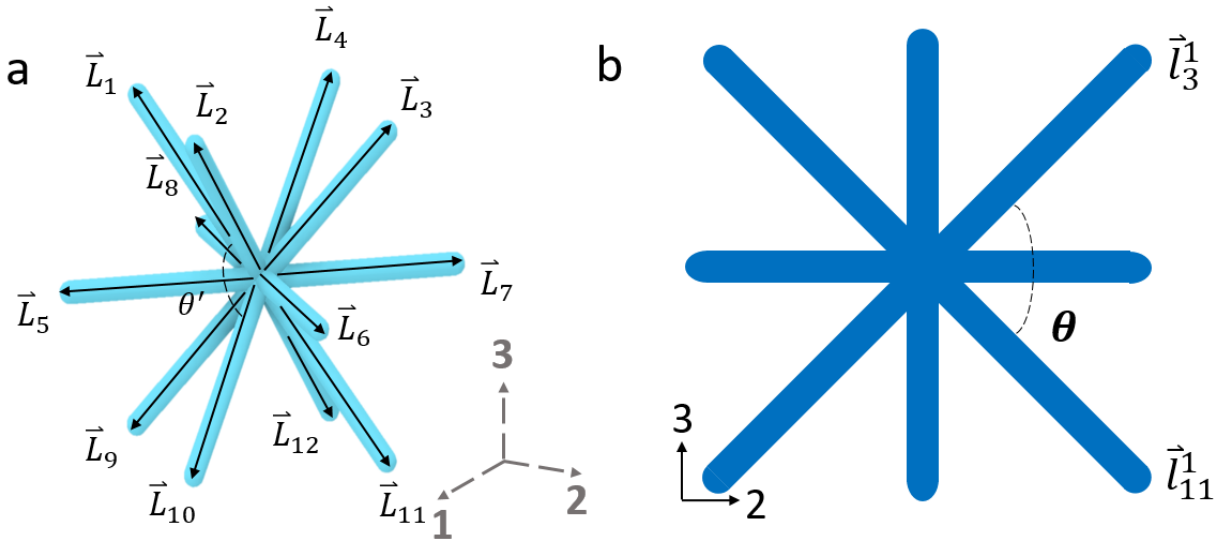

Figure 4-8. Piezoelectric cell design for N=12 case. (a) *N*=12 designs with its corresponding projection patterns (b) on 2-3 plane for analytical calculation.

To determine d_{3M}^{eff}, rewriting Eq. 4.4 in matrix form and in terms of strut stress for the convenience of analytical calculation, we obtain:

$$D_3^{eff} = \frac{1}{V}\sum_{i=1}^{N} A_i\left|\vec{L}_i\right| \cdot \begin{bmatrix} d_{31}^i & d_{32}^i & d_{33}^i & d_{34}^i & d_{35}^i & d_{36}^i \end{bmatrix} \begin{bmatrix} T_{11}^i & T_{12}^i & \dots & T_{16}^i \\ T_{21}^i & T_{22}^i & \dots & T_{26}^i \\ \vdots & \vdots & \ddots & \vdots \\ T_{61}^i & T_{62}^i & \dots & T_{66}^i \end{bmatrix} \begin{Bmatrix} \sigma_{xx}^i \\ \sigma_{yy}^i \\ \sigma_{zz}^i \\ \sigma_{xy}^i \\ \sigma_{xz}^i \\ \sigma_{yz}^i \end{Bmatrix} \quad (4.22)$$

$$\begin{Bmatrix} \sigma_{11} \\ \sigma_{22} \\ \sigma_{33} \\ \sigma_{12} \\ \sigma_{13} \\ \sigma_{23} \end{Bmatrix} = \frac{1}{V}\sum_{i=1}^{N} A_i\left|\vec{L}_i\right| \cdot \begin{bmatrix} T_{11}^i & 0 & \dots & 0 \\ 0 & T_{22}^i & \dots & 0 \\ \vdots & \vdots & \ddots & \vdots \\ 0 & 0 & \dots & T_{66}^i \end{bmatrix} \begin{Bmatrix} \sigma_{xx}^i \\ \sigma_{yy}^i \\ \sigma_{zz}^i \\ \sigma_{xy}^i \\ \sigma_{xz}^i \\ \sigma_{yz}^i \end{Bmatrix} \quad (4.23)$$

, where $\{\sigma_{xx}^i \quad \sigma_{yy}^i \quad \sigma_{zz}^i \quad \sigma_{xy}^i \quad \sigma_{xz}^i \quad \sigma_{yz}^i\}^T$ is the vector form in terms of the local coordinate of σ_{pq}^i, and T^i is the stress transformation matrix from local coordinate system to the global coordinate system. The architecture design with symmetric constraints significantly reduces the complexity of Eq. 4.22and Eq. 4.23 by grouping identical struts (i.e. identical electric displacement contribution, identical strut length, diameter and cross-sectional shape). This allows the evaluation of contribution of different types of struts to effective electric displacement field. Finally, according to Eq. 4.3, d_{3M}^{eff} in matrix form becomes:

$$\begin{Bmatrix} d_{31}^{eff} \\ d_{32}^{eff} \\ d_{33}^{eff} \end{Bmatrix} = \begin{Bmatrix} \frac{D_3^{eff}}{\sigma_{11}} \\ \frac{D_3^{eff}}{\sigma_{22}} \\ \frac{D_3^{eff}}{\sigma_{33}} \end{Bmatrix} \quad (4.24)$$

For *N*=12 structure, only axial stresses are considered due to its stretch-dominated nature. Eq. 4.22 - 4.24 then lead to the results of d_{3M}^{eff} (only M=1, 2, 3 is of interest) of *N*=12 structure. For d_{31}^{eff}, the parent material piezoelectric charge constants are identical for each strut (Table. 4-1). Eq. 4.22 and Eq. 4.23 then reduce to:

$$D_3^{eff} = \frac{1}{V}\sum_{i=1}^{12} A_i\left|\vec{L}_i\right| \cdot \left(d_{31}T_{11}^i + d_{32}T_{21}^i + d_{33}T_{31}^i\right)\sigma_{xx}^i \quad (4.25)$$

$$\sigma_{11} = \frac{1}{V}\sum_{i=1}^{N} A_i\left|\vec{L}_i\right| \cdot T_{11}^i\sigma_{xx}^i \quad (4.26)$$

.

Table 4-1. Properties of the PZT particles used in the piezoelectric composite

Relative dielectric constant	1900
Dielectric dissipation factor (tand)	<2.00
k_p	0.63
k_{33}	0.72
k_{31}	0.36
k_{15}	0.68
d_{33}	400
$-d_{31}$	175
d_{15}	590
g_{33}	24.8
g_{31}	12.4

g_{15}	36.0
Young's modulus Y_{11}	6.3
Y_{33}	5.4

Three groups of identical struts are identified: i) struts parallel to 1-3 plane subjected to axial compression ($\vec{L}_2, \vec{L}_4, \vec{L}_{10}, \vec{L}_{12}$); and ii) struts parallel to 1-2 plane subjected to axial compression ($\vec{L}_5, \vec{L}_6, \vec{L}_7, \vec{L}_8$); and iii) struts parallel to 2-3 plane subjected to axial tension ($\vec{L}_1, \vec{L}_3, \vec{L}_9, \vec{L}_{11}$). It is therefore sufficient to represent the group by one strut in each group. Therefore, regrouping Eq. 4.25 and 4.26 by identical struts yields:

$$D_3^{eff} = \frac{1}{V}\{d_{31} \quad d_{32} \quad d_{33}\}\left(4\begin{Bmatrix} T_{11}^2 \\ T_{21}^2 \\ T_{31}^2 \end{Bmatrix} A_2 \left|\vec{L}_2\right| \sigma_{xx}^2 + 4\begin{Bmatrix} T_{11}^5 \\ T_{21}^5 \\ T_{31}^5 \end{Bmatrix} A_5 \left|\vec{L}_5\right| \sigma_{xx}^5 + 4\begin{Bmatrix} T_{11}^1 \\ T_{21}^1 \\ T_{31}^1 \end{Bmatrix} A_1 \left|\vec{L}_1\right| \sigma_{xx}^1 \right) \quad (4.27)$$

$$\sigma_1 = \frac{1}{V}\left(4T_{11}^2 A_2 \left|\vec{L}_2\right| \sigma_{xx}^2 + 4T_{11}^5 A_5 \left|\vec{L}_5\right| \sigma_{xx}^5 + 4T_{11}^1 A_1 \left|\vec{L}_1\right| \sigma_{xx}^1\right) \quad (4.28)$$

, where, from geometric relationships,

$$\begin{cases} T_{11}^{2} = \dfrac{\sqrt{2}}{2}\cos\dfrac{1}{2}\theta \\ T_{21}^{2} = \dfrac{\sqrt{2}}{2}\cos\dfrac{1}{2}\theta \\ T_{31}^{2} = \sin\dfrac{1}{2}\theta\cos\dfrac{1}{2}\theta \\ T_{11}^{5} = \dfrac{1}{2} \\ T_{21}^{5} = \dfrac{1}{2} \\ T_{31}^{5} = 0 \\ T_{11}^{1} = 0 \\ T_{21}^{5} = \dfrac{1}{2} \\ T_{31}^{5} = \dfrac{1}{2} \end{cases} \quad (4.29)$$

, also, $\left|\vec{L}_2\right| = \left|\vec{L}_1\right| = \frac{\sqrt{2}}{\cos\frac{1}{2}\theta}\left|\vec{L}_5\right|$, $A_2 = A_5 = A_1$. In this case, $\theta = \angle\vec{l}_3^1\vec{l}_{11}^1 = \theta'$. Using nodal force equilibrium, we obtain the relationships between axial stresses of three types of struts: $\sigma_{xx}^2 = -\sigma_{xx}^1 = \frac{\sqrt{2}}{2}\frac{1}{\cos\frac{1}{2}\theta}\sigma_{xx}^5$. Thus, substituting Eq. 4.27 and 4.28 into Eq. 4.24, we obtain d_{31}^{eff} for *N*=12 structure as:

$$d_{31}^{eff} = \frac{\left(\frac{\sqrt{2}}{2}\cos\frac{1}{2}\theta + \frac{1}{2}\cos^2\frac{1}{2}\theta - \frac{1}{2}\right)(d_{32} + d_{31}) + \left(\sin\frac{1}{2}\theta\cos\frac{1}{2}\theta - \frac{1}{2}\right)d_{33}}{\frac{\sqrt{2}}{2}\cos\frac{1}{2}\theta + \frac{1}{2}\cos^2\frac{1}{2}\theta} \quad (4.30)$$

. Due to the symmetry, $d_{31}^{eff} = d_{32}^{eff}$. Similarly, d_{33}^{eff} can be obtained as:

$$d_{33}^{eff} = \frac{\left(cos^2\frac{1}{2}\theta - \frac{\sqrt{2}}{12sin\frac{1}{2}\theta - 4cos\frac{1}{2}\theta}\right)(d_{31} + d_{32}) + 2sin^2\frac{1}{2}\theta d_{33}}{\sqrt{2}sin\frac{1}{2}\theta} \quad (4.31)$$

Eq. 4.30 and 4.31 show that the variation of θ changes the effective piezoelectric charge constants by varying the contribution of material properties d_{31}, d_{32} and d_{33}.

A list of some other designed node units and their normalized effective piezoelectric charge constants are estimated. The 3D node unit with dissimilar projection patterns and its results are also shown. Despite that the projection patterns are 3-strut, with different skew angles between adjacent struts defined as $\theta_1 = \angle\vec{l}_1^1\vec{l}_2^1$ and $\theta_2 = \angle\vec{l}_1^2\vec{l}_2^2$, they yields a distribution of d_{3M} with $d_{31} \neq d_{32}$ (3-strut dissimilar projection patterns, Table S1). Another node unit with 3-strut pattern on 1-3 plane and 5-strut pattern on 2-3 plane is also illustrated (3-strut/5-strut dissimilar projection patterns, Table S1). This type of design further enhances the tunability of piezoelectric properties by utilizing the dissimilar projection patterns design.

Another superposition structure by summing two 3-strut projection patterns is also generated. d_{32} and d_{31} are nearly zero for $\theta = 60°$ due to the counteractive contributions of two groups of struts: i) struts paralleled to 1-3 plane; and ii) struts paralleled to 2-3 plane. d_{33} is predicted as negative at $\theta = 30°$ while $d_{31} = d_{32} > 0$, reaching a quadrant different from other designs. The node units with 6-strut dissimilar projection patterns are also shown to verify its d_{3M} distribution in (- + -) and (+ - +) quadrants.

4.3 Designing decoupled strain responses of piezoelectric metamaterials

4.3.1 Theoretical design of the decoupled strain responses for multi-mode sensor

The design strategy of the multi-mode sensor is modulating the effective electric displacement output of individual cells via leveraging the spatial orientation as well as material anisotropy of inclined piezo-active struts, when the sensor is subject to various macroscopic mechanical loads. The architectural design of individual cells starts from identifying a pair of spatially inclined ligaments that demonstrates distinct deformation patterns given external loads applied in different directions (Figure 4-9a). Both identified struts experience axial contraction under global compressive load; while one of the inclined ligaments demonstrate extension with shear load applied. Coupled with tailored material anisotropy, we are capable of selectively suppressing the effective electric displacement output of the identified piezo-active ligaments induced by specific macroscopic mechanical loading respectively (Figure 4-9b). These identified ligaments are then taken as the basic unit, and tessellated into the architectural cell of the multi-mode sensor. The structural phase and conductive phase are added accordingly to connect separated inclined struts and accumulate the generated charge of piezo-active ligaments induced by external loads. Via tailoring the orientation of the activation electric field, these individual cells are solely responsive to the selected mode, normal compression or tangential shear, of external mechanical load. Applying an identical electric field in both the upper and lower sections yield a compression-only cell design, where the local z-direction aligned with the central axis of inclined struts pointing towards the top surface (Figure 4-9b). Under macroscopic shear load, the electric displacements of two inclined struts cancel out, leading to zero effective voltage output from the compressive-only cell. Similarly, the shear-only cell is activated by applying opposite electric fields in the upper

and lower section. In specific, the separate detection of shear in two orthogonal directions is achieved via rotating the shear-only cell design by 90° with respect to the 3-axis.

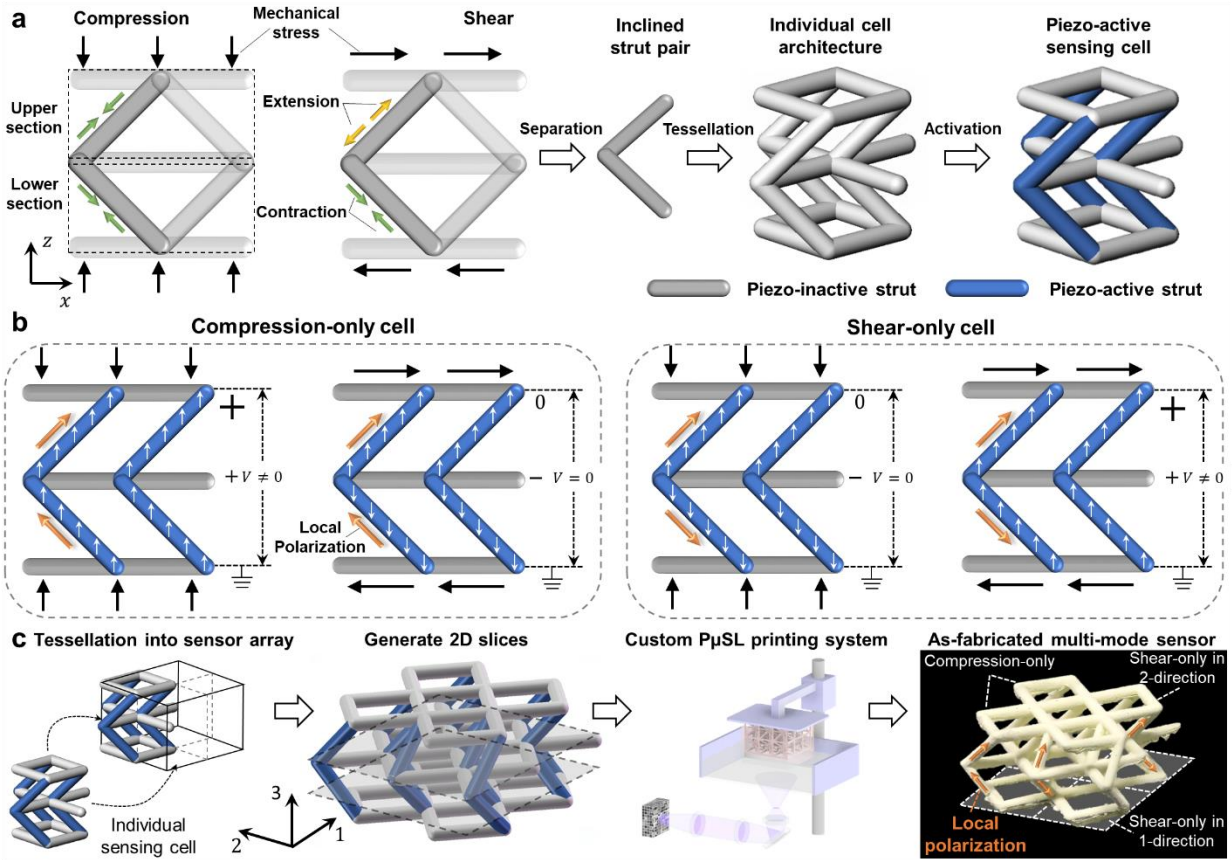

Figure 4-9. Design and fabrication of decouple strain response of multi-mode sensor**.** (a). Design concept of architectural cells of the multi-mode sensor. The identified pair of ligaments (opaque ligaments), that demonstrate distinct deformation mechanism under different external loads, are separated, tessellated, and activated with electric field forming the architectural design of individual sensing cell. (b). Voltage output pattern of architectural cells of the multi-mode sensor (compression-only and shear-only cell) under both compressive and shear load. (c). Fabrication process of multi-mode sensor, formed by architectural cells with 2x2 configuration, and as-fabricated sample.

The effective piezoelectric properties of individual sensing cells of multi-mode sensor are theoretically evaluated by collecting electric displacement contribution from each individual strut

under macroscopic strain. Following the homogenization method proposed in previous work, the theoretical derived piezoelectric properties of individual cells is given as:

$$d_{nM} = \frac{\sum_{i=1}^{6} \int_{V_i} d_{nm}^{i} T_{mr}^{i} \sigma_r^i dV_i}{\sum_{i=1}^{6} \int_{V_i} \delta_{mM} T_{mr}^{i} \sigma_r^i dV_i} \qquad (4.8)$$

where d_{nm}^{i} is the piezoelectric coefficient matrix of the base material on each ligament ($n = 1,2,3, m, M = 1-6$), T_{mr}^{i} denotes the transformation matrix that correlates the local and macroscopic stress vector, σ_r^i is the local stress vector on each piezo-active ligaments, V_i is the volume of the i-th inclined strut in the sensing cell and δ_{mM} is the Kronecker delta. With this theoretical derivation, we estimated the critical piezoelectric charge constants of individual sensing cells. These piezoelectric charge constants of interest, specifically d_{33}, d_{34}, and d_{35}, corresponds to load cases of normal compression, tangential shear in 1- and 2-direction, respectively. For compression-only cell, the d_{33} coefficient has a value of 87 pc/N, while d_{34} and d_{35} are both zero. Similarly, the d_{34} coefficient is the only non-zero term among three charge constants of interest of shear-only cell in 1-direction. These theoretically predicted electromechanical performances validate that the designed individual sensing cells are capable of output voltage signal in response to selected external mechanical load only.

These architectural cells are tessellated into multi-mode sensor with 2x2 configuration, consisting of 2 compression-only cells and 2 shear-only cells where each shear-only cells is responsive to tangential traction in one orthogonal direction, respectively. The designed multi-mode sensor is then passed to a custom multi-material 3D printing system for sample fabrication (Figure 4-9c), and the as-fabricated multi-mode sensor is activated by a strong electric field with prescribed configuration.

4.3.2 Decoupled load measurement with multi-mode sensor

Next, we demonstrated the sensing capability of the multi-mode sensor by imposing a series of spatially oriented loads uniformly on the top plate attached to the sensor with the bottom surface fixed to a substrate (Figure 4-10a). These spatial loads are differentiated by two spatial angles θ and φ, where θ is the angle between the force orientation vector and 3-axis, and φ is the angle between the projection of force orientation vector in the 1-2 plane and 1-axis. Varying these two spatial angles enables us to manipulate the spatial orientation of applied force and achieve an arbitrary ratio between three components of load on the top surface. And three voltage output signals ($V_i, i = I, II, III$) are collected with a data acquisition system. Herein, we investigated the performance of the multi-mode sensor under four different cases by varying the spatial angles of applied loads (Figure 4-10b): I. $\theta^1 = 0$ or pure compression; II. $\theta^2 = 90°, \varphi^2 = 0$ or tangential shear in 1-direction (equivalent to the case of $\theta^2 = 90°, \varphi^2 = 90°$ or pure shear in 2-direction); III. compound load $\theta^3 = 45°, \varphi^3 = 30°$; IV. compound load $\theta^4 = 60°, \varphi^4 = 75°$. For case I and II, we performed three tests with various input strain values using a commercial actuator. Figure 4-10c and 4-7d present the voltage signal outputs (V_I & V_{II}) from the compression-only and shear-only cells induced by various input strain values of compressive and shear loading, respectively. The compression-only cell generates ~0.15V voltage signal at a low compressive strain level (0.0076%), and the peak voltage magnitude increases along with the input strain value (Figure 4-10c). The shear-only cell only outputs detectable a voltage signal at 0.0192% compressive strain, while the voltage magnitude is 10 times lower than that collected from the compressive-only cell ($V_I = 0.438V, V_{II} = 0.0434V$). Similarly, we compared the voltage signals V_I and V_{II} given three input shear strains. The shear-only cell generates ~0.12V voltage signal at a low shear strain level (0.008%) (Figure 4-10d), while the compression-only cell only outputs detectable voltage signal

at a 0.0202% shear strain, which is ~12 times lower than that collected from the shear-only cell ($V_I = 0.0328V,\ V_{II} = 0.3896V$). These results demonstrate that the individual cells with designed sensing modes are solely responsive to the selected stress component, either compressive or shear stress, with high sensitivity.

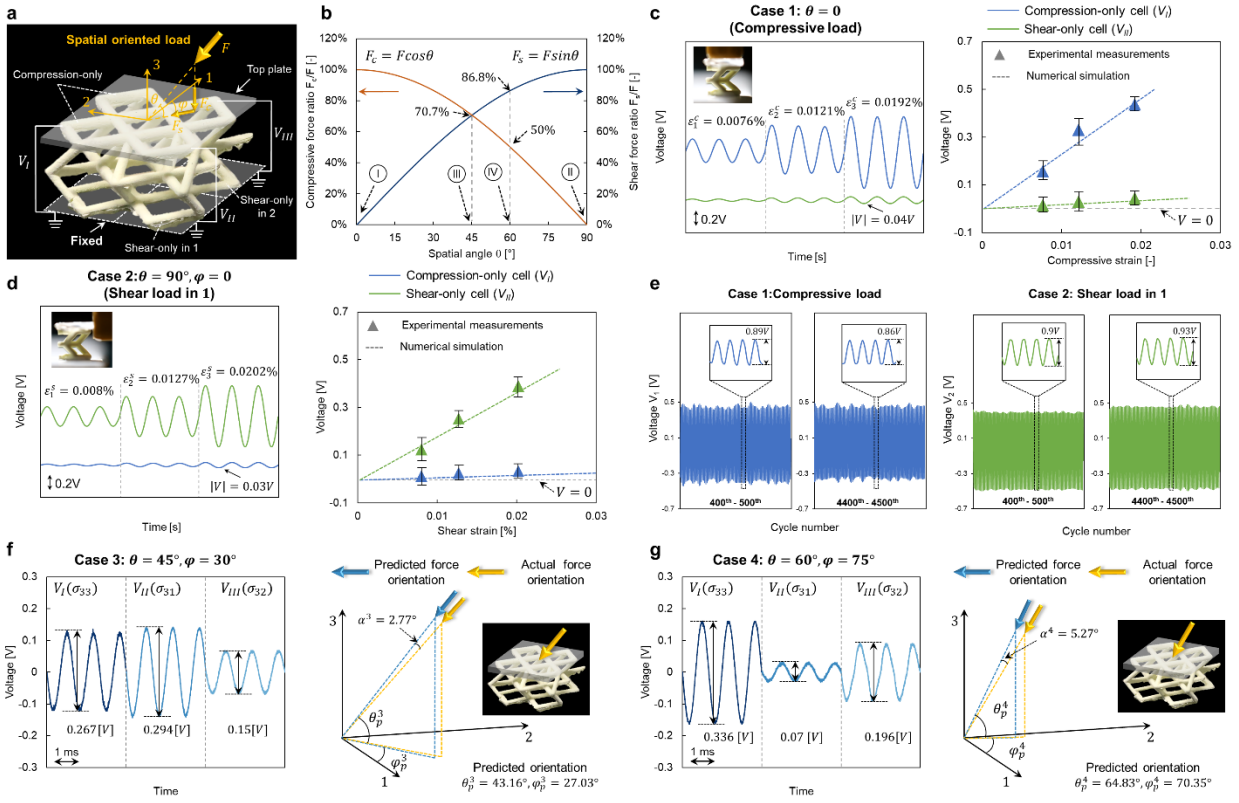

Figure 4-10. Characterization of the multi-mode performance under various spatial load**.** (a). Multi-mode sensor assembly for performance characterization. The load is uniformly applied to the top surface of the sensor via a top plate, where the bottom surface of the sensor is attached to fixed substrate. Three voltage signals are extracted as the output of the multi-mode sensor. (b). Evolution of compressive and shear force with respect to spatial angle θ and φ, and four representative load cases studied in this work. (c). Voltage responses of compression-only and shear-only cells under various input compressive strains. (d). Voltage responses of compression-only and shear-only cells under various input shear strains. (e). Cycling tests and durability of the voltage responses of the multi-mode sensor. (f)-(g). Voltage responses of the multi-mode sensor under spatial oriented loads and recreated force orientation with measured voltage signals.

We then investigated the linearity performance of the multi-mode sensor by evaluating the voltage outputs at various input strain values from both experimental measurements and numerical simulations. As shown in Figure 4-10c and 4-7d, the magnitudes of induced voltage extracted from both the compression-only and shear-only cells are proportional to the input strains, respectively. In specific, given the compressive load, the peak voltage magnitude of the compression-only cell ($|V_I|$) increases linearly from ~0.158V to ~0.438V as the input strain increases from 0.0076% to 0.0192%, while the peak voltage magnitude of the shear-only cell ($|V_{II}|$) remains within a close-to-zero level (Figure 4-10c). Similar linear responses were observed in the case when shear loads were applied (Figure 4-10d). The linear responses of the multi-mode sensor evaluated from experimental measures match the trend predicted by numerical analysis. These results effectively demonstrate the linearity performance of the designed multi-mode sensor, enabling the evaluation of input load over a wide stress range with consistent accuracy, minimum uncertainty, and high sensitivity.

Additionally, we evaluated the durability performance of the multi-mode sensor by comparing the voltage signal in response to the applied load with the same magnitude in cycling tests. Figure 4-10e demonstrate that the multi-mode sensor is capable of capturing the input load reproducibly over four thousand cycles with <5% deviation level, illustrating the robustness of the designed multi-mode sensor under long cyclic loading conditions.

We further exploited the sensing capability of the multi-mode sensor in full characterization of three-dimensional (3D) force (both magnitude and orientation). To this end, we applied two spatially oriented loads as representative cases, and recreated the applied force magnitude and orientation with voltage signals from multi-mode sensor ($V_i, i = I, II, III$) (Figure 4-10f and 4-7g).

Figure 4-10f presents the voltage signals of the multi-mode sensor under oriented load with prescribed spatial angle $\theta^3 = 45°, \varphi^3 = 30°$ (case III in Figure 4-10b). The stress components in three orthogonal directions $\sigma_j (j = 1,2,3)$ are derived with equation:

$$\sigma_j = \frac{\epsilon^{eff} V_i E_j}{h d_{ij}} \ (\ i = I, II, III;\ j = 1,2,3) \qquad (4.9)$$

where V_i is the extracted voltage signals from three architectural cells; ϵ^{eff} and h are the effective permittivity and height of the multi-mode sensor, respectively; E_j and d_{ij} are the elastic modulus and piezoelectric charge constants. Hence, we evaluated each stress component and reconstructed the force magnitude and orientation in Figure 4-10f**.** Similarly, for case IV ($\theta^4 = 60°, \varphi^4 = 75°$), the force magnitude and orientation was recreated from extracted voltage signal (Figure 4-10g). We observed an average 5% (estimated) deviation between the predicted force magnitude $|F_p|$ and the actual magnitude of applied force $|F_a|$. Meanwhile, a less than 4° average deviation angle of predicted force orientation with respect to actual orientation is observed. These results demonstrate that the designed multi-mode sensor is capable of capturing full information of spatially oriented load with satisfactory accuracy, enables its broad application in field of robot tactile sensing, etc.

4.3.3 Information encoding and storage with designed multi-mode sensor

Recent studies have exploited information processing capabilities, for instance mechanical computing and memory formation, as the novel material behaviors for mechanical metamaterials. The architected metamaterials display prescribed deformation pattern, revealing the encoded information like letters of alphabet, under external stimuli. In this study, we investigated and demonstrated the information encoding and storage performance of piezo-active metamaterial,

which output distinct encoded patterns of voltage signals in response to mechanical loads in different orthogonal directions. We encoded three letters (“U”, “C” and “B”) corresponding to three load cases (normal compression and tangential shear) as a representative demonstration (Figure 4-11a). To this end, we set the design volume of the piezo-active metamaterial as a region consists of 5x4 individual sensing cells, and each sensing cell is generated accordingly on the basis of the prescribed patterns (Figure 4-11b). The overlap of multiple patterns indicates the sensing cell at corresponding position output voltage signals when subject to mechanical loads applied in different directions.

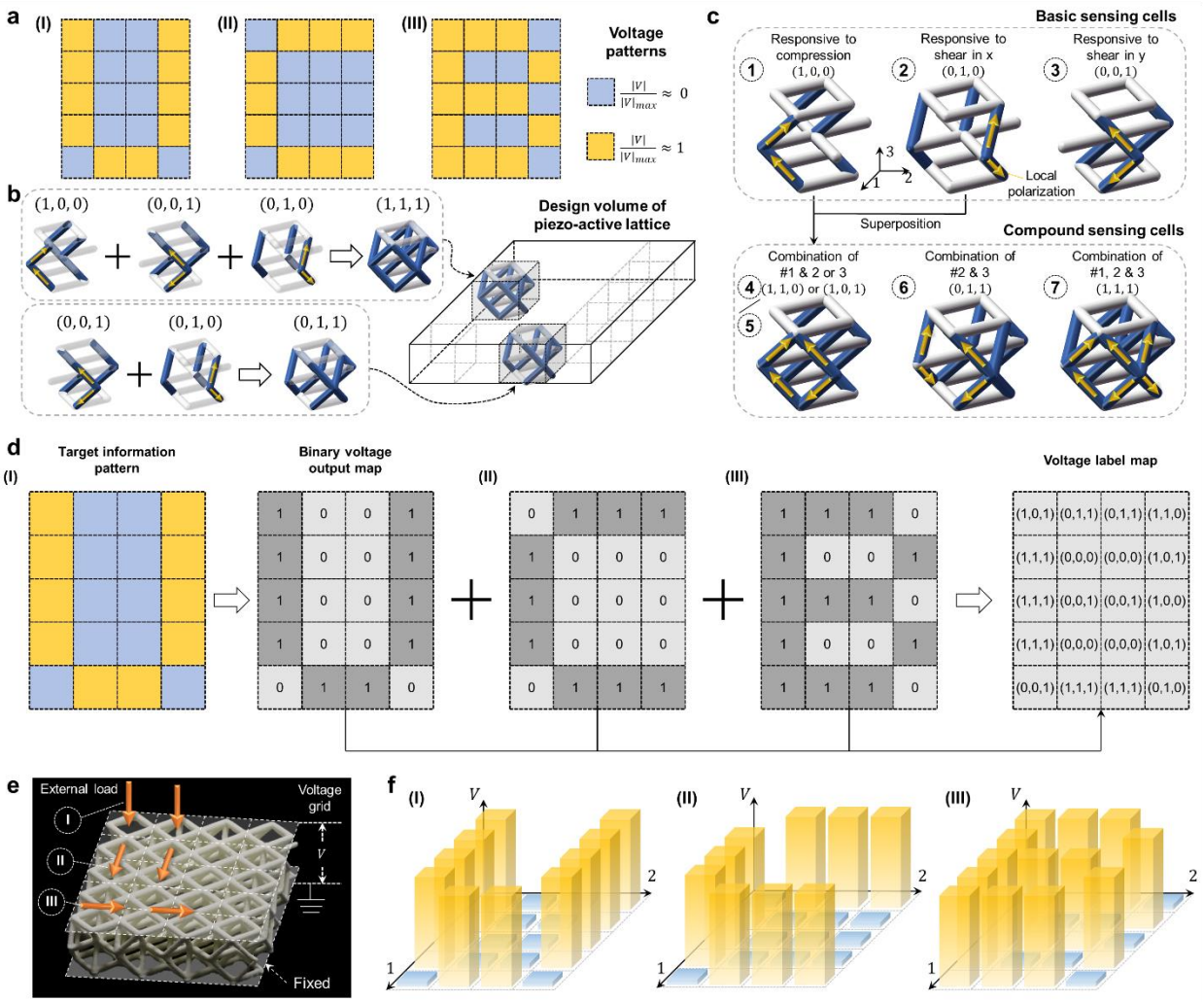

Figure 4-11. Demonstration of information encoding and storage performance of piezo-active metamaterial**.** (a). Target information to be encoded and stored in the piezo-active metamaterial. Three letters (U, C, and B) were set as target encoded information. (b). Assembling of piezo-active metamaterial. The design volume of the lattice consists of 20 (5x4) sensing cells, where each sensing cell is generated via superposition of basic sensing cell of multi-mode sensor. (c). Two categories of constitutive sensing cell of piezo-active metamaterial. Basic sensing cells where each sensing cell is solely responsive to a stress component in one principle axis (1-, 2-, or 3-direction). And compound sensing cells generated via superposition of basic sensing cells. Each compound sensing cell output voltage signal given stresses in multiple principle axes. (d). Information encoding process of the piezo-active metamaterial. The target information is transformed to binary voltage output maps, which is then combined as forming the voltage label map for lattice generation. (e). Testing setup of piezo-active metamaterial with information encoding and storage performance. Three loads, I – compression, II – shear in 1-direction, and III – shear in 2-direction, were applied, and the output patterns were formed with voltage signal from each individual sensing cell. (f). Voltage output patterns of piezo-active metamaterial under loadings in different directions. The patterns form letters "U", "C", and "B" when subject to compression, shear in x-direction, and shear in y-direction, respectively.

Herein, we labeled all sensing cells with three-element vector where the elements of the vector denote the voltage response of the cell given mechanical loads, normal compression, and tangential shear in 1- and 2-directions, respectively. For instance, (0, 1, 0) denotes the cell that is solely responsive to tangential shear in 1-direction; and (1, 0, 1) represent the cell that output voltage signals given normal compression and tangential shear in y-direction, which is the combination of sensing cell (1, 0, 0) and (0, 0, 1). Following this approach, we generated the label for sensing cells at each location in the design volume and generated the corresponding design via direct superposition of selected sensing cells of multi-mode sensor, cell (1, 0, 0), (0, 1, 0), and (0, 0, 1) developed in the previous section (Figure 4-11b). In total, we developed a family of constitutive cells consists of two categories (Figure 4-11c): basic sensing cells that is solely responsive to load in a specific direction; and compound sensing cells that output voltage signals given various mechanical loads. These constitutive cells were then spatially arranged and tessellated into the piezo-active metamaterial with encoded information.

Next, we encoded target information into piezo-active metamaterial design via: I). transform the target information patterns to binary voltage output maps; II). combine three voltage output maps into the voltage label map at all locations of piezo-active metamaterial design volume; III). assign the constitutive sensing cells based on the voltage label at each location, giving rise to the design of piezo-active metamaterial with target information encoded and stored. The piezo-active lattices were fabricated and activated with prescribed material orientations. The piezo-active metamaterial was assembled for the demonstration of information storage, where the bottom surface is mechanically fixed and electrically grounded (Figure 4-11e). The voltage output of each cell was collected with a data acquisition system, which was processed to generate the signal pattern of piezo-active metamaterial under various loading. Figure 4-11f presents three voltage output patterns when the as-fabricated sample is subject to mechanical loading along each orthogonal direction, respectively. Voltage patterns with the shape of letters “U”, “C”, and “B” were observed when compression, shear in the 1-direction, and shear in the 2-direction was applied, which is the same as the encoded information of deigned piezo-active metamaterial. These results demonstrate that the information can be encoded and stored into developed piezo-active metamaterial, which can be extracted via the application of various mechanical loads.

4.4 Designing arbitrary actuation mode of piezoelectric metamaterials

4.4.1 Rational design of piezoelectric metamaterial with arbitrary strain mode

The core concept of architected material is the free placement of materials in a 3D cellular topology that either bypass limitations in natural crystals or mimic them to achieve desired properties. We introduce a convenient and robust strategy to architect piezo-active, conductive and structural phase (Figure 4-12a) in 3D space. Such multi-material metamaterials are capable of taking an

input electric field and outputting a desired mode of strain including new DoFs beyond the Cauchy strain components[71,72] (e.g., normal and shear strain), including normal, shear, twisting, and flexure, as well as their combinations and amplifications.

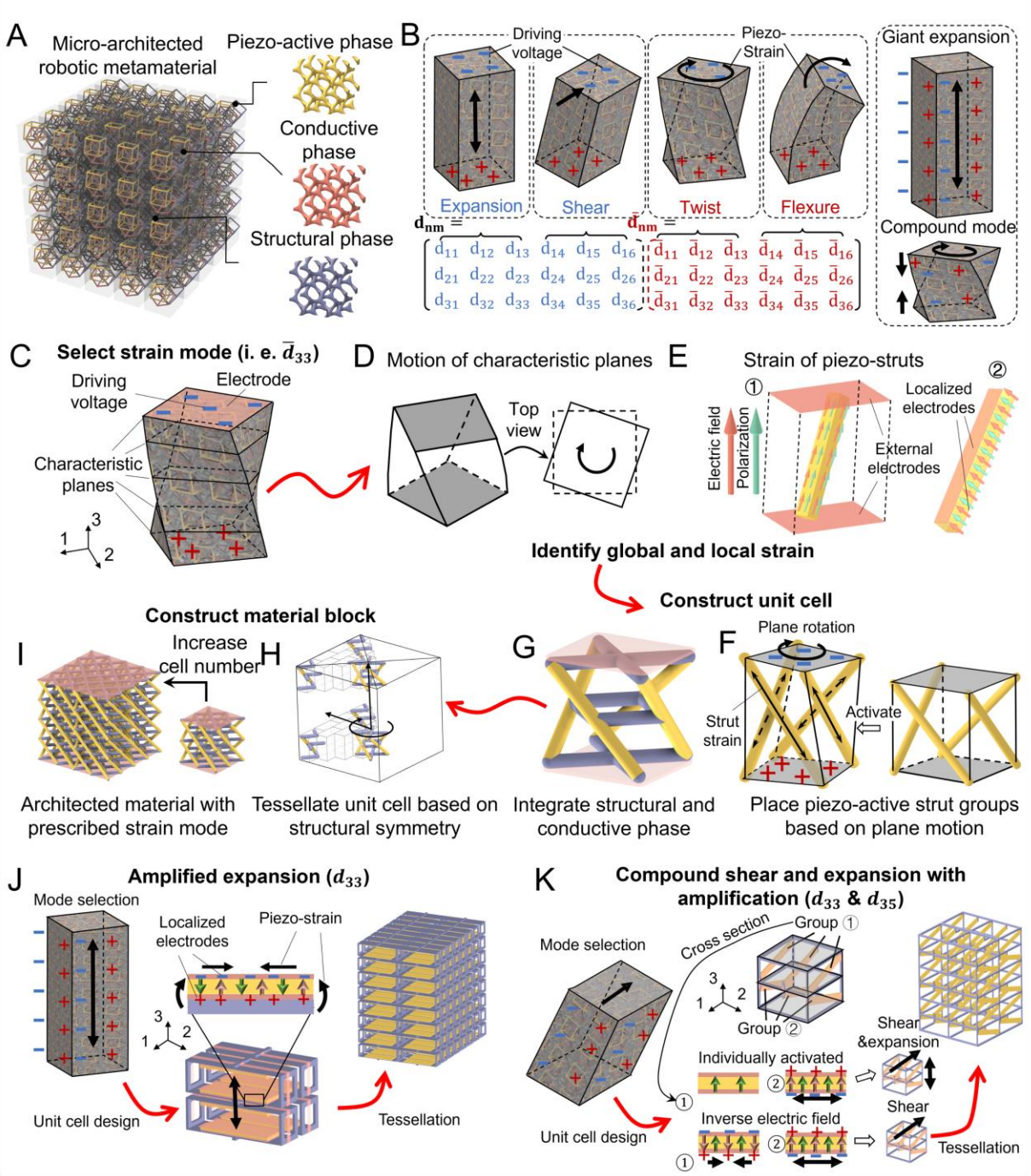

Figure 4-12. Rational designs of robotic metamaterials with arbitrary strain modes (a) Schematic of the piezoelectric metamaterial consisting of piezo-active, conductive and structural phases. (b) Schematic of various strain modes and piezoelectric strain matrix with extended tensors (red), as enabled by metamaterial design in contrast to only 18 tensors in natural piezoelectric ceramics (blue). (c)-(i) Schematic of the design rationale of the piezoelectric metamaterials. The example shown here is for the $\bar{d}_{33}$ (twisting) mode. (j) Designs of piezoelectric robotic metamaterial with amplified expansion. (k) Schematic of the compound and decoupled expansion-shear mode with strain amplification.

As the existing piezoelectric tensors are insufficient to describe the new DoFs, we define the generalized piezoelectric tensors d_{nm} and $\bar{d}_{nm}$ to describe the strain conversions of the architected piezoelectric materials (Figure 4-12b):

$$\varepsilon_m = d_{nm}E_n;\ \varphi_m = \bar{d}_{nm}E_n \qquad (4.10)$$

where E_n is the electric field along n-direction in the Cartesian coordinates (n=1-3); ε_m and φ_m(m=1-6) are the directional strain and coupled strain tensors, respectively; d_{nm} is the existing piezoelectric tensor; and $\bar{d}_{nm}$ is the extended piezoelectric tensor.

To design a piezoelectric micro-architecture that display a desired global strain mode d_{nm} (or $\bar{d}_{nm}$) (Figure 4-12b), we start by identifying the motion of a stack of virtual characteristic planes within a unit cell of the micro-architecture (Figure 4-12c and 4-9d) and the local strain of the piezo-active struts comprising the unit cell (Figure 4-12e). The virtual characteristic planes can be considered "pinned" by the piezo-active struts to allow unconstrained motion and will display a motion representing the desired global strain. As shown in Figure 4-13a to 4-10d, the characteristic planes undergo distance change, slip, rotation and tilt corresponding to strain modes including normal strain (ε_m, m=1-3), shear (ε_m, m=4-6), twist (φ_m, m=1-3) and flexure (φ_m, m=4-6), respectively. Figure 4-12d shows an example of a cube that twists upon application of electric field

in the 3-direction ($\bar{d}_{33}$ mode), which is represented by the in-plane rotation of characteristic planes (Figure 4-12d). The local strain of a piezo-active strut, either expand or contract, within the unit cell is determined by the direction of the strut, the polarization and the electric field (see Methods about the details on the identification of the local strain). The electric field are generated by the conducting phase either covering the sides of the lattice topology (external electrodes, Figure 4-12e①) or penetrating within the topology (localized electrodes, Figure 4-12e②), covering both sides of an active struts, leading to a shorter distance between electrodes and an elevated electric field.

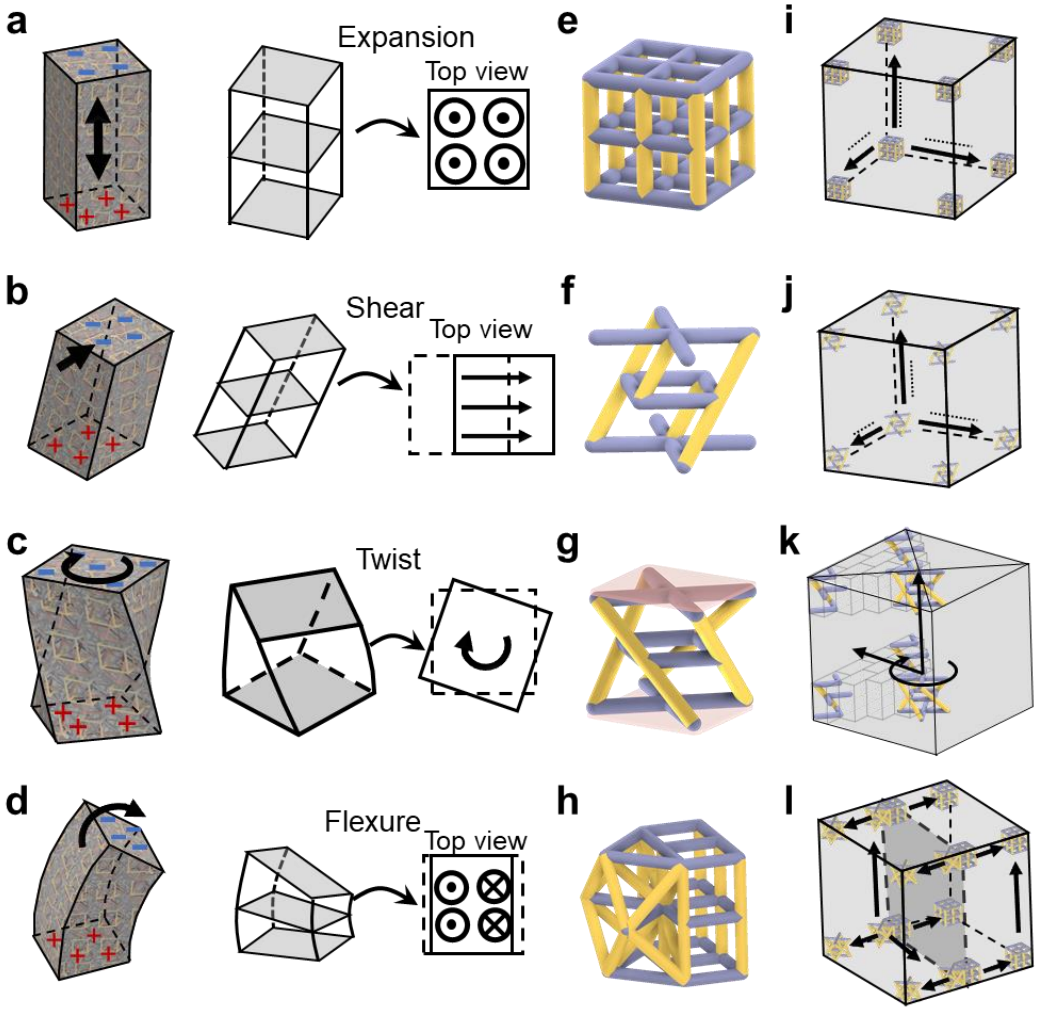

Figure 4-13. Schematic of the motion of characteristic planes, unit cells and tessellation methods for metamaterials with expansion, shear, twist and flexure strain modes.

The next design step is to place the piezo-active struts in a spatial layout such that their local strain will drive the virtual characteristic planes to display the motion path corresponding to the target global strain mode (d_{nm} or $\bar{d}_{nm}$). Figure 4-13f presents the designed piezo-active struts that generate a clockwise rotation of the characteristic planes, resulting in a new twist strain mode and corresponds to a nonzero piezoelectric twist coefficient, $\bar{d}_{33}$. 3D micro-architectural layout of piezo-active struts for other strain modes including expansion, shear and flexure, are summarized in Figure 4-13e to 4-10h. The full unit cell design is then completed by adding structural phase and conductive phase (Figure 4-12g) in a layout that matches the symmetry of the piezo-active struts.

In the last step, we tessellate the unit cells into a "metacrystal" that reflect effective response of the unit cell (see Figure 4-13i to 4-10l for choice of tessellation orientations). For example, to generate a twisting metamaterial, we tessellate the unit cell in cylindrical coordinates along the radial (r), angular (θ) and height (z) directions, as shown in Figure 4-12h and 4-12i. This novel aperiodic tessellation is scalable to an infinite number of unit cells and bypasses the effect of the number of unit cells when tessellated in Cartesian coordinates, where the twist strain would vanish when reduced to a Cauchy continuum as the unit cell number increases (Figure 4-14). As such, these metamaterial concepts are scalable, where the coefficient is invariant of the number of unit cells in all directions. Designs with all strain modes shown in the extended matrix are summarized in Table 4-1.

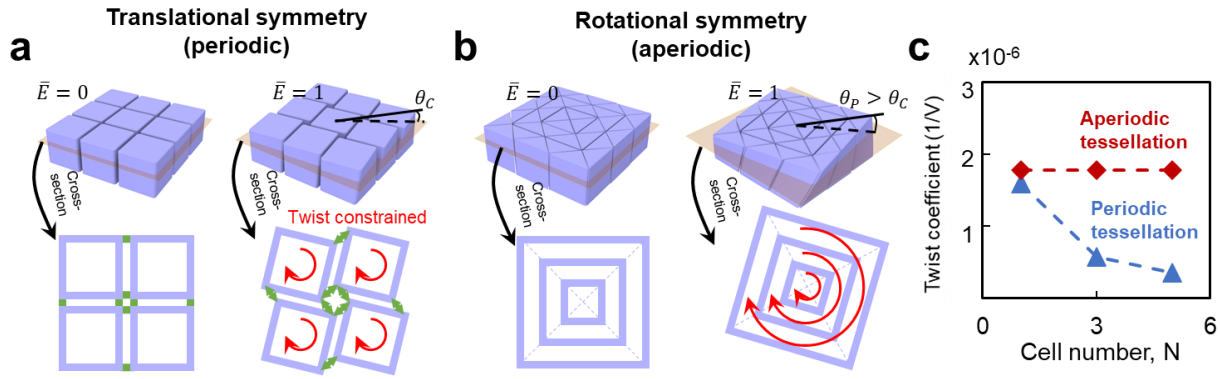

Figure 4-14. Comparison of the twist coefficients for unit cells tessellated with translational symmetry and rotational symmetry. (a), Schematic of the unit cells tessellated with translational symmetry. The green arrows represent the constraints induced by the deformation of the unit cells, while the red arrows represent the deformation direction of the unit cells or lattices. $\bar{E}$ shows the on ("1") and off ("0") of the electric field. θ_C is the twist angle of the lattice with periodic tessellation. θ_P is the twist angle of the lattice with aperiodic tessellation. (b), Schematic of the unit cells tessellated with rotational symmetry. (c), Twist coefficients of the unit cells tessellated with the two methods as a function of the cell number. The results are calculated with finite element analysis with the twist lattice design shown in Figure 4-12i.

Table 4-2. All designed actuation mode of piezoelectric metamaterials

	Shear			Twist			Bend		
Work mode	d_{14} (d_{25})	d_{15} (d_{24})	d_{16} (d_{26})	$\bar{d}_{11}$ ($\bar{d}_{22}$)	$\bar{d}_{12}$ ($\bar{d}_{21}$)	$\bar{d}_{13}$ ($\bar{d}_{23}$)	$\bar{d}_{14}$ ($\bar{d}_{25}$)	$\bar{d}_{15}$ ($\bar{d}_{24}$)	$\bar{d}_{16}$ ($\bar{d}_{26}$)
RVE deformation	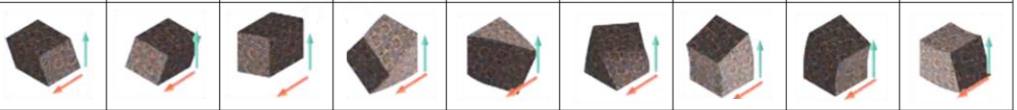								
Unit cell design	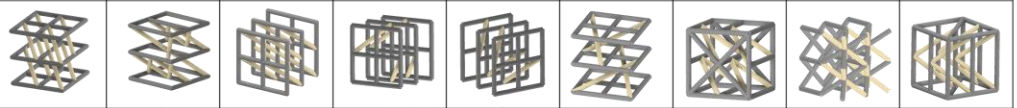								
Work mode	d_{34} (d_{35})		d_{36}	$\bar{d}_{31}$ ($\bar{d}_{32}$)		$\bar{d}_{33}$	$\bar{d}_{34}$ ($\bar{d}_{35}$)		$\bar{d}_{36}$
RVE deformation									
Unit cell design	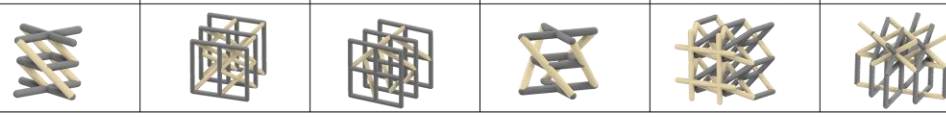								

Additionally, the interpenetrated piezo-active, structural and conductive phase allow amplification, logic subtraction and addition of strains, leading to the coupling and suppression of selected strain modes. Figure 4-12j shows the unit cell design featuring amplified expansion via tessellating pairs of piezo-active and structural struts(*28*). Figure 4-12k demonstrates the design with localized electrodes. The localized electrode architecture that cover selected groups of struts allows for programming the polarization and electric field direction within the unit cell (Figure 4-12k, see Figure 4-15 for polarization and driving voltage programming), thereby achieving compound strain mode with both shear and expansion strain output or decoupled strain mode with added up shear and suppressed expansion.

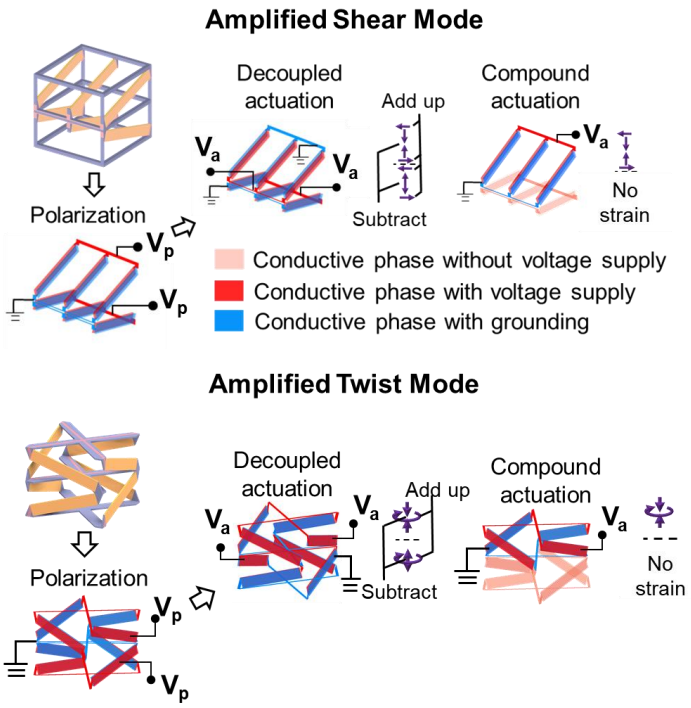

Figure 4-15. Polarization and driving voltage of the amplified shear and twist architecture with compound and decoupled mode**.** Va is the actuation voltage, Vp is the polarization voltage. During polarization, the struts within the unit cell are divided into two groups, and polarized via the localized electrodes. During decoupled actuation, the electric field direction of two groups of struts is inversed, resulting in expansion and contraction of two groups of struts, respectively. The expansion and contraction within the unit cell are canceled out while the shear deformation is

added up. During compound actuation, only one group of the struts are activated, allowing the unit cell to shear and expand simultaneously.

4.4.2 Theoretical characterization of the actuation performance

Identification of the local strain

We identify the deformation mode of spatially oriented piezo-active strut within the building block based on the direction of polarization (3-direction), electric field (denoted by n) and the angle between the electric field and the strut (ø). Due to the large permittivity difference between the piezo-active material and the air (or polarization liquid), upon application of the driving (or polarization) voltage, the electric field within the building block is mainly distributed along the struts that are not perpendicular to the electric field. When ø=90°, the strain of the strut is negligible. When n=1 or 2, the strut expands if ø<90° and shrinks if ø>90°. When n=3, the strut expands if ø>90° and shrinks if ø<90°.

Theoretical prediction of the piezoelectric strain constant

The electromechanical coupling behaviors of piezoelectric materials is characterized by the constituent equations as:

$$S = s^E T + d^t E \qquad (4.11)$$

$$D = d^E T + \varepsilon^t E \qquad (4.12)$$

Herein, S and D is the strain and the electric displacement field of the piezoelectric material, respectively; T and E is the external mechanical load and electric field; s, d and ε is the compliance, piezoelectric coefficient and dielectric constants.

To quantify the four categories of electromechanical coupling, we invoked micropolar mechanics to capture the novel mechanical deformations and extend the conventional piezoelectric coefficient matrix. Herein, we introduced 18 additional terms in the conventional coefficient matrix and established the extended piezoelectric coefficient as shown in Figure 4-12b. The expanded piezoelectric coefficients d_{nm} and $\bar{d}_{nm}$ (n=1-3, m=1-6, where m is in hexadecimal notation), could effectively represent the extension ($d_{nm,}$ m=1-3), shearing ($d_{nm,}$ m=4-6), twisting ($\bar{d}_{nm}$, m=1-3), and bending ($\bar{d}_{nm,}$ m=4-6) deformation. This is the first time to comprehensively characterize all physically feasible deformation mechanism of the piezo-active unit volume.

The piezoelectric charge constants d_{nm} and $\bar{d}_{nm}$ can be evaluated through quantifying the effective force and torque induced by the electric field and effective stiffness of the piezoelectric architectures. Due to the large permittivity difference between the piezo-active material and the air (or polarization liquid), upon application of the driving (or polarization) voltage, the electric field within the building block is mainly distributed along the struts that are not perpendicular to the electric field. As shown in Figure 4-12e, the angle between the localized polarization and the electric field direction is ø. When ø=90°, the strain of the strut is negligible. When ø<90°, the strut expands. When ø>90°, the strut shrinks. When n=3, the strut expands if ø>90° and shrinks if ø<90°. Herein, we define the L^i as the spatial orientation vector the i-th strut in the piezo-active structure, respectively. Configuring the spatial orientation vector L^i alters the effective force on this strut

induced by the electric field. Under external electric field E, the effective force and moment of the piezoelectric metamaterial is given as:

$$\mathbf{F_p} = \sum_{t=1}^{N} \mathbf{F_p^t} = \sum_{t=1}^{N} A^t C \mathbf{E}_i \mathbf{d_{ij}^t} \mathbf{N_{ip}^t} \qquad (4.13)$$

$$\mathbf{H_k} = \sum_{t=1}^{N} \mathbf{H_p^t} = \sum_{t=1}^{N} A^t C \mathbf{E}_i \mathbf{d_{ij}^t} \mathbf{N_{ip}^t} \mathbf{r_q^t} sin < e_p, e_q > \qquad (4.14)$$

where A^i is the cross-section area of the i-th strut, C and $\mathbf{d_{ij}^i}$ are the elastic modulus and piezoelectric coefficient matrix of the constituent materials, $\mathbf{E}_i$ is the electric field applied on the piezo-active ligaments, $\mathbf{N_{ip}^i}$ is the stress-transformation matrix from the local coordinate system of i-th strut (x-axis is the center line of the strut) to the global coordinate system , which is determined by its orientation vector $\mathbf{L}^i$, $\mathbf{r_q^i}$ is the distance vector that connects the origin of the global coordinate system (center of the unit cell) and the starting point of i-th strut, e is the unit vector in the corresponding direction ($|e_p| = 1$), and $e_p \times e_q = e_k$.

Considering the total effective force and moment induced by the electric field, along with the effective stiffness, yields the explicit expression of the piezoelectric coefficients as:

$$d_{nm} \frac{\sum_{t=1}^{N} \boldsymbol{F_p^t} \mathbf{C_{pm}^{-1}}}{E_n};\ \bar{d}_{nm} = \frac{\sum_{t=1}^{N} \boldsymbol{H_k^t} \mathbf{I_{km}^{-1}}}{E_n} \qquad (n = 1-3; p, m = 1-6) \qquad (4.15)$$

where F^i is the force of i-th strut induced by the electric field E_n; ε_m and φ_m is the electric-field induced strain and couple strain of the piezoelectric architectures; and $\mathbf{C_{pm}}$ and $\mathbf{I_{km}}$ is the effective stiffness and rigidity of the unit cell, which is estimated through homogenization method.

$$\mathbf{C_{pm}} = C\sum_{i=1}^{n}[\iint (r^i)^2 dA]\Big/A_{unit}\,;\ \mathbf{I_{km}} = C\sum_{i=1}^{n}\int_{\mathbf{L}^i}[\iint (r^i)^2 dA]\Big/V_{unit} \qquad (4.16)$$

This theoretical approach allows us to precisely characterize the actuation performance of the micro-architected piezoelectric materials via extracting certain component of the electric field induced force or moment and evaluating the corresponding term of piezoelectric coefficient d_{nm} and $\bar{d}_{nm}$.

Next, we derive the explicit expression of the piezoelectric coefficient under different deformation mode. To this end, we invoked the Euler beam theory to evaluate the deformation of the cubic representative volume element (unit cell). For axial extension, the strain is given as:

$$\varepsilon = \frac{F}{CA} \qquad (4.17)$$

where A is the cross section of the beam, and F is the external force. Therefore, for micro-architected piezoelectric lattice experience axial extension (m=1-3) in z-direction, the overall external force under electric field in z-direction is given as:

$$\sum F_z^i = \sum \pi {r^i}^2 E d_{33} sin\theta_4^i \qquad (4.18)$$

And the effective stiffness could be obtained via:

$$\mathbf{C_{pm}} = \frac{C\sum_{i=1}^{n}[\iint (r^i)^2 dA]}{a^2} \qquad (4.19)$$

Where a is the length of the unit cell. Therefore, the corresponding piezoelectric d_{nm} (m=1-3) is given as:

$$d_{nm} = \frac{\sum F_z^i \, \mathbf{C_{pm}^{-1}}}{E} = \frac{a^2 \sum \left[\pi {r^i}^2 E d_{33} sin\theta_4^i (sin\theta_4^i \delta_{m3} + cos\theta_4^i cos\theta_3 \delta_{m1} + cos\theta_4^i sin\theta_3 \delta_{m2})\right]}{C \sum_{i=1}^{n} [\iint (r^i)^2 dA]}$$

$$(m = 1 - 3) \qquad (4.20)$$

where δ_{xy} is the Kronecker delta: $\delta_{xy} = 1$ when x=y, and $\delta_{xy} = 0$ when x≠y.

Next, we derive the piezoelectric coefficient under shear deformation mode. The deformation of the continuum volume shear is characterized as:

$$\Delta y = \frac{F_s h^3}{12 C I_y} \qquad (4.21)$$

where F_s is the shear force, and I_y is the second moment of area. Therefore, we can derive the shear force in y-direction as:

$$F_y = \sum_{i=1}^{n} \left\{\pi {r^i}^2 E d_{33} sin\theta_4^i cos\theta_4^i sin\theta_3^i\right\} \qquad (4.22)$$

And the effective second moment of area is calculated as:

$$I_y^{eff} = \sum_{i=1}^{n} I_z^i =$$

$$\sum_{i=1}^{n} \left\{ \frac{\sqrt{1 + tan^2\theta_2^i + tan^2\theta_3^i}}{h} \left\{ \frac{\pi cos^2\beta}{4} r^4 (1 + csc^2\gamma_i tan^2\beta) \left(x_2^i - x_1^i\right) + \frac{\pi r^3}{3} csc\gamma_i \left(x_2^i - x_1^i\right)^3 \right\} \right\} \qquad (4.23)$$

where x_j^i $(j = 1,2)$ is the x-direction coordinate staring (j=1) and ending (j=2) point of the i-th strut. Hence, by substituting in the expression above, the piezoelectric coefficient dnm (m=4-6) for shear mode is given as:

$$d_{nm} = \frac{F_y a^2}{12ECI_y}$$

$$= \frac{\sum_{i=1}^{n}\left\{\pi r^{i^2} E d_{33} sin\theta_4^i (sin\theta_4^i \delta_{m6} + cos\theta_4^i cos\theta_3 \delta_{m4} + cos\theta_4^i sin\theta_3 \delta_{m5}\right\}}{12C\sum_{i=1}^{n}\left\{\frac{\sqrt{1+tan^2\theta_2^i + tan^2\theta_3^i}}{h}\left\{\frac{\pi cos^2\beta}{4} r^4 (1 + csc^2\gamma_i tan^2\beta)\left(x_2^i - x_1^i\right) + \frac{\pi r^3}{3} csc\gamma_i \left(x_2^i - x_1^i\right)^3\right\}\right\}}$$

$$(m = 4 - 6) \qquad (4.24)$$

Regarding the twisting mode, the deformation of the continuum volume twisting is characterized by the polar moment of inertia Iz as:

$$\theta = \frac{M}{CI_z} \qquad (4.25)$$

Where M is the external moment. Therefore, we derive the effective moment applied on the piezoelectric lattice as:

$$\sum M_m^j = \sum F_i^j x_{i+1}^j + F_{i+1}^j x_i^j \ \ (m = 1,2,3; i \neq m) \qquad (4.26)$$

And the effective polar moment of inertia is given as:

$$I_z^{eff} = \sum_{i=1}^{n} I_z^i =$$

$$\sum_{i=1}^{n} \left\{ \frac{\sqrt{1 + tan^2\theta_2^i + tan^2\theta_3^i}}{h} \left\{ \frac{\pi r^4}{4} (1 + csc^2\gamma_i)\left(x_2^i - x_1^i\right) \right.\right.$$

$$+ \frac{\pi r^3}{3} csc\gamma_i \left[\left({x_2^i}^3 - {x_1^i}^3 \right) + \left(x_2^i - x_1^i\right){y_1^i}^2 + tan\theta_2^i \left(x_2^i - x_1^i\right)^2 y_1^i \right.$$

$$\left.\left. \left. + \frac{tan^2\theta_2^i}{3} \left(x_2^i - x_1^i\right)^3 \right] \right\} \right\} \qquad (4.27)$$

Therefore, the piezoelectric twisting coefficient dnm (m=7-9) for shear mode is given as:

$$d_{nm} = \frac{M}{aECI_z} = \frac{\sum F_i^j x_{i+1}^j + F_{i+1}^j x_i^j}{aEC \sum_{i=1}^{n} I_z^i} \qquad (4.28)$$

Similarly, we can obtain the piezoelectric bending coefficient dnm (m=A-C) as:

$$d_{nm} = \frac{\sum F_m^j x_m^j}{aEC \sum_{i=1}^{n} I_y^i} \quad (m = A - C) \qquad (4.29)$$

Here, I_y^i is given as:

$$I_y^i = \frac{\sqrt{1 + tan^2\theta_2^i + tan^2\theta_3^i}}{h} \left\{ \frac{\pi cos^2\beta}{4} r^4 (1 + csc^2\gamma_i tan^2\beta) \left(x_2^i - x_1^i\right) \right.$$

$$\left. + \frac{\pi r^3}{3} csc\gamma_i \left(x_2^i - x_1^i\right)^3 \right\} \qquad (4.30)$$

4.4.3 Experimental validation of metamaterial design with target strain mode

To verify the arbitrary strain modes of the robotic metamaterial, we measured the electric field activated deformation of as-fabricated and poled samples via a high-precision full-field laser vibrometer (Polytec, PSV-500) (Figure 4-16a). Quasi-static driving voltage with 50V amplitude was applied through the layered external electrodes, while the activated deformation is measured by tracing the side surface of the metamaterial (as shown in Figure 4-16a) and reconstructed as a surface plot for visualization. Figure 4-16b and 4-13c show an optical image of a twist ($\bar{d}_{33}$) mode lattice with external electrodes and its side surface deformation, showing a wrapped shape corresponding to a twisted solid (Figure 4-12c). Deformation measurement for shear (d_{34}) and flexure ($\bar{d}_{35}$) mode lattices are summarized in Figure 4-16d and 4-13e and Figure 4-16f and 4-13g, respectively. Different strain modes can also be combined into a single element piezoelectric lattice to achieve a selection of multiple strain modes and multi-DoF metamaterial actuator with six individually actuatable architecture designs full-filling 6-DoF, including the d_{33}, d_{35}, $\bar{d}_{33}$, $\bar{d}_{34}$, $\bar{d}_{35}$ and d_{36} modes (Figure 4-16h and 4-16i). This multi-DoF actuator has a density of 0.88/cm^3, making it among the most compact 6-DoF actuators with high-speed and precision motions, with a density an order of magnitude lower than existing piezo-actuators with dense PZT[73] (Figure 4-17). The multi-DoF actuator is capable of high-speed high-precision motions. As an example, we demonstrate a high-speed galvanometer actuated by two multi-DoF actuators assembled with two reflective mirrors. Figure 4-18 shows a star pattern drawn by the steered laser beam (10 cycles at 20 Hz, with an RMS precision of 50±13 μm) by programming the input voltage that controls the tilt angle of the metamaterial.

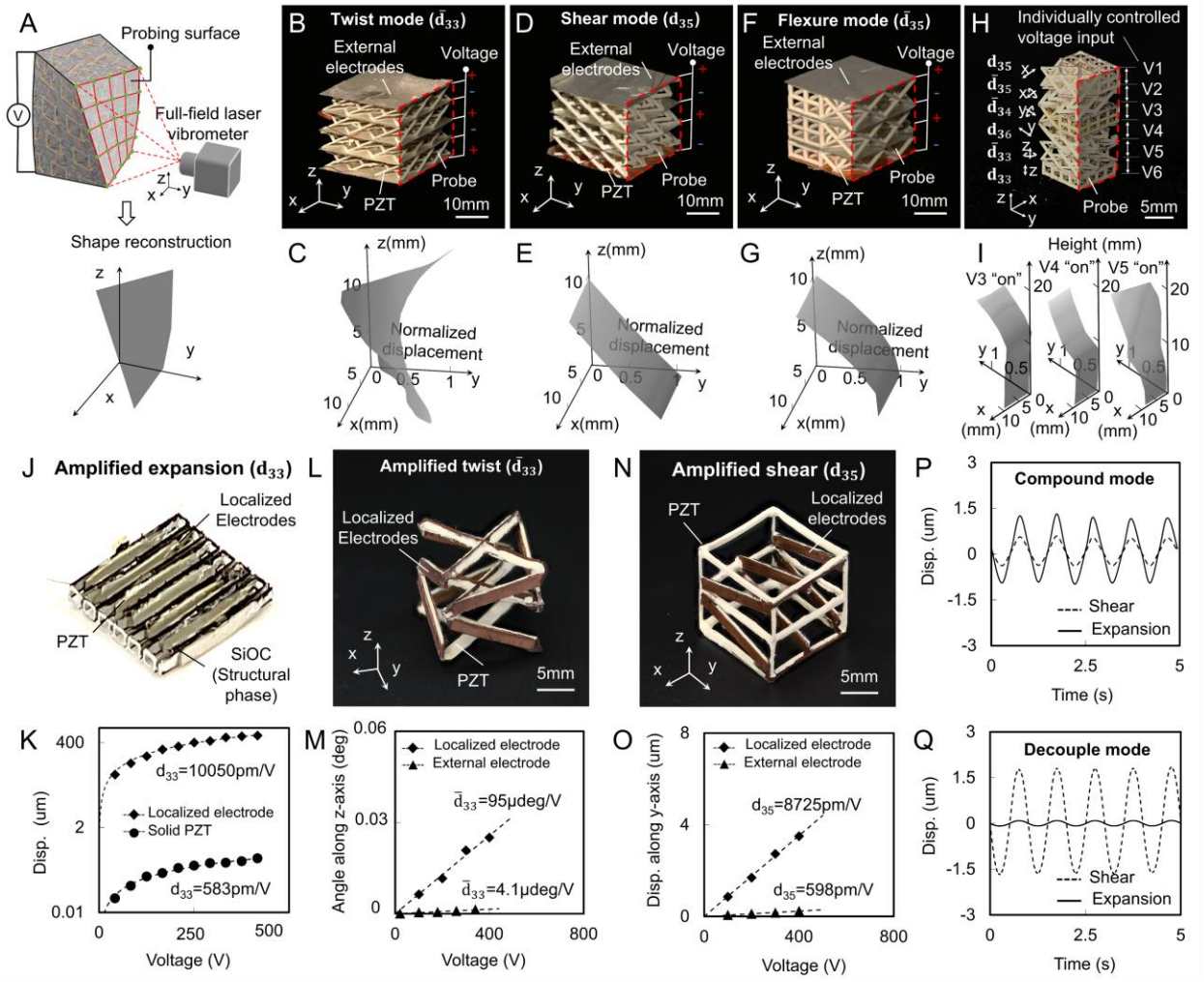

Figure 4-16. Experimental verification of robotic metamaterial designs (a) Schematic of the test set up with laser vibrometer to capture the deformation of the side surface of the lattice. (b)-(g) Optical image of the twist, shear and flexure mode lattice and their side surface deformation. (h) Optical image of a modularized 6-DoF piezoelectric actuator. (i) Deformation of the side surface of the 6-DoF piezoelectric actuator working in three representative working modes ($\bar{d}_{35}$, $\bar{d}_{33}$ and d_{36} modes). (j) Optical image of a piezoelectric metamaterial with amplified expansion. (k) Displacement of the metamaterial with localized electrodes and solid PZT material with external electrodes as a function of the input voltage. (l) Optical image of the piezoelectric metamaterial with amplified twist and suppressed expansion. (m) Twist angle of the metamaterial with external and localized electrodes as a function of input voltage. (n) Optical image of the piezoelectric metamaterial with amplified shear. (o) Shear displacement of the metamaterial with external electrodes and localized electrodes as a function of input voltage. (p)-(q) Displacement with compound and decoupled expansion-shear modes with sinusoidal voltage input.

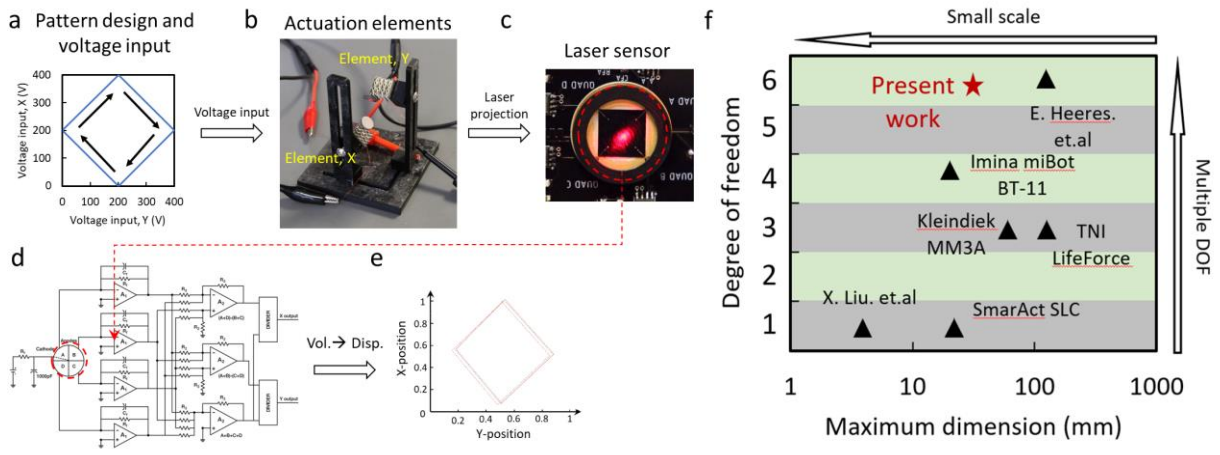

Figure 4-17. Experimental testing of piezoelectric metamaterials as beam steering elements. (a), Schematic of the designed pattern and programmed voltage input to the beam steering elements. (b), Optical image of the beam steering device. (c), Optical image of the laser sensor. (d), Schematic of the signal processing circuit of the laser sensor. (e), Laser spot trajectory captured by the laser sensor. (f), Benchmark the 3D printed 6-DOF element with the state-of-art multi-degrees-of-freedom manipulators.

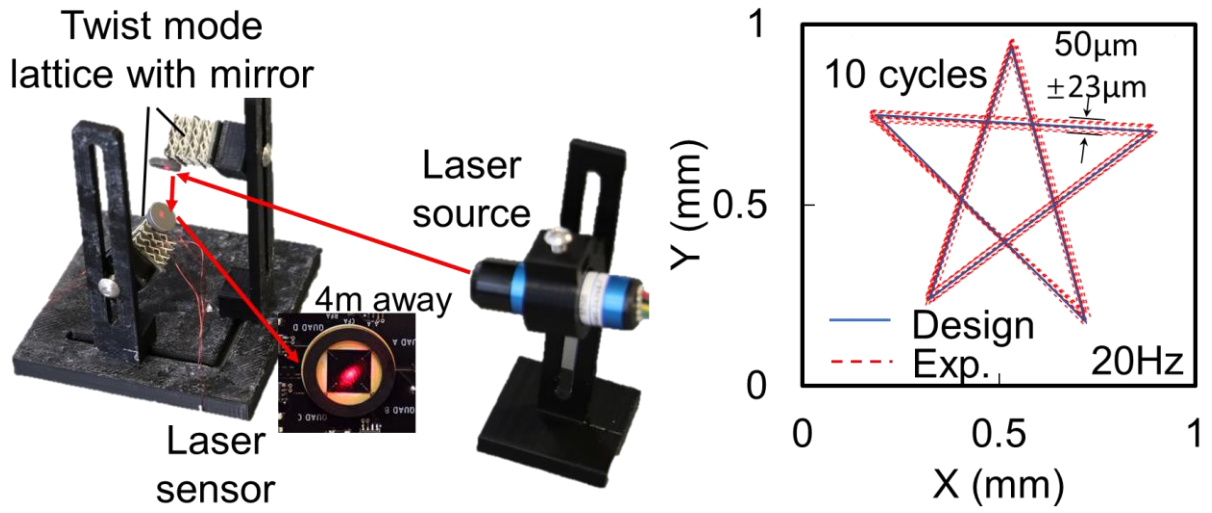

Figure 4-18. Optical image of the laser beam steering system and designed experimental laser spot trajectories for a star pattern executed at 20 Hz.

Next, we fabricated micro-architectures with embedded electrodes and demonstrate the strain amplification, strain compounding, strain addition and subtraction enabled by the localized electrodes and the micro-architecture design. Figure 4-16j, 4-16l and 4-16n presents as-fabricated lattice lattices with localized electrodes, featuring amplified expansion (d_{33}, Figure 4-12j), amplified twist ($\bar{d}_{33}$, Figure 4-15) and amplified shear (d_{34}, Figure 4-12k), respectively. The displacement versus the driving voltage of lattices is captured with the laser vibrometer and plotted in Figure 4-16k, 4-16m and 4-16o, which were used to derive the corresponding strain coefficients. Compared to the strain coefficients of lattices with layered external electrodes, the localized electrodes achieve giant piezoelectric coefficients (i.e. d_{33}=10050pm/V), which is two orders of magnitude higher than that of their native material (583pm/V). Figure 4-16p and 4-16q demonstrate the compound expansion-shear strain and the decoupled pure shear strain using designs from Figure 4-12k, via programming the local polarization and driving electric field within the embedded electrode architectures.

4.4.4 Numerical validation of metamaterial design with target strain mode

We implemented a computational framework that predicts and verifies the piezoelectric electric coefficients d_{nm} and $\bar{d}_{nm}$ of the metacrystal designs. This is achieved by calculating the total induced-load contribution of the connected piezo-active struts within the cubic volume under an electric field. Figure 4-19 shows the finite element analysis results that verify the actuation modes. Herein, commercially available finite element analysis (FEA) software COMSOL is invoked for all the numerically studied cases. We applied periodic boundary conditions (PBCs) on the unit cells to effectively characterize the overall electromechanical performance of the piezoelectric

metamaterials. Material properties used in the simulation process were experimentally measured as:

Density: $\rho = 6.9 \times 10^3 kg/m^3$

Elastic property :$E_1 = E_2 = 36\text{G}Pa, E_3 = 43GPa, \nu_{12} = 0.31, \nu_{23} = 0.33, \nu_{13} = 0.27$

Dielectric permittivity: $\epsilon_{11} = \epsilon_{22} = 1.201 \times 10^{-9} F/m,\ \epsilon_{33} = 1.3 \times 10^{-19} F/m$

Piezoelectric charge constant: $d_{15} = d_{24} = 597pC/N$, $d_{31} = d_{32} = -229pC/N$, $d_{33} = 523pC/N$, the other $d_{ij} = 0$.

The tetrahedron elements is used to mesh the unit cells for all the representative actuation cases. The bottom surface of the unit cells is fixed in all three translational degree-of-freedom. Electric field was applied on the unit cells to activate the deformation of the unit cells. As shown in Figure 4-19, all the representative designs of the piezoelectric unit cell demonstrate target actuation performances.

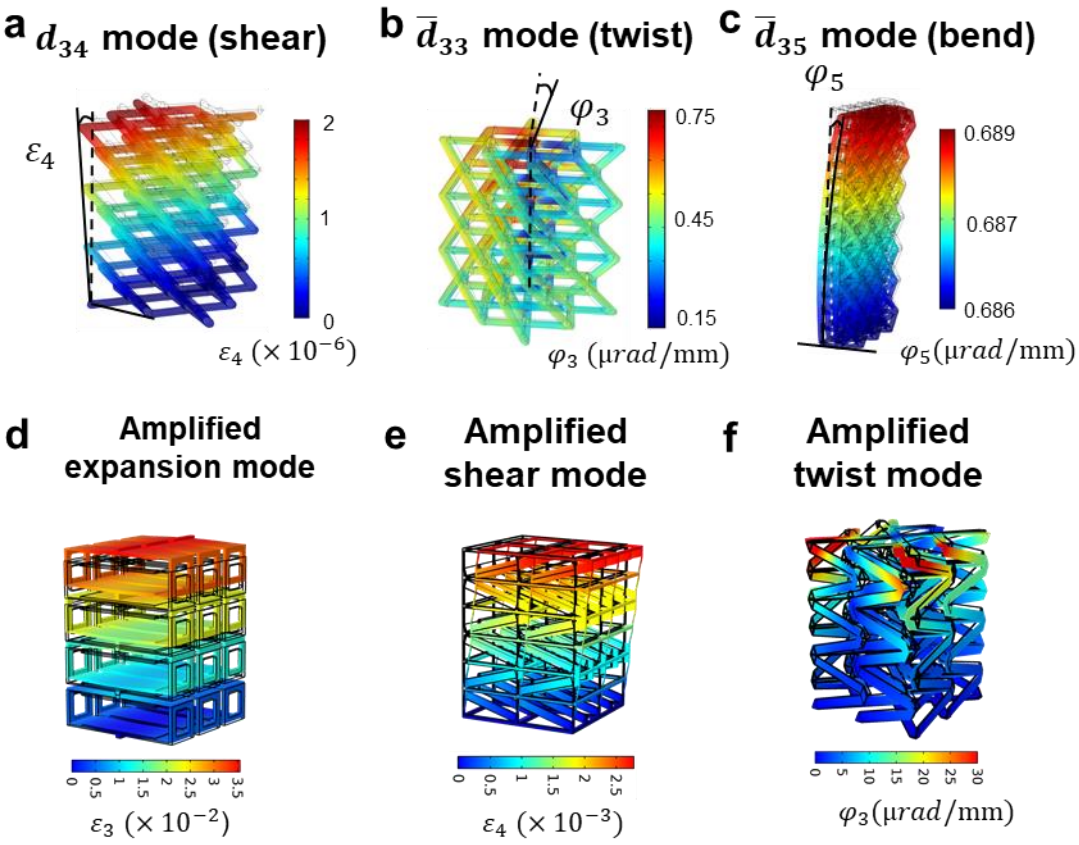

Figure 4-19. FEA results for lattices with $\mathbf{d_{34}}$ (shear), $\mathbf{\bar{d}_{33}}$ (twist), $\mathbf{\bar{d}_{35}}$ (bend), amplified expansion, amplified shear and amplified twist modes.

4.5 Conclusion

In this chapter, we presents a methodology to design electrical-mechanical coupling anisotropy and orientation effects and recreate them via additive manufacturing of highly responsive piezoelectric materials. This creates the freedom to inversely design an arbitrary piezoelectric tensor, including symmetry conforming and breaking properties, transcending the common coupling modes observed in piezoelectric monolithic and foams. We see this work as a step toward rationally designed 3D transducer materials for which users can design, amplify or suppress any

operational modes (d_{nM}) for target applications. Design and tessellation of the piezo-active units can lead to a variety of smart-material functionalities including vector and tactile sensing, source detection, acoustic sensing and strain amplifications from a fraction of the solid.

Additionally, we introduced a strategy to design and additive manufacture a class of robotic metamaterials that incorporate electronic, structural and conducting micro-scale strut elements in a 3D architecture. These multi-functional metamaterials uncovered a myriad of new strain modes including twisting, flexure, compound, decoupled and amplified strain without combing any leveraging or transmission system at a fraction of the weight. This bypasses the limitations of natural piezoelectric crystals where the piezoelectric strain relies on the available natural crystalline structures, of which only a fraction of the tensor has been discovered and measured thereby limited to only normal and shear directions with low amplitude. The design strategy can be further combined with a topology optimization algorithm to generate arbitrary piezoelectric tensors.

Chapter 5 Intelligent design method of full mechanical responses of metamaterial

This chapter demonstrate a ML based design framework to create the complete desired mechanical response, and its application in inversely design arbitrary types of compressive behaviors of the metamaterial. The chapter starts with the construction of the ML framework. The training data structure is described. Next, the application of the trained ML framework in designing various types of responses is presented. The advanced tailorability of mechanical behaviors is demonstrated with the developed ML model. The application of modified ML model for simultaneous inverse design of mechanical responses at different loading rates are demonstrated for an architected bumper.

5.1 Development of the generative ML framework

5.1.1 Overview of the generative ML framework

We implemented a generative ML pipeline composed of an inverse prediction and forward validation modules where each module is composed of five distinct NN models (Figure 5-1a). Each NN model in the inverse prediction module predicts a set of design parameters $\{\mathbf{Y}\}$ for a given target curve feature $\{\mathbf{X}^{T}\}$, whereas the forward validation module outputs the predicted curve features $\{\mathbf{X}^{P}\}$ for each set of the predicted design parameters and determines the optimal set via evaluating the differences between predicted and target curve features. This embedded approach solves the non-unique response-to-design mapping challenge in inverse design[27,28] (e.g., several micro-architectural features may give same output curves). During this process, the curve type classifier in the forward validation module estimates the type of predicted stress-strain curves

using the design parameters predicted from the inverse design module. This curve type along with such predicted design parameters are fed into each NN model of the forward module for the prediction of stress-strain curve features $\{\mathbf{X}^{P}\}$. Thereby, as the optimal design are chosen via a direct comparison of curve features, our approach ensures the uniqueness of the solution and hence bypasses the potential one-to-many mapping issue that can occur in the typical inverse design approach.

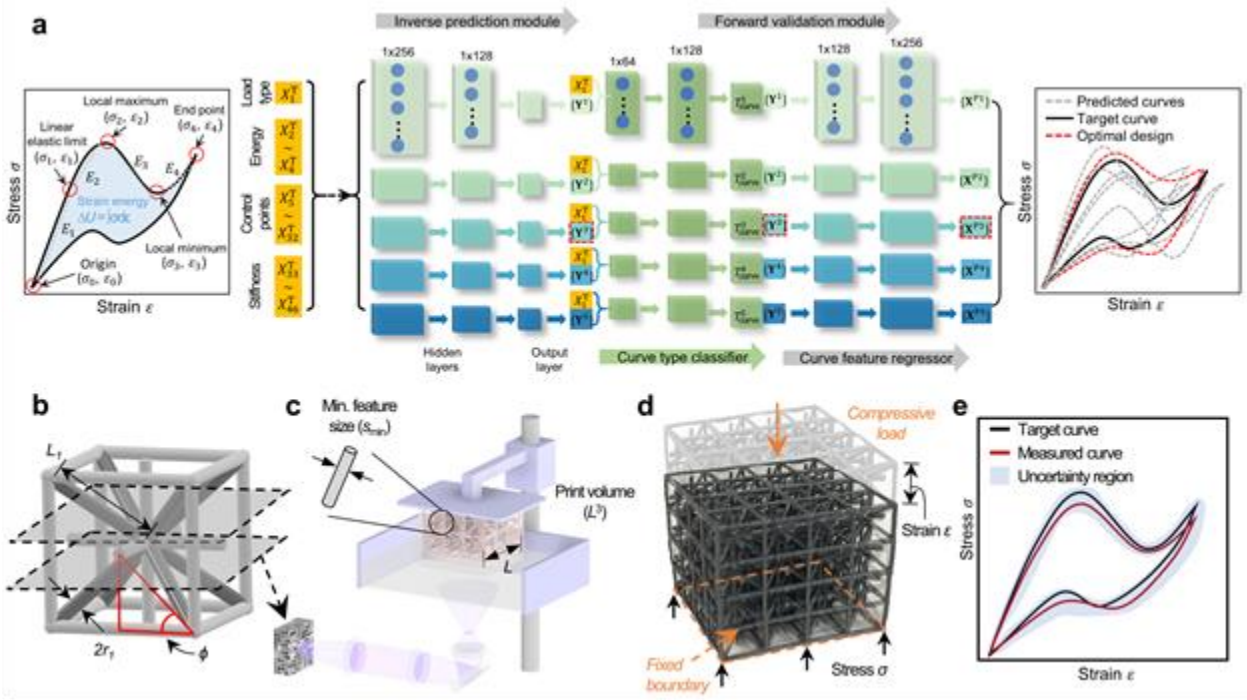

Figure 5-1. Overview of the ML-based rapid inverse design methodology**.** (a) Schematic of the generative ML pipeline presented in this work. By taking the target uniaxial compressive behavior in the form of curve features $\{\mathbf{X}^{T}\}$ as the input data, the inverse prediction module of our ML approach predicts five sets of design candidates [65] (described by the cell type (T_{cell}), characteristic angle (ϕ) and radius-to-length ratio (r_1/L_1)), where k ranges from 1 to 5. These design candidates are then passed to forward validation module to estimate the response $\{\mathbf{X}^{Pk}\}$ of the design candidates. Each of these responses $\{\mathbf{X}^{Pk}\}$ is compared to the target curve feature $\{\mathbf{X}^{T}\}$ for selection of the optimal design. (b) CAD model generated based on the optimal design selected in a. (c) A schematic of 3D printing system with specific fabrication parameters (minimal feature size s_{min} and maximum printing volume L^3). (d) Printed sample based on the optimal design predicted by the generative ML pipeline under compressive loading. (e) A comparison between the target

(black) and measured (red) compressive stress–strain curves. The uncertainty region (blue shaded area) represents the process variability obtained through the testing of multiple samples.

5.1.2 Generative ML pipeline

By inputting the target stress-strain curve feature $\{\mathbf{X}^{T}\}$, we aimed to build an inverse (backward) model that predicts the design parameters $\{\mathbf{Y}\}$ of a lattice architecture, which is capable replicating the targeted curve after fabricating and compression testing. In general, the inverse prediction from $\{\mathbf{X}^{T}\}$ to $\{\mathbf{Y}\}$ can theoretically be affected by the "one-to-many" issue, that is, although a given lattice architecture presents a unique stress-strain curve, several lattice architectures can potentially provide similar or same stress-strain curve. Therefore, the conventional inverse model's loss function $f_{L}=(\mathbf{Y}_{pred}-\mathbf{Y}_{true})^{2}$ (where $\mathbf{Y}$ is the design parameters of the designed lattice architecture) is ill-defined since several ground-truth values of $\mathbf{Y}_{true}$ are correct—that is, several lattice architectures $\{\mathbf{Y}\}$ can exhibit the same feature $\{\mathbf{X}\}$ of the stress-strain curve. The ill-defined nature of the cost function is an issue as it serves as the basis (i.e., cost function) for the training of the model.

Here, we implemented a generative machine learning model to address the "one-to-many" issue. Figure 5-2a illustrates the overall architecture of the machine learning (ML) generative pipeline. The ML model is composed of (i) a forward validation module (consists of a curve type classifier and five individual surrogate neural networks) that predicts curve feature $\{\mathbf{X}^{P}\}$ given the design candidate $\{\mathbf{Y}\}$ and (ii) an inverse prediction module (consists of five individual generative neural networks) that predicts the design candidate $\{\mathbf{Y}\}$ based on the target curve feature $\{\mathbf{X}^{T}\}$. Each generative neural network is linked to its corresponding surrogate neural network, forming a pair

of generative-surrogate model. In total, we have five pairs of generative-surrogate model in our ML pipeline (Figure 5-2b).

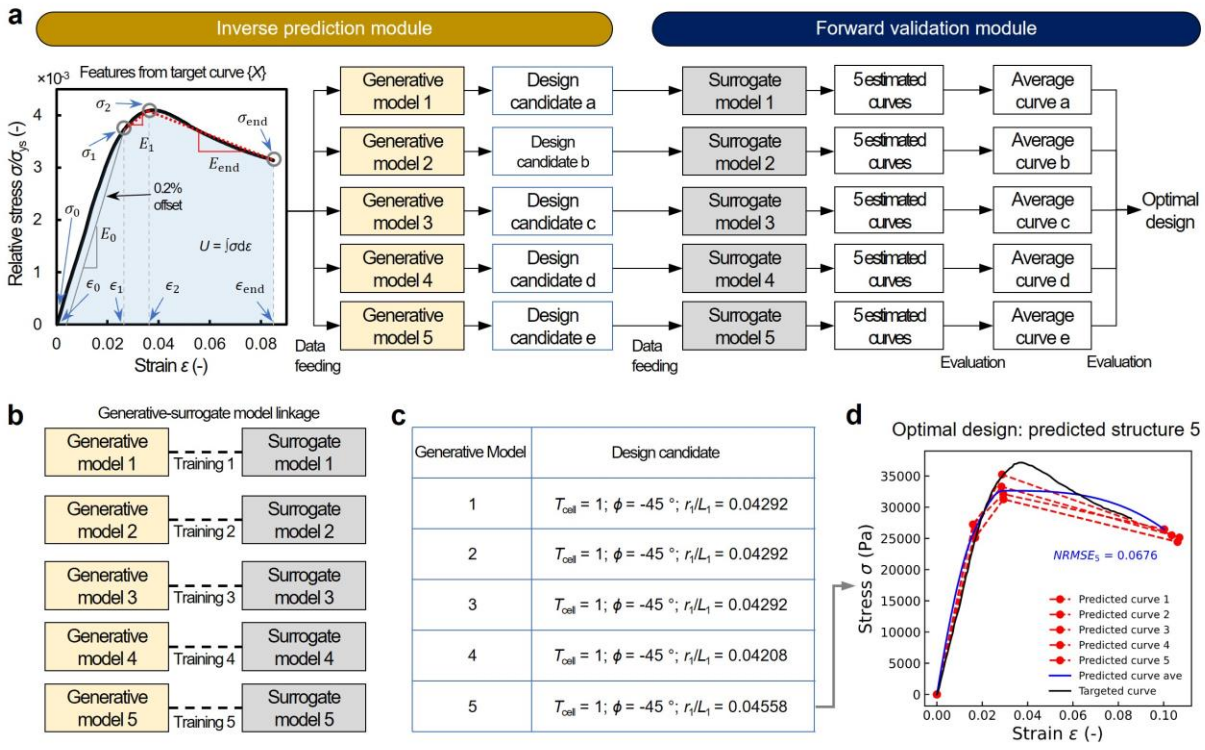

Figure 5-2. Details of ML approach**.** (a), The generative ML pipeline consists of two modules: inverse prediction module and forward validation module. Taken the target stress-strain curve feature as the input, the inverse prediction module predicts five design candidates, which are then passed to the forward validation module to evaluate the mechanical responses and select the optimal design. (b), Five pairs of generative neural networks and surrogate neural networks in the ML pipeline. (c), Multiple design candidates obtained from the inverse prediction module for the target curve shown in a. (d), Example of estimated curves from the surrogate model 5. These curves were averaged and compared with the target curve in terms of the normalized root-mean-square error (NRMSE). After repeating this process for all models, the optimal design paired with a curve exhibiting the minimum NRMSE was chosen. When the minimum NRMSE values are identical across multiple designs, the design candidate from a ML model with the highest prediction accuracy is chosen as the optimal design.

Although this model adopts generative neural networks that aim to predict an accurate lattice architecture $\{\mathbf{Y}\}$ for a given input target curve feature $\{\mathbf{X}^{T}\}$, our ML pipeline does not rely on any ill-defined cost function. Indeed, instead of defining the cost function based on a comparison between the predicted and true lattice architecture, the predicted lattice architecture $\{\mathbf{Y}\}$ is now converted back to a predicted stress-strain curve via the pretrained forward validation module. This modification allowed us to directly evaluate the difference between the predicted curve feature $\{\mathbf{X}^{P}\}$ and the target curve feature $\{\mathbf{X}^{T}\}$ via a new cost function $f_c=(\mathbf{X}_{pred}-\mathbf{X}_{true})^2$. As the stress-strain curve is unique to a lattice architecture, this approach effectively ensures the uniqueness of the solution and eliminates the "one-to-many" issue without compromising the properly defined nature of the cost function.

After predicting the curve features $\{\mathbf{X}^{P}\}$ by the surrogate neural network model, the associated curve can be reconstructed based on the curve features. Each curve is uniquely described by a series of control points, which can be classified into five categories: origin, linear elastic limit, local maximum points, local minimum points, and end point (Figure 5-3a). In turn, a linear connection of these control points can approximately represent the true stress-strain curve, as illustrated in Figure 5-3b. The linear connection is called feature-to-curve reconstruction, and this linearly connected curve is herein referred as a reconstructed curve for the curve features $\{\mathbf{X}\}$. We found that, when compared to the ground-truth stress-strain curves, the reconstructed curves exhibit very small discrepancy, with an average normalized root-mean-square error (NRMSE) of ~0.01; that is, the reconstructed curves largely overlap with the ground-truth curves. Figure 5-3c presents two representative cases of true curve and reconstructed curve. Herein, NRMSE is defined as:

$$\mathrm{NRMSE} = \sqrt{\frac{\sum_i^{46}\left(\overrightarrow{x^i}_{\mathrm{pred}}/\overrightarrow{x^i}_{\mathrm{target}} - 1\right)^2}{N_{\mathrm{features}}}} \tag{5.1}$$

where $\overrightarrow{x^i}_{\mathrm{pred}}$ and $\overrightarrow{x^i}_{\mathrm{target}}$ are i-th curve feature of $\{\mathbf{X}^{\mathrm{P}}\}$ and $\{\mathbf{X}^{\mathrm{T}}\}$, respectively, and N_{features} denotes the number of the curve features. This expression leads to the computed NRMSE bounded between 0 and 1, where 0 implies the two vectors are identical with 1 implying that they are completely dissimilar.

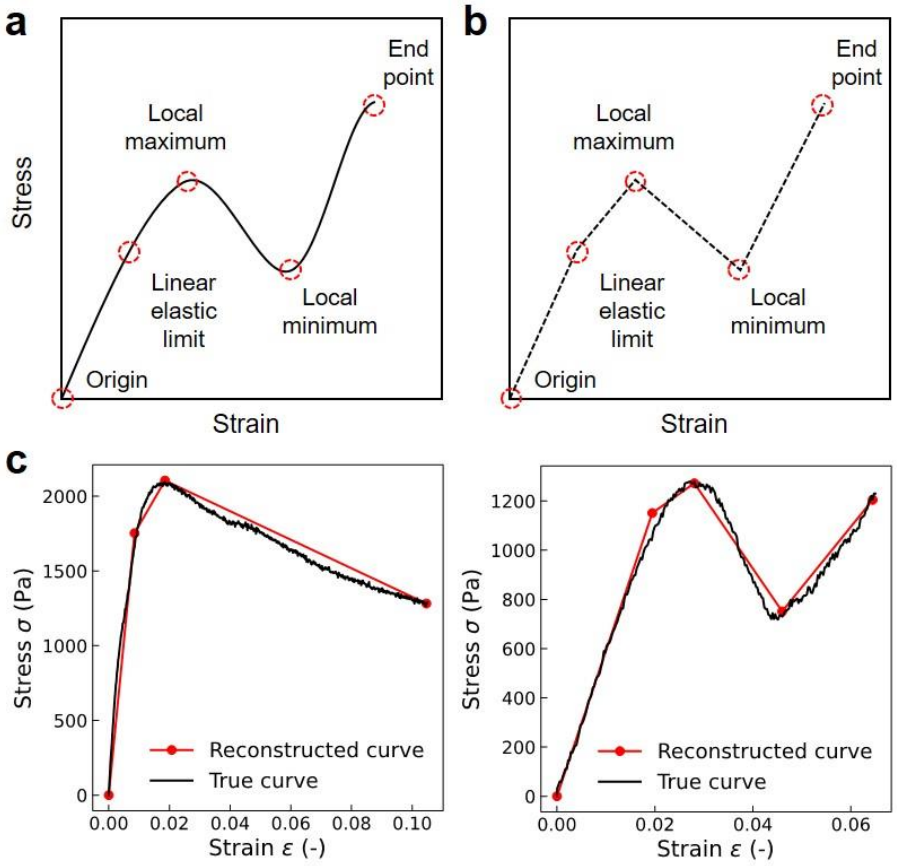

Figure 5-3. Stress-strain curve reconstruction based on curve features**.** (a), The original stress-strain curve with five types of control points. (b), Reconstructed stress-strain curve via linear connection of all the control points. (c), Two representative cases of comparison between true curve and reconstructed curve.

Note that not every curve contains all the five categories of control points. Along with the prediction of the curve features $\{\mathbf{X}^{P}\}$, we also used the curve type classifier to predict the curve type. Based on the curve type, we were able to filter out the nonzero predictions of some curve features that are expected to be zero.

5.1.3 Determination of optimal design parameters

We now discuss the strategy that was used herein to determine the optimal design from several candidate structures offered by multiple generative models (i.e., a series of independent generative models that are trained on the same dataset, but with different random initial weights and distinct hyperparameters). In detail, by inputting the same target stress-strain curve feature, each generative model independently predicts a design candidate, which might be different from each other. Although all the generative models may exhibit satisfactory accuracy, some predicted structure can provide a stress-train curve closer to the target curve than the other design candidates, which is the optimal design that should be picked out.

Figure 5-2a illustrates the model evaluation strategy to determine the optimal design. The inverse prediction module comprises five independent generative neural network models, wherein each one predicts its own design candidate $\{\mathbf{Y}\}$ for the given target curve feature $\{\mathbf{X}^{T}\}$. These design candidates are then passed to the corresponding surrogate forward model to evaluate its response $\{\mathbf{X}^{P}\}$ (Figure 5-2b). Each surrogate model predicts five sets of stress-strain curve feature for the input design candidate, and these five predicted curve features are then averaged to obtain the averaged stress-strain curve feature. In total, five surrogate forward model predicts five individual averaged stress-strain curve features, which are then compared with the input curve feature $\{\mathbf{X}^{T}\}$ for the selection of optimal design $\{\mathbf{Y}\}$. The optimal design is then determined as the one that

yields the smallest NRSME value compared with the input curve feature $\{\mathbf{X}^{T}\}$. Figure 5-2c and 5-2d present a representative case of optimal design selection. For a case where the minimum NRMSE values are identical between multiple predicted curves, the design candidate from a neural network model with the minimal training loss value is selected as the optimal design.

5.1.4 Curve type classifier

Given one set of design parameters $\{\mathbf{Y}\}$ and load type T_{load}, we first aimed to build a forward model that can predict the corresponding stress-strain curve $\{\mathbf{X}^{P}\}$. In practice, there exists a discrepancy between the true curve $\{\mathbf{X}^{T}\}$ and the predicted curve $\{\mathbf{X}^{P}\}$. For example, in the case of a buckling response, $\{\mathbf{X}^{P}\}$ generally exhibits a nonzero value (rather than a value of zero) for the local minimum stress and strain, which makes it difficult to differentiate with multiple peak-and-valley response.

To differentiate the curve type for each $\{\mathbf{X}^{P}\}$, we herein constructed a curve type classifier using a neural network model implemented in the Python TensorFlow platform. The classifier contains 2 hidden dense layers with 64 and 128 neurons, respectively (Fig. 1a). We used the rectified linear unit (ReLu) activation function for the hidden layers and softmax activation for the output layer. Each hidden layer is followed by a batch normalization layer to improve the training efficiency. By inputting the design parameter $\{\mathbf{Y}\}$ and load type T_{load}, the classifier outputs the probability of each curve type, i.e., linear, plastic yielding, buckling, and multiple peak-and-valley response (Figure 5-4).

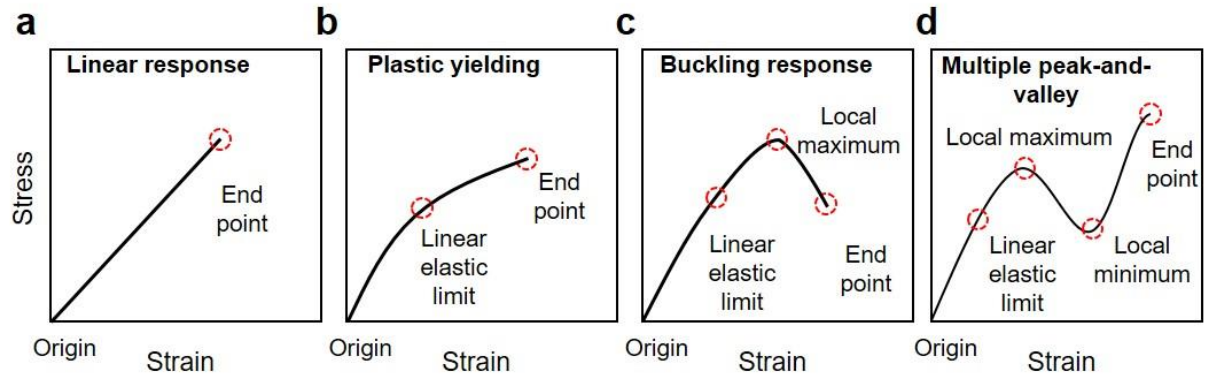

Figure 5-4. Categories of stress-strain curves in the training dataset**.** (a), Linear response. (b), plastid yielding response. (c), Buckling response. (d), Multiple peak-and-valley response.

5.2 Stress-strain curve design space for ML

5.2.1 Derivation of curve design space

The design region of our generative ML approach was formulated as a dimensionless design space enclosing the arbitrary mechanical behavior of cellular materials under both monotonic and cyclic uniaxial compression, where the *x*-axis specifies the strain ε and the *y*-axis specifies the relative compressive strength normalized to the yield strength of a given polymeric base material σ/σ_{ys} (the full curve design space is highlighted by a black dotted region in Figure 5-5a). This dimensionless design space comprises a series of subdesign spaces classified by the elastic limit (ε_{ys} or σ_{ys}/E_s) of each available polymeric base material (gray envelopes in Figure 5-5a). This representation allows for the inclusion and visualization of nearly all possible stress–strain curve shapes depending on the choice of polymeric base materials. Envelopes of the subdesign space were specified by the theoretical upper bounds of the elastic stiffness[29] and the yield strength[30] of isotropic cellular

materials (Ⓐ and Ⓑ) and an approximated failure bound (Ⓒ), assuming that available polymeric base materials are isotropic and their post-yield behavior are negligible (inset of Fig. 5-5a).

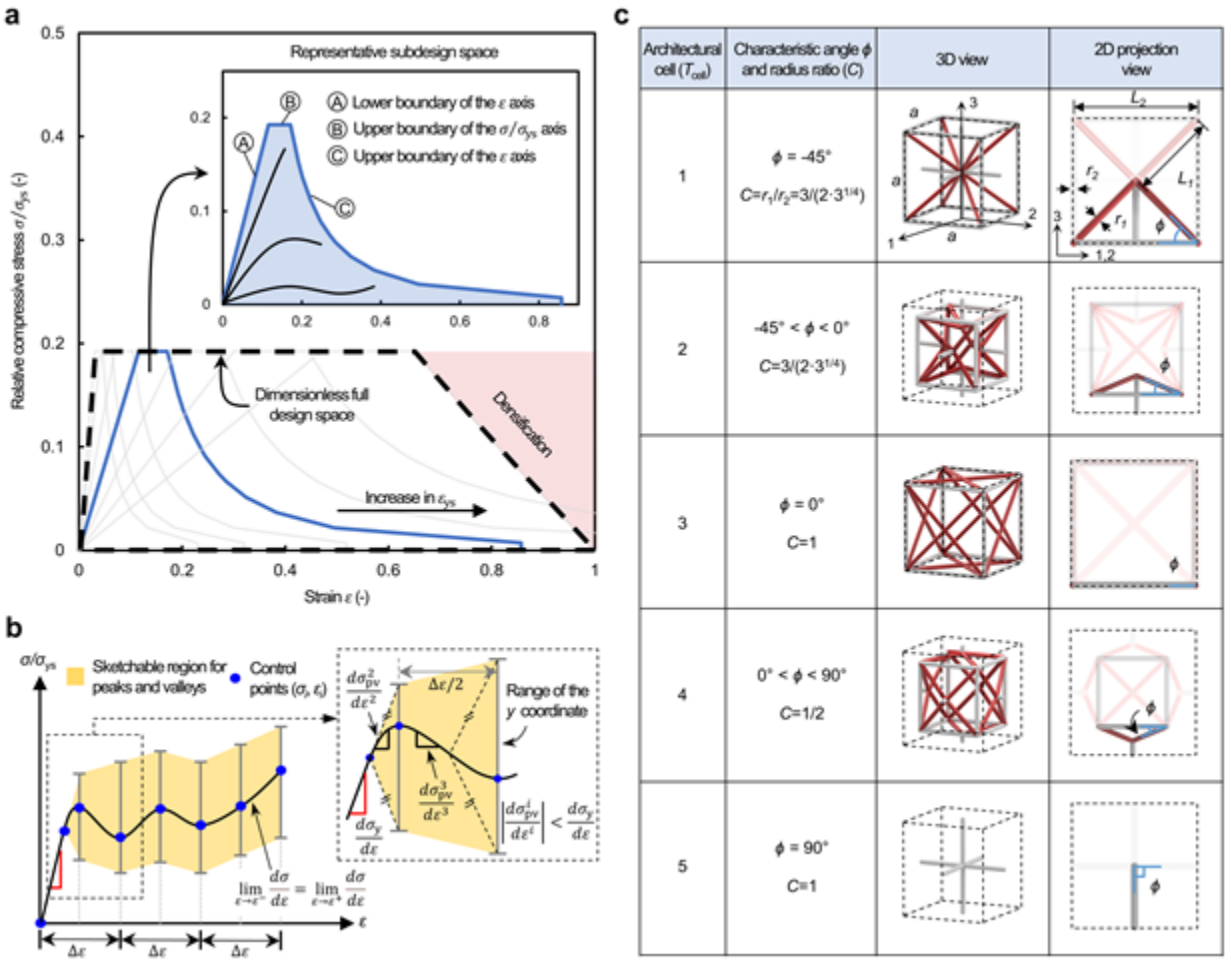

Figure 5-5. Design space, plottable stress–strain curve paths and architectural cells. (a) Full stress–strain curve design space composed of a series of subdesign spaces in a dimensionless plot, where the *x*-axis specifies the strain and the *y*-axis specifies the relative compressive strength σ/σ_{ys} (σ_{ys} denotes the yield strength of the base material). Each subdesign space is associated with a unique base material described by its elastic limit ε_{ys} and constructed with three boundaries (Ⓐ, Ⓑ, and Ⓒ in inset). A representative subdesign space is shown as a blue envelop. Example stress–strain curves are also shown in the inset figure. (b) Design rules for plotting target stress–strain curves. A target curve, described by control points (σ_i, ε_i), starts with a straight line, followed by peaks and valleys. Error bars represent bounds of the peaks and valleys determined by the tangent modulus which is lower or equal to the linear-elastic slope (i.e., $|(d\sigma_{pv}{}^i)/(d\varepsilon^i)|\leq(d\sigma_y{}^1)/(d\varepsilon^1)$, where i = 2,…, max(N_{pv}) and max(N_{pv}) denotes the maximum number of the peaks and valleys). (c) Architectural cells with cubic symmetry. A variation in the characteristic angle (ϕ) from -45 to 90 degrees results in an architectural transformation from a compound truss comprising simple and

body-centered cubic trusses (T_{cell} = 1), to an auxetic truss (T_{cell} = 2), to a reinforced face-centered truss (T_{cell} = 3), to a simple cubic truss combined with convex square pyramids truss (T_{cell} = 4), and to a simple cubic truss (T_{cell} = 5). Each cell occupies an identical representative (black-dotted) volume and comprises two types of struts: inclined (red) and support (gray) struts. These struts are related via a constant C, defined as the ratio of the radius of the inclined strut to the radius of the support strut (i.e., $C = r_1/r_2$).

In a dimensionless plot where the x-axis specifies the strain, and the y-axis specifies the relative compressive strength σ/σ_{ys} (σ_{ys} denotes the yield strength of the base material), each subdesign space, as illustrated in the inset of Fig. 2a, is constructed with three boundaries:

i. A lower boundary for the strain axis or x-axis (Ⓐ): described by the ratio of the maximum attainable strength to the highest attainable stiffness;

ii. An upper boundary for the relative compressive strength axis or y-axis (Ⓑ): represented by the maximum attainable strength;

iii. An upper boundary for the strain axis or x-axis (Ⓒ): characterized by failure strains and the corresponding maximum strengths.

The lower boundary for the strain axis Ⓐ can be determined by the maximum achievable stiffness and yield strength of an isotropic cellular material. These mechanical properties scale with the relative densities ($\bar{\rho}$) of the cellular materials[74]. Therefore, we estimate the maximum designable relative density ($\bar{\rho}_{max}$) as:

$$\bar{\rho}_{\max} \approx \sqrt{\frac{23}{12}} \frac{\sigma_{\text{target}}}{\max(\sigma_{\text{ys}})} \tag{5.2}$$

where σ_{target} is defined as the maximum strength of the target stress-strain curve and $\max(\sigma_{\text{ys}})$ denotes the maximum yield strength of available base materials. Based on the maximum relative density ($\bar{\rho}_{\max}$), the maximum achievable stiffness and yield strength are obtained using the Hashin-Shtrikman[75] and Suquet[76] bounds as:

$$\frac{E_{\text{HSU}}}{E_{\text{s}}} = \frac{2\bar{\rho}_{\max}(5\nu - 7)}{13\bar{\rho}_{\max} + 12\nu - 2\bar{\rho}_{\max}\nu - 15\bar{\rho}_{\max}\nu^2 + 15\nu^2 - 27} \tag{5.3}$$

$$\frac{\sigma_{\text{y,SU}}}{\sigma_{\text{ys}}} = \left(\frac{23}{12} - \frac{11}{12}\bar{\rho}_{\max}\right)^{-1/2} \tag{5.4}$$

where the subscript s denotes the material properties of the base material. The lower boundary for the strain axis is marked as Ⓐ in the inset of Figure 5-5a.

The upper boundary for the relative compressive strength axis Ⓑ is approximated as the theoretical upper bound of the yield strength Eq. 5.4 with $\bar{\rho}_{\max}$ (inset of Figure 5-5a). This treatment describes that failure occurs when local maximum stress within the lattice attains the yield strength of the solid constituent material.

The upper boundary for the strain axis Ⓒ is characterized by the maximum failure strain (ε_{f}) and the corresponding maximum strength ($\sigma_{\text{y,SU}}/\sigma_{\text{ys}}$) evaluated at designable relative densities ranging from 0 to $\bar{\rho}_{\max}$ (inset of Figure 5-5a). The estimated failure strain is given as:

$$\varepsilon_f = \left(\frac{\sigma_{ys}}{E_s}\right)\frac{1}{\bar{\rho}^{1/2}} \qquad (5.5)$$

and the corresponding maximum strength is given in Eq. 5.4. The failure strain (ε_f) follows a power function of base material properties (σ_{ys} and E_s) and reaches the elastic limit (ε_{ys}) of the base material when $\bar{\rho}$ = 1. This function reflects a general deformation trend of architected materials—low-density materials fail at a higher strain than high-density materials while the maximum strength at failure decreases gradually.

A representative subdesign space, constructed by the boundaries described above, is illustrated in the inset of Figure 5-5a. The full stress-strain curve design space is formulated by superimposing a series of subdesign spaces based on all available base materials, truncated by densification (the black dotted region in Figure 5-5a). Densification[74] is estimated as ε_d=1-1.4$\bar{\rho}$, where $\bar{\rho}$ varies from 0 to $\bar{\rho}_{max}$. This representation not only account for base material dependency on the stress-strain curves but also realize the broadest possible design space, owing to the subdesign space boundaries evolving with the base material properties (the gray curves in Figure 5-5a).

5.2.2 Plottable stress-strain curve with ML

Within the full design space formulated above, our generative ML approach takes an arbitrary compressive stress–strain curve, either monotonic or cyclic, as the input. This target curve is constructed via sequentially connecting control points assigned by the user, starting from the origin to linear elastic limit, followed by local maxima and/or minima, and terminating at the end point (the design rules are shown in Figure 5-5b, see Figure 5-6 for an example of the stress–strain curve

input process). The first segment of the target curve is a straight line described by two control points at the origin and the linear elastic limit (i.e., (ε_0, σ_0) and (ε_1, σ_1)), representing linear-elastic behavior, and the slope of this straight segment (E_0) denotes the elastic modulus of the material under compression. After the linear elastic segment, the subsequent segments between successive control points (ε_i, σ_i) denote the nonlinear behavior of the material, where the maximum number of control point index i is dictated by the initial slope (E_0) and given print parameters. These control points of the stress-strain curve, along with load type (T_{load}) (either monotonic or cyclic), strain energy (ΔU) (area enclosed by the curve), and slope (E_i) between two adjacent control points, forms a total of 46 curve features {**X**} and used as the input to the ML pipeline.

Linear segment: The first segment (linear-elastic segment) of the target stress-strain curve starts with a straight-line (Figure 5-6a). This line is defined by two control points—the first control point (ε_0,σ_0) is located at the origin, and the second control point (ε_1,σ_1) can be anywhere within the design space. Two representative straight lines are shown in this figure. The upper limit of the slope for this line is given by the theoretical upper limit of the elastic stiffness (Eq. 5.3), whereas the maximum value of σ_1 is defined by the theoretical upper limit of the yield strength (Eq. 5.4), as described in the previous section.

Nonlinear segment: The following segment of the target curve accompanies with peaks and valleys (Figure 5-6b and 5-6c). The maximum number of peaks and valleys ($\max(N_{\text{pv}})$) of the curve depends on which subdesign space of the first linear-elastic segment is contained within. Within the subdesign space, multiple peaks and valleys may exist when the slope of the first linear-elastic segment is low enough to trigger elastic instability (i.e., satisfying $\sigma_1/\varepsilon_1 < A(\varepsilon_{\text{ys}})^{\alpha}$, where A and α are lattice topology (strut orientation) dependent coefficients). The maximum number of achievable

peaks and valleys (max(N_{pv})) is determined by print volume (L^3) and minimal printable feature size (s_{min}) that could experience elastic instability compared to the overall volume of the sample to be designed (i.e., max(N_{pv})=$B(L/s_{min})(\sigma_1/\varepsilon_1)^{\beta}$, where B and β are lattice topology dependent coefficients).

The possible ranges and bounds of the peaks and valleys (yellow shaded region) are specified as shown in Figure 5-5b. The location of the peaks and valleys are determined by the tangent modulus and displacement of the sample from the previous peak. The tangent slope between the subsequent peaks and valleys is lower or equal to the linear-elastic slope before first yielding is reached (i.e., $|(d\sigma_{pv}{}^{i})/(d\varepsilon^{i})|\leq(d\sigma_{y}{}^{1})/(d\varepsilon^{1})$, where i = 2,…, max(N_{pv})). The x-coordinate (the strain axis) of the peaks and valleys corresponds to the already collapsed unit cell sections (i.e., $\Delta\varepsilon=(s_{min}/L)C^{\gamma}(\sigma_1/\varepsilon_1)^{\tau}$, where C, γ, and τ are lattice topology dependent coefficients). Then, the y-coordinate is determined by the tangent slope and the x-coordinate of the peaks and valleys.

Other curve features include: the y-coordinate of the last control point (σ_N) is larger than the previous value (i.e., $\sigma_N > \sigma_{N-1}$), and that no discontinuity shall be presented in the curve that should be differentiable at any control points (i.e., $\lim_{x\to x^-}\frac{dy}{dx}=\lim_{x\to x^+}\frac{dy}{dx}$).

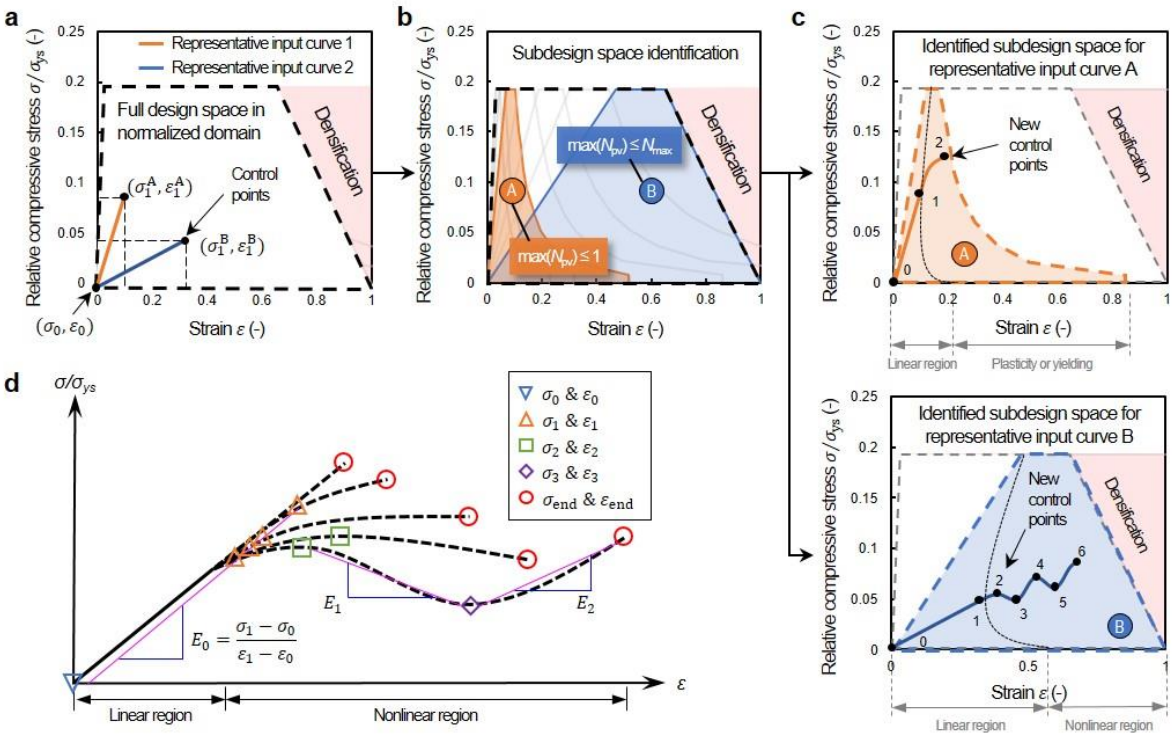

Figure 5-6. Plottable stress-strain curve paths**.** (a), Linear segments of two representative target curves in the full design space from user input. (b), Contour map showing the achievable number of peaks and valleys of the curves based on the subdesign space. (c), Nonlinear segments of the representative target curves within the corresponding subdesign space, which completes a sketch of the curves. (d), Example of compressive stress-strain curve paths described by several curve features for a special case of max(N_{pv}) equal to unity.

5.2.3 Stress-strain curve parameterization for ML input

Stress-strain curves were parameterized by curve features (X_i), where i ranges from 1 to 6× max(N_{pv})+10 and max(N_{pv}) describes the maximum number of achievable peaks and valleys. These curve features were specified by identifying control points (ε_j, σ_j) from the curve where j varies from 0 to 2×max(N_{pv})+2. A complete relationship between the curve features and control points are provided in Table 5-1. The stress-strain curve parameterization process was

implemented in Python with numpy[77], SciPy[78], and pandas[79] packages. The following sections describe the parameterization process in case of max(N_{pv}) equal to 6 in details.

Table 5-1. Feature variables parameterizing the stress-strain curve in case of max(N_{pv}) = 6.

Curve feature {X}	Description	Method of determination
X_1	Loading type (T_{load})	0 (i.e., monotonic response) if $\sigma(\varepsilon_0) \neq \sigma(\varepsilon_{end})$ 1 (i.e., cyclic response) if $\sigma(\varepsilon_0) = \sigma(\varepsilon_{end})$
X_2	Stored energy per unit volume ($U^{loading}$)	$U^{\text{loading}} = \int_{\epsilon_0}^{\epsilon_{\text{end}}} \sigma^{\text{loading}} d\epsilon$
X_3	Released energy per unit volume ($U^{unloading}$)	$U^{\text{unloading}} = \int_{\epsilon_0}^{\epsilon_{\text{end}}} \sigma^{\text{unloading}} d\epsilon$
X_4	Dissipated energy per unit volume (ΔU)	$\Delta U = U^{\text{loading}} - U^{\text{unloading}}$
X_5 , X_7, … X_{29}	Stress (σ_i)	Note: 0.2% offset method used for $i = 1$
X_6, X_8, … X_{30}	Strain (ϵ_i)	
X_{31}	End stress (σ_{end})	End of the curve if T_{load} = 0 Maximum strain and the corresponding stress if T_{load} = 1
X_{32}	End strain (ϵ_{end})	
X_{33} ~ X_{46}	Stiffness (E_i)	$E_i = \frac{\sigma_{i+1} - \sigma_i}{\epsilon_{i+1} - \epsilon_i}$ where $j = 1 \ldots 2 \times \max(N_{pv})+2$ Note: elastic stiffness when $i = 0$

In case of the training curve, the first step of the parameterization process was an identification of their control points (Figure 5-7a). The identified control points were then assigned to the curve features according to the descriptions listed in Table 5-1. In detail, the identification process begins with filtering noisy data presented in the curve to minimize any data fluctuations and inconsistency[80] by using the Savitzky-Golay definition[81]. Upon the completion of the filtering

process, the beginning of the curve was set to (ε_0, σ_0), and a load type (T_{load}) was determined by recognizing whether the initial and terminating stress values of the curve were identical. A non-linear segment at the beginning of the curve (also called as the toe-in region) was also detected and temporarily deactivated to minimize inaccuracy in the following elastic modulus (E_0) measurement (i.e., the slope of the linear segment of the curve). The elastic modulus was computed by using a linear least-squares regression[78] with the coefficient of determination set to 0.999. According to a typical 0.02% strain offset method, a straight line with a slope described by the computed E_0 was determined, from which an intersecting point of this line and the curve was set to (ε_1, σ_1), representing the termination of linearity. When this point was not detectable, the end point of the curve was set to (ε_{end}, σ_{end}) which represents failure without appreciable yielding as illustrated in the upper left sub-figure in Figure 5-7b. Subsequent stresses and strains after the linear segment—control points denoted by (ε_j, σ_j) where j = 2…13—were identified by locating local maxima and minima of the curve (using signal.find_peaks and signal.argrelmin of the SciPy package[78]). Finally, (ε_{end}, σ_{end}) were set by recognizing terminating stress and strain values of the curve. Once all control points were identified, they were assigned to the corresponding curve features (X_i where i = 5…32) according to the control point-curve feature relationship provided in Table 5-1.

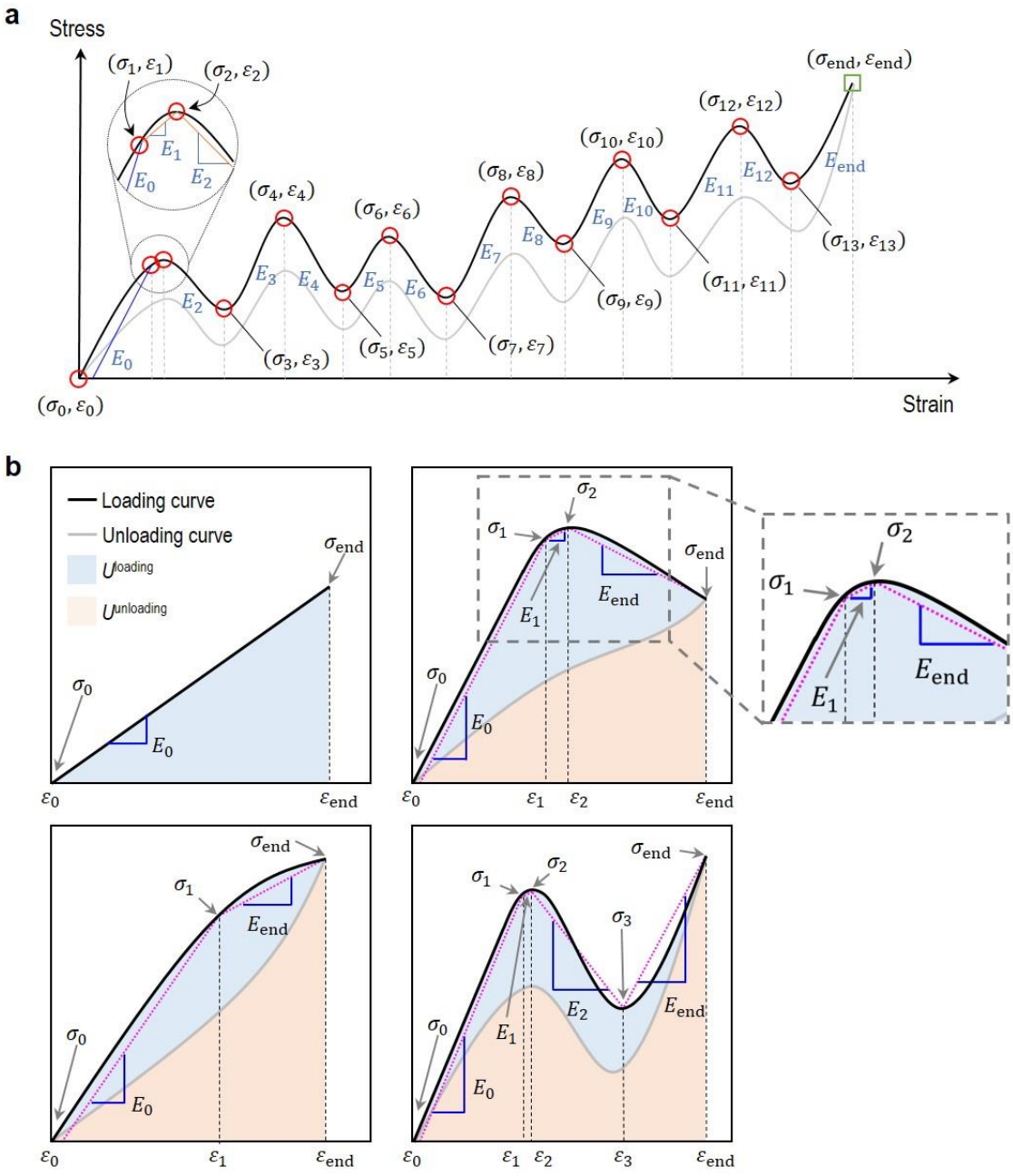

Figure 5-7. Curve parameterization used in this work. (a), Stress-strain curve parameterized in terms of curve features to fully describe its important mechanical properties. For clarity, a case of max(N_{pv}) = 6 is illustrated, and the variables describing the loading type and energy terms (i.e., T_{load}, $U^{loading}$, $U^{unloading}$, ΔU) are not shown. (b)**,** Examples of the curve parameterization for several curve paths.

The remaining curve features (X_i where i = 1…4 and 33…46) were recognized from the previously determined T_{load} and E_0 as well as additional variables such as strain energies and tangent moduli in the nonlinear segment of the curve. Tangent moduli ($E_1 \sim E_{13}$) were determined by computing a slope between two adjacent stress and strain values (i.e., $E_i = (\sigma_{j+1} - \sigma_j)/(\varepsilon_{j+1} - \varepsilon_j)$). In addition, stored and released strain energy per unit volume (denoted by U^{loading} and $U^{\text{unloading}}$, respectively) were computed by a trapezoidal integration method (e.g., $U^{\text{loading}} = \int_{\varepsilon_0}^{\varepsilon_{\text{end}}} \sigma d\varepsilon$) using numpy.trapz of the numpy package[77], and a dissipated strain energy (ΔU) was obtained by subtracting $U^{\text{unloading}}$ from U^{loading} (i.e., $\Delta U = U^{\text{loading}} - U^{\text{unloading}}$). As before, these variables were assigned to the corresponding curve features as listed in Table 5-1, and this completed the stress-strain curve parameterization in case of the training curve.

In case of the target curve, the aforementioned identification process of the control points was not necessary as these points were to be specified by the user. Hence, with the user-specified control points, the curve parameterization process was simply done by determining the additional variables discussed above and assigning them to the corresponding curve features, as listed in Table 5-1.

5.3 Training of the ML framework

5.3.1 Training data of the ML framework

We developed a family of cubic symmetric, strut-based architectural unit cells to generate training datasets of our ML approach (Figure 5-5c). The cells are represented by design parameters {**Y**} that describe a lattice architecture, namely, the cell type (Y_1 or T_{cell}), the characteristic angle (Y_2 or ϕ), and the radius-to-length ratio of the inclined strut (Y_3 or r_1/L_1) (Figure 5-5c). The evolution of ϕ, together with r_1/L_1 tuning, not only changes the relationships among tensile and compressive

load-bearing strut members, nodal connectivity, and strut slenderness ratio but also controls the deformation mechanism of the cells, thereby giving rise to distinct stress-strain curves. In addition, due to the inherent cubic symmetry of the reported architectural cells, their mechanical behaviors are invariant in three orthogonal directions. This characteristic enables an effective, direct tessellation across different architectures for the creation of compound lattices (i.e., a lattice made of different unit cells) offering enhanced stress-strain curve tunability. Hence, the developed unit cells allow our ML approach to capture diverse stress–strain curve paths while occupying nearly the full range of the design space.

We conducted FE simulations to compare plate-based (BCC, FCC, and SC-FCC) and open-cellular lattices (the five cell types used in this study) at the relative density ($\bar{\rho}$) ranging from 5 to 25% in representative subdesign spaces (Figure 5-8). The stress-strain curve results show that plate-base lattices (i.e., BCC, FCC, and SC-FCC) cover narrow (green-shaded) regions indicated in these figures and are limited to a linear-elastic response followed by failure due to yielding. The curve shapes are owing to their highly connected edges between plate members (rather than node connectivity)—their limited stress-strain curves were revealed in recent studies[82,83]. The open cellular lattices, when modeled with the same range of the relative densities, exhibit more diverse stress-strain curves and broader coverage in both subdesign spaces than those of the plate-lattices (light-blue shaded regions in Figure 5-8b and 5-8c; representative curves in Figure 5-8b). While the plate-based lattice covers the upper left corner on the design space (approaching the theoretical upper bound), such a region can be achieved by open cellular lattices made with higher relative densities (highlighted by blue-shaded regions in Figure 5-8b and 5-8c). We note that these findings

are also valid for other base materials, given that the two subdesign spaces represent relatively extreme cases of available base materials.

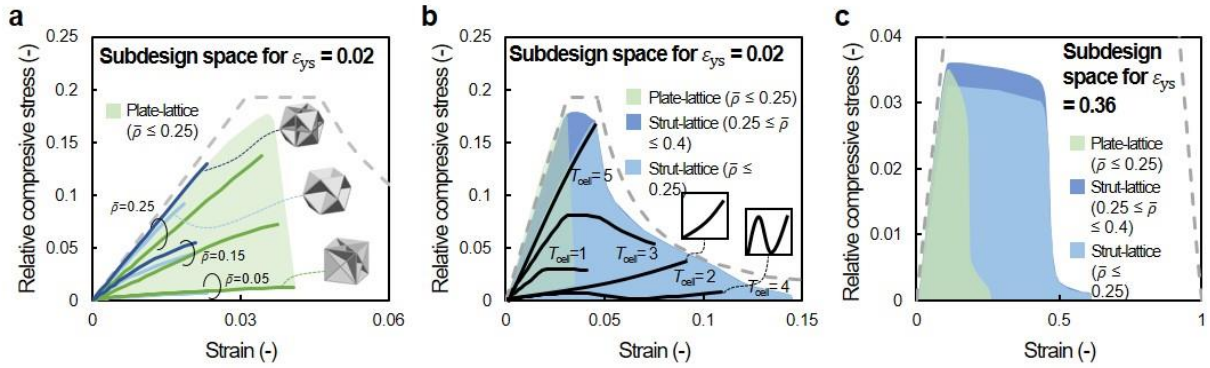

Figure 5-8. Mechanical performance assessment of the architectural unit cells developed in this work**.** (a), Results of FE simulations showing representative stress-strain curves of typical plate-lattices in a subdesign space for ε_{ys} of 0.02 (relatively brittle base material). In this figure, responses of SC-FCC, BCC, and FCC are colored as blue, light blue, and green, respectively. (b), The results of FE simulations showing representative stress-strain curves of the strut-based architectural unit cells (T_{cell} of 1 through 5) and their coverages in the same subdesign space for a comparison. (c), The results of FE simulations illustrating coverages of the strut-lattices and plate-lattices in another representative subdesign space for ε_{ys} of 0.36 (relatively flexible base material).

FE simulations were performed on lattices made of the proposed architectural cells to study their size effect. Periodic lattices for each cell were modeled with identical overall dimensions with the number of unit cells per side (N_{cell}) from 2 to 10. In compound lattices, a 3×3×3 compound lattice configuration was treated as the smallest repeating geometry (N) and was tessellated in three orthogonal directions. We started from a compound lattice having one design gradient (G_1: cell type), and other design gradients (G_2: strut radius ratio, G_3: inclined strut radius, and G_4: cell size) were consecutively added to the previous configuration one-by-one.

FE results show that both the elastic stiffness and peak strength have minimal size effects regardless of the cell type and lattice uniformity (Figure 5-9 and Figure 5-10). These findings align well with the previous study[84-86].

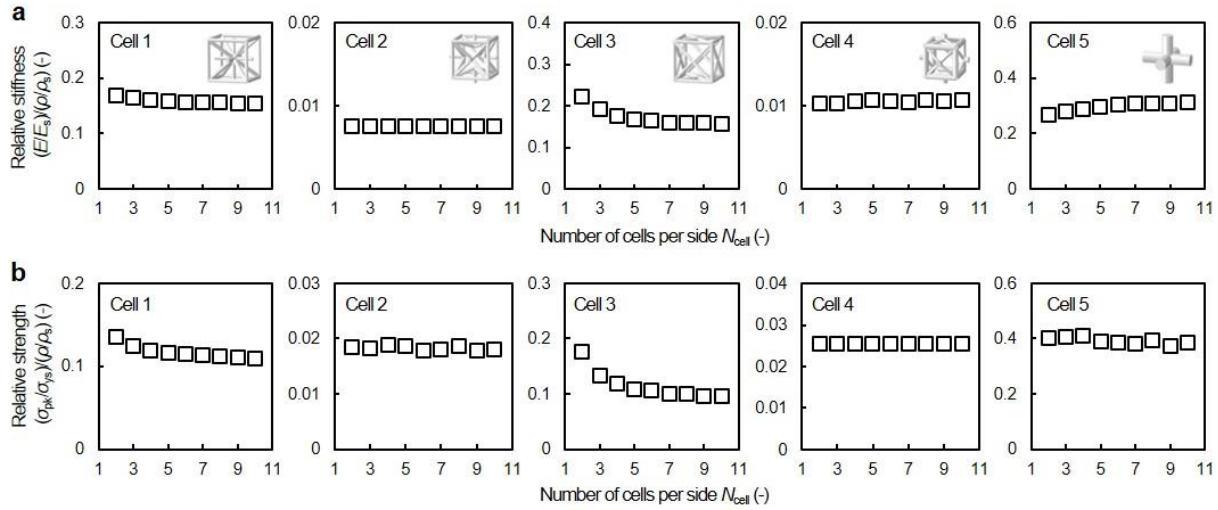

Figure 5-9. FE results showing size effects of the periodic lattices made of the presented architectural cells as a function of the number of unit cells (N_{cell}). (a), Relative compressive stiffness. (b), Relative compressive strength.

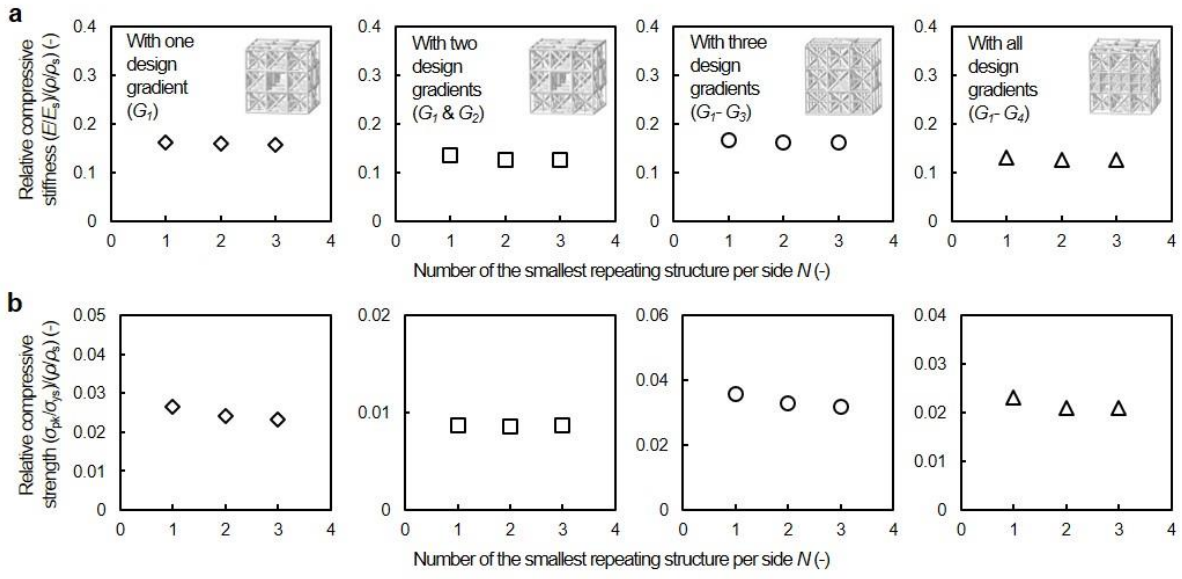

Figure 5-10. FE results showing size effects of the compound lattices as a function of the number of the smallest repeating geometry (N). (a), Relative compressive stiffness. (b), Relative compressive strength. Each design gradient (G_1: cell type, G_2: strut radius ratio, G_3: inclined strut radius, and G_4: cell size) were consecutively added to the previous configuration one-by-one.

Next, using the developed architectural cells, we generated a training dataset containing design parameters {**Y**} and their corresponding stress–strain curve features {**X**} (i.e., {**X**}-{**Y**} pairs). We first discretized ϕ (or Y_2) and r_1/L_1 (or Y_3) into a number of intervals to create hundreds of basic architectural configurations. Each configuration was tessellated in three principal directions to create a 3D lattice digital model with the overall dimension of 20 x 20 x 20 mm^3 (two unit cells in each orthogonal direction). Three samples were fabricated for each digital model using digital light 3D printing with a brittle polymer (see Methods for its chemical formulation). Stress–strain curves of the as-printed lattice samples were measured by monotonic compression and cyclic compression experiments (measured stress–strain curves illustrated in Figure 5-11). The measured stress–strain curve of each architectural configuration was then parameterized into 46 curve feature variables $\{X_i, i = 1 \dots 46\}$ and paired with the corresponding design parameters[27], leading to 1212 {**X**}-{**Y**} pairs in the pristine dataset. As these pairs provide links between the curve features of the experimentally measured curves and the corresponding lattice designs, the training dataset inherently accounts for process variability (e.g., uncertainty and imperfections) stemming from fabrication and experimental measurements. Additionally, as the forward module performs "many-to-one" mapping, we carried out data augmentation on these pairs to account for prediction fluctuation, resulting in 9360 {**X**}-{**Y**} pairs in the augmented dataset.

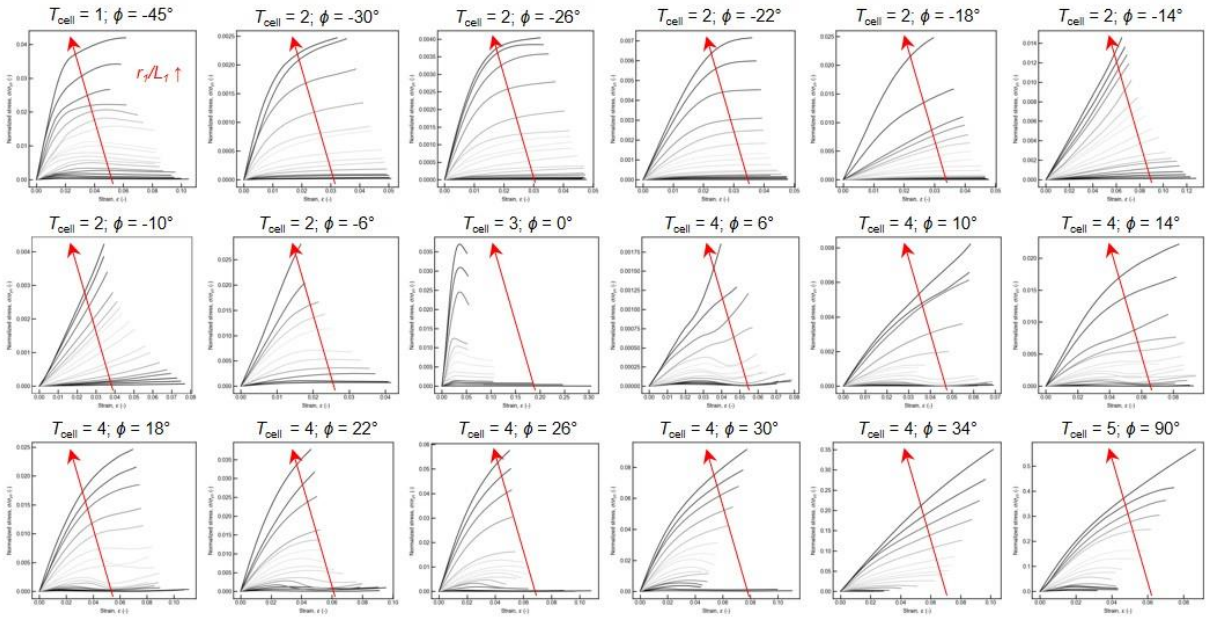

Figure 5-11. Experimentally measured stress-strain curves of the as-printed lattice samples using the architectural cells developed in this study. For clarity, the curves under monotonic compression loading are shown. An architectural transformation from varying the characteristic angle (ϕ) facilitates a stress-strain curve evolution. Together with controlling the radius-to-length ratio of the inclined strut (r_1/L_1), each configuration exhibits a family of its own respective stress-strain curves.

To generate training instances on the basis of the developed architectural cells (Figure 5-5c), we discretized the characteristic angle (ϕ) (i.e., the projected inclined strut onto the 13- or 23-plane) into 18 discrete values ranging from -45 to 90°. More specifically, the angle for the architectural cell 2 was uniformly distributed between -30 and -6° with an interval of 4° to fill the gap in the ϕ domain between the architecture cells 1 and 3. Similarly, the angle for the architectural cell 4 was evenly spaced by 8 intervals from 6 to 34° to fill the gap in the ϕ domain between the architectural cells 3 and 5. The angles for the architectural cells 1, 3, and 5 were naturally prefixed to -45, 0, and 90° by design, respectively. We intentionally excluded some ϕ near cell boundaries (i.e., ϕ ranging between -30 and -45° for the architecture cell 2 and between 34 and 90° for the architecture

cell 4) to distinctly differentiate stress-strain curves of neighboring architectural cells while avoiding possible overlaps.

Next, for each discretized characteristic angle ϕ, we discretized the radius-to-length ratio of the inclined strut (r_1/L_1) into approximately 17 intervals. This discretization resulted in hundreds of architectural configurations with a range of the relative density ($\bar{\rho}$) spanning from ~3 to ~25% (Table 5-2). The rationale of this relative density range is that, at higher relative densities, tuning stress-strain curves is limited as the curves become self-similar regardless of architectural cell types—they converge to those of a solid. This is attributed to an increased nodal volume which triggers failure at the node by plastic yielding and stress concentration rather than exploiting deformation mechanisms such as stretching, bending, and buckling of struts.

Table 5-2. Structure of training dataset.

Cell type T_{cell} (Y_1) (-)	Characteristic angle ϕ (Y_2) (deg)	Radius-to-length ratio of inclined strut r_1/L_1 (Y_3) (-)	Relative density ($\bar{\rho}$) (%)	Number of samples per loading condition	
				Monotonic compression	Cyclic compression
1	-45	0.027 ~ 0.069	2 ~ 15	19	57
2	-30	0.047 ~ 0.117	3.0 ~ 15	18	54
	-26	0.044 ~ 0.111	2.9 ~ 16	18	54
	-22	0.040 ~ 0.106	2.9 ~ 17	18	54
	-18	0.039 ~ 0.101	2.9 ~ 17	18	54
	-14	0.036 ~ 0.095	2.9 ~ 18	18	54
	-10	0.033 ~ 0.086	2.8 ~ 17	17	51
	-6	0.031 ~ 0.081	2.9 ~ 18	17	51
3	0	0.025 ~ 0.068	1.9 ~ 13	16	48
4	6	0.022 ~ 0.057	3.0 ~ 17	16	48
	10	0.027 ~ 0.084	2.9 ~ 26	16	48
	14	0.031 ~ 0.093	2.9 ~ 24	16	48
	18	0.035 ~ 0.103	3.0 ~ 23	16	48
	22	0.039 ~ 0.113	3.0 ~ 22	16	48
	26	0.044 ~ 0.123	3.0 ~ 20	16	48

	30	0.047 ~ 0.132	2.8 ~ 19	16	48
	34	0.052 ~ 0.172	2.8 ~ 25	16	48
5	90	0.112 ~ 0.292	2.8 ~ 17	16	48
Number of stress-strain curves per loading type				303	909
Total number of stress-strain curves				1212	

Following this, each architectural configuration was tessellated in three orthogonal directions to create a 3D digital model and was fabricated through additive manufacturing (see Methods – Sample fabrication). The printed samples were tested with two different loading conditions: uniaxial monotonic compression prior to failure and cyclic compression with three different maximum strains (measured stress-strain curves in Figure 5-11). Each measured stress-strain curve was then parameterized into 46 curve features {**X**} and paired with its corresponding design parameters {**Y**} (T_{cell}, ϕ and r_1/L_1) forming the pristine training dataset, containing around a thousand {**X**}-{**Y**} pairs.

Here, in the pristine training dataset, we adopted the one-hot representation of T_{cell} and normalized ϕ and r_1/L_1 to improve the training efficiency. The cell type is represented using a 1x5 vector as: cell 1 – [1,0,0,0,0] and cell 4 – [0,0,0,1,0]. While cells 1, 3 and 5 have a fixed value of ϕ, cells 2 and 4 have a fixed range of ϕ, we normalized the characteristic angle ϕ a fixed range of (0,1), where 0 and 1 represent the lower and upper limit of the angle respectively. The radius-to-length ratio r_1/L_1 is standardized to a normal distribution with a zero mean and a variance equal to 1.

Next, we performed data augmentation based on the pristine dataset to account for prediction fluctuation and achieve satisfactory prediction accuracy in the training of surrogate neural network models, which is "many-to one" mapping. This was achieved by adopting a standard SMOTE oversampling approach[87]. For cell types 1, 3 and 5, which characteristic angle ϕ is fixed, any

predicted ϕ value between 0 to 1 shall represent the same ϕ value as the original fixed angle. Thus, for cell types 1, 3, and 5, we augmented the dataset by generating new datasets with new varying normalized ϕ values between 0 and 1 (here, we select 0, 0.25, 0.5, 0.75, and 1). Moreover, since the inverse prediction of the one-hot-encoded T_{cell} is performed by using a "softmax" activation function, the predicted one-hot element would be close to, but less than 1, e.g., 0.95. To account for the prediction fluctuation in the one-hot-encoded T_{cell} feature, we further augmented the dataset by generating new data points with various new one-hot T_{cell} values—herein, we generate four new one-hot-encoded T_{cell} values for each datapoint, i.e., each {**X**}-{**Y**} pair. In detail, the one-hot-encoded element was randomly selected from a uniform distribution between 0.9 and 1.0, and the remaining non-hot-encoded elements were also randomly selected from a uniform distribution between 0.0 and 1.0, with a prerequisite that the sum of all elements in each one-hot representation is equal to 1, e.g., [0.95, 0.01, 0.02, 0.005, 0.015] for cell type 1. After the data augmentation, the dataset contains approximate ten thousand {**X**}-{**Y**} pairs.

Each stress-strain curve is uniquely then described by 46 curve features {**X**}. During training, we standardized these 46 curve features to improve the training efficiency. Considering the fact that the strain and stress values range over several orders of magnitude, we transformed each curve feature into a logarithmic representation prior to standardization so as to reduce their standard deviation. Note that some of the curve features does not exist in the curve for partial training dataset. For instance, some curves may not exhibit any local minimum or maximum. In such cases, we simply set the relevant feature values to zero.

However, we found that the zero representation of nonexistent curve features herein turns out to be very challenging to be accurately predicted and, in addition, negatively affectively affect the

prediction of existent features in the training process. This situation is likely to arise from the giant gap of magnitude between the zero value and the existent curve features. To address the "zero-type" issue, the zero value for each nonexistent feature was replaced by a relevant curve feature with nonzero representation. Specifically, in case of a monotonic curve, ΔU was set as the area under the curve. Similarly, we reset the nonexistent strain and stress features to the values of their end strain ε_{end} and stress σ_{end} values, respectively. By doing so, the nonexistent features exhibit a magnitude that is similar to that of the existent features, and the nonexistent points are able to overlap with the end point to yield an identical stress-strain curve.

Based on the updated dataset, the load type T_{curve} is required to be added into $\{\mathbf{X}\}$ to identify the curve type associated with $\{\mathbf{X}\}$. Herein, we classified the stress-strain curves into 4 categories: linear response, plastic yielding response, buckling response and multiple peak-and-valley response. The curve type T_{curve} is encoded by one-hot representation, that is, [1,0,0,0], [0,1,0,0], [0,0,1,0], and [0,0,0,1] represent linear, plastic yielding, buckling, and multiple peak-and-valley response, respectively.

5.3.2 Training of the ML framework

For training of our generative ML approach, we first trained the forward module with the augmented dataset. The forward validation module predicts the curve type (via a curve type classifier) and curve features $\{\mathbf{X}^{\text{P}}\}$ (via a curve feature regressor) of given lattice design. This forward module effectively acts as a surrogate model that replaces conventional simulations used to evaluate the responses of a design. As compared to the conventional simulation typically requiring hours to compute the mechanical behavior of a 3D lattice design, this forward module

takes a few seconds to evaluate the mechanical behavior, which greatly shortens the time span of the entire design process.

Once the forward module was trained, this module was kept frozen (i.e., the weight and bias parameters of all surrogate models were fixed) and was then used to train the inverse prediction module with the pristine training dataset. In the entire training process of the inverse module, the cost function $f_c = (\mathbf{X}^P - \mathbf{X}^T)^2$, which evaluates the difference between the predicted stress–strain curve features $\{\mathbf{X}^P\}$ and the target curve features $\{\mathbf{X}^T\}$ for a given architecture $\{\mathbf{Y}\}$, was used to optimize the hyperparameters of all the NN models. This strategy prevents any instability during training, which could otherwise cause $\{\mathbf{Y}\}$ to become a meaningless latent space variable. Our ML approach with the optimized hyperparameters showed satisfactory overall prediction accuracy via a typical cross-validation technique (i.e., random 70/30 train/test split). Specifically, each NN model reaches a plateauing loss and eventually features prediction accuracy (~90%) when the training size exceeds about 50% of the dataset with minimal signature of over- and under-fitting, indicating that the training data size is adequate to reasonably satisfy the design goal.

Training of the curve type classifier

We trained the classifier based on the augmented training dataset. Following a random train-test split 30% of the dataset was kept hidden to the model and used as test set later. We then adopted 10-fold cross-validation on the remaining 70% to adjust the hyperparameters (so as to minimize the cross-validation error). In detail, each batch contains 32 curves. The loss function L is defined as the mean square error between the predicted and targeted curve types. We adopted a stochastic gradient descent (SGD) optimizer to minimize the loss function with an initial learning rate of 0.01 and a Nesterov momentum of 0.9. The learning rate was set to decay one order of magnitude after

a patience of 10 training epochs. Figure 5-12a shows the test set loss as a function of training epochs. After 100 training epochs, the test set loss converges to a miniscule level (~0.01).

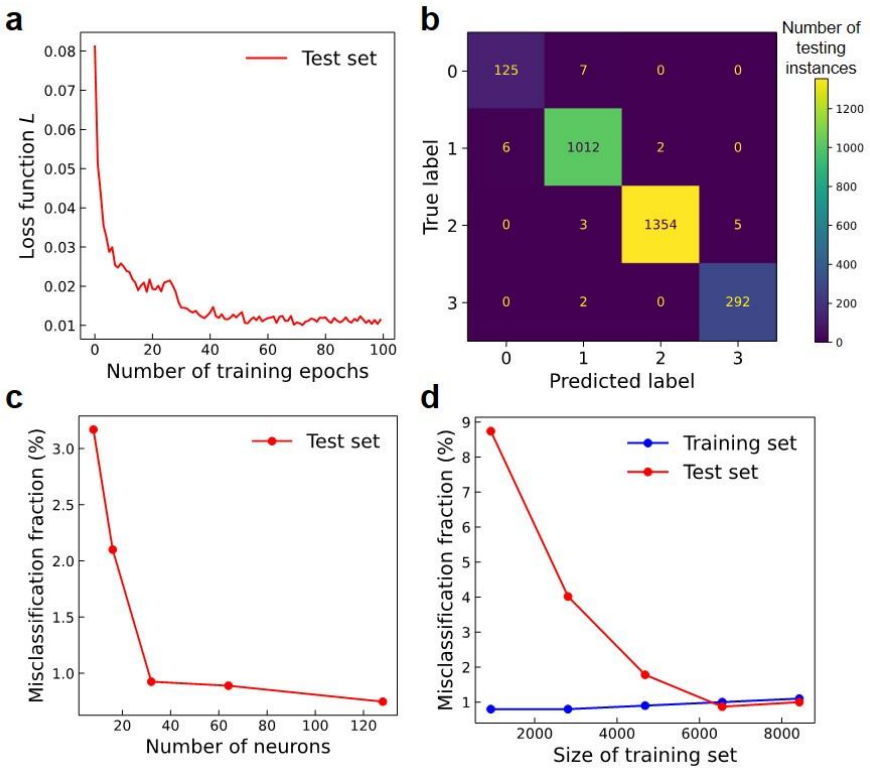

Figure 5-12. Training results of the curve type classifier**.** (a), Classifier loss L as a function of the number of training epochs for the test set. The test set contains 2808 curves and accounts for 30% of the dataset. (b), Confusion matrix of the test set predicted by the curve type classifier. The label index ranging from 0 to 3 represents linear, plastic yielding, buckling, multiple peak-and-valley response, respectively. (c), Misclassification fraction of the test set as a function of the number of neurons in the first hidden layer. Note that the number of neurons in the second hidden layer is set to be 2 times that of the first hidden layer. (d), Misclassification fraction (for both the training and test sets) as a function of the size of the training set.

We now investigate the classification accuracy of the curve type classifier. Figure 5-12b shows the confusion matrix of the classifier's predictions for the test set, where the test set contains 2808 curves in the augmented dataset. It is notable that the classifier can accurately predict the categories

of all curve types, with the accuracy reaching ~98% for each curve type. Due to its high classification accuracy, the classifier can be used to filter nonzero predictions of curve features that are expected to be zero, thus facilitating the feature-to-curve reconstruction.

It should be pointed out that, we have optimized the classifier performance by tuning all relevant training hyperparameters (so as to maximize the cross-validation accuracy). For instance, Figure 5-12c shows the misclassification fraction of the test set as a function of the number of neurons in the first hidden layer. The number of neurons in the second hidden layer was herein set to be 2 times that of the first hidden layer, while other hyperparameters remain unchanged. We find that the classifier with a first hidden layer of ≥ 32 neurons can offer very accurate predictions of curve type, with a misclassification fraction lower than 1%. Hence, we selected 64 neurons in the first hidden layer to achieve an optimal balance between model accuracy and simplicity.

Moreover, we investigate the influence of the size of the training set on the classifier's accuracy, i.e., by constructing a learning curve. In that regard, Figure 5-12d shows the misclassification fraction (both the training and test sets) as a function of the size of training set, wherein five training sizes (i.e., 10%, 30%, 50%, 70%, 90% of the augmented dataset) were selected, and the dataset is randomly split into training and test sets. We found that, as expected, with more and more learning examples in the training set, the classifier exhibited an enhanced classification accuracy for the test set and then eventually reaches a plateau when the training size exceeds 50% of the dataset, with a classification accuracy of ~99% for both the training and test sets. These results confirmed that the model is not notably over- or under-fitted. We selected herein 70% of the dataset as training set to avoid the issue of sample deficiency that impairs the classifier performance.

Training of forward validation module

The forward validation module contains both a curve feature regressor (consists of five surrogate neural network models) and a pretrained curve type classifier. During training, the curve type classifier was kept frozen with fixed hyperparameters. Similar to the training process of curve type classifier, we utilized the augmented dataset for the training of the forward validation module and first defined the test set comprising 30% of the data points by a random train-test split. We then trained the forward surrogate model (i.e., the curve feature regressor herein) using 10-fold cross-validation on the remaining 70% of the data points. In detail, each batch contains 32 curves. The loss function f_c is defined as the mean square error between predicted and targeted curve features, with the curve type being included. We adopted the stochastic gradient descent (SGD) optimizer to minimize the loss function with an initial learning rate of 0.01 and a Nesterov momentum of 0.9. The learning rate was set to decay 1 order of magnitude after a patience of 10 training epochs. Figure 5-13a shows the test set loss as a function of the number of training epochs. After 200 training epochs, the test set loss converges to a miniscule level (~0.05).

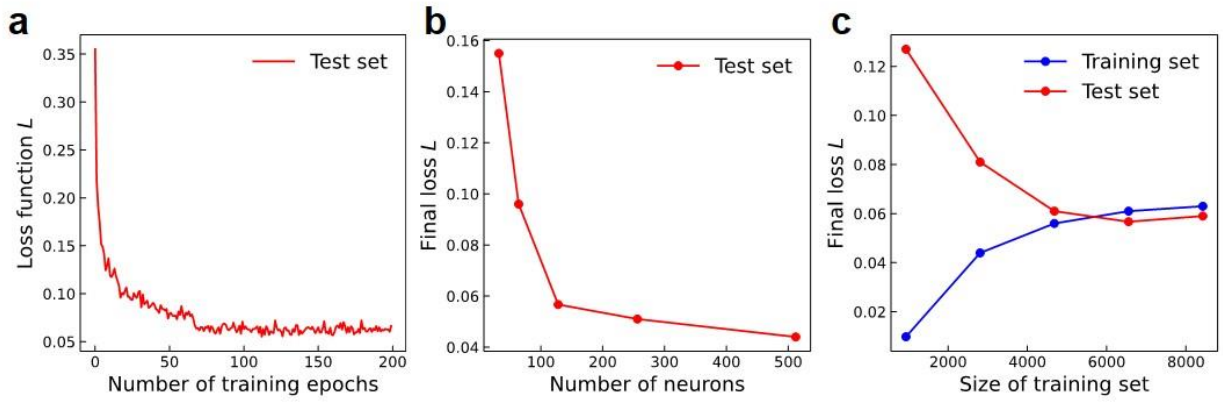

Figure 5-13. Training results of the forward validation module. (a), Forward prediction loss L as a function of the number of training epochs for the test set. The test set contains 2808 curves and accounts for 30% of the dataset. (b), Final test loss as *L* as a function of the number of neurons in

the first hidden layer. Note that the number of neurons in the second hidden layer is set to be 2 times that of the first hidden layer. (c), Final loss L (for the training and test sets) as a function of the size of training set.

Note that, here, we have optimized the forward model performance by tuning all relevant training hyperparameters (to maximize the cross-validation accuracy). Figure 5-13b shows the final test loss as a function of the number of neurons in the first hidden layer in the curve feature regressor, wherein the number of neurons in the second hidden layer is twice as large as in the first hidden layer, while the other hyperparameters remain unchanged. As expected, larger number of neurons leads to smaller test loss, and we find that the test loss converges to a miniscule level when the first hidden layer contains ≥ 128 neurons. We selected herein 128 neurons in the first hidden layer, which offers an optimal balance between model accuracy and simplicity.

Next, we investigated the influence of the training size on the forward model performance by constructing a learning curve. Figure 5-13c shows the final loss as a function of the size of training set for both the training and test sets, wherein five training sizes (i.e., 10%, 30%, 50%, 70%, 90% of the dataset) are selected, and the dataset was randomly split into training and test sets. As expected, at small training size, the model exhibits a high test-loss due to the deficiency of training samples. Notably, with more and more learning examples in the training set, the forward model exhibits an enhanced prediction accuracy for the test set and then eventually reaches a plateau when the training size exceeds 50% of the dataset, with a miniscule final loss of ~0.06 for both the training and test sets. These results confirm that the model does not exhibit any notable level of over- or under-fitting. We selected herein 70% of the dataset as training set to avoid the issue of sample deficiency that impairs the forward model performance.

Once trained, the forward neural network model acts as a surrogate model (that effectively replaces the simulations) that predicts the stress-strain curve of an input lattice design. To ensure that this model acts as an accurate surrogate simulator, we further investigated the prediction accuracy of the surrogate forward model. Figure 5-14 provides the predicted versus true values of come representative curve features offered by the forward surrogate model for the test set, where the test set contains 2808 curves. Note that the output curve features are standardized. For each feature, it is notable that all the datapoints are located at the vicinity of the $y = x$ identity line. These results demonstrate that the forward surrogate model can accurately predict all the curve features used to describe a stress-strain curve.

Based on the predicted curve features, we can reconstruct the stress-strain curves associated with these features, to conduct a visual comparison between the predicted and true stress-strain curve. Figure 5-15 provides some examples of predicted versus true test curves offered by the forward validation module, where the predicted curves are reconstructed from their predicted curve features, and the predictions range over all types of stress-train curves, including linear, plastic yielding response, buckling response, and multiple peak-and-valley response. It is notable that, for all the curves in the test set, the predicted and true curves largely overlap with each other, with a NRMSE that is smaller than 0.1. Once again, these results illustrate that the surrogate forward model can offer an accurate prediction of stress-strain curve for a given design of the lattice. This confirms that the forward model can be used as an accurate surrogate simulator and, hence, can be used to train the generative forward model. Note that the ground-truth simulation engine itself cannot be used to train the generative model as it is not differentiable and, hence, does not enable back-propagation training—so that it is here necessary to replace the ground-truth simulator by a differentiable deep learning surrogate forward model.

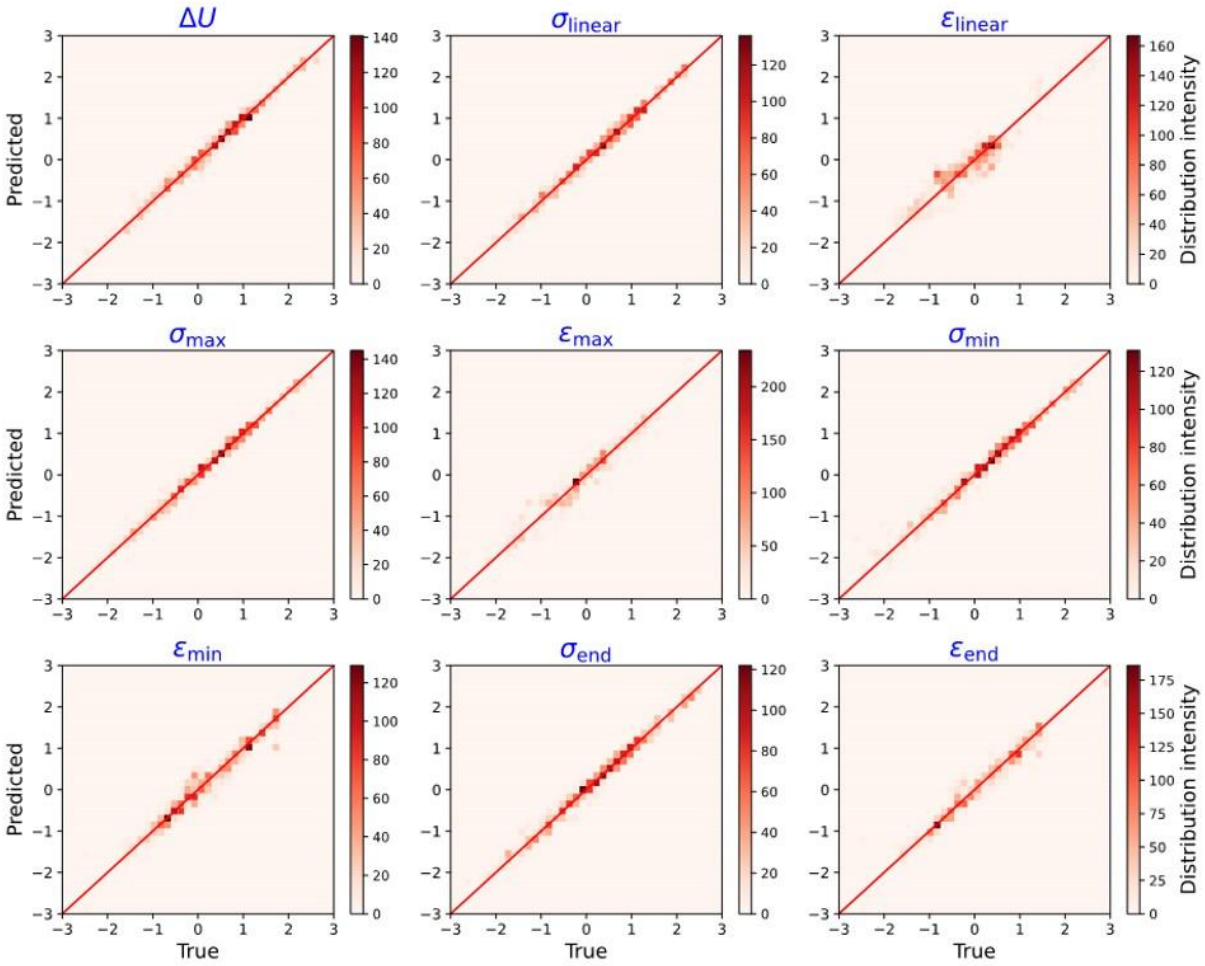

Figure 5-14. Prediction accuracy of the forward validation module. Predicted versus true curve features offered by the forward surrogate model for the test set. Note that the output curve features are standardized.

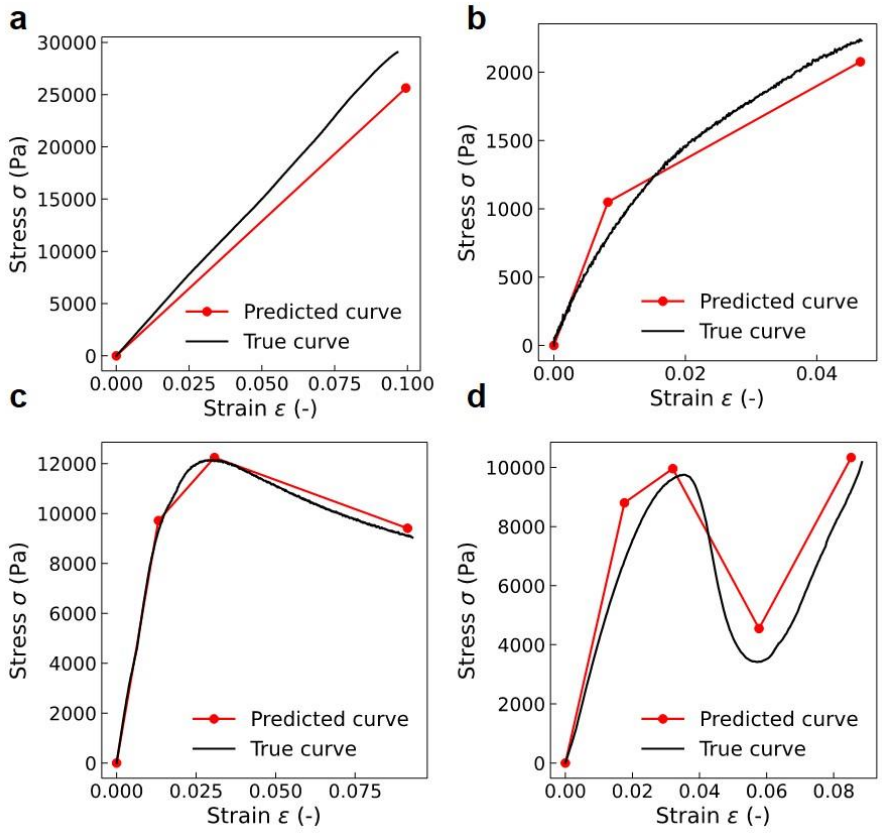

Figure 5-15. Examples of predicted (red) versus true (black) test curves offered by the forward validation module. (a), Linear response. (b), Plastic yielding response. (c), Buckling response. (d), Multiple peak-and-valley response. The predicted curves are reconstructed from their predicted curve features.

Training of the inverse prediction module

Next, utilizing the pristine training dataset, we train the backward generative neural networks by connecting it to the surrogate forward model. In detail, by inputting the target stress-strain curve feature $\{\mathbf{X}^{T}\}$, the backward generative model predicts a design candidate of the lattice $\{\mathbf{Y}\}$, which is then fed into the surrogate forward model to evaluate its corresponding curve feature $\{\mathbf{X}^{P}\}$ for validation. As described in the previous section, we defined the loss function as the mean squared

error between $\{\mathbf{X}^T\}$ and $\{\mathbf{X}^P\}$ ($f_c=(\mathbf{X}_{pred}-\mathbf{X}_{true})^2$) and minimize the loss via gradient backpropagation, where the surrogate forward model is kept frozen (i.e., with fixed hyperparameters). Note that the dataset adopted in this training process is the pristine dataset (~1000 data points) without any data augmentation, where both the input and output the curve features $\{\mathbf{X}\}$ along with the information of curve type T_{curve}. The dataset was randomly split into training and test sets, where the test set contains 280 curves and accounts for 30% of the dataset. We conducted a 10-fold cross validation on the remaining training set to optimize the hyperparameters in the backward generative model. A SGD optimizer was adopted to minimize the loss function, with an initial learning rate of 0.01, a Nesterov momentum of 0.9, and a batch size of 32 curves. The learning rate was set to decay 1 order of magnitude after a patience of 10 training epochs. Figure 5-16a shows the test set loss as a function of the number of training epochs. After 200 training epochs, the test set loss converges to a miniscule level (~0.1).

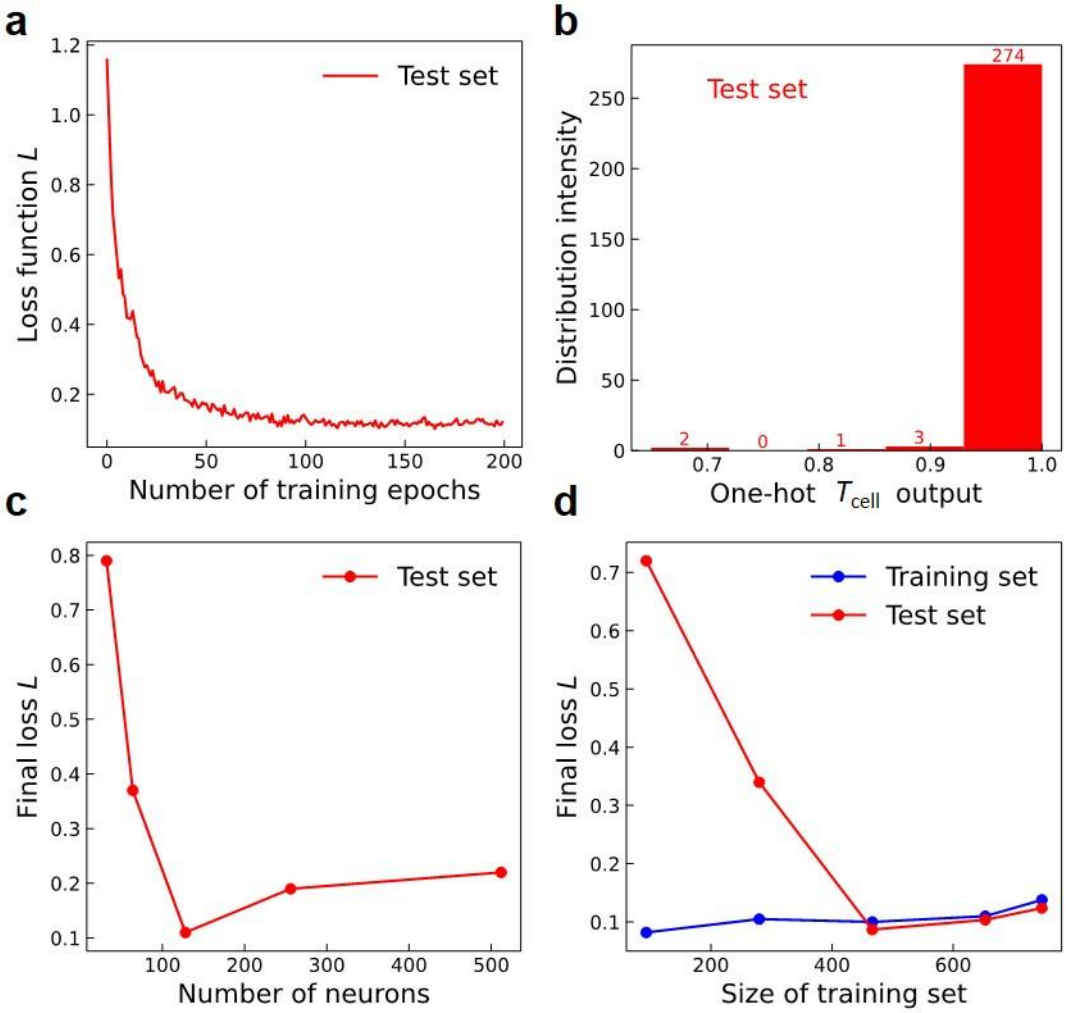

Figure 5-16. Training results of the inverse prediction module. (a), Inverse prediction loss L as a function of the number of training epochs for the test set. The test set contains 280 curves and accounts for 30% of the dataset. (b), Distribution histogram of the one-hot-encoded T_{cell} output for the test set. Note that the backward generative model adopts a softmax activation for the T_{cell} output. (c), Final test loss as L as a function of the number of neurons in the second hidden layer. Note that the number of neurons in the first hidden layer is set to be 2 times that of the second hidden layer. (d), Final loss L (for both the training and test sets) as a function of the size of training set.

Note that, since the T_{cell} output of the generative model is based on a softmax activation function, the predicted T_{cell} values are not a standard one-hot representation (i.e., not an array composed of zero and one), which is likely to be outside the estimation range of the forward surrogate model.

In order to make the predicted T_{cell} close to the standard one-hot representation, we designed a regularization term as the sum of (1 – max(T_{cell})) to restrict the T_{cell} output toward a one-hot representation. Figure 5-16b shows the distribution histogram of the one-hot-encoded T_{cell} output for the test set. As expected, the one-hot-encoded values of T_{cell} are mostly located in the range of [0.95, 1.0), with only 6 out of the 280 test curves being slightly smaller than 0.95. Thus, the predicted T_{cell} remains an approximation of a one-hot representation, and the small deviations of T_{cell} output are within the estimation range of forward surrogate model, given the fact that the forward model was trained by an augmented dataset with one-hot-encoded T_{cell} values ranging from 0.9 to 1.

It is worth mentioning that we have optimized the inverse model performance by tuning all relevant training hyperparameters (to maximize the cross-validation accuracy). Figure 5-16c shows the final test loss as a function of the number of neurons in the second hidden layer, wherein the number of neurons in the first hidden layer is twice as large as in the second hidden layer, while other hyperparameters remain unchanged. We found that the test loss exhibits a minimum loss at 128 neurons, and that more neurons are not necessary to reduce the final test loss. Therefore, we selected herein 128 neurons in the second hidden layer to achieve an optimal balance between model accuracy and simplicity.

Finally, we investigated the influence of training size on the inverse model performance by constructing a learning curve. Figure 5-16d shows the final loss as a function of the size of training set for both the training and test sets. We selected five training sizes, i.e., 10%, 30%, 50%, 70%, 90% of the dataset, and randomly split the dataset into training and test sets. Due to the sample deficiency issue, the model initially exhibited a high test-loss at small training size. As the training

size increases, the test loss decreased and finally reached a plateau when the training size exceeds 50% of the dataset, with a miniscule final loss of ~0.1 for both the training and test sets. This shows that the backward model does not exhibit any notable level of over- or under-fitting. We selected herein 70% of the dataset as training set to avoid the issue of sample deficiency that impairs the inverse model performance.

Once trained, the backward generative model aims to predict a lattice structure for a target stress-strain curve. To ensure the reliability of the inverse prediction module on prediction of architectures with tailored mechanical behaviors, we further investigated the prediction accuracy of the backward generative model. Figure 5-17 shows some representative stress-strain curve features of the structures generated by the backward model for the test set (predicted) as a function of the true stress-strain curve features used as target (where the test set contains 280 curves). Note the output curve features are standardized. For each feature, it is notable that the datapoints are largely located around the $y = x$ identity line. These results demonstrate that the backward generative model can indeed generate some structures that exhibit curve features that show a good match with the targeted input curve features. This confirms that the inverse prediction module is able to properly generalize, that is, it is able to generate structures exhibiting tailored stress-strain curves—despite the fact that the model was never exposed to this stress-strain curve during its training.

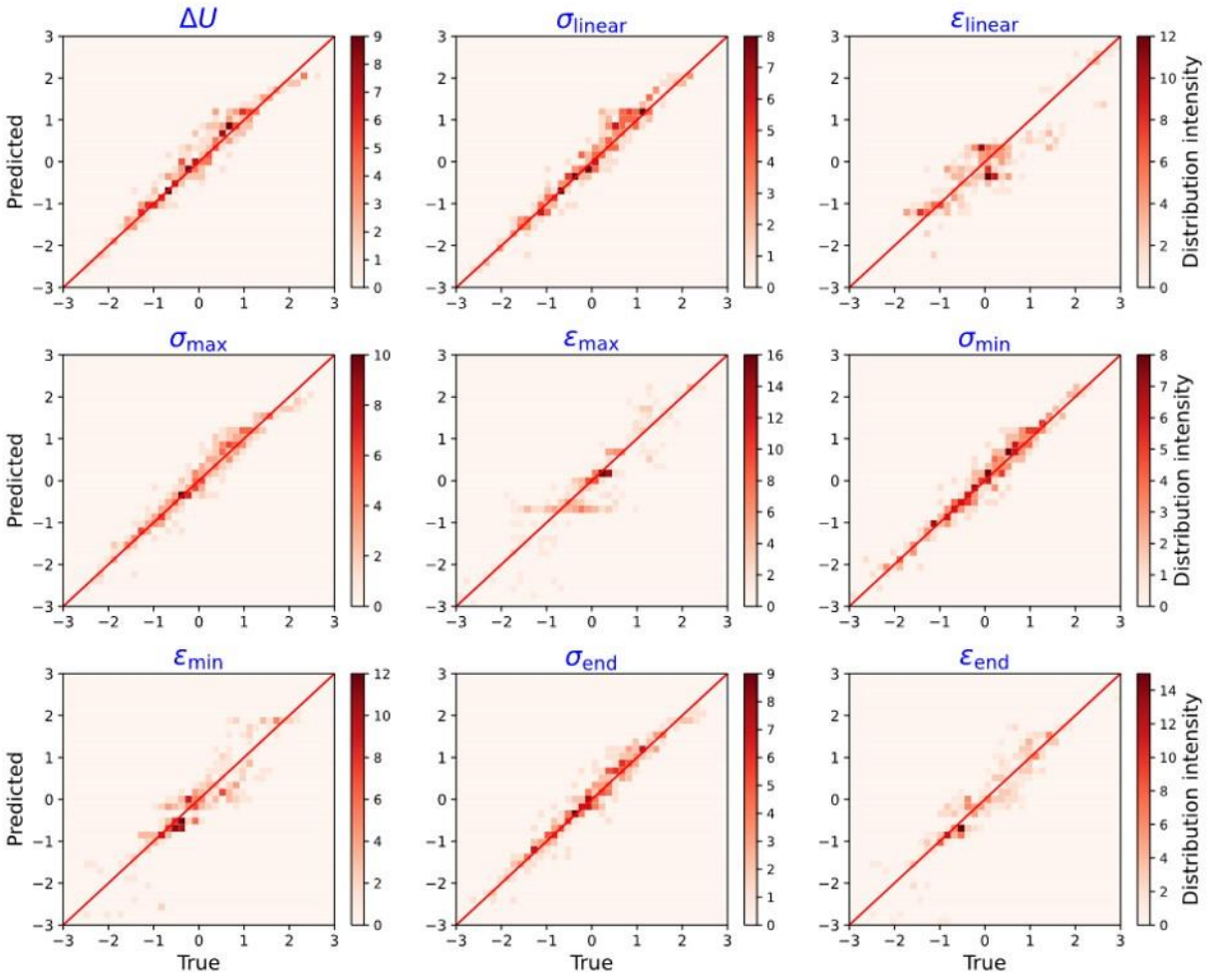

Figure 5-17. Prediction accuracy of the inverse prediction module. Representative stress-strain curve features of the structures generated by the backward model for the test set (predicted) as a function of the true stress-strain curve features used as target. Note that the output curve features are standardized.

Based on the predicted curve features, we can reconstruct the stress-strain curves associated with these features, to conduct a visual comparison between the stress-strain curve of the generated structure and the target curve. Figure 5-18 provides some examples of stress-strain curves offered by the backward generative model, where the backward generative model generates a predicted structure that is fed into the forward surrogate model for validation, and the predicted curves are

reconstructed from their predicted curve features offered by the forward surrogate model. The predictions range over all types of stress-train curves, including linear, plastic yielding response, buckling response, and multiple peak-and-valley response. It is notable that, for most curves in the test set, the generated and true curves largely overlap with each other, with a NRMSE smaller than 0.2. Again, these results illustrate that the backward generative model can accurately generate lattice design featuring tailored target stress-strain curves.

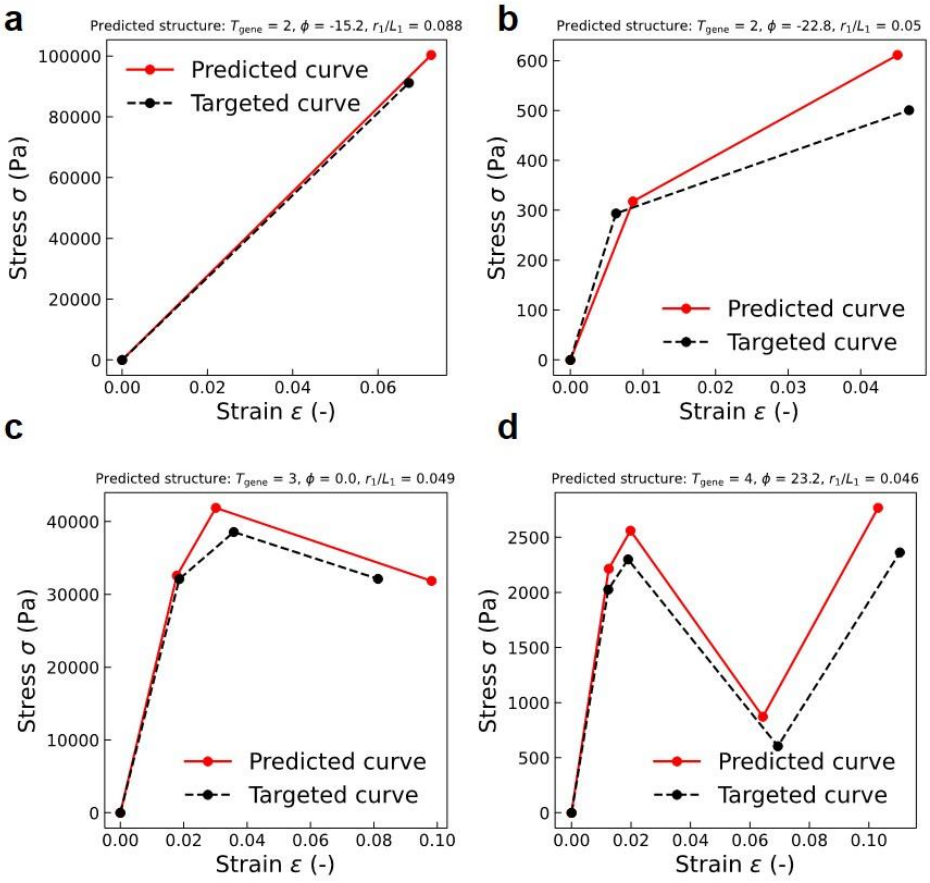

Figure 5-18. Examples of predicted (red) versus true (black) test curves offered by the inverse prediction module. (a), linear response. (b), plastic yielding response. (c), buckling response. (d), multiple peak-and-valley response. By inputting a targeted curve, the inverse prediction module generates a predicted structure that is fed into the forward surrogate model for validation. The predicted curves are reconstructed from the predicted curve features offered by the forward surrogate model.

Training of multiple models with different initialization

In the previous sections, we described the training process of each individual neural network model, which is the foundation of optimal design selection. Here, we prepared five pairs of the forward surrogate neural network models and generative neural network models in our ML pipeline. All the surrogate neural networks in the forward validation module and generative neural networks in the inverse prediction module are differentiated from other models in the same module with training hyperparameters, e.g., number of neurons, initialization, etc. Figure 5-19a shows a schematic of five generative training pipelines under different initialization, where each generative model is linked to its pairing surrogate models during the training and prediction process. The five individual surrogate forward models are obtained by different training initialization, which are kept frozen once trained and used to subsequently train their corresponding generative models, respectively.

In detail, we first conducted trainings of five surrogate neural network models with different initialization, while the augmented dataset is used. Figure 5-19b shows the test set loss as a function of the number of training epochs for five surrogate models, where the test set is randomly selected from the augmented dataset and contains 2808 curves (accounting for 30% of the augmented dataset). We found that the five trainings resulted in different final losses for the surrogate forward models, indicating they resulted in different surrogate neural network models. Nevertheless, all the losses eventually converge to a miniscule level between 0.05 and 0.1. We then used the five pretrained surrogate models to train their corresponding generative neural network models, respectively. Figure 5-19c shows the test set loss as a function of the number of training epochs for the generative models under the five trainings, where the test set is randomly selected from the

pristine dataset and contains 280 curves (accounting for 30% of the pristine dataset). Similar to the training results of forward models, we found that each training resulted in a different generative model, with a distinguishable, convergent final loss between 0.1 and 0.2. Overall, relying on different training initialization, we obtain five different surrogate models and five different generative models.

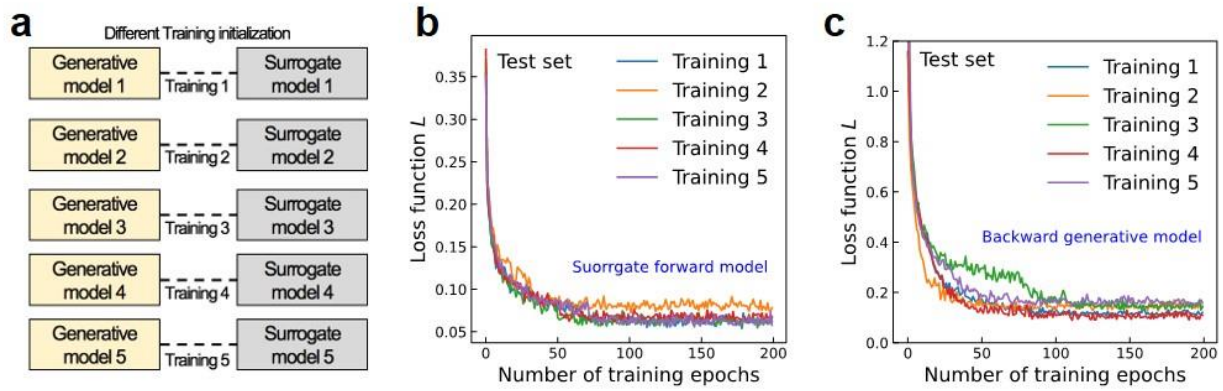

Figure 5-19. Training results of multiple models with different initialization. (a), Schematic illustrating five generative pipelines, wherein the five different surrogate forward models are obtained by different training initialization, which are used to train the five backward generative models, respectively. (b), Test set loss as a function of the number of training epochs for the surrogate forward model under five different training initializations. The test set is randomly selected from the augmented dataset and contains 2808 curves, which accounts for 30% of the dataset. (c), Test set loss as a function of the number of training epochs for the backward generative model under five different training initializations. The test set is randomly selected from the pristine dataset and contains 280 curves, which accounts for 30% of the dataset.

5.4 Inverse design based on various stress–strain curves

Next, using our ML approach, we demonstrated the inverse design of representative stress-strain curve paths of a cellular solid subjected to monotonic and cyclic compression. As illustrated in Figure 5-20a, these target curve paths include (i) a linear-elastic section followed by an negative

stiffness section, depicting buckling (cases I and V); (ii) a linear-elastic section followed by positive and nearly zero stiffness sections, illustrating strain hardening and plateau regions, respectively (cases II and VI); (iii) a linear-elastic section followed by immediate fracture, characterizing brittle behavior (cases III and VII); and (iv) a linear-elastic section followed by controlled post-buckling, showing a snap-through response (cases IV and VII). These target curve paths (gray solid curves) were significantly different from any curves in the training dataset, which guarantees that our ML approach does not have explicit prior knowledge of these curves. We fed the curve paths into our ML pipeline to obtain the optimal design parameters, from which ten samples for each curve path were additively manufactured via the same 3D printing apparatus used for our training database generation. Representative printed samples and the predicted optimal design parameters are shown in Figure 5-20b.

Results of the inverse design of the representative stress-train curve paths are shown in Figure 5-20a. In this figure, the best matching curve (black dotted curve) from ten measured stress-strain curves for each case is compared against the corresponding target curve (gray solid curves), and a blue-shaded uncertainty zone, describing the distribution of the test curves from ten printed samples, represents manufacturing variability. We found excellent similarity between the target curve and best matching curve for all cases (highlighted by the computed normalized root-mean-square error close to zero), revealing that our method can automatically take into account various manufacturing defects in stereolithography, which vary sample by sample and even strut by strut. This scope is very challenging or impractical to capture with other approaches, such as topology optimization[24].

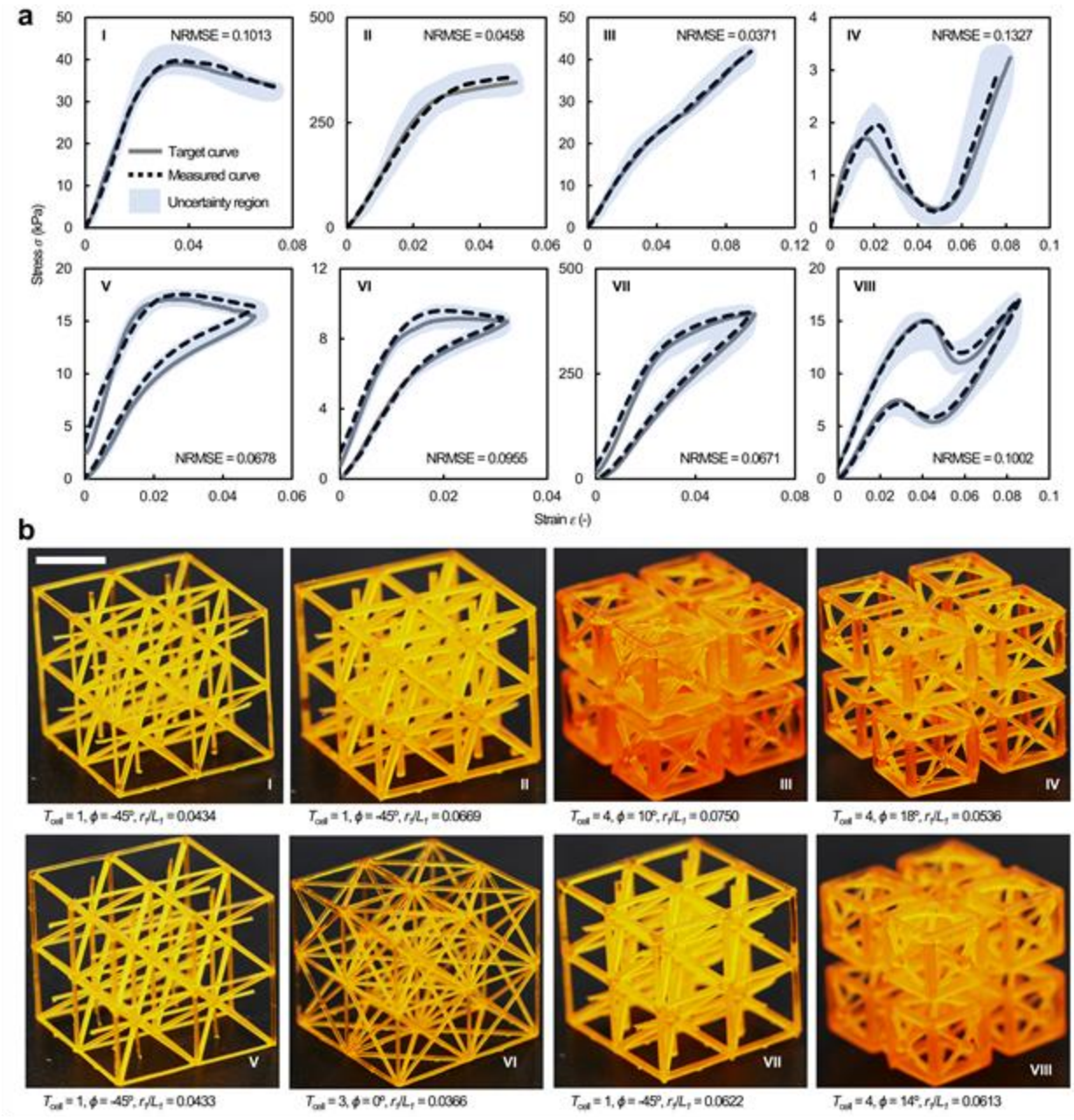

Figure 5-20. Inverse design based on representative target stress–strain curves and experimental design validation. (a) Inverse design based on representative target stress–strain curves describing various compressive responses, spanning linear elastic behavior followed by either a negative, nearly zero, or positive tangent modulus to a multislope tangent modulus, in response to monotonic (I ~ IV) and cyclic (V ~ VIII) uniaxial compression loadings. The gray curves denote the target curves, whereas the black dotted curves represent selected measured curves (from ten measured curves) of the printed samples. The uncertainty region, highlighted by blue shading, covers the distribution of ten experimentally measured curves, illustrating process variability. The normalized root-mean-square error (NRMSE) quantifies the curve similarity between the target and all the measured curves (0: identical curve pair; 1: completely dissimilar curve pair). (b) Photographs of

the printed samples inversely designed by the presented ML pipeline in response to each target curve shown in a. The ML-predicted design parameters are listed. The scale bar is 10 mm.

Our ML approach is also applicable to other polymer-based AM platforms exhibiting larger process variabilities with minimal decreases in reliability. When the process variability (η), defined as the ratio of the deviation to averaged value of mechanical properties of printed samples, increased by a factor of ~2.6, which makes the printing process used in this study comparable to that of the selective laser sintering process[31-34], the overall prediction accuracy of our ML approach was reduced by ~7%, resulting in an acceptable uncertainty region for the inverse design. While accuracies for recreating materials in response to larger processing errors could be compensated by incorporating larger training data sets, other manufacturing defects, such as anisotropy, porosity, shrinkage and micro-structural evolution that are unique to metal additive manufacturing is not accounted for in the present method.

5.5 Study of process variability

5.5.1 Training data with stochastic noise and variability

We introduced noise to our training dataset to match variability in mechanical properties to that of other AM techniques. Herein, the variability was described by the variation in the elastic stiffness (i.e., $\eta = \frac{1}{n}\sum\frac{E_{\text{measured}}-E_{\text{fitted}}}{E_{\text{fitted}}}$, where E_{fitted} denotes a scaling relation between the elastic stiffness and the radius-to-length ratio of the inclined strut and n is the total number of data in our training dataset). Compared to the process variability of stereolithography printing approach used in this work (denoted by η_{SLA} = 13%), η of selective laser sintering (SLS) process is significantly higher

(35%)[88-91]. Thus, we considered a range of η (25, 35, and 45%) to represent larger process variabilities than η_{SLA}.

These η were used to amplify variability in mechanical properties in our training dataset. This process started with generating a set of random numbers following a normal distribution with zero mean and standard deviation equal to a given η (Figure 5-21a). Then, a randomly selected value (x) from this set was used to amplify a distance between each curve feature and the corresponding fitted value in our training dataset (d_{ini}) so that a collection of increased distances (d_{new}) follows the normal distribution described by the given η (Figure 5-21b)—that is, $\frac{d_{new}}{d_{ini}} = \left(1 + \frac{x-\eta_{SLA}}{\eta_{SLA}}\right)$. This process was repeated for each η and led to three training datasets, of which each one represents different, larger process variability than that in our training dataset (η_{SLA} = 13%). Figure 5-21c and 5-21d show representative probability distributions of before and after manipulation of the original training dataset using the process described above.

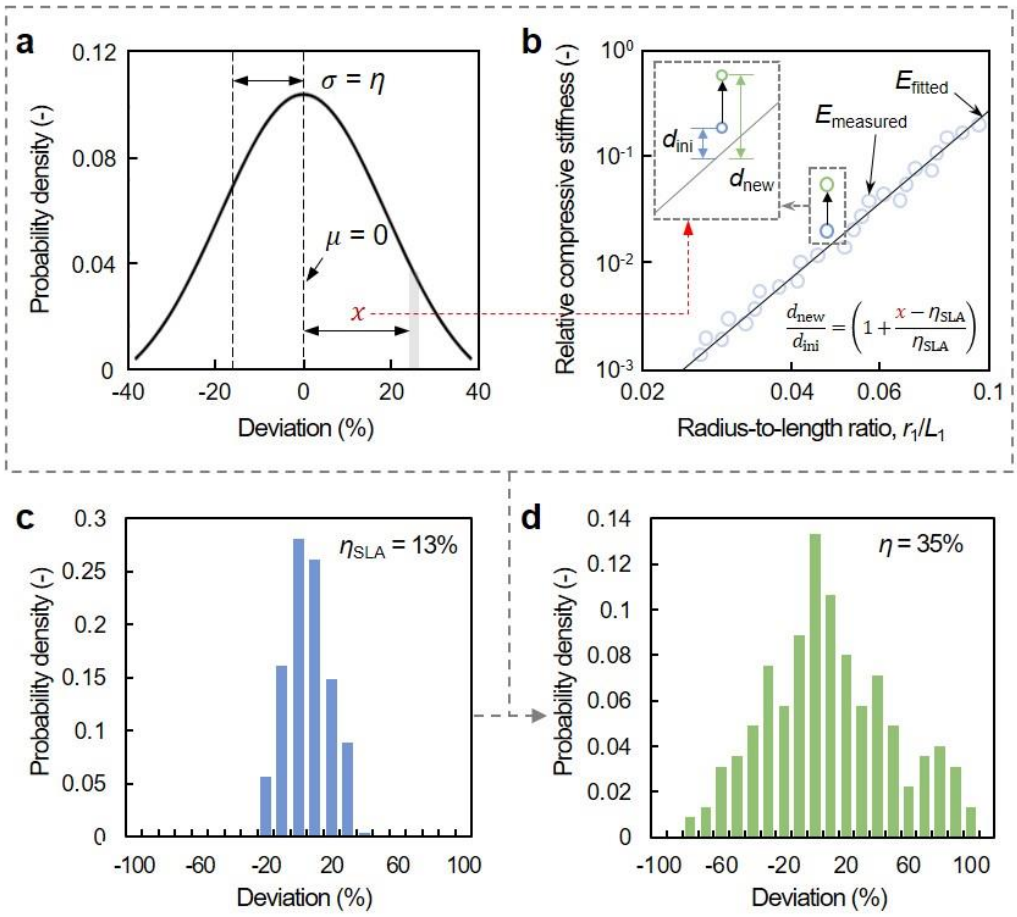

Figure 5-21. Training datasets with stochastic noise and variability. (a), A set of random values following a normal distribution with zero mean and standard deviation equal to a given η. (b), Manipulation of curve features in our training dataset to match process variability described by a given η_P. A randomly selected value (x) from the set in a was used to amplify a distance between each curve feature and the corresponding fitted value (d_{ini}) so that increased distances (d_{new}) follow the normal distribution in a. (c), Percentage deviation in the elastic stiffness in our training dataset, representing η_{SLA} of 13% (before manipulation). (d), Percentage deviation in the elastic stiffness in a manipulated training dataset with η of 35% (after manipulation).

5.5.2 Evaluation of process variability: Prediction accuracy

Here the effects of disparate process variabilities on the overall prediction accuracy of our ML approach are presented. As done previously, we employed the 10-fold cross-validation technique

to evaluate the overall prediction accuracy for each training dataset with larger process variabilities (η) as a function of data size.

The results show that the overall prediction accuracy scales with the data size and tends to converge to a plateau regardless of the level of process variability (Figure 5-22a). This implies that the model is capable of learning the underlying patterns even with the presence of considerable process variability. Furthermore, a degradation in the overall prediction accuracy was found to be marginal (~7%) when the process variability (η) increased from 13 to 35% (Figure 5-22b).

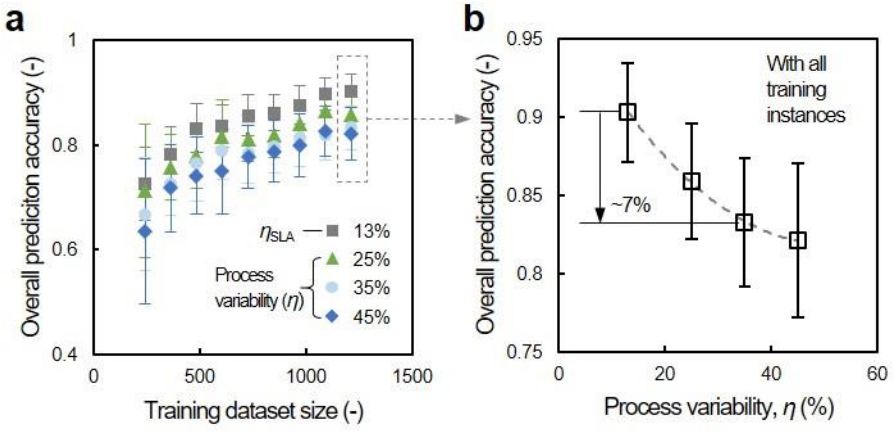

Figure 5-22. Effects of the process variability on our ML approach. (a), Overall prediction accuracy as a function of data size with various process variabilities (η) of 13, 25, 35, and 45 %. Monotonically increasing trends indicate applicability of our ML approach to disparate process variability. (b), Overall prediction accuracy as a function of process variability when all training instances are utilized. Error bars represent one standard deviation of uncertainty.

5.5.3 Using ML prediction in disrupted AM processes with larger variability

To experimentally mimic larger process variabilities, we integrated a gray-mask technique (Figure 5-23a) into the projection stereolithography system. The grayscale distribution for each digital

mask was modulated to introduce non-uniformity in each layer and therefore realize larger geometric variations and defect levels. The gray-mask was formed by modulating the grayscale of each pixel with a random value in percentage. The range of these random percentages was determined by the target process variability. For instance, to replicate the property variability η of 35% (resembling SLS process), the range of the percentage is bounded between 20 and 90% (two representative gray masks shown in Figure 5-23b). Once the gray-masks were applied to all slices, the manipulated slices were utilized for printing.

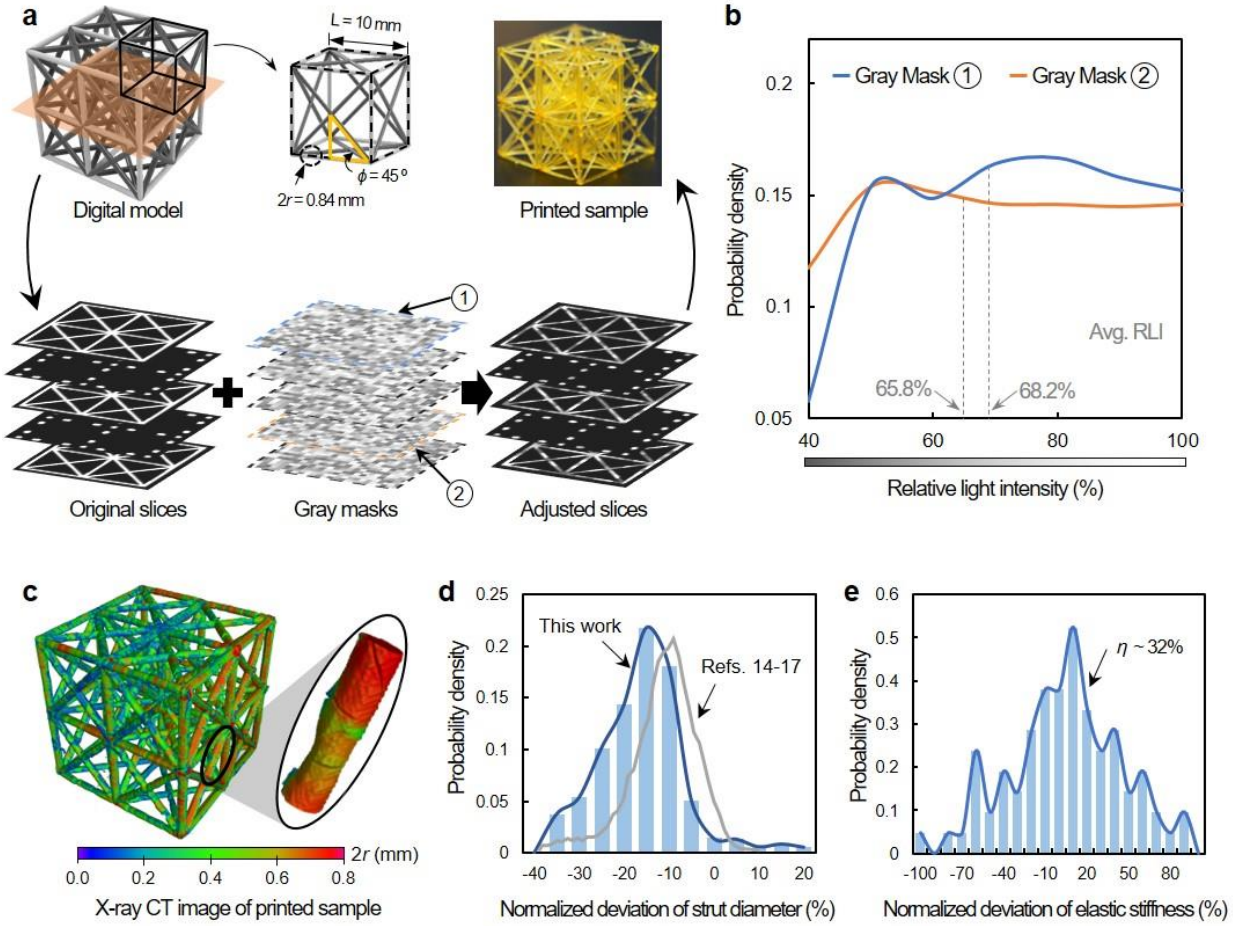

Figure 5-23. Gray-mask technique and measurement of geometric and process variability in the printed sample. (a), Schematic of gray-mask technique process allowing tuning of process variability. Intensity of white pixels in each slice from a digital model was stochastically varied to replicate geometric variation. (b), Two representative gray masks applied to 2D sliced images

shown in a. (c), A representative X-ray image of the printed sample used to analyze a variation in strut diameter. A magnified view of a representative strut in the printed sample is shown to highlight the effects of process variability. (d), Comparison of probability distributions of the normalized deviation of strut diameter between samples printed with the gray mask technique and data from the previous study[88-91]. (e), Percentage deviation of the measured elastic moduli with respect to the nominal value, confirming the measured process variability (η) of ~32 % in line with that found in literature[88-91].

The results from X-ray tomographic measurements on printed samples using the varied gray-mask technique are shown in Figure 5-23c. Both distributions of deviation in the strut diameter and the measured process variability in terms of the elastic stiffness agree well with those reported in prior studies[88-91] (the measured variability of ~32% vs. the reported variability of 35%) (Figure 5-23c and 5-23d).

The effect of a representative larger process variability (η = 35%) on the curve recreating is examined here. A representative target stress-strain curve displaying linear-elastic response followed by elastic instability was fed into the ML pipeline. A total of ten samples representing the output design was fabricated using the developed gray-mask technique, and their cyclic compressive responses were measured and recorded as shown in Figure 5-24. The light-blue shaded region is an envelope covered by all tested stress-strain curves from the same printed design with the 35% process variability (i.e., η = 35%). For a comparison, the same target curve was inversely designed based on the process variability of the stereolithography process (η_{SLA} = 13%) used in this study (dark-blue colored uncertainty region in Figure 5-24). The results show that larger process variability introduces higher deviation from the tested stress strain curves and that our ML approach is sensitive to the process variability but still capable of re-creating the target curve with reasonable accuracy.

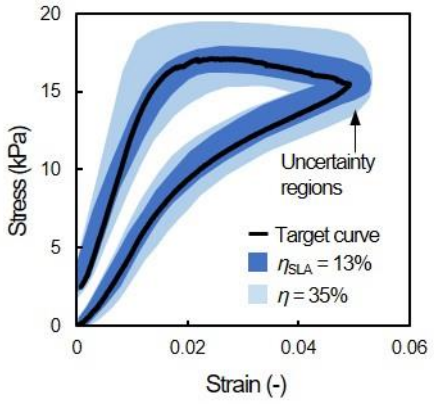

Figure 5-24. Inversely designed, representative target stress-strain curve η = 35% (resembling the process variability of selective laser sintering process) and the gray-mask technique (light-blue shaded uncertainty region). For a comparison, the same target curve inversely designed based on the process variability of the stereolithography process (η_{SLA} = 13%) used in this study (dark-blue shaded uncertainty region).

5.6 Tailorability of stress-strain curve with ML

Architected materials that meet multiple target properties could be inversely designed via graphically tailoring curve features of a target stress–strain curve, for example by adjusting stiffness, peak stress, compressibility, and/or nonlinear response (Figure 5-25a). To demonstrate tailorability of our design process, we inversely designed an architected shoe midsole by graphically tailoring stress–strain curves measured from a commercial midsole (i.e., baseline curves) for enhanced running performance. The midsole was partitioned into four sections upon different levels of loads during heel-toe running[35], and the target stress-strain curve for each section was created by tailoring a baseline curve for the purpose of maximizing running propulsion and cushioning (Figure 5-25b and 5-25c; the measured baseline curves shown in Figure 5-26). The

tailored midsole consists of a stiff but comfortable toe section, firmer and higher propulsion forefoot section, and stiffer yet energy dissipative heel section. Moreover, the target curves were scaled according to the scaling relationship of the base material (TMPTA) between strain rate and its mechanical properties so that dynamic responses in running scenario can be inversely designed using quasistatic training data (the detailed inverse design of non-quasistatic strain rates illustrated in Figure 5-27a to 5-27d). The as-fabricated midsole sample with optimal design parameters for each section is shown in Fig. 4c (the predicted design parameters in Figure 5-27e). The results revealed excellent agreement (>90% average prediction accuracy) between the experimentally tested curves and target curves of each tailored section (Figure 5-25d; their cyclic responses shown in Figure5-27f), indicating that the ML pipeline is capable of creating materials satisfying multiple tailored mechanical responses under different loading conditions.

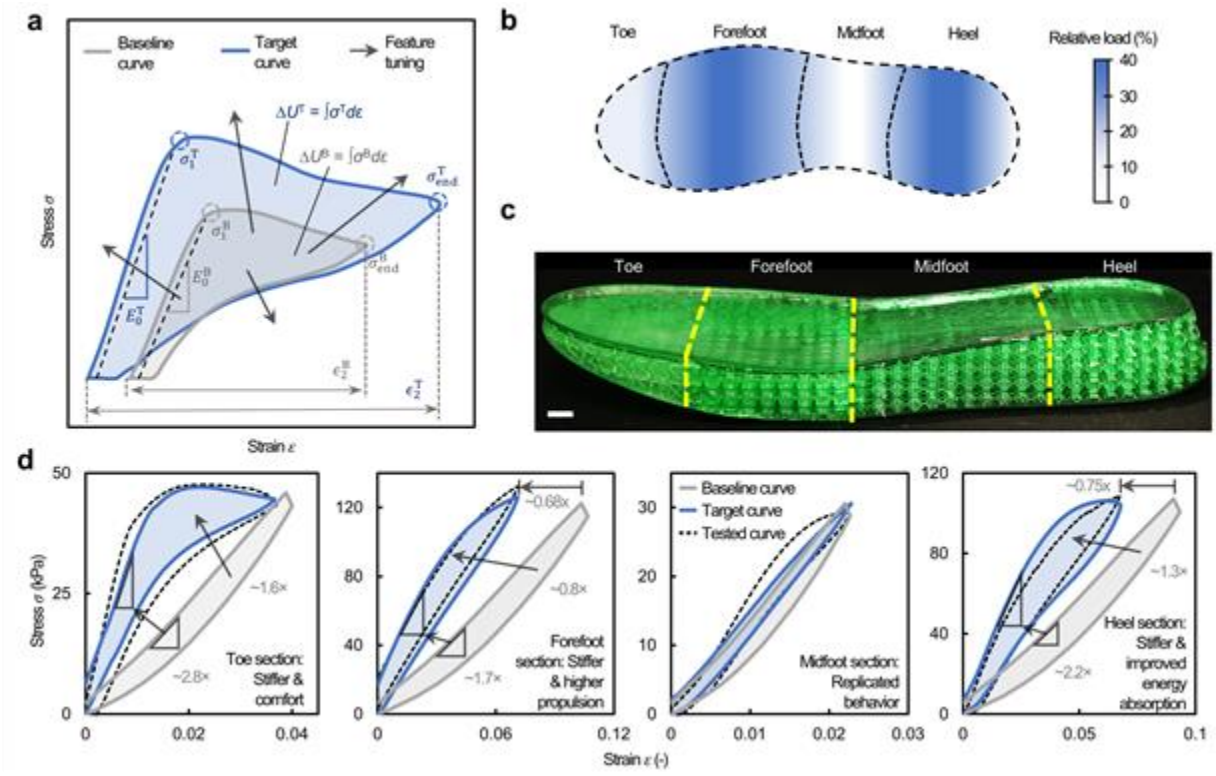

Figure 5-25. Tailorability of stress–strain curves demonstrated by inverse design of an architected shoe midsole. (a), A schematic of the tailoring process to improve the energy absorption behavior. (b), Relative load distribution of the midsole during running[32]. (c), A photograph of the ML-designed architected midsole sample, where each section was designed to exhibit disparate target behaviors. The scale bar is 10 mm. (d), Target and measured stress–strain curves of the architected shoe midsole sample. The baseline response of the commercial midsole (gray curves) for each section was tailored to achieve a specific design target aiming at an improved running performance (blue curves). The tailored curves were then fed into our ML pipeline to obtain optimal designs for each design target, from which the predicted designs were verified via experiments (black dotted curves).

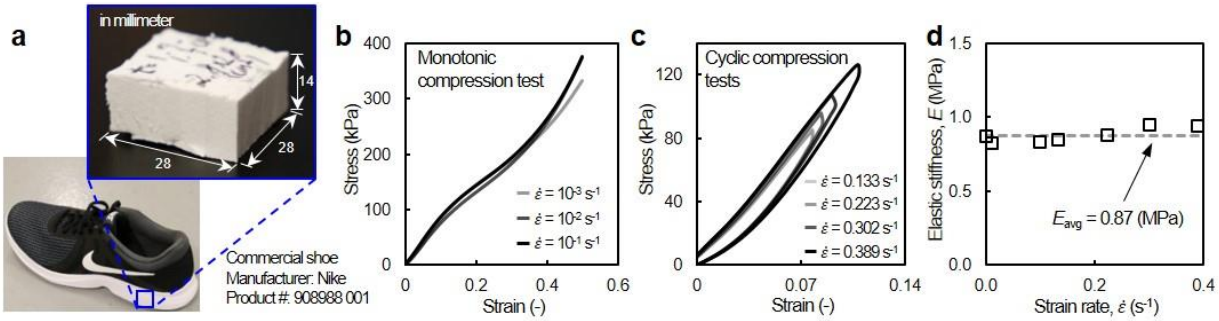

Figure 5-26. Measurement of baseline curves from a commercial shoe midsole. (a), Trimmed sample from the commercial shoe midsole. (b)-(d), Measured responses of the trimmed sample for a range of strain rates.

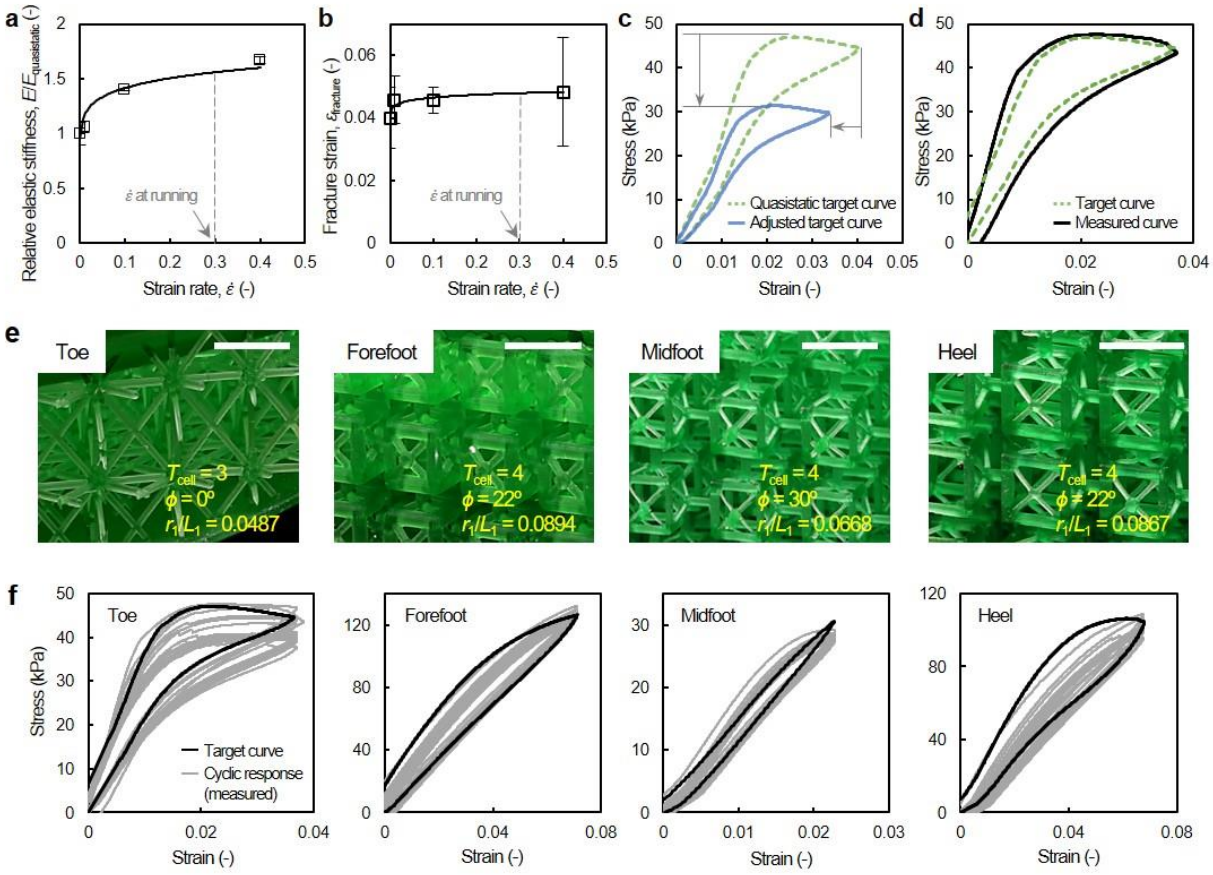

Figure 5-27. Inverse design of the architected shoe midsole with strain rate effect. (a)-(b), Rate dependency of bulk TMPTA on its material properties (i.e., $E/E_{\text{quasistatic}}$ versus $\dot{\varepsilon}$ and $\varepsilon_{\text{fracture}}$ versus $\dot{\varepsilon}$). Error bars represent one standard deviation of uncertainty. (c), A representative target curve (i.e., toe section) adjusted for a higher strain rate (i.e., $\dot{\varepsilon} = 0.3\text{s}^{-1}$) using scaling relations in rate dependency of TMPTA in a and b. (d), Measured curve of an inversely designed toe section at $\dot{\varepsilon} = 0.3\text{s}^{-1}$ (black curve) compared to the (green dotted) original target curve. (e), Spatially tailored sections of the inversely designed architected shoe midsole. The predicted design parameters for each section are also listed. A scale bar is 10 mm. (f), Measured cyclic response of the inversely designed midsole with many cycles ($N_{\text{cycle}} = 20$) at strain rate of 0.3s^{-1}.

5.7 Enhanced tailorability via compound lattices

The inverse design of architected materials can be further expanded to include advanced curve features that do not exist in natural materials, such as variable tangent modulus, controllable

softening/hardening effects, and multiple peaks and valleys. These curve features offer improved crushing behavior and energy absorption performance and could be realized by inversely designing compound lattices (non-uniform lattice comprised of design parameters varying by location) with tailorable mechanical behaviors that go beyond mechanical responses from uniform lattices (lattice materials comprised of identical unit cells throughout the lattice) (see Figure 5-28). Hence, we created a training dataset containing compound lattices made of a flexible polymeric base material via FE simulations. Instead of being represented by uniform design parameters, these compound lattices were described by variation of design parameters (topology gradients) within a confined lattice volume, such as the unit cell type (G_1), strut aspect ratio (G_2), inclined strut diameter (G_3), and cell size (G_4) gradients. Additionally, to adopt the structure of the gradient labels, we employed a sequential integrated strategy for the inverse design process (Figure 5-29).

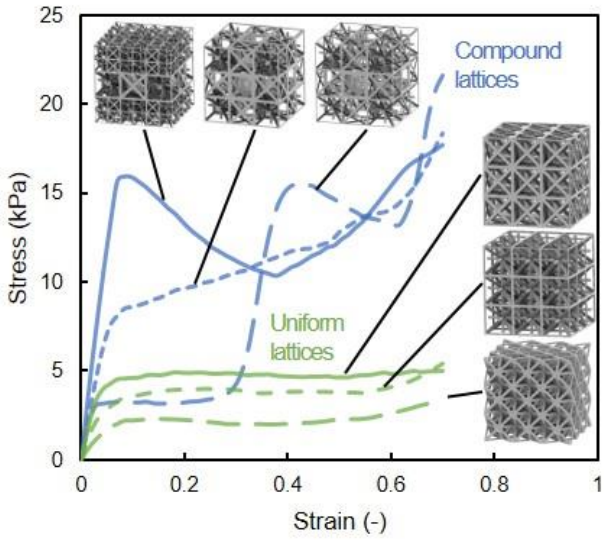

Figure 5-28. Capability of the compound lattices. Comparison of stress-strain curve tailorability between the compound lattices created with superposed design gradients and the uniform lattices is shown.

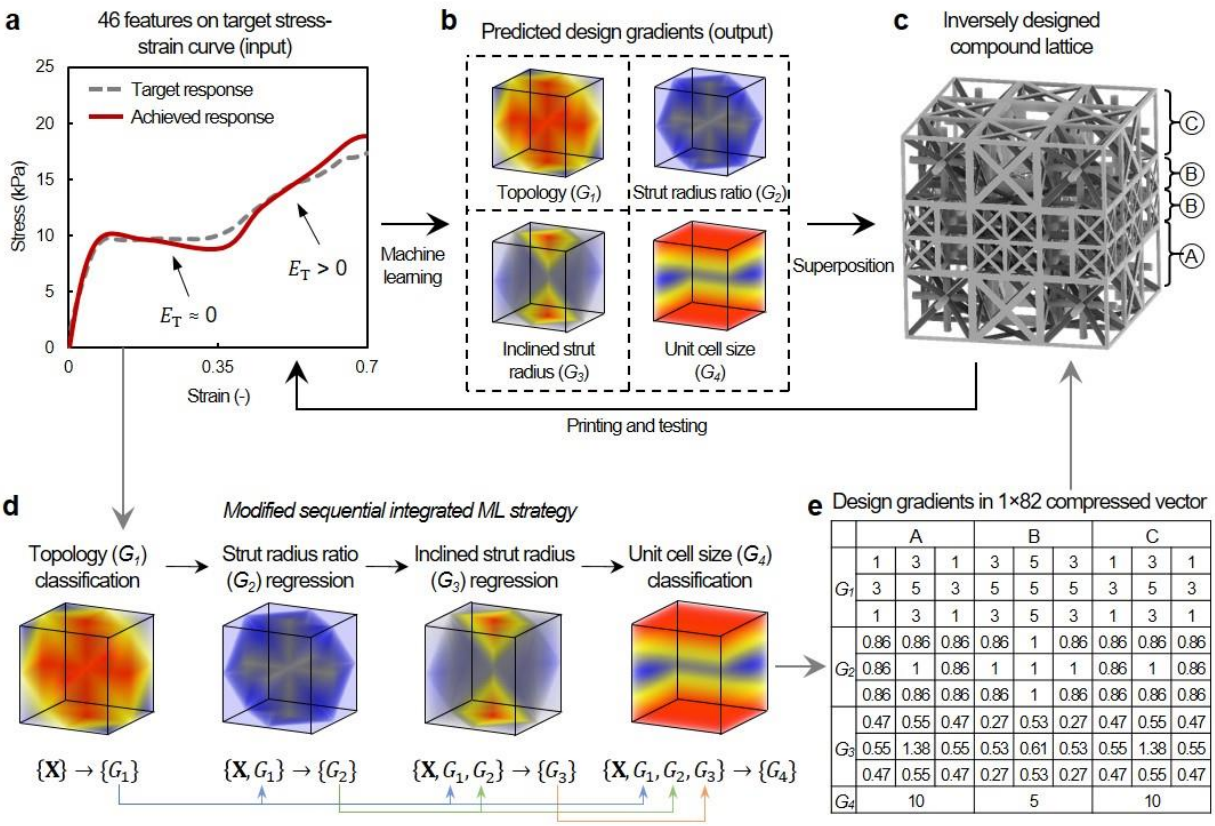

	A			B			C		
G_1	1	3	1	3	5	3	1	3	1
	3	5	3	5	5	5	3	5	3
	1	3	1	3	5	3	1	3	1
G_2	0.86	0.86	0.86	0.86	1	0.86	0.86	0.86	0.86
	0.86	1	0.86	1	1	1	0.86	1	0.86
	0.86	0.86	0.86	0.86	1	0.86	0.86	0.86	0.86
G_3	0.47	0.55	0.47	0.27	0.53	0.27	0.47	0.55	0.47
	0.55	1.38	0.55	0.53	0.61	0.53	0.55	1.38	0.55
	0.47	0.55	0.47	0.27	0.53	0.27	0.47	0.55	0.47
G_4	10			5			10		

Figure 5-29. Inverse design workflow of a compound lattice creation for enhanced stress-strain curve tailorability. (a), Target stress-strain curve digitized with 46 feature points. (b), Four design gradients: namely, the unit cell topology-, the strut radius ratio-, the inclined strut radius-, and the unit cell size-design gradients (G_1, G_2, G_3, G_4). (c), Inversely designed compound lattice with superposed design gradients. (d), Modified sequential integrated ML strategy for inverse design of compound lattices. (e), The predicted design gradients represented in 1×82 compressed vector.

To showcase inverse design of advanced curve features discussed earlier, we fed three sets of stress-strain curves into our revised ML pipeline separately, where each case focuses on separately tailoring tangent modulus, first peak stress, and second peak stress (Figure 5-30a to 5-30c). The corresponding inversely designed 3D digital models describing compound lattices and the spreads of their gradient labels describing the variation of the gradient labels within the lattice in terms of the coefficient of variance are also presented in this figure. The ML-predicted results revealed that

manipulating pairs of gradient labels independently modulate advanced curve features, including multiple peak stresses and signs of the tangent modulus. This enables fine control of a variety of sectioned stress–strain curves (Figure 5-30a to 5-30c) not seen with uniform lattices. For example, in the case of tuning tangent modulus (Figure 5-30a), we noticed negligible variation in unit cell and strut radius ratio gradients (G_1 and G_2), indicating the sign of the tangent modulus is mainly controlled by a combination of the inclined strut radius and unit cell size gradients (G_3 and G_4). Similarly, G_1 and G_2 together modulated the first peak stress (Figure 5-30b). Additionally, in the case of tuning second peak stress (Fig. 5c), significant variation in G_2 was observed while the other three gradients almost remained the same, indicating G_2 were mainly responsible for the second peak stress manipulation.

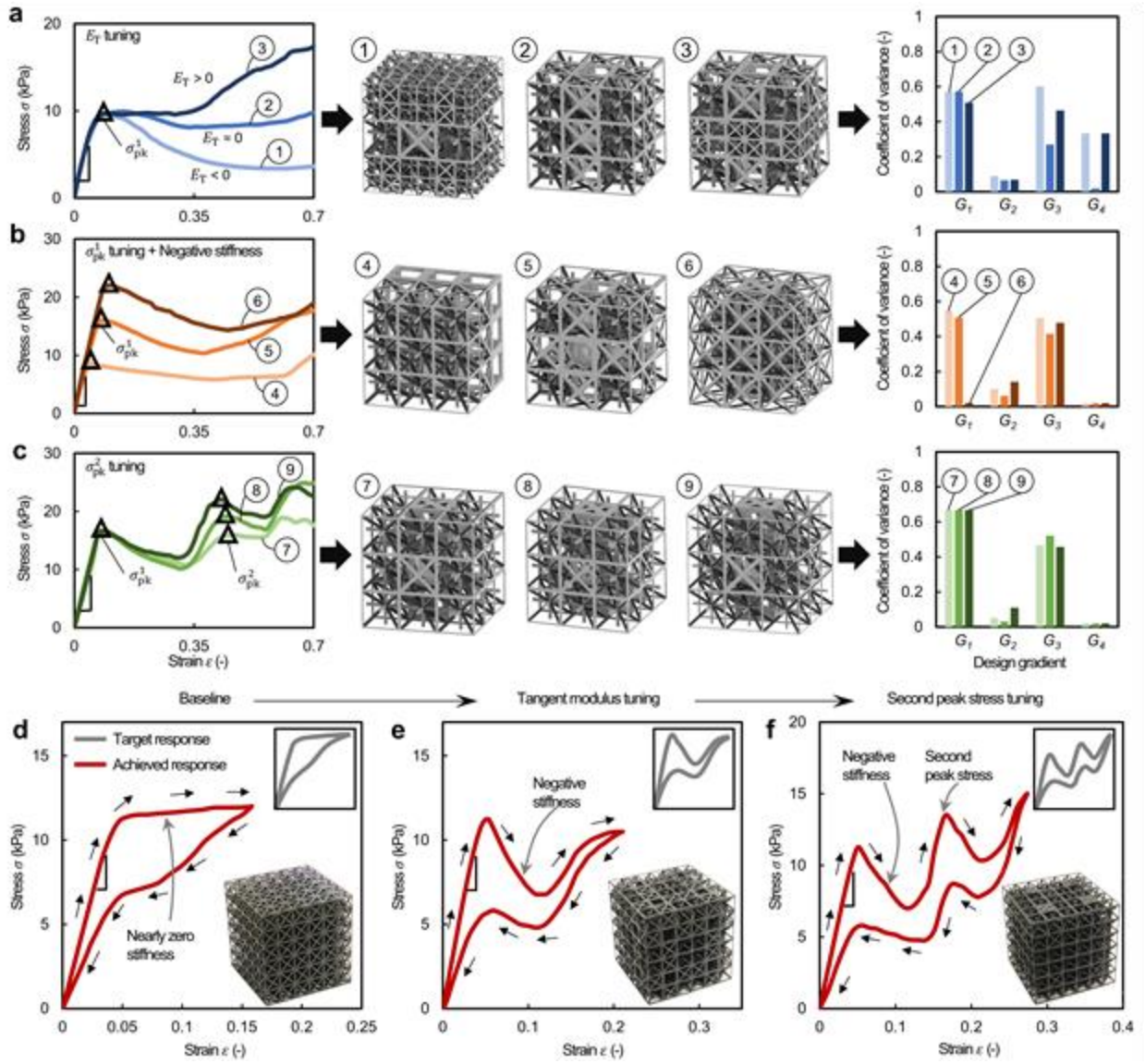

Figure 5-30. Enhanced stress–strain curve tailorability through compound lattice creations using superposed design gradients. (a)-(c) Three sets of target stress–strain curves, in which the set of curves 1-3 represents the tailorability of the tangent modulus (E_T), the set of curves 4-6 represents the tailorability of the first peak stress σ1 pk and subsequent negative stiffness, and the set of curves 7-9 represents the tailorability of the second peak stress (σ2 pk). Insets show 3D digital models representing compound lattices inversely designed by the ML-predicted design gradients (G_1: unit cell gradient, G_2: strut radius ratio gradient, G_3: inclined strut radius gradient, G_4: unit cell size gradient) for the target curves, and their coefficients of variance characterizing the spread of the corresponding design gradients are also shown. (d)-(f) Experimental demonstration of tailored stress–strain hysteresis loops displaying deformations at different strains. The stress–strain hysteresis loop in (d) was tailored to exhibit negative stiffness in (e) and further tailored to exhibit multiple stress peaks in (f). The target curves and photographs of the as-fabricated, ML-designed compound lattices are shown in the insets.

Next, we experimentally validated the efficacy of our approach via inversely designing three stress-strain curves which feature different numbers of stress peak and valley events as well as a controlled tangent modulus. These target curves can be found in the insets of Figure 5-30d to 5-30f, and the primary graphs show the recreated stress–strain curves of the predicted designs (Figure 5-31). For the target curve with a nearly zero tangent modulus (the inset of Figure 5-30d), the predicted gradient labels indicated minimal variation, and homogeneous deformation of a designed compound lattice was observed. The target curve in the inset of Figure 5-30d was then tailored to exhibit a negative tangent modulus after the first peak (the inset of Figure 5-30e). The measured mechanical behavior shown in Fig. 5e revealed the localized nonaffine deformation (see Figure 5-31) and corroborated the role of the gradient labels discussed earlier; the first peak stress was dominated by G_1 and G_2, followed by a subsequent shifting/snapping event with a negative tangent modulus controlled by G_3 and G_4 The target curve shown in the inset of Fig. 5e was further tailored to contain a second peak stress (the inset of Figure 5-30f), while keeping all preceding curve features. The predicted gradient labels included a change in G_2 (~50%) substantially different from that of the former lattice shown in Figure 5-30e, confirming the role of this gradient in peak stress manipulation (nonaffine deformation shown in Figure 5-31).

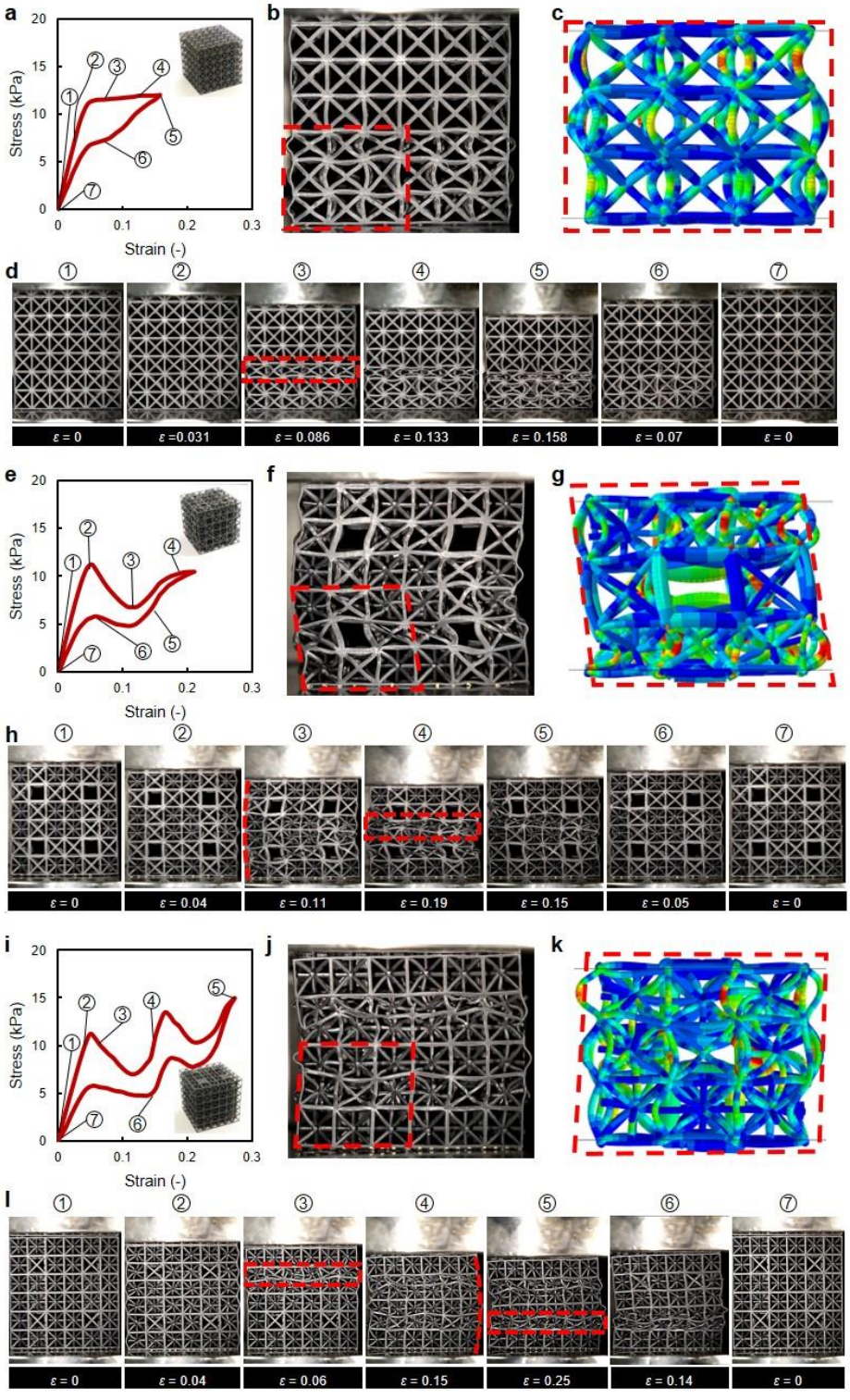

Figure 5-31. Experimentally measured stress-strain curves of ML-designed compound lattices shown in Figure 5-30d to 5-30f and progression of deformation at different strains of the printed samples. (a)-(d), Sample 1 shown in Figure 5-30d. (e)-(h), Sample 2 shown in Figure 5-30e. (i)-

(l), Sample 3 shown in Fig. 5f. FE simulations for each lattice were performed and showed good agreements in deformation observed in experiment.

These advanced, inversely designed stress–strain curves featuring successive peak stresses and coordinated collapse mechanisms together with tailored softening effects make the inversely designed compound lattice shown in Figure 5-30f an excellent candidate for ML-designed custom padding materials for energy absorption. To test its energy absorption performance, drop tests were conducted on the sample (Figure 5-32a), showcasing that the measured acceleration and potential energy due to impact were reduced by ~30% and ~25%, respectively, as a result of the compound lattice (Figure 5-32b and 5-32c). In the normalized energy absorption vs. transmitted strength property map ($(U/E_s)/\bar{\rho}$ vs. $(\sigma_{tr}/\sigma_{ys})/\bar{\rho}$), this compound lattice shows energy absorbing performance outperforming that of previously reported lattice materials[36-42] (Figure 5-32d).

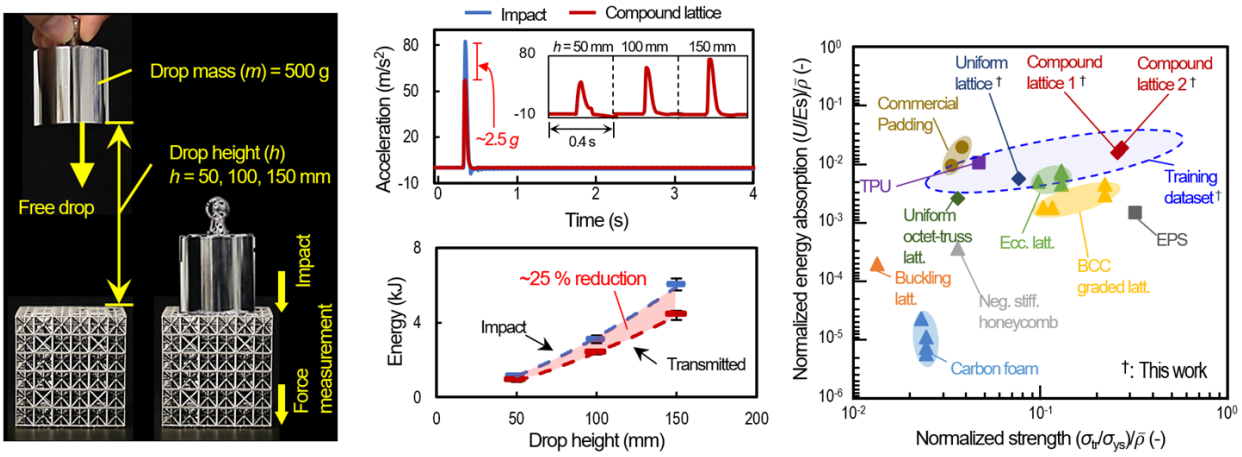

Figure 5-32. Energy absorption characteristics of the ML-designed compound lattice. (a), Drop test setup with different heights on the as-fabricated compound lattice shown in Figure 5-30f. (b), Acceleration-vs-time curve of the compound lattice with the dead weight dropped from h = 150 mm, revealing a reduced peak acceleration (~2.5g). An inset displays acceleration-vs-time curves of the compound lattice with different drop heights of h = 50, 100, 150 mm. (c), Potential energy

recorded from the force transducer for the compound lattice with different drop heights. The error bars indicate standard deviations from multiple ($N > 3$) measurements. A significant gap (shaded area) indicates energy absorption capability of the ML-designed compound lattice as a potential padding material. (d), A normalized energy absorption-transmitted strength pair (i.e., $(U/E_s)/\bar{\rho}$ vs. $(\sigma_{tr}/\sigma_{ys})/\bar{\rho}$) of the ML-designed compound lattices compared with the state-of-the-art energy absorbing materials[37-43] as well as uniform lattices.

5.8 Simultaneous design of mechanical responses under multiple loading rates with ML

5.8.1 Development of the ML framework for the design task

In this design task, we developed the integrated machine learning model with sequential prediction strategy as shown in Figure 5-33. Given the target mechanical properties, the inverse model outputs design parameters of the lattice via two-stage prediction process. These predicted parameters are then passed to a set of forward models for the evaluation of corresponding mechanical properties of inversely designed lattice structure

The input data {X} for inverse model consists of 16 critical mechanical properties for both loading cases (i.e., peak stress & strain energy density in Figure 5-33a). The output data {Y} consists of lattice cell type $\{Y_1\}$ and material index $\{Y_2\}$ in upper and low section of the bumper, respectively. The inverse model first takes the mechanical properties {X} as the input to predict the cell types of the lattice $\{Y_1\}$. The predicted cell type $\{Y_1\}$, along with the input mechanical properties {X}, forms the new input for the evaluation of material combination $\{Y_2\}$ in the lattice structure (Figure 5-33a).

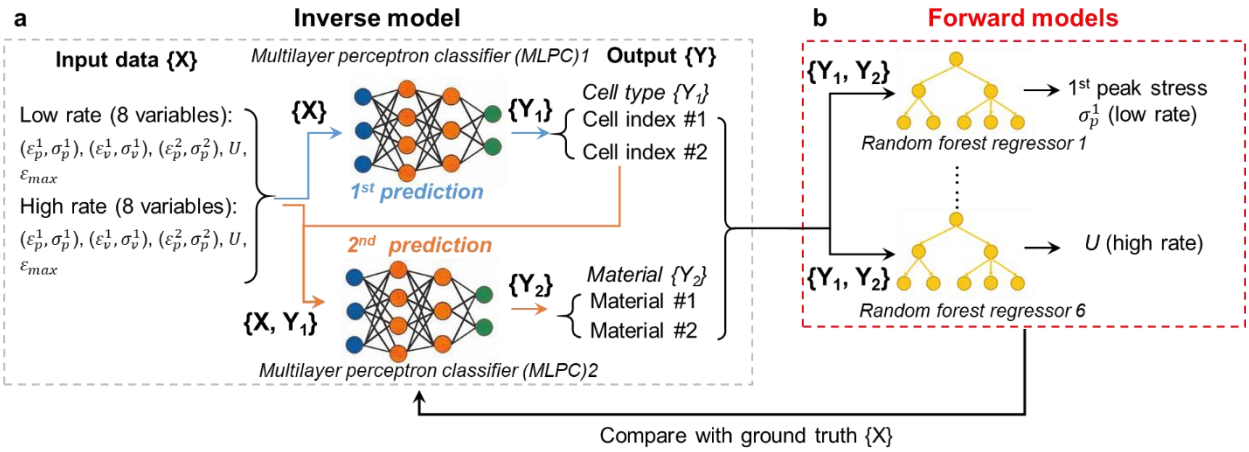

Figure 5-33. Workflow of the integrated machine learning model. (a) The inverse model takes 16 mechanical properties as the input and predict the design parameters of the lattice in a sequential manner. (b) The forward models evaluate the mechanical properties of the designed lattice.

The design parameters {Y} ({Y_1, Y_2}) are then passed to 6 forward models (Figure 5-33b). Each model estimates a single mechanical property of the design lattice (1st peak stresses, 2nd peak stress, and strain energy density for each loading-rate case). These predicted mechanical properties are the compared with the target properties to evaluate the prediction accuracy of the inversely designed lattice structure.

5.8.2 Architectural cell design and material properties for the training dataset

Herein, we proposed the architectural genes for the machine learning design framework, which consist of 7 different unit cells (Figure 5-34b). These unit cells are generated via evolution of the incline angle θ in a quarter of representative area volume, as shown in Figure 5-34a. Tuning the angle θ not only manipulates competitions between tensile and compressive load-bearing strut members, nodal connectivity, but also enables each architectural configuration to be registered with its own respective stress-strain curve paths, describing linear elasticity, yielding, nonlinearity,

tangent modulus, hardening/softening. Then we performed the numerical simulation to investigate the mechanical properties of architectural genes.

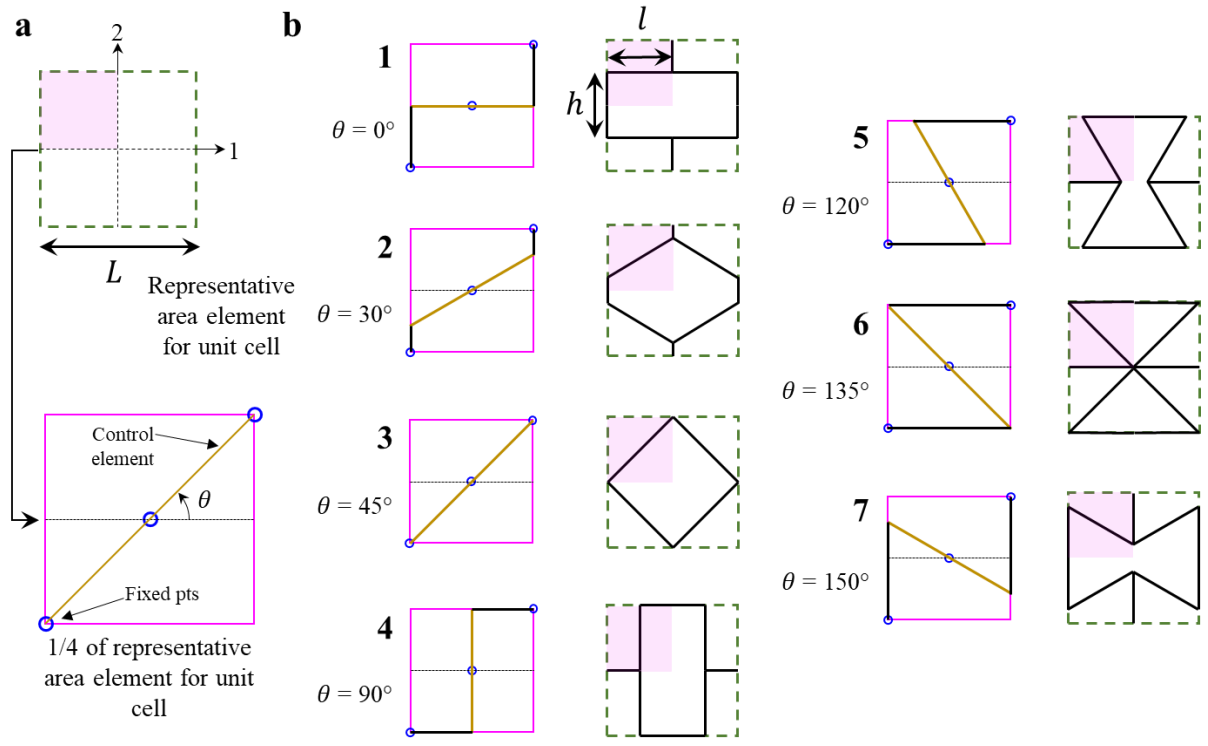

Figure 5-34. Transformative architectural genes. (a) Evolution of incline angle θ in the representative area element. (b) 7 architectural genes in the training data set.

Figure 5-35 presents the FEA model (3x2 lattice) used to evaluate the mechanical response of the genes and Figure 5-35b show the corresponding stress-strain curves under low loading-rate case. Here, we summarized the evolution of elastic modulus and peak stress against the incline angle θ (Figure 5-35c). The elastic modulus E and peak stress σ_p increase along with the incline angle θ with the range of $0° < \theta < 90°$ and reach the maximum value simultaneously at $\theta = 90°$ (gene 4). This result matches with previous literature: $\frac{E}{E_S} = \left(\frac{t}{l}\right)^3 \frac{\left(\frac{h}{l}+sin\theta\right)}{\cos^3\theta}$; $\frac{\sigma_p}{E_S} = \frac{\pi^2}{6}\frac{t^3}{lh^2}\frac{1}{cos\theta}$, where cell

wall thickness $t = 3.8mm$ and E_S is the elastic modulus of the constituent material. Then we formulated the design map (Figure 5-35d) of the uniform lattices using the peak stress and volumetric energy absorption (strain energy density) as critical properties, where strain energy density is the area enclosed by the stress-strain curve. As shown in the design map, gene 4 demonstrates highest peak stress among all the architectural genes, and gene 7 shows best volumetric energy absorption. The design map helps us to analyze the mechanical properties of when different architectural genes are mixed in the lattice structure.

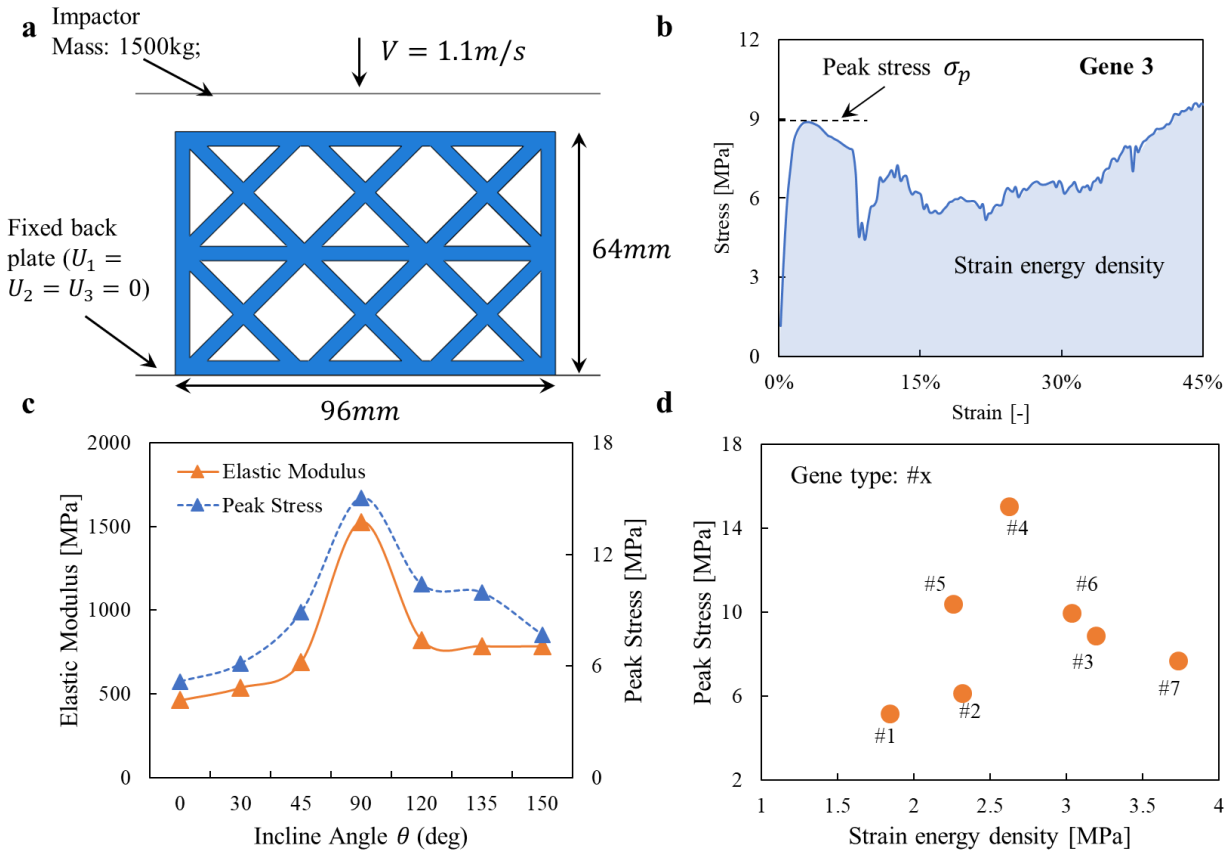

Figure 5-35. Mechanical properties of the architectural genes. (a) FEA model for the preliminary numerical analysis. (b) Representative stress-strain curve and critical mechanical properties under low loading-rate case. (c) Evolution of elastic modulus and peak stress along with incline angle θ. (d) Design map of architectural genes.

The materials used to develop the training dataset are the blends of CFABS with TPU, a sets of filament can be readily extruded 3D printer facilities. We introduced various materials in the design via changing the blending ratio between two constituent materials: CFABS & TPU. In total, we had five blending ratios available: (0 CFABS – 100% TPU, 25% CFABS – 75% TPU, 50% CFABS – 50% TPU, 75% CFABS – 25% TPU, 100% CFABS – 0 TPU). The elastic modulus and yield strength of these five materials is plotted in Figure 5-36.

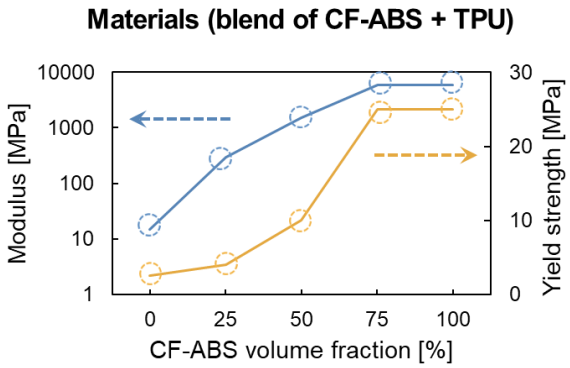

Figure 5-36. Material properties of 5 available material in this task. The base materials are the blend of CF-ABS and TPU filament with different volume fraction ratios.

Herein, we developed the training dataset by numerical simulation on the mechanical responses of lattice structure, which consists of different architectural cells and constitutive materials. In specific, a representative volume element (RVE) is used with periodic boundary conditions enforced in the numerical analysis to simulate the mechanical responses of large-scale lattice with low cost of computational resources. Two cell types (one for region 1 and the other one for region 2&3) and two materials (one for region 1&2 and the other for region 3) were picked to form the RVE in the numerical model. The stress-strain curves of the RVE under two loading-rate cases were simulated and combined with the design parameters (architectural cell type and material

index) of the metamaterial as the pristine training dataset. The pristine training dataset was formed via combining the design parameters of compound lattices {Y} ({Y_1, Y_2}) with their simulated mechanical properties of both loading rates {X}, leading to 123 {X}-{Y} pairs in the dataset. Herein, as the forward models performs "many-to-one" mapping, we carried out data augmentation on these pairs to account for prediction fluctuation and achieved satisfactory prediction accuracy (i.e., >90% accuracy), resulting in 1230 {X}-{Y} pairs in the augmented dataset.

5.8.3 Training of the ML framework

For training of the machine learning framework, we first trained 6 individual forward models with the augmented dataset. The forward models were implemented using Gradient Boosting regressor (GBR) and Random Forest regressor (RFR) in open-source package (scikit-learn). Each forward model is trained with 70% of the augmented dataset and then tested with the other 30% of the dataset (not used in training process). The hyperparameters of the forward models were optimized Scikit-learn's GridSearchCV function for maximum testing score. We observed over 90% prediction accuracy for all forward models as shown in Figure 5-37. These results validate that the forward models effectively act as a surrogate model that replaces the conventional simulations used to evaluate the responses of a lattice design.

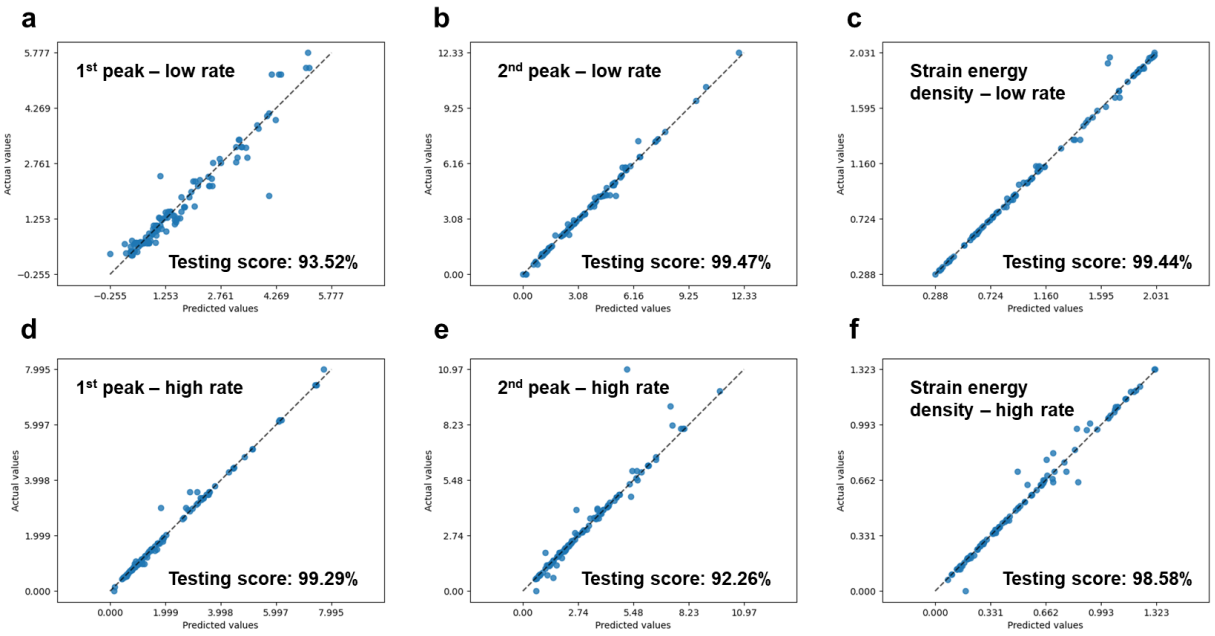

Figure 5-37. Prediction accuracy of forward models. (a)-(c) Testing accuracy of 1st peak, 2nd peak, and strain energy density for low loading-rate case. (d)-(f) Testing accuracy of 1st peak, 2nd peak, and strain energy density for high loading-rate case.

Once the forward models were trained, these models were kept frozen (i.e., the hyperparameters of all forward models were fixed) and were then used to train the inverse model with the pristine training dataset. The inverse model was implemented using Multilayer Perceptron Classifier (MLPC) in open-source package (scikit-learn). Due to the low number of data points in the pristine dataset, we used 10% of the pristine dataset as the testing set (not used in training) for the evaluation of the prediction accuracy. In this training process, the prediction accuracy of all mechanical properties, outputted from the forward models, was used to optimize the hyperparameters of the inverse model. This training strategy of the inverse model prevents any instability during training, which could otherwise cause {Y} to become a meaningless latent space variable. The testing accuracy of the inverse model is shown in Figure 5-38. As shown in the

Figure 5-38, we have achieved over 80% prediction accuracy for most mechanical properties of the lattice design from inverse model. In the next phase of the project, we will expand the training dataset, via introducing additional cells in the compound lattice design, to further improve the prediction performance of the machine learning framework. As more data is generated and included in the training set, the prediction accuracy of the inverse model will be further increased and reach satisfactory level (i.e., >90% for all mechanical properties). The integrated machine learning framework, along with the expanded training dataset, will achieve the lattice design satisfying the design requirements of the bumper.

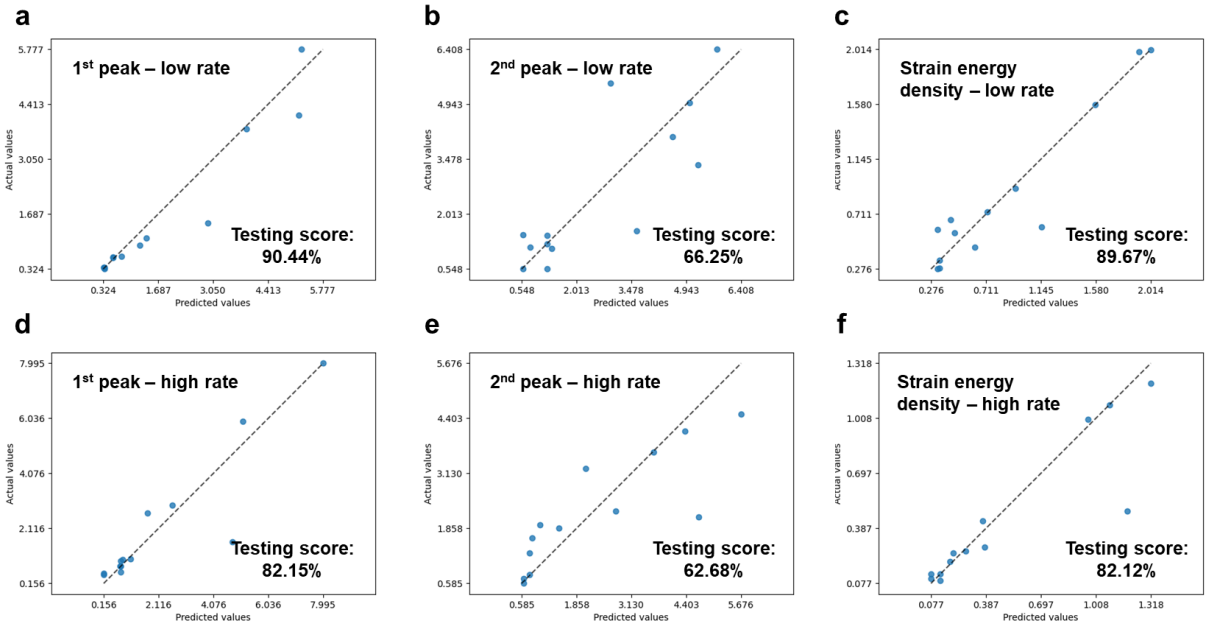

Figure 5-38. Prediction accuracy of inverse model. (a)-(c) Testing accuracy of 1st peak, 2nd peak, and strain energy density for low loading-rate case. (d)-(f) Testing accuracy of 1st peak, 2nd peak, and strain energy density for high loading-rate case.

5.8.4 Inverse design of the architected structures with desired responses at different loading rates

The inverse design of architected structures with desired responses at different loading rates starts with the formulation of the property design spaces of each rate case (Figure 5-39). Each design map present the property pair, peak stress and strain energy density, of each designed structure in the training dataset. The property pairs of all structures in the training dataset forms the design map of each loading rate case.

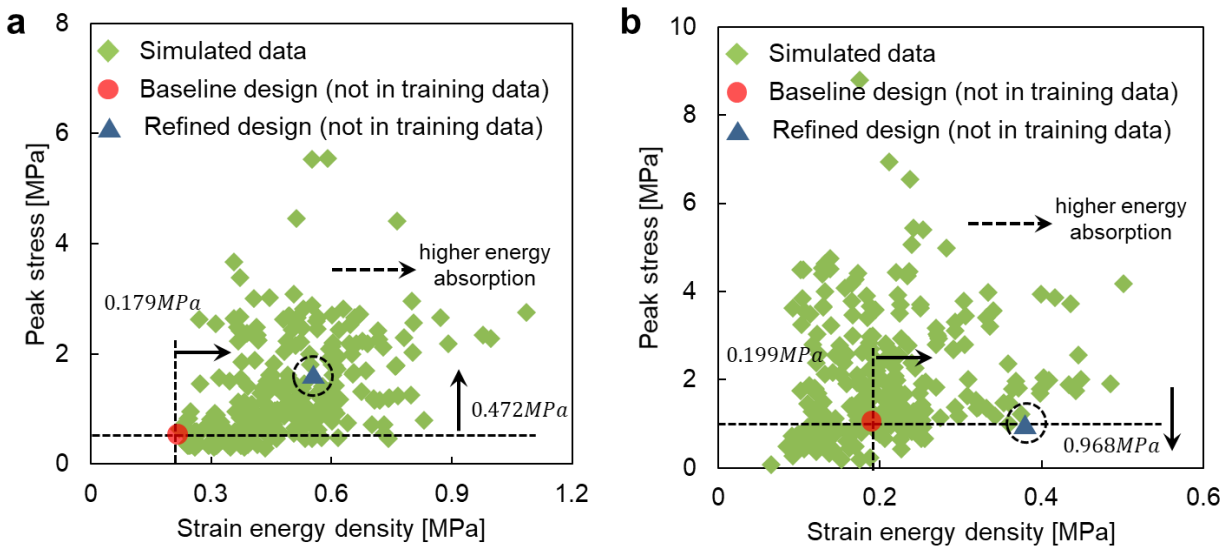

Figure 5-39. Mechanical property maps for each loading rate cases. (a) Design map for property pair: peak stress and strain energy density of low loading rate case. (b) Design map for property pair: peak stress and strain energy density of high loading rate case.

Once the property design map is obtained, the critical value of corresponding properties is labeled. Next step of the inverse design is to select target property pairs in the design map. The cross-section point of two critical property value denotes the baseline structure design that just satisfies

the design requirement. By shifting the property pair point towards the allowable area, property value corresponding to refined design is picked. The picked property pairs are used to tailor the baseline stress-strain curve of each loading rate case, and the tailored curve is parameterized to extract full set of input feature of the ML ({X}). With the input of processed stress-strain curve features, the ML predicts the corresponding design parameters of architected structure ({Y}). The mechanical responses of re-constructed structure design under both loading rate cases are simulated and compared with input curve features for the evaluation of the prediction accuracy. Figure 5-40 presents the comparison between predicted and target mechanical properties at different loading rate cases. The comparison results shows that the trained ML framework is capable of creating the design satisfying the target mechanical properties in both loading rate cases simultaneously.

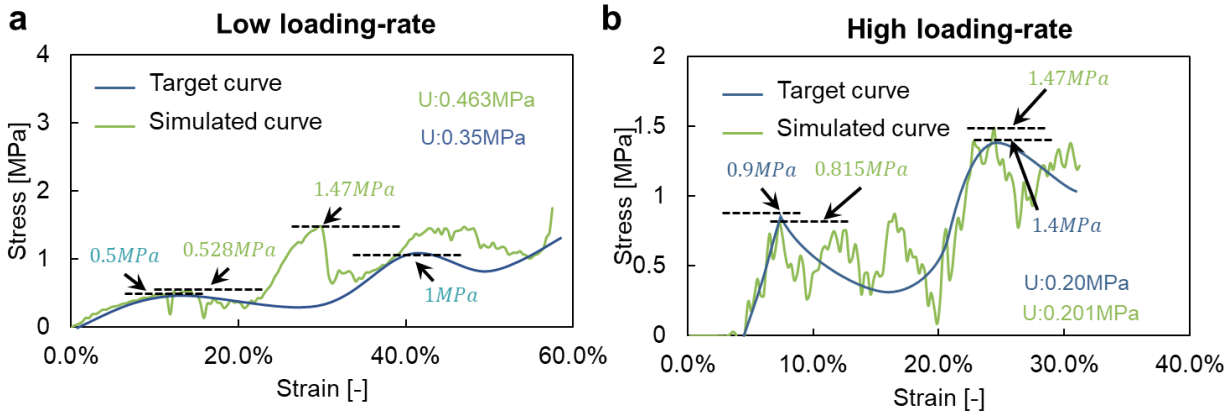

Figure 5-40. Comparison between predicted and target mechanical properties at different loading rate cases.

Next, we evaluated the prediction performance of ML framework in exploration of tailored mechanical responses. Herein, we picked another set of property pairs, denoting higher energy

absorption performance, in both design maps. Following the same prediction process, the refined design is predicted and the corresponding responses is evaluated with simulation. Figure 5-41 demonstrates the comparison between the mechanical responses of baseline and refined design under both low and high loading rate cases. The simulation results indicate that a higher energy absorption performance is obtained from refined design for both rate cases. These results validates the prediction capabilities of developed ML in creating the mechanical responses at different loading rate simultaneously.

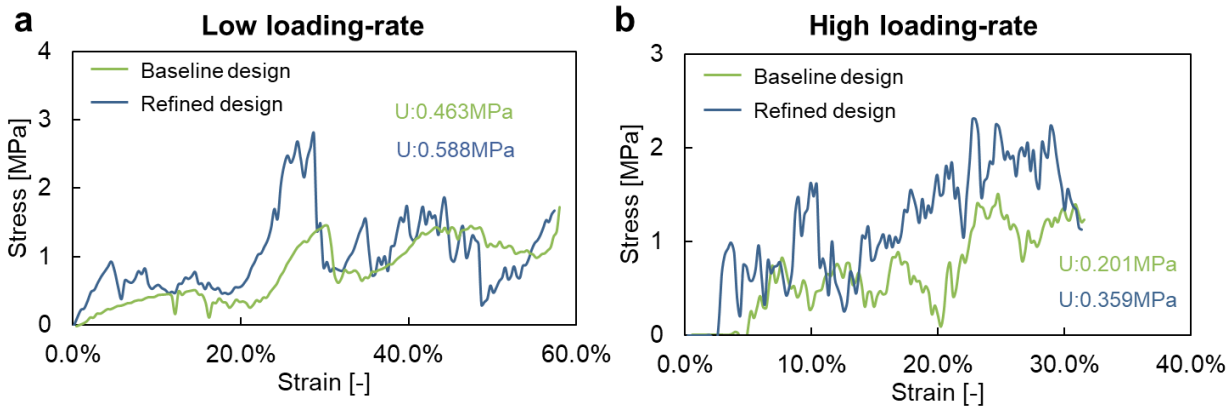

Figure 5-41. Comparison between mechanical properties of baseline and refined design at different loading rate cases.

5.9 Conclusion

This chapter presents a ML-based rapid inverse design methodology to recreate and tailor mechanical behavior based on stress–strain curves. Our generative ML strategy is capable of mimicking nearly all possible uniaxial compressive stress–strain curves of architected materials, including linear elasticity, strain softening/hardening, tunable tangent modulus, yielding, fracture, tailorable stress peaks and valleys, and energy absorption, while accounting for existing 3D

process defects, resolutions and uncertainty. We demonstrated the inverse design of the architected shoe midsole with tunable dynamic performance with spatially tailored sections described by specific stress–strain responses, and also showed enhanced stress-strain curve tailorability by incorporating gradient labels in the ML pipeline, enabling advanced curve features with programmed stepwise energy absorption. Moreover, our ML approach permits optimized structures to be produced with less experimental testing and fast evaluation time. Indeed, a nonlinear stress–strain curve can be analyzed and inversely designed into a 3D digital model from a typical consumer desktop computer within a few seconds with the reported approach, compared to simulations and optimization approaches that would otherwise take days without even taking full account of manufacturing variabilities. Furthermore, while the current work is limited to design compressive behaviors, our ML pipeline could be adapted to inverse-design other mechanical responses separately or simultaneously, when accompanied with a family of training data of which each describes a specific loading case (e.g., tensile, compressive, bending, shear, and so on). This is attributed to the fact that the stress-strain curve was adopted as the input, which can describe mechanical behaviors under other types of loading. We also envision that our ML strategy is not limited to mechanical behaviors and can be extended to other complex behavior such as acoustic, magnetic, and electromechanical responses when such responses are expressed in form of a curve similar to the stress-strain curve (e.g., absorbance-frequency, magnetization-magnetic field, polarization-voltage and so on). This work represents progress toward a rapid inverse design and manufacturing methodology that allows for prescribing the full spatial and temporal behaviors of a product that can be printed via a simple desktop computer. It has direct implications for future development of protective wears, automobile and aircraft parts, energy absorbers and smart materials via simplified design-manufacturing cycle.

Chapter 6 Conclusion and future work

6.1 Conclusion and answering the research questions

This dissertation present the design of effective behaviors via optimizing the formulation of base material feedstock and manipulating the micro-architecture of the functional metamaterials. The developed design methodologies addressed the challenges that constraints the accurate creation of functional responses with AM.

One critical constraints of designing functional responses is precisely characterizing the constitutive composite material properties. The functionality-processibility tradeoff hinders the feedstock formulation with high concentration of functional phases. Surface functionalization has been employed to improve interfacial adhesion and resulting functional responses, but the mechanics of this enhancement remains elusive, which further constraints the accurate design of composite properties. The author developed a theoretical model which enables the creation of highly responsive piezoelectric materials going beyond the existing compliance and functional property tradeoff highlight their potentials as the next generation of flexible self-sensing materials and wearables.

Structural metamaterials provided a series of exotic material properties that unseen in their constitutive counterpart. However, the approach of translating the multi-physics coupling response to the concept of architectural design for the realization of new functional behaviors has not been demonstrated yet. To address this limitation, the author developed a comprehensive design framework that allows the design of functional responses via tailoring the architectural arrangement of metamaterials. With this design framework, the author demonstrated the design of

arbitrary anisotropy of piezoelectric metamaterial that exceeds the constraints of crystalline structures. Decoupled strain responses of piezoelectric metamaterial for detection of full load components was presented. Additionally, the author developed a family of robotic piezoelectric metamaterials that display all physically feasible actuation mode in any directions.

A critical constraints of existing structural metamaterial design methods is that only a few number of mechanical properties can be designed each time. This presents significant challenges in accessing advanced material behaviors like energy absorption performance. Hence, the author developed a ML based inverse design framework which enables the creation of full temporal and spatial response of structural metamaterials. The generative ML framework is also capable of realizing enhanced stress-strain curve tailorability by incorporating gradient labels in the ML pipeline, enabling advanced curve features with programmed stepwise energy absorption. This work represents progress toward a rapid inverse design and manufacturing methodology that allows for prescribing the full spatial and temporal behaviors of a product that can be printed via a simple desktop computer. It has direct implications for future development of protective wears, automobile and aircraft parts, energy absorbers and smart materials via simplified design-manufacturing cycle.

Research Question 1 How to design the formulation of functional composite feedstock to achieve desired properties?

This is achieved by selecting optimal design parameters in the property map of composite feedstock. The developed theoretical model, effective interphase model, enables the accurate characterization of functional response of composite feedstock, considering all composition parameters like concentration and morphology of the functional infill phase, interfacial interaction between infill and matrix phases, etc. Therefore, a series of property surfaces, where each surface corresponds to a specific aspect ratio of functional particles, can be generated accordingly. Given the desired properties, multiple sets of composite formulation is provided, and the optimal design parameters can be picked per requirement of structural performance in the application case.

In this dissertation, the author sketched the property design surfaces of the functionalized piezoelectric composite. With these property surfaces, the author demonstrated the highly sensitive airflow sensor and wireless self-sensing boxing gloves. The design and additive manufacturing routes allow for achieving target flexibilities while keeping high piezoelectric responses via rational designs of inclusion morphologies and monomer stiffness of the constituent materials.

Research Question 2 What is the rational of tailoring effective response of functional metamaterial with architecture design?

The key difference between homogeneous material and architected metamaterial is the strain transformation from macroscopic to local scale. Attributed to compact tessellation of the crystal units, the strain field is consistent in both macroscopic and local level. Therefore, it is impractical

to tune the functional responses of the homogeneous material. The only possible approach is to tune the crystal structure of the material. For instance, doping process enables tailoring of piezoelectric coupling behaviors via replacing the replaces the original center atom with a new element.

As the local strain field of constitutive ligaments is dependent on their spatial orientation. Therefore, structural metamaterial allows the strain transformation via manipulating the spatial arrangement of each ligaments. Coupling with the functional response of constitutive material, the effective functional response contribution of individual struts can be tuned accordingly. Therefore, designing the micro-architecture of metamaterials enables the tailoring the effective functional responses.

In this dissertation, the author demonstrated the design of anisotropy, decoupled strain response , and arbitrary actuation mode of piezoelectric metamaterial with this comprehensive design methodology.

Research Question 3 What is the purpose of designing full material response in temporal domain? Why ML based method is required?

The full material response under external loading, denoted by a stress-strain curve, encodes all mechanical behaviors of a material. Therefore, engineering the stress-strain curve enables the manipulation of the entire deformation path of the material and corresponding mechanical behaviors in both linear and nonlinear regime. While, existing design methods is capable of capturing a few mechanical responses of metamaterials.

The theoretical design approaches, established on the basis of force equilibrium, only provide valid prediction of mechanical properties of a material within linear deformation regime (i.e., elastic modulus and yield strength). These approach can't capture the nonlinear behavior of a material, due to the complexity of the deformation process, like energy absorption performance which is a critical index in certain application scenarios.

Topology optimization, a numerical design approaches built on iterative process of FEA and design adjustment, might be able to design certain nonlinear behavior of the material. While, extensive preparation to adjust simulation setup for reliable results, and an effective design adjustment algorithm is required. Additionally, achieving the design satisfying requirements of multiple behaviors is not guaranteed, as multi-objective optimization does not provide a unique solution for every case.

Machine learning design methods, which employ complex mathematical model and data propagation algorithm, are capable of learning the intrinsic correlation between the architecture and the deformation of the material. Therefore, with property manipulation and good training data, the ML model can create arbitrary mechanical responses of interest. The complexity of design task scales up with the number of target behaviors.

In this dissertation, the author presented a generative ML design framework capable of creating the full temporal and spatial mechanical responses of a material. With proper encoding strategy, the ML learns the relationship between the stress-strain curves with the design parameters of the metamaterial. The developed ML framework also enables the access of designing advanced mechanical behaviors, like energy absorption, with enhanced tailorability.

6.2 Future work

1. Integration of multiple functionalities into 3D printable materials will enable the fabrication smart devices working as a complex system with various functions. To this end, further research is needed to characterize the interaction between functionalities and to design the formulation for optimal effective performances. One critical challenge of integrating multiple functionalities is the interference between different physical quantities. For instance, piezoelectric material induces electric charge accumulation when subject to mechanical loads. The accumulated charge will generate electro-magnetic field, which might affect the performance of magnetic particles in the composite. Therefore, the interactions between different functionalities should be considered for additively manufactured materials with multiple functionalities.

2. Consider a multi-functional metamaterial as a smart devices that can process the input information with prescribed functions. When subject to external stimuli, or information input, the effective information processing procedure happens in a timed manner. In other words, the functions should be carried out in a desired sequence, a combination of sequential and parallel process. Current functional metamaterial respond to the external stimuli at the moment of loaded. The potential direction of future research is to program the working sequence of different functionalities in the metamaterial with architectural design. Realization of programmable working sequence will open up the new application of functional metamaterial. The additively manufactured multi-functional metamaterials will replace the existing integrated system like MEMS.

3. In this dissertation, the design of base material properties and architecture of functional

metamaterial is demonstrated in sequence. The architectural design is achieved on the basis of obtained base material properties. The future research could focus on the integrated design of constitutive material behaviors and architectural structure. To achieve a desired function responses, the composite feedstock and architecture is designed simultaneously. The interaction between these two contributing factors might provide novel material responses. Attributed to the complex physics of this interaction, machine learning design framework will be employed to achieve this task. One potential challenge of this task is the uniqueness of the design. Similar to the inverse design task in this dissertation, a forward module can be attached to validate the deviation of the designs.

Reference

1 Lakes, R. Foam structures with a negative Poisson's ratio. *Science* **235**, 1038-1041 (1987).

2 Prall, D. & Lakes, R. Properties of a chiral honeycomb with a Poisson's ratio of -1. *International Journal of Mechanical Sciences* **39**, 305-314 (1997).

3 Buckmann, T. *et al.* On three-dimensional dilational elastic metamaterials. *New Journal of Physics* **16**, 033032 (2014).

4 Grima, J., Attard, D. & Gatt, R. Truss-type systems exhibiting negative compressibility. *Phys. Status Solidi B* **245**, 2405-2414 (2008).

5 Lakes, R. & Wojciechowski, K. Negative compressibility, negative Poisson's ratio, and stability. *Phys. Status Solidi B* **245**, 545-551 (2008).

6 Bauer, J. *et al.* Push-to-pull tensile testing of ultra-strong nanoscale ceramic–polymer composites made by additive manufacturing. *Extreme Mechanics Letters* **3**, 105-112 (2015).

7 Zheng, X. *et al.* Multiscale metallic metamaterials. *Nat Mater* **15**, 1100-1106 (2016).

8 Meza, L., Das, S. & Greer, J. Strong, lightweight, and recoverable three-dimensional ceramic nanolattices. *Science* **345**, 1322-1326 (2014).

9 Shan, S. *et al.* Multistable architected materials for trapping elastic strain energy. *Adv. Mater.* **27**, 4296-4301 (2015).

10 Ha, C., Lakes, R. S. & Plesha, M. E. Cubic negative stiffness lattice structure for energy absorption: Numerical and experimental studies. *Int J Solids Struct* **178-179**, 127-135 (2019).

11 Wehmeyer, S. *et al.* Post-buckling and dynamic response of angled struts in elastic lattices. *J. Mech. Phys. Solids* **133**, 103693 (2019).

12 Ganilova, O. A. & Low, J. J. Application of smart honeycomb structures for automotive passive safety. *Proceedings of the Institution of Mechanical Engineers, Part D: Journal of Automobile Engineering* **232**, 797-811 (2018). https://doi.org:10.1177/0954407017708916

13 Deshpande, V. S., Ashby, M. F. & Fleck, N. A. Foam topology bending versus stretching dominated architectures. *Acta Mater* **49**, 1035-1040 (2001). https://doi.org:Doi 10.1016/S1359-6454(00)00379-7

14 Xia, L. & Breitkopf, P. Concurrent topology optimization design of material and structure within FE2 nonlinear multiscale analysis framework. *Computer Methods in Applied Mechanics and Engineering* **278**, 524-542 (2014).

15 Takezawa, A. & Kobashi, M. Design methodology for porous composites with tunable thermal expansion produced by multi-material topology optimization and additive manufacturing. *Compos. B. Eng.* **131**, 21-29 (2017).

16 Gu, G., Chen, C., Richmond, D. & Buehler, M. Bioinspired hierarchical composite design using machine learning: simulation, additive manufacturing, and experiment. *Materials Horizons* **5**, 939-945 (2018).

17 Bessa, M., Glowacki, P. & Houlder, M. Bayesian machine learning in metamaterial design: fragile becomes supercompressible. *Adv. Mater.* **31**, 1904845 (2019).

18 Bock, F. E. *et al.* A review of the application of machine learning and data mining approaches in continuum materials mechanics. *Frontiers in Materials* **6**, 110 (2019).

19 Kim, H. *et al.* 3D Printing of BaTiO3/PVDF Composites with Electric In Situ Poling for Pressure Sensor Applications. *Macromol Mater Eng* **302** (2017). https://doi.org:ARTN 1700229

10.1002/mame.201700229

20 Qi, F. W., Chen, N. & Wang, Q. Dielectric and piezoelectric properties in selective laser sintered polyamide11/BaTiO3/CNT ternary nanocomposites. *Mater Design* **143**, 72-80 (2018). https://doi.org:10.1016/j.matdes.2018.01.050

21 Mitkus, R., Piechowiak, L. & Sinapius, M. Characterization of UV Light Curable Piezoelectric 0-0-3 Composites Filled with Lead-Free Ceramics and Conductive Nanoparticles. *Journal of Composites Science* **7** (2023).

22 Maillard, F., Savinova, E. R. & Stimming, U. CO monolayer oxidation on Pt nanoparticles: Further insights into the particle size effects. *J Electroanal Chem* **599**, 221-232 (2007). https://doi.org:10.1016/j.jelechem.2006.02.024

23 Sundstrom, D. W. Viscosity of Suspensions in Polymeric Solutions. *Rheol Acta* **22**, 420-423 (1983). https://doi.org:Doi 10.1007/Bf01333774

24 Griffith, M. L. & Halloran, J. W. Freeform fabrication of ceramics via stereolithography. *J Am Ceram Soc* **79**, 2601-2608 (1996).

25 Wong, E. H., Koh, S. W., Lee, K. H. & Rajoo, R. Advanced moisture diffusion modeling & characterisation for electronic packaging. *Elec Comp C*, 1297-1303 (2002). https://doi.org:Doi 10.1109/Ectc.2002.1008273

26 Kim, K. *et al.* 3D Optical Printing of Piezoelectric Nanoparticle - Polymer Composite Materials. *Acs Nano* **8**, 9799-9806 (2014). https://doi.org:10.1021/nn503268f

27 Yang, J. *et al.* Designing electromechanical metamaterial with full nonzero piezoelectric coefficients. *Science Advances* **5**, eaax1782 https://doi.org:10.1126/sciadv.aax1782

28 Mikata, Y. Explicit determination of piezoelectric Eshelby tensors for a spheroidal inclusion. *Int J Solids Struct* **38**, 7045-7063 (2001). https://doi.org:Doi 10.1016/S0020-7683(00)00419-4

29 Kumar, A. & Chakraborty, D. Effective properties of thermo-electro-mechanically coupled piezoelectric fiber reinforced composites. *Mater Design* **30**, 1216-1222 (2009). https://doi.org:10.1016/j.matdes.2008.06.009

30 Wang, B. T. & Rogers, C. A. Laminate Plate-Theory for Spatially Distributed Induced Strain Actuators. *J Compos Mater* **25**, 433-452 (1991). https://doi.org:Doi 10.1177/002199839102500405

31 Taya, M. Electronic Composites: Modeling, Characterization, Processing, and MEMS application. *Cambridge University Press: Cambridge* (2009). https://doi.org:10.1017/CBO9780511550508

32 Hashin, Z. Theory of Fiber Reinforced Materials. *NASA, Washington, United States* (1972).

33 Nafari, A. & Sodano, H. A. Tailored nanocomposite energy harvesters with high piezoelectric voltage coefficient through controlled nanowire dispersion. *Nano Energy* **60**, 620-629 (2019). https://doi.org:10.1016/j.nanoen.2019.03.097

34 Nafari, A. & Sodano, H. A. *Voltage coefficient of a piezoelectric nanocomposite energy harvester: modeling and experimental verification*. Vol. 10973 SS (SPIE, 2019).

35 Iyer, S. & Venkatesh, T. A. Electromechanical response of (3-0,3-1) particulate, fibrous, and porous piezoelectric composites with anisotropic constituents: A model based on the homogenization method. *Int J Solids Struct* **51**, 1221-1234 (2014). https://doi.org:10.1016/j.ijsolstr.2013.12.008

36 Lin, C. H. & Muliana, A. Micromechanical models for the effective time-dependent and nonlinear electromechanical responses of piezoelectric composites. *J Intel Mat Syst Str* **25**, 1306-1322 (2014). https://doi.org:10.1177/1045389x13504477

37 Knauert, S. T., Douglas, J. F. & Starr, F. W. The effect of nanoparticle shape on polymer-nanocomposite rheology and tensile strength. *J Polym Sci Pol Phys* **45**, 1882-1897 (2007). https://doi.org:10.1002/polb.21176

38 Benveniste, Y. A New Approach to the Application of Mori-Tanaka Theory in Composite-Materials. *Mech Mater* **6**, 147-157 (1987). https://doi.org:Doi 10.1016/0167-6636(87)90005-6

39 Todd, M. G. & Shi, F. G. Characterizing the interphase dielectric constant of polymer composite materials: Effect of chemical coupling agents. *J Appl Phys* **94**, 4551-4557 (2003). https://doi.org:10.1063/1.1604961

40 Odegard, G. M. Constitutive modeling of piezoelectric polymer composites. *Acta Mater* **52**, 5315-5330 (2004). https://doi.org:10.1016/j.actamat.2004.07.037

41 Mori, T. & Tanaka, K. Average Stress in Matrix and Average Elastic Energy of Materials with Misfitting Inclusions. *Acta Metall Mater* **21**, 571-574 (1973). https://doi.org:Doi 10.1016/0001-6160(73)90064-3

42 Kim, H., Fernando, T., Li, M. Y., Lin, Y. R. & Tseng, T. L. B. Fabrication and characterization of 3D printed BaTiO3/PVDF nanocomposites. *J Compos Mater* **52**, 197-206 (2018). https://doi.org:10.1177/0021998317704709

43 Odegard, G. M., Clancy, T. C. & Gates, T. S. Modeling of the mechanical properties of nanoparticle/polymer composites. *Polymer* **46**, 553-562 (2005). https://doi.org:10.1016/j.polymer.2004.11.022

44 Fischer-Cripps, A. C. Nanoindentation Testing. *Mech Eng Ser*, 21-37 (2011). https://doi.org:10.1007/978-1-4419-9872-9_2

45 Hodzic, A., Stachurski, Z. H. & Kim, J. K. Nano-indentation of polymer-glass interfaces Part I. Experimental and mechanical analysis. *Polymer* **41**, 6895-6905 (2000). https://doi.org:Doi 10.1016/S0032-3861(99)00890-3

46 Nano Indenter II Operating Instructions. *Nano Instruments Inc.*, (1995).

47 Bhushan, B. Handbook of micro/nanotribology. *Boca Raton: CRC Press* (1995).

48 COMSOL Multiphysics. 2008b. *COMSOL Multiphysics Modeling Guide: Version 5.3*, Stockholm, Sweden: COMSOLAB.

49 Kar-Gupta, R. & Venkatesh, T. A. Electromechanical response of piezoelectric composites: Effects of geometric connectivity and grain size. *Acta Mater* **56**, 3810-3823 (2008). https://doi.org:10.1016/j.actamat.2008.04.031

50 Cui, H. C. *et al.* Three-dimensional printing of piezoelectric materials with designed anisotropy and directional response. *Nat Mater* **18**, 234-+ (2019). https://doi.org:10.1038/s41563-018-0268-1

51 Sperling, R. A. & Parak, W. J. Surface modification, functionalization and bioconjugation of colloidal inorganic nanoparticles. *Philos T R Soc A* **368**, 1333-1383 (2010). https://doi.org:10.1098/rsta.2009.0273

52 Jabbari, M. & Hattel, J. Bingham plastic fluid flow model in tape casting of ceramics using two doctor blades - analytical approach. *Mater Sci Tech-Lond* **30**, 283-288 (2014). https://doi.org:10.1179/1743284713y.0000000313

53 Kim, H. *et al.* Integrated 3D printing and corona poling process of PVDF piezoelectric films for pressure sensor application. *Smart Materials and Structures* **26** (2017). https://doi.org:ARTN 085027

10.1088/1361-665X/aa738e

54 El Ouafi, J., Azrar, L. & Aljinaidi, A. A. Analytical and semi-analytical modeling of effective moduli bounds: Application to transversely isotropic piezoelectric materials. *J Intel Mat Syst Str* **27**, 1600-1623 (2016). https://doi.org:10.1177/1045389x15600081

55 Kim, K. *et al.* Tunable Surface and Matrix Chemistries in Optically Printed (0-3) Piezoelectric Nanocomposites. *Acs Appl Mater Inter* **8**, 33394-33398 (2016). https://doi.org:10.1021/acsami.6b12086

56 Grinberg, D. *et al.* 4D Printing based piezoelectric composite for medical applications. *Journal of Polymer Science Part B: Polymer Physics* **57**, 109-115 (2019). https://doi.org:10.1002/polb.24763

57 Tiller, B. *et al.* Piezoelectric microphone via a digital light processing 3D printing process. *Mater Design* **165** (2019). https://doi.org:ARTN 107593

10.1016/j.matdes.2019.107593

58 Park, J. I., Lee, G. Y., Yang, J., Kim, C. S. & Ahn, S. H. Flexible ceramic-elastomer composite piezoelectric energy harvester fabricated by additive manufacturing. *J Compos Mater* **50**, 1573-1579 (2016). https://doi.org:10.1177/0021998315577685

59 Chen, X. F. *et al.* The development of an all-polymer-based piezoelectric photocurable resin for additive manufacturing. *Proc Cirp* **65**, 157-162 (2017). https://doi.org:10.1016/j.procir.2017.04.025

60 Yamaguchi, M., Hashimoto, K. Y. & Kogo, H. Elastic, Piezoelectric and Dielectric-Properties of Composite-Materials. *Ieee T Ultrason Ferr* **34**, 425-426 (1987).

61 Glushanin, S., Topolov, V. Y. & Krivoruchko, A. V. Features of piezoelectric properties of 0-3 PbTiO3-type ceramic/polymer composites. *Mater Chem Phys* **97**, 357-364 (2006). https://doi.org:10.1016/j.matchemphys.2005.08.027

62 Huang, J. H. & Kuo, W. S. Micromechanics determination of the effective properties of piezoelectric composites containing spatially oriented short fibers. *Acta Mater* **44**, 4889-4898 (1996). https://doi.org:Doi 10.1016/S1359-6454(96)00090-0

63 Bowen, C. R. Electromechanical Properties in Composites Based on Ferroelectrics. *Eng Mater Process*, 1-202 (2009).

64 Nix, E. L. & Ward, I. M. The measurement of the shear piezoelectric coefficients of polyvinylidene fluoride. *Ferroelectrics* **67**, 137-141 (1986). https://doi.org:10.1080/00150198608245016

65 Wang, H., Zhang, Q. M., Cross, L. E. & Sykes, A. O. Piezoelectric, dielectric, and elastic properties of poly(vinylidene fluoride/trifluoroethylene). *J Appl Phys* **74**, 3394-3398 (1993). https://doi.org:10.1063/1.354566

66 Wan Hu, J. & Park, T. *Continuum Models for the Plastic Deformation of Octet-Truss Lattice Materials Under Multiaxial Loading*. Vol. 135 (2013).

67 Cui, H. C., Hensleigh, R., Chen, H. S. & Zheng, X. Y. Additive Manufacturing and size-dependent mechanical properties of three-dimensional microarchitected, high-temperature ceramic metamaterials. *J Mater Res* **33**, 360-371 (2018). https://doi.org:10.1557/jmr.2018.11

68 Challagulla, K. S. & Venkatesh, T. A. Electromechanical response of piezoelectric foams. *Acta Mater* **60**, 2111-2127 (2012). https://doi.org:10.1016/j.actamat.2011.12.036

69 Singhal, N., Sharma, M. & Mangal, S. K. Optimal placement of piezoelectric patches over a smart structure. *Integr Ferroelectr* **183**, 60-90 (2017). https://doi.org:10.1080/10584587.2017.1375823

70 Annamdas, V. G. M. & Soh, C. K. Influence of Loading on the Near Field Based Passive Metamaterial in Structural Health Monitoring. *Struct Hlth Monit*, 633-640 (2015).

71 in *Mechanics of Deformable Bodies* (ed Arnold Sommerfeld) (Academic Press, 1950).

72 Eringen, A. C. in *Microcontinuum Field Theories: I. Foundations and Solids* (ed A. Cemal Eringen) 101-248 (Springer New York, 1999).

73 Li, Z. *et al.* Designing Artificial Vibration Modes of Piezoelectric Devices Using Programmable, 3D Ordered Structure with Piezoceramic Strain Units. *Adv Mater* **34**, 2107236 (2022). https://doi.org:https://doi.org/10.1002/adma.202107236

74 Gibson, I. & Ashby, M. F. The mechanics of three-dimensional cellular materials. *Proceedings of the royal society of London. A. Mathematical and physical sciences* **382**, 43-59 (1982).

75 Hashin, Z. & Shtrikman, S. A variational approach to the theory of the elastic behaviour of multiphase materials. *J Mech Phys Solids* **11**, 127-140 (1963).

76 Suquet, P. Overall potentials and extremal surfaces of power law or ideally plastic composites. *J Mech Phys Solids* **41**, 981-1002 (1993).

77 Oliphant, T. *A guide to NumPy*. (Trelgol Publishing USA, 2006).

78 Virtanen, P. *et al.* SciPy 1.0: fundamental algorithms for scientific computing in Python. *Nat. Methods* **17**, 261-272 (2020).

79 McKinney, W. pandas: a foundational Python library for data analysis and statistics. *Python for High Performance and Scientific Computing* **9**, 14 (2011).

80 Schutt, K. *et al.* How to represent crystal structures for machine learning: Towards fast prediction of electronic properties. *Phys. Rev. B* **89**, 205118 (2014).

81 Savitzky, A. & Golay, M. Smoothing and differentiation of data by simplified least squares procedures. *Anal. Chem.* **36**, 1627-1639 (1964).

82 Tancogne-Dejean, T., Diamantopoulou, M., Gorji, M. B., Bonatti, C. & Mohr, D. 3D Plate-Lattices: An Emerging Class of Low-Density Metamaterial Exhibiting Optimal Isotropic Stiffness. *Adv Mater* **30**, 1803334 (2018).

83 Crook, C. *et al.* Plate-nanolattices at the theoretical limit of stiffness and strength. *Nature communications* **11**, 1-11 (2020).

84 Onck, P., Andrews, E. & Gibson, L. Size effects in ductile cellular solids. Part I: modeling. *International Journal of Mechanical Sciences* **43**, 681-699 (2001).

85 Andrews, E., Gioux, G., Onck, P. & Gibson, L. Size effects in ductile cellular solids. Part II: experimental results. *International Journal of Mechanical Sciences* **43**, 701-713 (2001).

86 Morrish, S., Pedersen, M., Wong, K., Todd, I. & Goodall, R. Size effects in compression in Electron Beam Melted Ti6Al4V diamond structure lattices. *Materials Letters* **190**, 138-142 (2017).

87 Chawla, N. V., Bowyer, K. W., Hall, L. O. & Kegelmeyer, W. P. SMOTE: Synthetic Minority Over-sampling Technique. *Journal of Artificial Intelligence Research* **16**, 321-357 (2002). https://doi.org:10.1613/jair.953

88 Mazur, M. *et al.* Deformation and failure behaviour of Ti-6Al-4V lattice structures manufactured by selective laser melting (SLM). *The International Journal of Advanced Manufacturing Technology* **84**, 1391-1411 (2016).

89 Liu, L., Kamm, P., García-Moreno, F., Banhart, J. & Pasini, D. Elastic and failure response of imperfect three-dimensional metallic lattices: the role of geometric defects induced by Selective Laser Melting. *J Mech Phys Solids* **107**, 160-184 (2017).

90 Hitzler, L. *et al.* On the anisotropic mechanical properties of selective laser-melted stainless steel. *Materials* **10**, 1136 (2017).

91 Xiao, Z. *et al.* Evaluation of topology-optimized lattice structures manufactured via selective laser melting. *Mater Design* **143**, 27-37 (2018).